

NORTHUMBRIA UNIVERSITY

DOCTORAL THESIS

Radiative and diffusive instabilities in moving fluids

Author:
Joris LABARBE

Supervisor:
Dr. Oleg N. KIRILLOV

*A thesis submitted in fulfillment of the requirements
for the degree of Doctor of Philosophy
in the*

Department of Mathematics, Physics and Electrical Engineering

August 27, 2021

“Le seul véritable voyage, le seul bain de Jouvence, ce ne serait pas d’aller vers de nouveaux paysages, mais d’avoir d’autres yeux, de voir l’univers avec les yeux d’un autre, de cent autres, de voir les cent univers que chacun d’eux voit, que chacun d’eux est [...]”

Marcel Proust, *La prisonnière*

NORTHUMBRIA UNIVERSITY

Abstract

Faculty of Engineering and Environment
 Department of Mathematics, Physics and Electrical Engineering

Doctor of Philosophy

Radiative and diffusive instabilities in moving fluids

by Joris LABARBE

Radiation and diffusion are inherent phenomena in Nature that anyone of us already witnessed in the form of, e.g., the propagation of gravity waves at the surface of water or the thermal conduction in solid structures. A certain emission of energy is evidently associated with the presence of damping in all sorts of dynamical systems, from the simplest spring-mass configurations to the more complex stellar structures. For instance, as historically predicted for the model of a rotating self-gravitating mass of fluid, presence of dissipation in the form of viscosity may lead to the onset of a secular instability, in the form of oscillatory motions. This discovery is nowadays well-accepted as the first illustration of the so-called *dissipation-induced instability*, a particular sort of instability arising in the presence of damping. A similar effect can be encountered in the context of the emission of waves carrying modes of opposite energy sign and yields the analogue *radiation-induced instability*. We propose hereafter along this thesis to present a selection of problems involving radiative or diffusive mechanisms and to carry out an exhaustive linear stability analysis on them. Respectively, the different chapters are ordered as referring to the stability of the Maclaurin spheroids, the lenticular vortices, the rotating magnetohydrodynamics flows and the fluid-structure interactions of an elastic membrane with a uniform potential flow. A particular attention will be addressed to systems subject to two simultaneous dissipative mechanisms, in order to estimate the predominance of the damped mode of importance. By means of various analytical treatments, as well as supporting numerical methods, we manage to solve the different boundary value problems associated with each system and thus establish new stability criteria in the spaces of parameters. The developed methods remain general in their formulation and are not solely designed to only solve the problems of interest. As a matter of fact, one can easily adapt our approach to a broad range of applications.

Contents

Abstract	v
Acknowledgements	xv
Declaration of Authorship	xvii
Introduction	1
I Dissipation-induced instabilities in rotating flows	5
1 Secular instabilities of Maclaurin spheroids	7
1.1 Historical Context	7
1.2 Characteristic equation in the post-Newtonian approximation	9
1.3 Stability of undamped spheroids	11
1.4 Double-diffusive CFS instability	13
1.5 Instability windows and Whitney's umbrella	18
1.6 Conclusion	22
1.A Expansion of the Hurwitz determinant	24
1.B Characteristic polynomial of Comins (1979)	24
2 Dissipation-induced instabilities of lenticular vortices	29
2.1 Introduction	30
2.2 Equations of a rotating and stratified fluid	31
2.2.1 Density stratification	31
2.2.2 Dimensional equations of motion	31
2.2.3 Non-dimensionalization	32
2.3 Steady state	33
2.4 Linearized equations of motion	35
2.5 Geometrical optics approximation	35
2.6 Dispersion relation	38
2.6.1 Diffusionless and $Sc = 1$ cases	40
Centrifugal instability of a barotropic circular vortex	40
Connection to Acheson and Gibbons Acheson and Gibbons, 1978	41
2.6.2 Particular cases when either $\gamma_1 = 0$ or $\gamma_2 = 0$	42
2.7 General stability analysis	43
2.7.1 Bilharz algebraic criterion	43
2.7.2 Stationary and oscillatory axisymmetric instabilities	44
A codimension-2 point on the neutral stability line	44

2.7.3	Exchange of stationary and oscillatory instabilities	47
2.7.4	OA as a genuine dissipation-induced instability	48
2.7.5	Sufficient conditions for the vortex stability at any $Sc > 0$	48
2.8	Conclusion	49
3	Double-diffusive instabilities in magnetohydrodynamic flows	51
3.1	Introduction	53
3.1.1	Standard magnetorotational instability	53
3.1.2	Helical and azimuthal MRI and Tayler instability	54
3.1.3	The Hain-Lüst equation and its extensions	54
3.1.4	Overview of the article	55
3.2	Extending the Hain-Lüst equation	55
3.3	Dispersion relation in short radial wavelength approximation	56
3.4	Axisymmetric perturbations	57
3.4.1	Standard MRI in the ideal MHD and beyond	57
3.4.2	Helical MRI in the limit $Pm \rightarrow 0$	58
3.5	Nonaxisymmetric perturbations	58
3.5.1	Weak field	59
3.5.2	Strong field	59
The limit $\hat{k} \rightarrow 0$	60
The limit $\hat{k} \rightarrow \infty$	60
Growth rate optimized by \hat{k} and \hat{q}	61
Evolution of AMRI region in the (Ro, Rb) -plane with \hat{k}	61
3.5.3	Tayler instability in the limit of $Pm \rightarrow 0$	62
3.6	AMRI and Tayler instability at finite Pm	64
3.6.1	Case of $Ro = Rb = -1$ and $m = 1$ with $q = 3r_0^{-1}$	65
3.6.2	Case of $Ro = Rb = -1/2$ and $m = 1$ with $q = 3r_0^{-1}$	66
3.6.3	Case of $Ro = -3/4$, $Rb = -1$ and $m = 1$ with $q = 3r_0^{-1}$	67
3.7	Global stability analysis	68
3.7.1	Background fields and Rossby numbers	68
3.7.2	Pseudospectral expansion	69
3.7.3	Numerical results	69
3.8	Conclusion	71
3.A	Derivation of Eq.(14)	72
3.B	Connection to Ref.[43]	72
3.C	Connection to Ref.[63]	73
II	Radiation-induced instabilities in flow-structure interactions	75
4	Radiative instability of an infinite Nemytsov membrane	77
4.1	Introduction	80
4.2	Model of a membrane interacting with a free surface	82
4.2.1	Physical system	82
4.2.2	Dimensionless mathematical model	84
4.3	Methods and results	85

4.3.1	Membrane of infinite chord length	85
	Dispersion relation for the fluid layer of arbitrary depth	86
	Analysis of the dispersion relation	88
	Wave energy of the Nemtsov system for membrane of infinite chord length	96
4.4	Discussion	100
4.5	Conclusion	102
4.A	Sensitivity analysis of dispersion relation	104
	4.A.1 Sensitivity of simple roots	104
	4.A.2 Double root of the dispersion relation: generic case	105
	4.A.3 Double root of the dispersion relation: degenerate case	106
4.B	References	107
5	Radiative instability of a finite Nemtsov membrane	111
5.1	Introduction	114
5.2	Mathematical formulation	118
	5.2.1 Velocity potential via inverse Fourier transform	119
	5.2.2 Integro-differential equation for membrane's deflection	119
5.3	Shallow water analysis of the finite-chord Nemtsov membrane	120
	5.3.1 Velocity potential in the shallow water limit	120
	5.3.2 Explicit form of the velocity potential by means of residue calculus	121
	5.3.3 Explicit expression for the membrane displacement by means of Laplace transform	122
	5.3.4 Integral eigenfrequency relation	123
	5.3.5 Perturbation of eigenfrequencies	123
	5.3.6 Stability diagrams in the shallow water limit	124
	5.3.7 Exploring fluid dynamics analogy to superlight normal and inverse Doppler effects	127
5.4	Deep water limit of the finite-chord Nemtsov membrane	129
5.5	The finite-chord Nemtsov membrane in the finite-depth layer	131
	5.5.1 Counting and localizing the poles of a non-polynomial integrand in the integro-differential equation	132
	5.5.2 Galerkin discretization and reduction to an algebraic nonlinear eigenvalue problem	134
	5.5.3 Jacobian of the nonlinear matrix pencil $\mathcal{F}(\omega)$	135
	5.5.4 Numerical evaluation of the integral in (88)	136
	5.5.5 Newton-like numerical method for solving the nonlinear eigenvalue problem	137
	5.5.6 Stability maps for the finite-chord Nemtsov membrane in the finite-depth flow	139
5.6	Concluding remarks	141
Conclusion		145
Bibliography		147

List of Figures

1.1	Spectral analysis of the undamped Maclaurin spheroids	12
1.2	Spectral analysis of the viscous Maclaurin spheroids	14
1.3	Spectral analysis of the double-diffusive Maclaurin spheroids	14
1.4	Movement of eigenvalues for the undamped and damped Maclaurin spheroids	15
1.5	Critical eccentricity over χ and Taylor expansion around e_0 . .	17
1.6	Whitney's umbrella and cross-section of the stability domain .	18
1.7	Generalized undamped f -modes of spheroids for arbitrary azimuthal wavenumbers m	19
1.8	Instability window for a model of neutron star – representation of the critical angular frequency over the temperature . .	22
2.1	Illustrative pictures of stratified lenticular vortices encountered in Nature	30
2.2	Stability maps with codimension-2 points for various values of Sc	40
2.3	Loci of the codimension-2 points for $Ek = 1$	44
2.4	Growth rates and frequencies for $m = 0$, $Ek = 1$, $Ro = 1$, and various values of γ_1 and γ_2	45
2.5	Stability maps for $Ek = 1$ and various values of γ_1 , γ_2 and Sc .	46
2.6	Parabolic envelope for $Ek = 1$	47
3.1	Growth rate over \hat{k} for various values of Rb	59
3.2	Growth rate over the azimuthal Hartmann number Ha_θ for $\hat{k} \rightarrow 0$	60
3.3	Growth rate over the azimuthal Hartmann number Ha_θ for $\hat{k} \rightarrow \infty$	61
3.4	Growth rate over the magnetic Rossby number Rb	61
3.5	Stability maps in the Rossby plane Rb , Ro for various values of \hat{k}	62
3.6	Regions of Tayler instability in the m , Rb -plane for $\hat{q} = 0$. .	64
3.7	Regions of Tayler instability in the m , Rb -plane for $\hat{q} = 3$. .	64
3.8	AMRI regions in the Ha_{θ_1} , Re_1 -plane for various values of Pm	65
3.9	Maximized over k growth rate versus Ha_{θ_1} for various values of Re_1	66
3.10	Instability regions in the Ha_{θ_1} , Re_1 -plane for various values of Pm	66
3.11	Maximized over k growth rate versus Ha_{θ_1}	67
3.12	AMRI regions in the Ha_{θ_1} , Pm -plane for various values of Re_1	67
3.13	Instability regions in the Ha_{θ_1} , Re_1 -plane for various values of Pm	68

3.14	Growth rate over the magnetic Rossby number Rb computed from the Hain-Lüst equation and the numerical solution of the BVP in different wavelength limits	69
3.15	Growth rate over the wavenumber k computed from the Hain-Lüst equation, WKB approximation and the numerical solution of the BVP in different wavelength limits	70
3.16	Stability maps in the Rossby plane Rb, Ro computed from the Hain-Lüst equation and the numerical solution of the BVP in different wavelength limits	70
4.1	Sketch of the Nemtsov system	83
4.2	Dispersion curves of the membrane with infinite extension for various values of the parameter α	89
4.3	Real and imaginary parts of the roots of the dispersion relation over M with their approximation	91
4.4	Stability maps in the different parameter spaces with the approximations around the crossings	92
4.5	Stability maps in the (M_w, β) -plane for various values of wavenumbers κ with their approximations	93
4.6	Real and imaginary parts of the roots of the dispersion relation over M_w with their approximation	94
4.7	Stability map in the (M_w, κ) -plane and the associated conical singularity with its approximation	94
4.8	Cross-sections of the neutral stability surface with their approximations	96
4.9	Averaged wave energy and mode over M for various values of the parameter α	100
4.10	Averaged wave energy and mode over M_w for various values of the wavenumber κ	100
4.11	Dispersion curves over the wavenumber κ for various values of M_w	102
5.1	Sketch of the Nemtsov system with views from aside and from above	120
5.2	Instability regions in the (M_w, M) -plane for the shallow water limit with various membrane modes n	125
5.3	Growth rate of perturbed frequencies of the shallow water membrane over M	126
5.4	Stability maps in the (μ, M) -plane for the shallow water limit with various membrane modes n	127
5.5	Surface ‘modes’ of the fluid layer for fixed value of ω	128
5.6	Instability domain in the (M, Γ) -plane and growth rate over M for the deep water limit	131
5.7	Convergence of integral ν over the radius R for different pairs of ω and M	132
5.8	Convergence of the roots of finite-depth dispersion relation to the roots of shallow and deep water limits over the membrane length Γ	133

5.9	Stability maps in the (M_w, M) -plane for the finite-depth layer with various membrane modes n	136
5.10	Stability maps in the (μ, M) -plane for the finite-depth layer with various membrane modes n	137
5.11	Instability domains of the finite-depth system and finite-chord membrane in the (Γ, M) -plane with various membrane modes n and zooms on the panels	138
5.12	Finite-depth growth rate comparison with shallow water solution as $\Gamma \rightarrow \infty$	138
5.13	Instability domains of the finite-depth system and finite-chord membrane in the (Γ, M) -plane with various membrane modes n and comparison of growth rates of finite-depth and shallow water solution as $\Gamma \rightarrow \infty$	139
5.14	Instability domains of the finite-depth system and finite-chord membrane in the (Γ, M) -plane with various membrane modes n and zooms on the panels	140

Acknowledgements

First and foremost, I am undoubtedly grateful to my supervisor and mentor, Oleg, with whom this thesis has been nothing but a pleasant journey. I am still impressed by the ideas you can develop during your research, always trying to go further from the simple statement and to connect the different communities altogether. I really enjoyed all the moments we shared discussing about science, or about life in general and I assume it made me not only a better scientist, but a better person in general. Many thanks for everything, I am convinced that we will be able to work together again in the future and I am looking forward to this moment.

I would also like to thank the members of my panel at Northumbria, Gert, Stephane, and Richard, for their support and their help. In general, I am grateful to Northumbria University for all the aid they provided to me and for allowing me access to the different facilities when I needed. A special mention to Jimmy Gibson, who helped me accessing the HPC cluster and gave me experience with parallel computing. Thank you also to the members of the PhD office in the Mathematics department, we shared some nice moments though the pandemic restrained us to meet again in this room. I wish you all the best for the future.

Many thanks to all my friends in Newcastle-upon-Tyne, especially from my accommodation, it was wonderful to meet you and to go through this experience by your side. We supported each other during the difficult times of the pandemic, and I am grateful today to know every one of you. Now I carry a long list of countries to visit, to meet all of you again in the future.

Obviously, I am indebted to my friends from France who not only supported me through this PhD, but since the day I met them. I cannot list you all but please remember that I care for each of you. Thank you, Maxime, and Paul, to always be here for me, I know that wherever I could go I will always find you two sooner or later. I consider you as my brothers and I wish both of you the best in your life.

Last but not least, I would like to thank the persons without whom nothing would have ever been possible, my family. Many thanks to my parents for their love and wisdom, for constantly supporting me regardless of the decisions I would make and for always cheering me. Thank you also to my brother for everything, you always inspired me, and I know we will continue to share good moments whenever I will see you.

This thesis is not my achievement, but the one of every persons mentioned in this memoir and I could only say one more word to all of you ...

Merci

Declaration of Authorship

I, Joris LABARBE, declare that this thesis titled, "Radiative and diffusive instabilities in moving fluids" and the work presented in it are my own. I confirm that:

- This work was done wholly or mainly while in candidature for a research degree at this University.
- Where any part of this thesis has previously been submitted for a degree or any other qualification at this University or any other institution, this has been clearly stated.
- Where I have consulted the published work of others, this is always clearly attributed.
- Where I have quoted from the work of others, the source is always given. With the exception of such quotations, this thesis is entirely my own work.
- I have acknowledged all main sources of help.
- Where the thesis is based on work done by myself jointly with others, I have made clear exactly what was done by others and what I have contributed myself.
- Any ethical clearance for the research presented along this thesis has been approved. Approval has been sought and granted through the Researcher's submission to Northumbria University's Ethics Online System/external committee on August 29th, 2019.

I declare that the Word Count of this Thesis is 34,067 words.

Signed: JORIS LABARBE

Date: AUGUST 27, 2021

Dedicated to my family

Introduction

Radiation and dissipation within dynamical systems are natural and ineluctable phenomena arising in a broad class of physical applications and leading to counter-intuitive concepts. Historically, dissipation of energy has for a long time been thought to act as a damping effect in oscillatory systems, due to viscous drag or electrical resistance to name a few illustrations. Despite this general belief, Kelvin and Tait have argued that viscosity could possibly destroy relative motions within a dynamical system consisting in a homogeneous mass of fluid in self-gravitation and hence leads to unstable configuration (Kelvin and Tait, 1867). This well-known problem is that of the so-called Maclaurin spheroid, the most stable configuration of rotating liquid ellipsoids subject to no other forces than its gravitational field. This seminal work thus led to the first formal proof for the occurrence of instability due to the presence of dissipation – in the form of viscosity here – for an oscillatory system. Such phenomenon is nowadays well-accepted under the designation of '*dissipation-induced instabilities*' and is inherent to a large range of domains of application, e.g., meteorology with the Holopäinen instability of atmospheric baroclinic flows (Holopäinen, 1961), solid mechanics with the Ziegler destabilization paradox of the Pflüger column (Bigoni et al., 2018) or even quantum mechanics with nonstationary longtime dynamics observed in a two-component Bose-Einstein condensate coupled to an optical cavity (Buća and Jaksch, 2019). Although several methods exist for the detection of such form of instability, it has been proven that spectral methods – namely the study of the spectrum of the linearized operator – are a powerful tool in this situation. We will thence be using such approach among the different projects constituting this manuscript. In the case of Maclaurin spheroids, it is worth mentioning that the secular instability due to the presence of viscosity – predicted by Kelvin and Tait (Kelvin and Tait, 1867) – has only been confirmed analytically in 1963 by Roberts and Stewartson, nearly a century after the publication of this conjecture (Roberts and Stewartson, 1963). It constitutes thus an evidence that stability analysis of systems subject to this instability mechanism is a challenging topic of research.

Another surprising phenomenon related to radiation of energy away from the oscillating system has been discovered through the Lamb model in 1900 (Lamb, 1900), consisting of a semi-infinite taut string with edge directly fixed to an undamped mass-spring system. In this context, it is shown that emission of travelling waves along the string – due to the motion of the mass – yields to a decay of the vertical oscillation. Mathematically, this result is explained from to the presence of a Rayleigh dissipation term in the equations of motion. This phenomenon of radiation damping has since been acknowledged as fundamental in its description and became paradigmatic for a broad

range of finite – infinite – dimensional dynamical systems. More recently, gyroscopic versions of the Lamb model have been proposed as an evidence for the '*radiation-induced instabilities*', namely instabilities due to wave radiation. This new class of system, although conceptual in their definitions, relate to destabilizing mechanisms such as the Chandrasekhar-Friedman-Schutz (CFS) instability for rotating neutron stars, internal-gravity waves radiation in stratified vortices or membrane flutter due to fluid coupling to name a few. All these different models highlight various connections with interesting physical phenomena, gathered around the emission of waves in the medium considered.

Formally speaking, the investigation of such systems presented above is mainly based on the determination of relative Hamiltonian equilibria (Bloch et al., 2004). It is assumed in general that possessing Hamiltonian structure for a dynamical system confines its spectrum along the imaginary axis, while the system remains stable. However, departure of eigenvalues from the imaginary axis has been proved to be a direct consequence of the presence of dissipation within the system and yields loss of energy equilibrium. This observation is explained physically in terms of the presence of modes carrying negative energy inside the system. As an illustration, a wave possessing such characteristic is extracting some part of the total energy of the system, while increasing the wave energy modulus of the radiator acts in a similar way as a pump. Undoubtedly, such a mechanism is only possible in configurations breaking the equipartition of energy – defined according to the virial theorem (Maïssa, Rousseaux, and Stepanyants, 2016) – due to the presence of dissipation or the coupling with positive energy waves in a non-static system. Because the amplitude of the wave is growing as the energy is radiated away, it generates an instability of the system. We thus propose to investigate systems where such mechanism occurs and more accurately, this manuscript mainly focuses on systems involving moving fluids.

Hence, we are presenting hereafter different configurations, all subject to the same class of instabilities, but arising from various physical applications. As a first step, we illustrate in Chapter 1 the phenomenon of dissipation-induced instability through the revival of the classical CFS mechanism, from its historical formulation to its recent extension as a promising candidate for the detection of gravitational waves from single rotating stars. This study will give us the opportunity to extend the stability analysis to the case where two types of damping are present. We follow the latter chapter with the analysis of rotating stratified vortices in Chapter 2 to highlight the spontaneous emission of internal gravity waves and to better understand the destabilization of rotating ellipsoids in oceans (the so-called Meddies) with its conceptual connection to the phenomenon of gravitational waves emission in the frame of general relativity. After the review on this classical problem, we will bifurcate to another class of double-diffusive problems in Chapter 3, namely the resistive magnetohydrodynamics (MHD) equations. This system, despite being widely studied in the literature, is analyzed in the context of a Lagrangian formulation leading to a new dispersion relation, as well as previously unknown domains of instability. To illustrate the mechanism of

instability due to radiation of waves as for the Lamb model, we pursue our investigation with a fundamental problem of fluid-structure interaction in Chapter 4 for an elastic structure with infinite extension first. In addition of playing the role of an unprecedented hydrodynamical model for the understanding of anomalous Doppler effect and its connection to flutter theory, we establish this problem in the general context of radiation-induced instability. The extension of the previous study to the case when the elastic structure is assumed finite in the direction of the flow is considered in Chapter 5 and new patterns of instability are presented. We introduce in this study a general treatment for such class of systems, possibly adaptable for other related problems involving fluid-structure interaction.

It is worth mentioning that, despite arising from different fields of application, all these problems are directly related to the concepts of radiative and diffusive instabilities in their mere form. Therefore, we expect this manuscript to be appreciated as a non-exhaustive but worthwhile review on several fundamental problems of great interest for the different scientific communities involved.

Part I

Dissipation-induced instabilities in rotating flows

Chapter 1

Secular instabilities of Maclaurin spheroids

“Pour les uns, qui voyagent, les étoiles sont des guides. Pour d’autres elles ne sont rien que de petites lumières. Pour d’autres qui sont savants elles sont des problèmes.”

Antoine de Saint-Exupéry, *Le Petit Prince*

In this chapter, we introduce the reader to the valuable notion of instabilities induced by dissipation, or equivalently, from the presence of damping mechanisms. For this purpose, we present hereafter a classical problem on the stability of a hydrodynamic model of rotating stars to highlight the existence of such phenomenon and its impact.

1.1 Historical Context

Maclaurin spheroids are known to be the simplest stable configuration of a self-gravitating mass of fluid in rotation. They have been discovered in 1742 by Maclaurin, a Scottish mathematician, and primarily used to describe the ellipsoidal shape of our planet Earth (Maclaurin, 1742). These geometrical figures are defined from the eccentricity of meridional cross-sections (Chandrasekhar, 1969)

$$e = \sqrt{1 - \left(\frac{a_3}{a_1}\right)^2}, \quad (1.1)$$

where a_3/a_1 is the ratio of semi-minor to semi-major axes of the ellipsoid. Even nowadays, these structures are still well-accepted as a decent model for studying the stellar evolution of stars or planets among the astrophysical community (Glampedakis and Gualtieri, 2018). Following from the introduction of Maclaurin spheroids, other sphere-like configurations departing from the Maclaurin sequence have been found from famous scientists, such as the Jacobi or Dedekind ellipsoids to name a few. A classical monograph on the classification and analysis of these figures of equilibrium has been published

by Chandrasekhar, 1969 and remains the most reliable source of information on the subject. Hereafter along this study, our focus is directed along the stability of homogeneous figures of Maclaurin spheroids exclusively due to the existence of noteworthy physical phenomena that have been found for this particular geometry.

The first predicted instability for this class of spheroids is due to Riemann, who established in 1861 the onset of a dynamical instability when exceeding a precise value of eccentricity (Riemann, 1861). This effect is in opposition of the equilibrium observed below this threshold and yields destabilization of the spheroids in the form of oscillating motions. Slightly prior to Riemann, nearly a century after Maclaurin, Meyer and Liouville have deduced from the bifurcation of ellipsoids from Maclaurin to Jacobi sequences a critical eccentricity for this transition (Meyer, 1842; Liouville, 1851). Moreover, Kelvin and Tait proposed the hypothesis that under the presence of viscosity, damped Maclaurin spheroids may become unstable due to the radiation of energy outside the system (Kelvin and Tait, 1867). Surprisingly, the onset of this '*dissipation-induced instability*' sets exactly at the eccentricity established by Meyer and Liouville a few decades earlier. This neutral stability threshold is nowadays well-accepted as the bifurcation point towards a secular instability due to damping in the form of viscosity, as confirmed by Roberts and Stewartson (Roberts and Stewartson, 1963).

In a seminal work on the theory of gravitational radiation, Chandrasekhar rigorously proved that Maclaurin spheroids may transit to an unstable configuration while emitting gravitational waves, due to a similar mechanism of secular instability as in the case of viscous damping (Chandrasekhar, 1970a). What is further remarkable in this discovery is that it does not necessarily require to enter within the global framework of general relativity, but only necessitates to consider a sufficient approximation of Einstein's field equations (Chandrasekhar, 1970b). Such prediction, beyond its extraordinary theoretical insights in the understanding of stars evolution, is today an even more important pledge as gravitational wave events have been formally detected by LIGO and Virgo (Abbott, 2016). Although at the present all detections were due to collisions of massive binary stars and black holes, we still carry great hope in the new generation of detectors to possibly confirm the eventuality of emissions of gravitational waves from a single rotating object. One of the main candidates for such phenomenon is the Chandrasekhar-Friedman-Schutz (CFS) mechanism, which arises from Chandrasekhar secular instability and its further extension by Friedman and Schutz to the general frame of rotating neutron stars (Schutz and Friedman, 1978a; Schutz and Friedman, 1978b). In the continuation of the precedent analysis, a consideration of viscosity and gravitational radiation contributions has been examined altogether by means of perturbation theory (Lindblom and Detweiler, 1977). This study investigated the influence of each damping mechanism in the double-diffusive system to determine the predominant mode for the secular instability of Maclaurin spheroids.

We intend along this chapter to present an exhaustive review on the CFS instability of the Maclaurin spheroids subject to double-diffusive mechanisms

of both viscosity and radiation of gravitational waves and place this phenomenon into the modern context of the theory of dissipation-induced instabilities. This allows us to introduce the reader to a number of important concepts, e.g. of singularity theory, and analytical methods that will be used throughout the rest of this thesis. On the other hand, our perturbative approach leads to an original and universal treatment of the CFS that contributes in the blending of fundamental ideas into a comprehensive review that is, from the best of our knowledge, not available in the literature.

1.2 Characteristic equation in the post-Newtonian approximation

If Maclaurin spheroids are a mere model to easily examine the stability of self-gravitating masses of fluid from simplified equations of motion, even in the presence of viscosity, to include the effects due to the theory of general relativity is a challenging effort to overcome. From the *post-Newtonian* limit, originally developed by Thorne while seeking the presence of gravitational radiation in the weak-field approximation of Einstein's equations (Thorne, 1969a; Thorne, 1969b), Chandrasekhar and Esposito developed a similar approach to the equations of hydrodynamics to include the influence of damping due to radiation of gravitational waves (Chandrasekhar and Esposito, 1969b). As presented in two outstanding papers, the characteristic equation for a Maclaurin spheroid of mass M and density ρ in the presence of kinematic viscosity ν and damping term due to the emission of gravitational radiation reduces to a high-degree polynomial in the eigenvalue λ (Chandrasekhar, 1970a; Chandrasekhar, 1970b). We present such expression while reminding that it corresponds to the toroidal modes of the spheroid, namely the modes of oscillation with even parity as derived from the second-order virial equations (Chandrasekhar, 1969). Written in terms of a polynomial matrix pencil \mathcal{L} for the eigenvalue λ , it yields

$$\mathcal{L}(\lambda) = \lambda^2 \mathcal{M} + \lambda (\mathcal{G} + \mathcal{D}) + \mathcal{K} + \mathcal{N}(\lambda) = 0, \quad (1.2)$$

where \mathcal{M} and \mathcal{K} are symmetric mass and stiffness matrices, respectively,

$$\mathcal{M} = \begin{pmatrix} 1 & 0 \\ 0 & 1 \end{pmatrix}, \quad \mathcal{K} = \begin{pmatrix} 4b - 2\Omega^2 & 0 \\ 0 & 4b - 2\Omega^2 \end{pmatrix},$$

with expressions b and Ω defined later in this section. Matrix \mathcal{G} is a skew-symmetric gyroscopic matrix given by

$$\mathcal{G} = \frac{5}{2} \begin{pmatrix} 0 & -\Omega \\ \Omega & 0 \end{pmatrix}.$$

The matrices \mathcal{D} and \mathcal{N} in pencil (1.2) represent the nonconservative effects due to viscous dissipation and gravitational radiation reaction. Explicitly,

these matrices read

$$\mathcal{D} = \begin{pmatrix} 10\mu + 16\delta\Omega^2(6b - \Omega^2) & -3\Omega/2 \\ -3\Omega/2 & 10\mu + 16\delta\Omega^2(6b - \Omega^2) \end{pmatrix},$$

$$\mathcal{N} = \delta \begin{pmatrix} 2q_1 & 2q_2 \\ -q_2/2 & 2q_1 \end{pmatrix},$$

where the dimensionless parameters

$$\mu = \frac{\nu}{a_1^2(\pi G\rho)^{1/2}}, \quad \delta = \frac{GMa_1^2(\pi G\rho)^{3/2}}{5c^5}, \quad (1.3)$$

correspond respectively to a viscous damping and gravitational radiation reaction terms, with G the universal gravitational constant and c the speed of light in vacuum.

As one can notice, matrices constituting expression (1.2) are expressed in terms of subsidiary functions that are inherent of the geometry of these spheroids. For instance, we present the Maclaurin's law for the angular velocity Ω in terms of the eccentricity e defined in (1.1), as (Chandrasekhar, 1969)

$$\Omega^2(e) = \frac{2\sqrt{1-e^2}}{e^3} \left(3 - 2e^2\right) \sin^{-1} e - \frac{6}{e^2} \left(1 - e^2\right). \quad (1.4)$$

Moreover, we define the remaining functions from first, the integral definition (Chandrasekhar, 1969)

$$b = \int_0^\infty \frac{a_1^2 a_3 u du}{(a_1^2 + u)^3 (a_3^2 + u)^{1/2}}, \quad (1.5)$$

which, when expressed in terms of e , yields

$$b(e) = \frac{\sqrt{1-e^2}}{4e^5} \left(4e^2 - 3\right) \sin^{-1} e + \frac{1}{4e^4} \left(3 - 2e^2\right) \left(1 - e^2\right). \quad (1.6)$$

The expression (1.6) allows us to write the terms q_1 and q_2 from the post-Newtonian approximation explicitly as Chandrasekhar, 1970a and Chandrasekhar, 1970b

$$\begin{aligned} q_1 &= 2\lambda^3 \left(\Omega^2 - 2b\right) - \frac{3}{5}\lambda^5 + 8\lambda^3\Omega^2, \\ q_2 &= -8\Omega \left(3\lambda^2 - 4\Omega^2\right) \left(\Omega^2 - 2b\right) + 8\lambda^4\Omega - \frac{128}{5}\Omega^5. \end{aligned}$$

Note that $b(e)$ can be expressed via $\Omega(e)$ as follows

$$b(e) = -\frac{1}{8e^2} \frac{4e^2 - 3}{2e^2 - 3} \Omega^2(e) + \frac{e^2 - 1}{2e^2 - 3}. \quad (1.7)$$

The polynomial pencil (1.2) governs the stability of Maclaurin spheroids and read the following characteristic equation

$$p(\lambda) = \det \mathcal{L}(\lambda) = 0. \quad (1.8)$$

We may notice that the system is said to be undamped only when the dissipative coefficients μ and δ are identically equal to zero.

1.3 Stability of undamped spheroids

We start our analysis from the undamped system, i.e. the case corresponding to the absence of dissipative effects ($\mu = \delta = 0$). In this limit, the characteristic polynomial (1.8) reduces to

$$p_0(\lambda) = 4\lambda^2\Omega^2 + (2\Omega^2 - \lambda^2 - 4b)^2. \quad (1.9)$$

We immediately find the four roots of the polynomial (1.9) as the eigenvalues of the inviscid Maclaurin spheroids $\pm(i\Omega \pm i\sqrt{4b - \Omega^2})$. We denote two of these four roots as

$$\lambda_0^\pm = i\Omega \pm i\sqrt{4b - \Omega^2}. \quad (1.10)$$

Taking into account expressions (1.4) and (1.6), we can determine the point of neutral stability (the exact same point where the Maclaurin sequence bifurcates to the Jacobi family, as found by Meyer and Liouville (Meyer, 1842; Liouville, 1851)). Substituting the neutral value of $\lambda = 0$ in (1.9), we recover the critical eccentricity as being equal to $e_L = 0.812670\dots$, which is a solution of the transcendental equation $4b(e) = 2\Omega^2(e)$, equivalent to

$$e = \sin \left(\frac{e(3 + 10e^2)\sqrt{1 - e^2}}{3 + 8e^2 - 8e^4} \right). \quad (1.11)$$

In a similar way, we obtain from the analysis of solutions (1.10) the critical eccentricity e_0 that yields dynamical instability (historically found by Riemann (Riemann, 1861)) as a root of the equation $4b(e) = \Omega^2(e)$, reading

$$e = \sin \left(\frac{e(3 + 4e^2)\sqrt{1 - e^2}}{3 + 2e^2 - 4e^4} \right). \quad (1.12)$$

Solving (1.12) for the eccentricity e , we recover the bifurcation point $e_0 = 0.952886\dots$ for the onset of dynamical instability in Maclaurin spheroids. Substituting (1.7) into the equation $4b(e) = \Omega^2(e)$, we find the value of the angular velocity at the Riemann point

$$\Omega_0^2 = \Omega^2(e_0) = \frac{8(1 - e_0^2)e_0^2}{3 + 2e_0^2 - 4e_0^4} = 0.440219\dots, \quad (1.13)$$

so that $\Omega_0 = 0.663490\dots$. It is worth noticing that eigenvalues at the Riemann point are double imaginary, such that $\lambda_0^\pm(e_0) = i\Omega_0$.

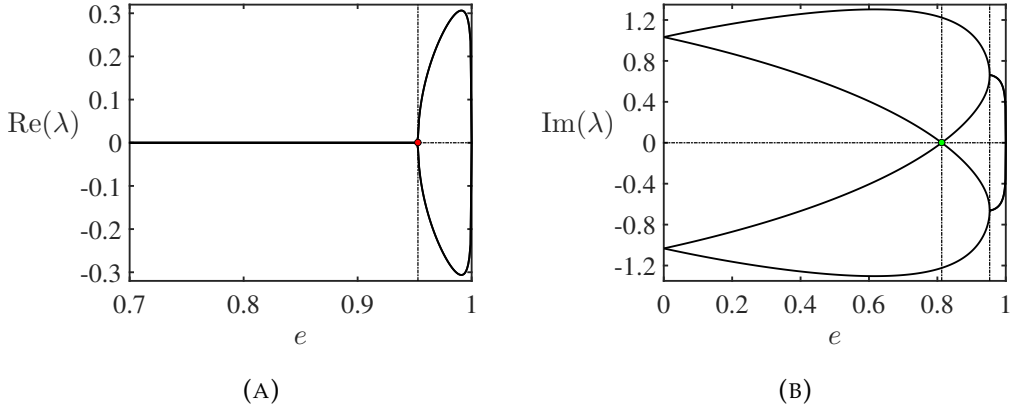


FIGURE 1.1: The growth rate and frequency of the inviscid Maclaurin sequence related to the eccentricity of the spheroid. The red dot in the left panel represents the Riemann point of bifurcation at $e_0 = 0.952886\dots$ while the green dot in the right panel represents the Meyer-Liouville point of neutral stability, i.e. $e_L = 0.812670\dots$.

With the departure of the eccentricity from e_0 , the double eigenvalue $i\Omega_0$ splits as follows (Kirillov, 2021)

$$\lambda_0^\pm = i\Omega_0 \pm i\sqrt{\frac{\partial p_0}{\partial e} \left(\frac{1}{2}\frac{\partial^2 p_0}{\partial \lambda^2}\right)^{-1}(e_0 - e)} + O(e_0 - e), \quad (1.14)$$

where the partial derivatives are evaluated at $e = e_0$, so that

$$\frac{\partial p_0}{\partial e} = \frac{256(1 - e_0^2)(2e_0^4 + e_0^2 - 2)e_0}{(4e_0^4 - 2e_0^2 - 3)^2} = \frac{4\Omega_0^4(2e_0^4 + e_0^2 - 2)}{e_0^3(1 - e_0^2)},$$

and

$$\frac{1}{2}\frac{\partial^2 p_0}{\partial \lambda^2} = 6(\lambda_0^+(e_0))^2 + 8b(e_0) = -6\Omega_0^2 + 8b(e_0).$$

Taking into account the relation (1.7) along with expression (1.13), we find that

$$\frac{1}{2}\frac{\partial^2 p_0}{\partial \lambda^2} = \frac{32(1 - e_0^2)e_0^2}{4e_0^4 - 2e_0^2 - 3} = -4\Omega_0^2.$$

Then,

$$\frac{\partial p_0}{\partial e} \left(\frac{1}{2}\frac{\partial^2 p_0}{\partial \lambda^2}\right)^{-1} = \Omega_0^2 \frac{2e_0^{-2} - 2e_0^2 - 1}{e_0(1 - e_0^2)},$$

and the Newton-Puiseux expansion (1.14) takes the explicit form (Kirillov, 2005)

$$\lambda_0^\pm = i\Omega_0 \pm i\Omega_0 \sqrt{\frac{2e_0^{-2} - 2e_0^2 - 1}{e_0(1 - e_0^2)}}(e_0 - e) + O(e_0 - e). \quad (1.15)$$

Hence, the Maclaurin spheroids without dissipation are marginally stable for all eccentricities smaller than the Riemann value e_0 and unstable for $e_0 \leq e \leq 1$, see Fig. 1.1. In the interval between the Meyer-Liouville and the

Riemann points, the Maclaurin spheroids are gyroscopically stabilized. This gyroscopic stabilization can be lost in the presence of dissipation (Bloch et al., 1994; Kirillov, 2007; Krechetnikov and Marsden, 2007; Kirillov and Verhulst, 2010; Kirillov, 2021).

1.4 Double-diffusive CFS instability

As predicted first by Kelvin and Tait (Kelvin and Tait, 1867), and further confirmed by Roberts and Stewartson using asymptotic analysis (Roberts and Stewartson, 1963), the presence of viscosity – regardless of how small the damping parameter is – leads to the onset of a secular instability in the Maclaurin spheroids. In our case, assuming the presence of a non-vanishing coefficient μ in the dispersion relation (1.8), we find the roots λ of this characteristic equation and present the results in Fig. 1.2. From the observation of both panels, onset of the secular instability takes place at the Meyer-Liouville eccentricity (represented with a green dot in Fig. 1.2) reading thus a positive growth rate for $e_L < e < 1$. As we can notice, the crossing observed in the frequency of the undamped case, cf Fig. 1.1, corresponds now to an avoided crossing around the Riemann point of bifurcation. This phenomenon is a well-known and typical feature of systems subject to dissipation-induced instabilities (Bloch et al., 1994; Krechetnikov and Marsden, 2007; Kirillov and Verhulst, 2010; Kirillov, 2021). Similarly, we present the same analysis for the case of a spheroid subject also to gravitational losses (with $\delta \neq 0$) in Fig. 1.3 and we notice comparable patterns of secular instability as in the purely viscous limit. However, in the presence of both damping mechanisms, as highlighted in this figure, the instability triggers at a critical eccentricity $e \in [e_L, e_0]$, with $e \rightarrow e_L$ as $\delta \rightarrow 0$ (when the double-diffusive system asymptotically converges to the viscous configuration). We therefore propose to analyze further the case where viscosity and gravitational radiation reaction terms are simultaneously present to investigate their influence on the stability of the spheroids.

It was emphasized by Chandrasekhar (Chandrasekhar, 1970a) that the mode becoming secularly unstable in the presence of viscosity arises from a distinct branch in the dispersion relation than the mode unstable due to the emission of gravitational waves. A further investigation on the predominance of these modes in terms of the damping parameters (μ, δ) was provided by Lindblom and Detweiler (Lindblom and Detweiler, 1977) for the double-diffusive CFS instability. It becomes clear from their study that the minimal value of eccentricity for which a secular instability is admissible is indeed the Meyer-Liouville point of bifurcation. From a geometrical point of view, this argument is due to the branching of the Jacobi and Dedekind ellipsoids from the Maclaurin sequence at this critical value, allowing thus the spheroids to release energy due to the presence of dissipation. Naturally, the upper limit for the onset of a secular instability corresponds to the Riemann threshold for dynamical instability, namely $e = e_0$. This idea of predominance of damped modes is popular among dissipation-induced instabilities and can easily be identified from the analysis of the spectrum of operator

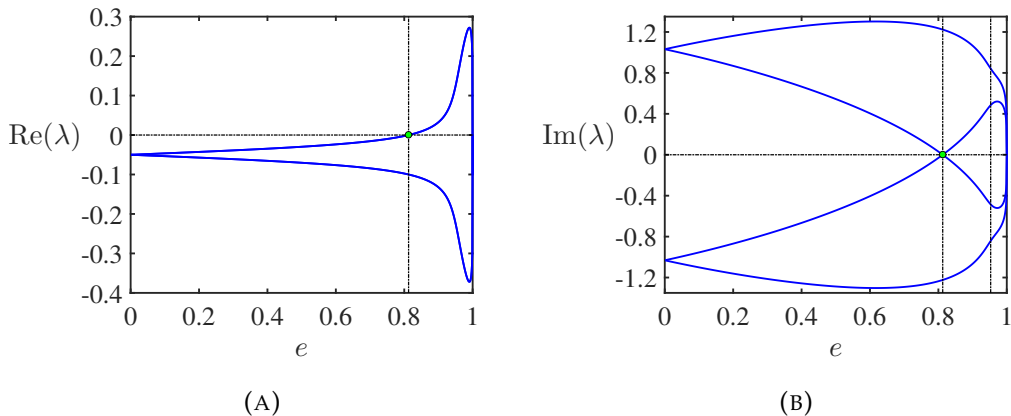


FIGURE 1.2: The growth rate and frequency of the viscous Maclaurin sequence with damping coefficient $\mu = 0.01$, related to the eccentricity of the spheroid. The green dot in both panels represents the Meyer-Liouville point of neutral stability.

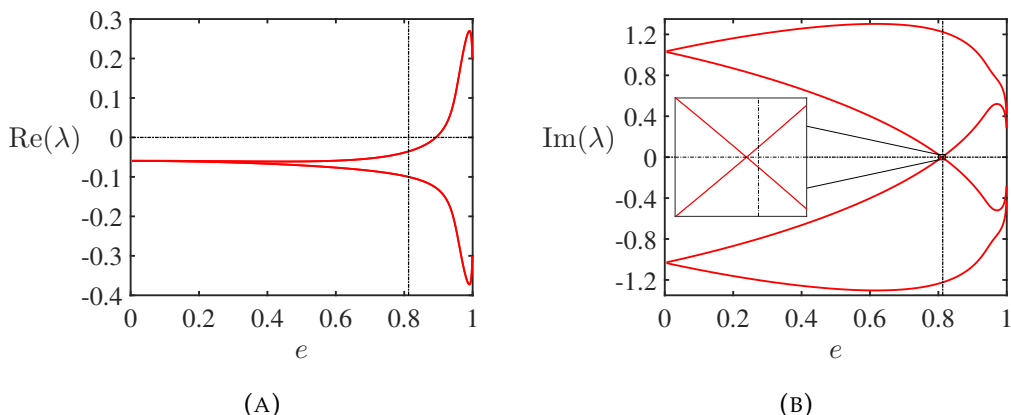


FIGURE 1.3: The growth rate and frequency of the double-diffusive Maclaurin sequence with damping coefficients $\mu = 0.01$ and $\delta = 0.02$, related to the eccentricity of the spheroid. The vertical dashed black line in both panels represents the Meyer-Liouville point of neutral stability and a zoom is made on the frequency to highlight that crossing at the origin is apart from this value.

(1.2). Indeed, from the Hamiltonian theory, stability corresponds to a spectrum strictly lying on the imaginary axis. When the system enters into dynamical instability, these eigenvalues collide and split along this axis exactly at the point of bifurcation, while carrying energy modes with opposite signs. Under the influence of dissipation, the collision of eigenvalues is avoided and the modes are shifted in opposite directions of the complex plane, determining thus the predominance of the damping mode in the system. This behavior is clear from the movement of the spectrum represented in Fig. 1.4 where we observe first, the collision of modes in the undamped case and then, the avoided crossing in the presence of dissipation. As one can notice, the direction in which the eigenvalues are shifted clearly proves that modes damped by viscosity are separate from the modes damped due to the emission of gravitational waves, as previously explained (Chandrasekhar, 1970a).

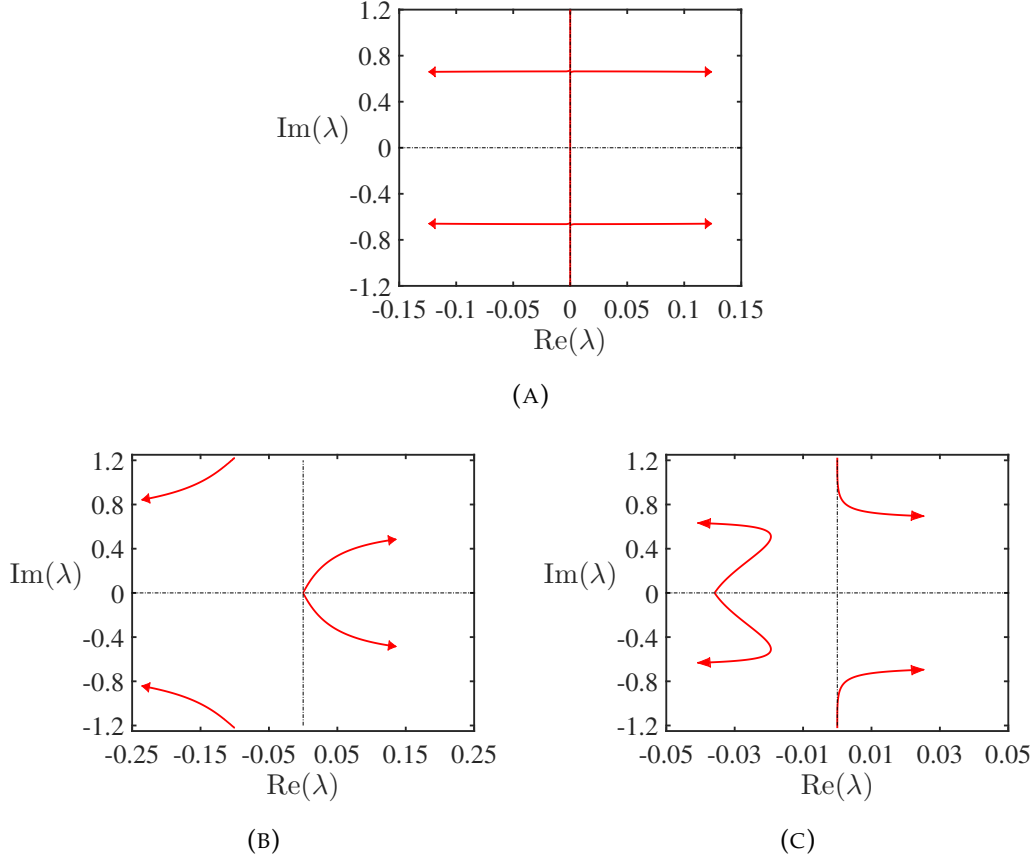


FIGURE 1.4: Movement in the spectrum of operator (1.2). Upper panel corresponds to the undamped case, while left and right panels are influenced only by viscosity ($\mu = 0.01$) or gravitational losses ($\delta = 0.02$), respectively.

In the interest of understanding how the two dissipation mechanisms interplay, we consider the characteristic polynomial $p(\lambda)$ defined in (1.8) in its expanded form

$$p(\lambda) = (2\Omega\lambda - q_2\delta)^2 + (2\Omega^2 - \lambda^2 - 4b - 10\lambda\mu + 16\Omega^2\lambda(\Omega^2 - 6b)\delta - 2q_1\delta)^2.$$

The polynomial (1.16) reduces to (1.9) at $\mu = 0$ and $\delta = 0$.

Let us consider the Maclaurin series of a simple root of the polynomial (1.16) in the neighbourhood of one of the four roots $\pm\lambda_0^\pm$, computed in the case where dissipation is not present, as $\lambda \approx \lambda_0 + \Delta\lambda$. It yields

$$\Delta\lambda_0^\pm = \left. \frac{\partial\lambda^\pm}{\partial\mu} \right|_{(\mu,\delta)=0} \mu + \left. \frac{\partial\lambda^\pm}{\partial\delta} \right|_{(\mu,\delta)=0} \delta + o(\mu, \delta). \quad (1.16)$$

The partial derivatives of a simple root with respect to parameters μ and δ are expressed by means of the partial derivatives of the polynomial $p(\lambda)$ as

follows

$$\frac{\partial \lambda}{\partial \mu} = \frac{\partial p}{\partial \mu} \left(\frac{\partial p}{\partial \lambda} \right)^{-1}, \quad \frac{\partial \lambda}{\partial \delta} = \frac{\partial p}{\partial \delta} \left(\frac{\partial p}{\partial \lambda} \right)^{-1}. \quad (1.17)$$

Evaluating the derivatives in (1.17) at $\mu = 0$ and $\delta = 0$, and expressing $b = \frac{1}{2}\Omega^2 + \frac{i}{2}\lambda\Omega - \frac{1}{4}\lambda^2$ from the equation $p_0(\lambda) = 0$, where p_0 is defined by (1.9), we find

$$\begin{aligned} \frac{\partial p}{\partial \lambda} \Big|_{\mu, \delta=0} &= 8\Omega\lambda(\Omega + i\lambda), \\ \frac{\partial p}{\partial \delta} \Big|_{\mu, \delta=0} &= \frac{16\lambda\Omega(2\Omega + i\lambda)^5}{5}, \\ \frac{\partial p}{\partial \mu} \Big|_{\mu, \delta=0} &= 40i\lambda^2\Omega. \end{aligned}$$

Hence,

$$\Delta\lambda_0^\pm = -\frac{5i\lambda_0^\pm}{\Omega + i\lambda_0^\pm}\mu - \frac{2(2\Omega + i\lambda_0^\pm)^5}{5(\Omega + i\lambda_0^\pm)}\delta + o(\mu, \delta).$$

Taking into account the relation $\lambda_0^\pm = 2i\Omega - \lambda_0^\mp$ that follows from (1.10), we get

$$\begin{aligned} \Delta\lambda_0^\pm &= -\frac{5i\lambda_0^\pm}{\Omega + i\lambda_0^\pm}\mu + \frac{2i(\lambda_0^\mp)^5}{5(\Omega + i\lambda_0^\pm)}\delta + o(\mu, \delta) \\ &= \frac{2i\delta}{5(\Omega + i\lambda_0^\pm)} \left[(\lambda_0^\mp)^5 - \lambda_0^\pm \frac{25}{2} \frac{\mu}{\delta} \right] + o(\mu, \delta) \\ &= \frac{2i\delta}{5(\Omega + i\lambda_0^\pm)} \left[(\lambda_0^\mp)^5 - \chi\Omega_0^4\lambda_0^\pm \right] + o(\mu, \delta), \end{aligned} \quad (1.18)$$

where

$$\chi = \frac{25}{2\Omega_0^4} \frac{\mu}{\delta}, \quad (1.19)$$

and Ω_0 is defined in (1.13).

Since the eigenvalues (1.10) of the ideal system are imaginary, then for $2b \leq \Omega^2 \leq 4b$, the linear increment

$$\frac{\mp 2\delta}{5(\sqrt{4b - \Omega^2})} \left[(i\lambda_0^\mp)^5 - \chi\Omega_0^4 i\lambda_0^\pm \right], \quad (1.20)$$

is real and a secular instability is possible.

Note that in the case when

$$(i\lambda_0^\mp)^5 - \chi\Omega_0^4 i\lambda_0^\pm = 0, \quad (1.21)$$

the increment (1.20) is zero no matter how small the damping coefficient δ is.

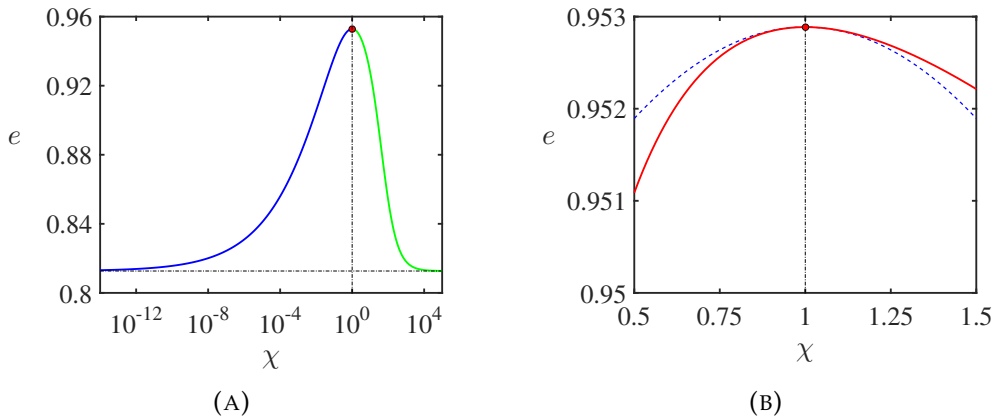


FIGURE 1.5: (A) The critical eccentricity in the limit of vanishing dissipation for different values of the ratio of the strengths of the dissipative terms χ according to the equation (1.24). The blue (respectively green) line represents the region dominated by gravitational waves emission (respectively viscous dissipation). The maximum occurs at the Riemann point for $\chi = 1$ (red dot) and the minimum at the Meyer-Liouville point for $\chi = 0$ and $\chi \rightarrow +\infty$. (B) Taylor expansion (blue dashed line) according to (1.25) in comparison with the exact curve (red line) given in (1.24).

With $i\lambda_0^\pm = -\Omega \mp \sqrt{4b - \Omega^2}$, we re-write (1.21) as

$$-(\Omega \mp \sqrt{4b - \Omega^2})^5 + (\Omega \pm \sqrt{4b - \Omega^2})\Omega_0^4\chi = 0, \quad (1.22)$$

which we transform into

$$-\left(\Omega \mp \sqrt{4b - \Omega^2}\right)^6 + 2(\Omega^2 - 2b)\Omega_0^4\chi = 0,$$

and finally, to

$$-4 \left(2b \mp \Omega \sqrt{4b - \Omega^2}\right)^3 + (\Omega^2 - 2b) \Omega_0^4 \chi = 0, \quad (1.23)$$

which is equivalent to the equation

$$\chi^2 + \chi \frac{16b(3\Omega^4 - 12b\Omega^2 - 4b^2)}{\Omega_0^4(\Omega^2 - 2b)} + \frac{16(\Omega^2 - 2b)^4}{\Omega_0^8} = 0. \quad (1.24)$$

Expanding $b(e)$ and $\Omega(e)$ defined from expressions (1.6) and (2.14), respectively, in the Taylor series in the vicinity of $e = e_0$ for this quadratic equation, we find the following approximation for the critical eccentricity in the vicinity of $\chi = 1$

$$e = e_0 - \frac{e_0}{36} \frac{(1-e_0^2)(\chi-1)^2}{1+2e_0^2-2e_0^{-2}} + O((\chi-1)^3), \quad (1.25)$$

Alternatively, one can derive approximation (1.25) by using the expansion (1.15) in the equation (1.21).

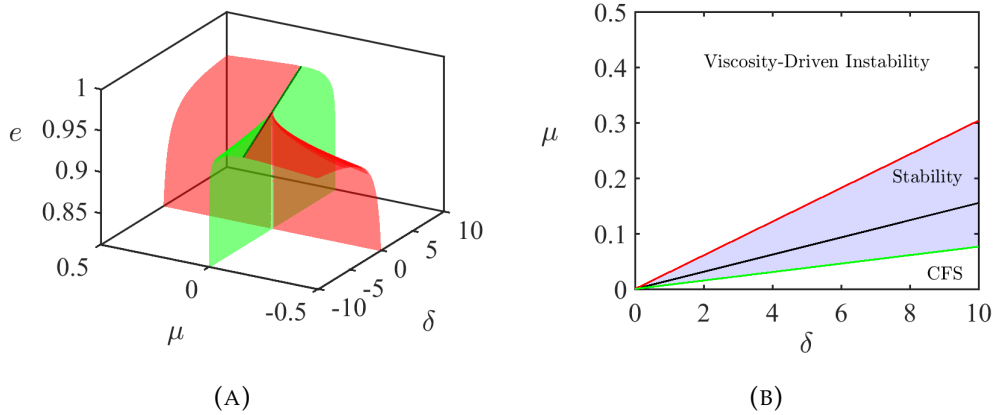


FIGURE 1.6: (A) Neutral stability surface from the expression (1.24) or, equivalently, (1.26) for eccentricities in the interval $e_L \leq e \leq e_0$. (B) Cross-section of the stability domain (1.26) given by the Hurwitz determinant (1.31) for $e = 0.951$. The green line (respectively red) represents the slope when the system is dominated by gravitational radiation (respectively viscosity) from expression (1.24). The white region denotes instability and the black line $\mu = (2\Omega_0^4/25)\delta \approx 0.015503\delta$ represents the limit of the Whitney's umbrella surface at $e = e_0$.

Following equation (1.24) we define two distinct regions in this stability analysis, the first one where the emission of gravitational waves dominates the system (associated to $\chi < 1$) and the second where the system is mostly subject to viscous damping (related to the values of $\chi > 1$). Finally, when $\chi = 1$ the system is undamped and the critical eccentricity is therefore given by the Riemann point of bifurcation. Solution of expression (1.24) over the parameter χ is given in the left panel of Fig. 1.5, where the first region is represented in blue while the region dominated by viscosity is represented in green. We may notice that both domains are asymptotically tending to the value of neutral stability of the ideal system, i.e. the Meyer-Liouville eccentricity. Our approximation (1.25) in the neighbourhood of $\chi = 1$ depicted in the right panel of Fig. 1.5 is well fitting the exact solution of the full equation (1.24).

1.5 Instability windows and Whitney's umbrella

One weakness in the approach presented above is that stability is interpreted in the vicinity of vanishing damping parameters. This condition is fairly restricting and restrain us in our analysis. A way to compute the stability domains of the Maclaurin spheroids over a broad range of dissipative coefficients is to consider a global stability criterion for the characteristic polynomial (1.8), which contains high-order terms in λ up to λ^{10} .

Application of the well-known Liénard-Chipart criterion (Liénard and Chipart, 1914) suggests us computing the determinant of the Hurwitz matrix for the polynomial. The positiveness of this determinant yields a stability domain in the space of parameters. For the sake of presentation, we give

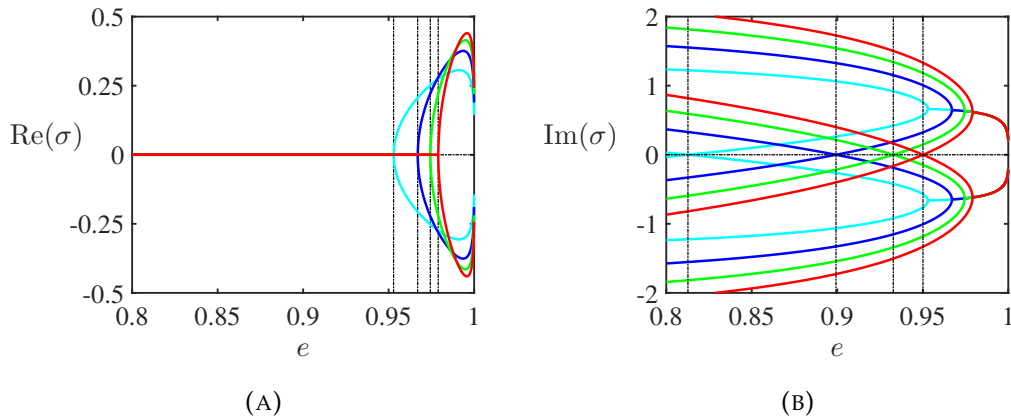


FIGURE 1.7: Generalized undamped f -modes of spheroids obtained from expression (1.27) for azimuthal wavenumbers $m = 2$ (cyan), $m = 3$ (blue), $m = 4$ (green) and $m = 5$ (red). (A) Real part with Riemann eccentricities (vertical dashed black lines). (B) Imaginary part with Meyer-Liouville eccentricities (vertical dashed black lines).

the expansion of the 10×10 determinant in appendix 1.A. From the analysis of expression (1.31), we determine that the only term with a non-constant sign over the parameters is that in the coefficient at $(-\delta^5)$, which reduces our stability domain to the following quadratic term

$$Q = -\frac{\Omega^2 - 2b}{512} \left\{ \left(\frac{25\mu}{2} \right)^2 + 16(\Omega^2 - 2b)^4 \delta^2 + \frac{16b(3\Omega^4 - 12\Omega^2b - 4b^2)}{\Omega^2 - 2b} \frac{25\mu\delta}{2} \right\} > 0. \quad (1.26)$$

Comparing (1.26) with (1.24) we see that the expression in the braces reduces exactly to the left-hand side of (1.24) if we assume $\mu = (2\Omega_0^4 \delta \chi)/25$. Hence, the approximation (1.24) obtained by the first-order in μ and δ perturbation theory of eigenvalues gives the exact neutral stability boundary provided by the Liénard-Chipart criterion and is therefore valid for arbitrary damping coefficients. The right panel of Fig. 1.6 illustrates this remarkable agreement.

We can extend the stability domain obtained from (1.26) even for negative values of damping coefficients. Computing it in the interval $e_L \leq e \leq e_0$ provides the evidence of a singularity at $(\delta = 0, \mu = 0, e = e_0)$ known as the Whitney's umbrella as it is presented in the left panel of Fig. 1.6. In the latter, the right panel shows a cross section of the domain given by the quadratic term (1.26) in the Hurwitz determinant and the lines defined by expression (1.24) for an arbitrary eccentricity. We notice that the angle between the boundaries of the domain is shrinking as the eccentricity is reaching the Riemann critical value until it is reduced to the line $\mu = (2\Omega_0^4/25)\delta \approx 0.015503\delta$ specified by the condition $\chi = 1$.

One information that we did not specify along this chapter is that we are considering a particular mode of the Maclaurin spheroids, usually referred to as the 'bar' mode (Chandrasekhar, 1969). In the general context

TABLE 1.1: Table of the Liouville and Riemann eccentricities e_0 and e_L , describing neutral stability and onset of dynamical instability, respectively, as a function of the azimuthal mode m .

m	e_L	e_0
2	0.8126700106	0.9528867020
3	0.8992572296	0.9669520613
4	0.9327469471	0.9743651705
5	0.9501271468	0.9789783168
10	0.9791361085	0.9887398973
100	0.9984095845	0.9986997996
10^3	0.9998533778	0.9998625560

of oblate spheroids with arbitrary azimuthal wavenumbers $m = l$, we refer to these configurations as the f -modes of the CFS instability, with the particular case of bar modes corresponding to $m = 2$. As it turns out, modes corresponding to $m > 2$ are also subject to destabilization due to viscosity or gravitational radiation reaction and provide a generalization to the spherical harmonics that are exploited in various physical applications (Braviner and Ogilvie, 2014; Braviner and Ogilvie, 2015).

In a series of two pioneer papers (Comins, 1979a; Comins, 1979b), Comins introduced the characteristic polynomial (1.8) for arbitrary values of m , as an extension of the previous studies that considered $m = 2$ (Roberts and Stewartson, 1963; Chandrasekhar, 1970a; Chandrasekhar, 1970b), and proved the statement that Maclaurin spheroids become indeed secularly unstable when $m > 2$. As presented in appendix 1.B, Comins polynomial reduces to the expression (1.16) presented above for the bar modes ($m = 2$) of the spheroids. From equation (1.32), in the absence of viscosity and gravitational losses, the eigenfrequency of the ideal system yields (Comins, 1979b)

$$\tilde{\sigma}_{0,m}^\pm = \tilde{\Omega} \pm \left(\tilde{\Omega}^2 - 4\pi G\rho m \zeta_S R \right)^{1/2}, \quad (1.27)$$

where all the functions are defined in appendix 1.B.

These modes are represented in Fig. 1.7 with the Riemann and Liouville eccentricities over different values of m tabulated in Tab. 1.1. We can thus observe that both points of secular and dynamical instabilities are asymptotically approaching the value of $e = 1$.

Now that we have presented the extension of the stability analysis in the case of arbitrary azimuthal dependence of the Maclaurin spheroids, we can compare our stability criterion with previous works (Lindblom, 1986; Ipser and Lindblom, 1991) where the roots of the inverse of the e -folding time τ gives us the eigenfrequency of the system and hence, the critical rotation rate

for instability to develop

$$\tau^{-1} = \text{Im}(\tilde{\sigma}) = -i\Delta\tilde{\sigma} = 0, \quad (1.28)$$

and where $-i\Delta\tilde{\sigma}$ is given by the work of Comins (Comins, 1979b) and the perturbation of expression (1.27), which leads to

$$-i\Delta\tilde{\sigma} = \frac{2\pi G\rho m \zeta_S Z + \tilde{\sigma}_{0,m}^\pm (m-1)(2m+1) \frac{\nu}{a_1^2}}{\tilde{\sigma}_{0,m}^\pm - \tilde{\Omega}}.$$

This expression yields to the same exact result given by equation (1.24) for the $m = 2$ case

$$\tau^{-1} = \frac{2\delta}{5} \left(\tilde{\sigma}_{0,2}^\pm - 2\Omega \right)^5 + 5\mu\tilde{\sigma}_{0,2}^\pm = 0. \quad (1.29)$$

In the interest of providing a direct application of the theory developed along this chapter, we follow the previous analyses on the modelling of single rotating neutron stars with damped Maclaurin spheroids (Lindblom, 1986; Ipser and Lindblom, 1991; Lindblom, 1995). We decide to consider a star with a polytropic index $n = 0$, a mass of $1.5M_\odot$ and a radius of 17.171km to match with the results from the literature (Ipser and Lindblom, 1991; Lindblom, 1995).

From a direct computation of the roots of expression (1.29), we determine the critical angular velocity associated with the corresponding damping coefficients μ and δ . Classically, the kinematic viscosity ν is expressed in terms of the dynamic (shear) viscosity η . The latter is obtained from the empiric law established for stellar matter in (Flowers and Itoh, 1976) and expressed in terms of the temperature T . We decide to consider only the case where diffusion is dominated by neutron-neutron interactions, since the subsidiary case where the system is governed by electron-electron scattering yields similar results. We obtain (Flowers and Itoh, 1976)

$$\eta_n = 1.95 \times 10^{18} \left(\frac{\rho}{10^{15}} \right)^{9/4} \left(\frac{T}{10^9} \right)^{-2}. \quad (1.30)$$

We may notice that formula (1.30) uses CGS units to be computed.

Using formula (1.30) to compute the damping coefficient μ in (1.3), we represent in Fig. 1.8 the instability window of the critical angular velocity in terms of the temperature T of the star, from a direct computation of equation (1.29) or equivalently, by (1.24). Interestingly, we observe that a neutron star with such mass and radius reaches the same instability threshold as prescribed by the value of $\chi = 1$ that we analyzed previously, at a temperature of $T \approx 3 \times 10^4$ K. This limit corresponds to the onset of dynamical instability at the Riemann eccentricity e_0 . As presented previously in the left panel of Fig. 1.6, the left side of the curve, where the temperature remains relatively small, corresponds to the configuration where viscosity destroys the effects due to gravitational radiation reaction. On the contrary, when the temperature of the star is rather large (as in the case for newly formed neutron

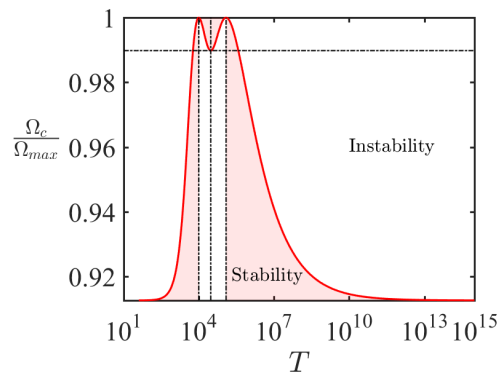


FIGURE 1.8: Stability window (red domain) of a $m = 2$ Maclaurin spheroid with a mass of $1.5M_{\odot}$ and a radius of 17.171km. The critical angular velocity of the star is given in the units of Ω_{max} (the maximal angular velocity determined from expression (1.4)) over the temperature T , with shear viscosity (1.30). This window is computed from expression (1.29) or equivalently, by (1.24). The horizontal dashed black line corresponds to the value Ω_0 .

stars), emission of gravitational waves dominates the viscous damping in the spheroid. However, we have to emphasize that we did not take into consideration the effects of the bulk viscosity in our calculations, as it has been done in the classical papers on the subject (Ipser and Lindblom, 1991; Lindblom, 1995). In these references, the authors pointed out that at high temperatures the damping term due to the presence of bulk viscosity suppresses the CFS instability, in a similar way as shear viscosity at low temperatures.

1.6 Conclusion

Although the model of Maclaurin spheroids is historically regarded as a simplified configuration of a stable self-gravitating mass of fluid in rotation, the implications behind this theoretical idea are crucial. We displayed along this chapter a review on this classical subject, from the initial discovery of the dynamical instability towards the development of the Chandrasekhar-Friedman-Schutz formalism for treating the instability caused by radiation of gravitational waves. We proposed a detailed derivation of the characteristic polynomial under the influence of both damping mechanisms of viscosity and gravitational radiation reaction, along with the stability analysis of the corresponding double-diffusive system with the help of the perturbation theory for eigenvalues. After exploring the secular instabilities due to the combination of viscous dissipation and the emission of gravitational waves on the different modes of the spheroids, we unite the classical results of the literature by finding a topological singularity known as the Whitney's umbrella on the boundary of the asymptotic stability domain in the space of the spheroid eccentricity and damping parameters. In the last section, we presented a direct application of the theory to a model of a single neutron star with specific mass and radius to find an instability window for the critical angular velocity

over the temperature of the star. The combination of the algebraic stability criteria, perturbation of eigenvalues and concepts from the singularity theory allowed us to present the first exhaustive review on this fundamental problem and place it to the modern context of *dissipation-induced instabilities*.

1.A Expansion of the Hurwitz determinant

Expansion of the 10×10 determinant of the Hurwitz matrix \mathcal{H}

$$\begin{aligned} \det \mathcal{H} = & \alpha \left[q_0 \delta^6 + q_1 \delta^5 + q_2 \delta^4 + q_3 \delta^3 + q_4 \delta^2 + q_5 \delta + q_6 \right] \times \\ & \left[-\frac{\Omega^2 - 2b}{512} \left\{ \left(\frac{25\mu}{2} \right)^2 + 16(\Omega^2 - 2b)^4 \delta^2 \right. \right. \\ & \left. \left. + \frac{16b(3\Omega^4 - 12\Omega^2 b - 4b^2)}{\Omega^2 - 2b} \frac{25\mu\delta}{2} \right\} (-\delta^5) \times \right. \\ & \left. \left[\Omega^6 \left(-\frac{\Omega^2}{10} + b \right)^2 \delta^2 + \frac{(-\Omega^2/2 + b)^2}{256} \right] \right], \end{aligned} \quad (1.31)$$

with coefficients α and q_i given by

$$\begin{aligned} \alpha &= 7968993439842526298112/78125 \\ q_0 &= \Omega^8 \left(-\frac{9\Omega^2}{10} + b \right)^6 \\ q_1 &= -\frac{\Omega^6 \mu}{256000} (239\Omega^4 + 900\Omega^2 b + 60b^2) (9\Omega^2 - 10b)^3 \\ q_2 &= \frac{\mu^2}{262144} (3600\Omega^4 b^4 + 741240\Omega^{10} b + 493080\Omega^8 b^2 + 236000\Omega^6 b^3 - 36191\Omega^{12}) + \\ &\quad \frac{\Omega^2}{163840000} (10000b^6 + 10000\Omega^2 b^5 + 298017\Omega^{10} + 639900\Omega^6 b^5 + \\ &\quad 9381103\Omega^8 b^2 - 4225160\Omega^6 b^3 - 398920\Omega^{14}) \\ q_3 &= \frac{\Omega^4 \mu^3}{131072} (112500\Omega^2 b + 7500b^2 + 29875\Omega^4) + \\ &\quad \frac{\Omega^2 \mu}{3276800} (101070\Omega^6 b - 206775\Omega^4 b^2 + 6625\Omega^2 b^3 + 950b^4 - 1247\Omega^8) \\ q_4 &= \frac{15625}{262144} \Omega^4 \mu^4 + \frac{\Omega^2 \mu^2}{8388608} (27385\Omega^6 + 16300\Omega^4 b + 4100\Omega^2 b^2) + \\ &\quad \frac{1}{419430400} (181\Omega^8 + 18794\Omega^6 b - 4064\Omega^4 b^2 + 72\Omega^2 b^3 + 144b^4) \\ q_5 &= \frac{1875}{8388608} \mu^3 \Omega^2 + \frac{1}{33554432} (327\Omega^4 + 18b^2 + 27\Omega^2 b) \\ q_6 &= \frac{1}{1073741824} (225\mu^2 + 9\Omega^2). \end{aligned}$$

1.B Characteristic polynomial of Comins (1979)

Comins (Comins, 1979a; Comins, 1979b) generalized the result of Lindblom and Detweiler to the case of arbitrary m . Characteristic polynomial by Comins

is

$$\begin{aligned}\tilde{\sigma}(\tilde{\sigma} - 2\tilde{\Omega}) &+ 4\pi G\rho m \zeta_s R \\ &= 4\pi i G\rho m \zeta_s Z + \frac{2i\tilde{\sigma}\nu(m-1)(2m+1)}{a_1^2},\end{aligned}\quad (1.32)$$

where $\tilde{\sigma} = \sigma\sqrt{\pi G\rho}$, $\tilde{\Omega} = \Omega\sqrt{\pi G\rho}$. We introduce the following functions

$$\begin{aligned}\zeta_s &= \frac{a_3}{\sqrt{a_1^2 - a_3^2}} = \frac{\sqrt{1-e^2}}{e}, \\ R &= \frac{i(-1)^m}{(2m)!} P_m^m(i\zeta_s) Q_m^m(i\zeta_s) - \frac{A_3}{2} a_1^3 e(1-e^2), \\ Z &= e(\tilde{\sigma} - m\tilde{\Omega})^{2m+1} \frac{(m+1)(m+2)}{m(m-1)[(2m+1)!!]^2} \left(\frac{a_1}{c}\right)^{2m+1},\end{aligned}$$

where $P_m^m(i\zeta_s)$ and $Q_m^m(i\zeta_s)$ are associated Legendre functions of the first and second kinds respectively, and

$$A_3 = \frac{2}{(a_1 e)^3} \left[\frac{e}{\sqrt{1-e^2}} - \sin^{-1} e \right].$$

If $m = 2$, we have

$$\tilde{\sigma}(\tilde{\sigma} - 2\tilde{\Omega}) + 8\pi G\rho \zeta_s R = 8\pi i G\rho \zeta_s Z + \frac{10i\tilde{\sigma}\nu}{a_1^2},$$

and

$$\zeta_s Z = \sqrt{1-e^2}(\tilde{\sigma} - 2\tilde{\Omega})^5 \frac{2}{75} \left(\frac{a_1}{c}\right)^5.$$

We can express the mass of the ellipsoid through the formula

$$M = \frac{4}{3}\pi a_1^3 \sqrt{1-e^2} \rho,$$

which leads to

$$\pi\rho\zeta_s Z = \frac{Ma_1^2}{50c^5}(\tilde{\sigma} - 2\tilde{\Omega})^5.$$

Therefore,

$$\begin{aligned}\tilde{\sigma}(\tilde{\sigma} - 2\tilde{\Omega}) + 8\pi G\rho \zeta_s R &= 4i \frac{GMa_1^2}{25c^5}(\tilde{\sigma} - 2\tilde{\Omega})^5 + \frac{10i\tilde{\sigma}\nu}{a_1^2} \\ &= \frac{4i\delta(\tilde{\sigma} - 2\tilde{\Omega})^5}{5(\pi G\rho)^{3/2}} + \frac{10i\tilde{\sigma}\nu}{a_1^2}.\end{aligned}\quad (1.33)$$

We also have for $m = 2$

$$R = \frac{i}{24} P_2^2(i\zeta_s) Q_2^2(i\zeta_s) - \frac{A_3}{2} a_1^3 e(1-e^2),$$

where

$$P_2^2(i\zeta_s) = -3(\zeta_s)^2 - 3 = -\frac{3}{e^2}.$$

Then,

$$R = -\frac{iQ_2^2(i\zeta_s)}{8e^2} - \left[\frac{e}{\sqrt{1-e^2}} - \sin^{-1} e \right] \frac{1-e^2}{e^2}.$$

We transform the Legendre function

$$Q_2^2(i\zeta_s) = \frac{3(\zeta_s^2 + 1)^2 \ln \left(\frac{\zeta_s + i}{\zeta_s - i} \right) - i\zeta_s(6\zeta_s^2 + 10)}{2\zeta_s^2 + 2},$$

by using the identity

$$\ln \left(\frac{\zeta_s + i}{\zeta_s - i} \right) = 2i \cot^{-1}(\zeta_s),$$

and

$$\cot^{-1}(\zeta_s) = \sin^{-1} \left(\frac{1}{\sqrt{1+\zeta_s^2}} \right).$$

Along with $\zeta_s = \frac{\sqrt{1-e^2}}{e}$, it yields

$$Q_2^2(i\zeta_s) = i \frac{3 \sin^{-1} e - e(2e^2 + 3)\sqrt{1-e^2}}{e^2}.$$

Then,

$$\begin{aligned} R &= -\frac{iQ_2^2(i\zeta_s)}{8e^2} - \left[\frac{e}{\sqrt{1-e^2}} - \sin^{-1} e \right] \frac{1-e^2}{e^2} \\ &= \frac{-(e^4 - e^2 - 3/8) \sin^{-1} e}{e^4} \\ &= \frac{-(5/4)e^5 + (7/8)e^3 + (3/8)e}{e^4 \sqrt{1-e^2}}, \end{aligned} \tag{1.34}$$

and

$$\begin{aligned} 8\zeta_s R &= \frac{(3 + 8e^2 - 8e^4)\sqrt{1-e^2} \sin^{-1} e + 10e^5 - 7e^3 - 3e}{e^5} \\ &= \frac{2\tilde{\Omega}^2}{\pi G \rho} - 4b. \end{aligned} \tag{1.35}$$

Therefore,

$$\tilde{\sigma}(\tilde{\sigma} - 2\tilde{\Omega}) + (2\tilde{\Omega}^2 - \pi G \rho 4b) = \frac{4i(\tilde{\sigma} - 2\tilde{\Omega})^5}{5(\pi G \rho)^{3/2}} \delta + \frac{10i\tilde{\sigma}}{a_1^2} \nu,$$

and, if σ and Ω are measured in units of $\sqrt{\pi G \rho}$,

$$\sigma(\sigma - 2\Omega) + 2\Omega^2 - 4b = \frac{4i(\sigma - 2\Omega)^5}{5}\delta + \frac{10i\sigma}{a_1^2 \sqrt{\pi G \rho}}\nu,$$

so that finally (Chandrasekhar, 1970b; Comins, 1979a; Comins, 1979b)

$$\sigma(\sigma - 2\Omega) + 2\Omega^2 - 4b = \frac{4i(\sigma - 2\Omega)^5}{5}\delta + 10i\sigma\mu, \quad (1.36)$$

with μ and δ defined in (1.3).

Consider an expression (Chandrasekhar, 1970b)

$$f = 2b - \Omega^2 + \frac{(2\Omega - \sigma)(4\Omega + 3\sigma)}{10}.$$

Consider another expression

$$\sigma(\sigma - 2\Omega) + 2\Omega^2 - 4b = 0.$$

Substituting $b = \sigma(\sigma - 2\Omega)/4 + \Omega^2/2$ into f we find the identity, first established by Chandrasekhar (Chandrasekhar, 1970b) (page 568)

$$f = 2b - \Omega^2 + \frac{(2\Omega - \sigma)(4\Omega + 3\sigma)}{10} = \frac{(2\Omega - \sigma)^2}{5}.$$

Chapter 2

Dissipation-induced instabilities of lenticular vortices

"Mind and matter," said the lady in the wig, "glide swift into the vortex of immensity. Howls the sublime, and softly sleeps the calm Ideal, in the whispering chambers of Imagination."

Charles Dickens, *Martin Chuzzlewit*

In this chapter we consider a model of a circular lenticular vortex immersed into a deep and vertically stratified viscous fluid in the presence of gravity and rotation. The vortex is assumed to be baroclinic with a Gaussian profile of angular velocity both in the radial and axial directions. Assuming the base state to be in a cyclogeostrophic balance, we derive linearized equations of motion and seek for their solution in a geometric optics approximation to find amplitude transport equations that yield a comprehensive dispersion relation. Applying algebraic Bilharz criterion to the latter, we establish that stability conditions are reduced to three inequalities that define stability domain in the space of parameters. The main destabilization mechanism is either stationary or oscillatory axisymmetric instability depending on the Schmidt number (Sc), vortex Rossby number and the difference between the radial and axial density gradients as well as the difference between the epicyclic and vertical oscillation frequencies. We discover that the boundaries of the regions of stationary and oscillatory axisymmetric instabilities meet at a codimension-2 point, forming a singularity of the neutral stability curve. We give an exhaustive classification of the geometry of the stability boundary, depending on the values of the Schmidt number. Although we demonstrate that the centrifugally stable (unstable) Gaussian lens can be destabilized (stabilized) by the differential diffusion of mass and momentum and that destabilization can happen even in the limit of vanishing diffusion, we also describe explicitly a set of parameters in which the Gaussian lens is linearly stable for all $Sc > 0$.

This chapter is written in the form of an article that has been submitted to the peer-reviewed journal *Physics of Fluids*.

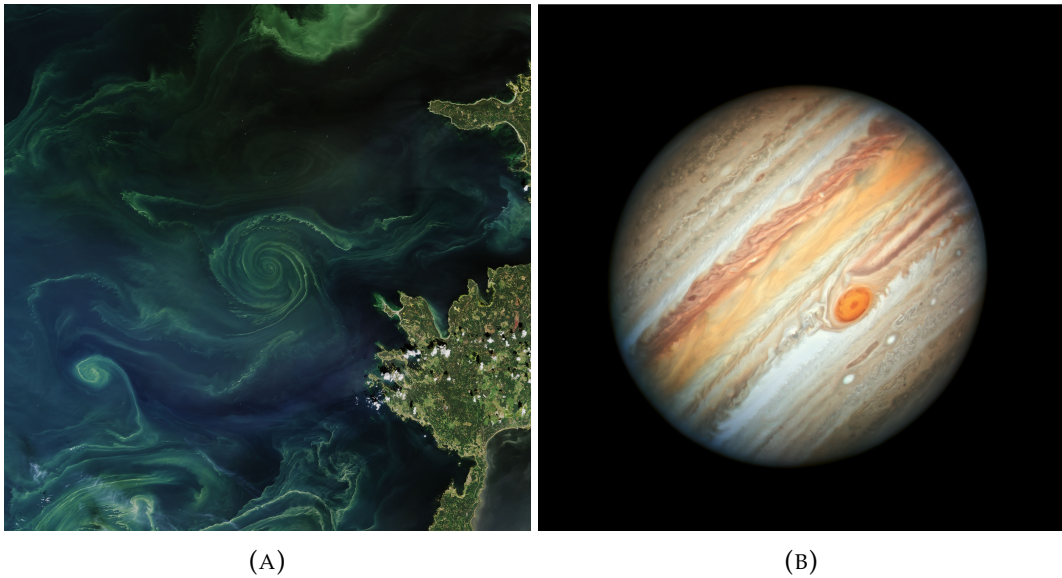


FIGURE 2.1: (A) Giant bloom of phytoplankton in the Baltic Sea (Gulf of Finland) that has been swirled into a meso-scale vortex by an ocean eddy. Image from NASA Earth Observatory (July 18, 2018). (B) Jupiter’s Great Red Spot. Image from Hubble Space Telescope (June 27, 2019).

2.1 Introduction

An interesting class of dynamical system of geo- and planetary physics resides in the so-called *lenticular vortices*, consisting of a meso-scale ellipsoidal model of rotating flows for the study of, e.g., oceanic eddies or atmospheric currents, such as the Great Red Spot in Jupiter (Orozco Estrada et al., 2020), cf. Figure 2.1a and Figure 2.1b, for respective illustrations. Due to their important size, these systems exhibit dependence on inertia forces in the rotating frame, disturbing the original axisymmetric motion of the flow, as it is the case for planets in rotation (Yim, Stegner, and Billant, 2019). We therefore denote by f the background angular frequency of rotation in the vortex frame, where f stands for the Coriolis parameter. We further assume the lenticular vortex to be immersed in a deep water and surrounded by motionless fluid far away from the core center, so that boundaries do not influence the inner motion.

As in realistic configurations, the medium is considered stratified in density along the direction of application of gravity. In our case, we also include dissipation in the fluid in the form of viscosity and we assume the diffusion of stratifying agent to be present.

This model of *pancake* vortex is dynamically driven by the *cyclogeostrophic* balance, an equilibrium state between the Coriolis and centrifugal forces, along with the pressure gradient. Then, the evolution of such a pancake structure (since the velocity field is not constant along the vertical direction) results from the deformation of isopycnals (i.e. lines connecting points of a specific density) to satisfy this balance (Yim and Billant, 2016).

It has been proven previously that in addition of being subject to centrifugal instabilities (Yim, Stegner, and Billant, 2019), thermohaline baroclinic circular vortices can be destabilized in the presence of dissipation (McIntyre, 1970). The latter is a consequence of an axisymmetric perturbation of the flow due to the presence of dissipation and still holds in the limit of vanishing viscosity. In this chapter we establish similar results for the case of pancake lenticular vortices in a stratified fluid. Although the literature contains several studies on the linear stability of pancake vortices (Beckers et al., 2001; Yim and Billant, 2016; Yim, Stegner, and Billant, 2019), the vast majority of these works are purely numerical and an analytical treatment of this problem is therefore timely to find general and rigorous stability criteria.

2.2 Equations of a rotating and stratified fluid

Let \tilde{t} denote time and $(\tilde{r}, \theta, \tilde{z})$ be a cylindrical coordinate system fixed with the ellipsoidal vortex of interest, in such a manner that the vortex center corresponds to $(\tilde{r}_0, \tilde{z}_0) = (0, 0)$.

2.2.1 Density stratification

We consider a base state of a linearly stratified fluid in the presence of an eddy. The linear density variation in the vertical direction \tilde{z} is described within the *Boussinesq approximation* by the stable background density gradient $-\rho_0 N^2/g$, where $N = \sqrt{-\frac{g}{\rho_0} \frac{d\tilde{\rho}}{d\tilde{z}}}$ is the Brunt-Väisälä frequency of the unperturbed flow and ρ_0 is the constant reference density.

The influence of the vortex velocity is captured by the density *anomaly* term $\tilde{\rho}_A$ such that the total density $\tilde{\rho}$ takes the form (Dritschel and Viúdez, 2003; Yim, Stegner, and Billant, 2019; Eunok, Billant, and Menesguen, 2016; Buckingham, Gula, and Carton, 2021)

$$\tilde{\rho}(\tilde{r}, \tilde{z}) = \rho_0 - \rho_0 \frac{N^2}{g} \tilde{z} + \tilde{\rho}_A(\tilde{r}, \tilde{z}). \quad (2.1)$$

2.2.2 Dimensional equations of motion

Writing the conservation of linear momentum (the Navier-Stokes equations), the material conservation of density and the incompressibility condition results in the system of equations governing the evolution of the velocity field $\tilde{\mathbf{u}}$, density $\tilde{\rho}$ and pressure \tilde{P} , cf. (Yim, Stegner, and Billant, 2019):

$$\frac{\partial \tilde{\mathbf{u}}}{\partial \tilde{t}} + (\tilde{\mathbf{u}} \cdot \nabla) \tilde{\mathbf{u}} + f \mathbf{e}_z \times \tilde{\mathbf{u}} = -\frac{1}{\rho_0} \nabla \tilde{P} - \frac{g \tilde{\rho}}{\rho_0} \mathbf{e}_z + \nu \nabla^2 \tilde{\mathbf{u}}, \quad (2.2a)$$

$$\frac{\partial \tilde{\rho}}{\partial \tilde{t}} + (\tilde{\mathbf{u}} \cdot \nabla) \tilde{\rho} = \kappa \nabla^2 \tilde{\rho}, \quad (2.2b)$$

$$\nabla \cdot \tilde{\mathbf{u}} = 0, \quad (2.2c)$$

where e_z is the unit vector of rotational symmetry of the vortex, g denotes uniform gravity acceleration and ν and κ are the coefficients of kinematic viscosity and diffusivity, respectively.

Furthermore, we introduce the horizontal projection e_h , defined as the vector living in the plane that is orthogonal to the vertical axis e_z and spanned by vectors e_r and e_θ . Following this definition, the vector fields of the system can be split into their horizontal and axial components. Equations (2.2) projected along those two directions become

$$\frac{\partial \tilde{u}_h}{\partial \tilde{t}} + (\tilde{u}_h \cdot \tilde{\nabla}_h) \tilde{u}_h + \tilde{u}_z \frac{\partial \tilde{u}_h}{\partial \tilde{z}} + f e_z \times \tilde{u}_h = -\frac{1}{\rho_0} \tilde{\nabla}_h \tilde{P} + \nu \tilde{\mathcal{D}} \tilde{u}_h, \quad (2.3a)$$

$$\frac{\partial \tilde{u}_z}{\partial \tilde{t}} + (\tilde{u}_h \cdot \tilde{\nabla}_h) \tilde{u}_z + \tilde{u}_z \frac{\partial \tilde{u}_z}{\partial \tilde{z}} = -\frac{1}{\rho_0} \frac{\partial \tilde{P}}{\partial \tilde{z}} - \frac{g \tilde{\rho}}{\rho_0} + \nu \tilde{\mathcal{D}} \tilde{u}_z, \quad (2.3b)$$

$$\frac{\partial \tilde{\rho}}{\partial \tilde{t}} + (\tilde{u}_h \cdot \tilde{\nabla}_h) \tilde{\rho} + \tilde{u}_z \frac{\partial \tilde{\rho}}{\partial \tilde{z}} = \kappa \tilde{\mathcal{D}} \tilde{\rho}, \quad (2.3c)$$

$$\tilde{\nabla}_h \cdot \tilde{u}_h + \frac{\partial \tilde{u}_z}{\partial \tilde{z}} = 0, \quad (2.3d)$$

with the operator $\tilde{\mathcal{D}}$ defined as

$$\tilde{\mathcal{D}} = \tilde{\nabla}_h^2 + \frac{\partial^2}{\partial \tilde{z}^2}. \quad (2.4)$$

2.2.3 Non-dimensionalization

Let us now introduce the scaling laws for this system as follows

$$\begin{aligned} \tilde{r} &= r^* r, & \tilde{z} &= z^* z, & \tilde{t} &= t^* t, & \tilde{u} &= u_h^* u_h + u_z^* u_z e_z, \\ \tilde{\rho} &= \rho^* \rho, & \tilde{P} &= P^* P, \end{aligned} \quad (2.5)$$

where $t^* = R/U$ is an advective time scale, $(r^*, z^*) = (R, Z)$ are characteristic radial and axial length scales and where $(u_h^*, u_z^*) = (U, W)$ are typical horizontal and vertical velocities. Dividing equation (2.3a) by the factor (fU) , we obtain the scaling law for pressure as being

$$P^* = \rho_0 f R U. \quad (2.6)$$

We use a similar methodology to recover the dimensional factor ρ^* for the density, from the balance between hydrostatic pressure and buoyancy forces in expression (2.3b), yielding

$$\rho^* = \frac{P^*}{g Z} = \frac{\rho_0 f U}{g \alpha}, \quad (2.7)$$

while introducing the aspect ratio of the vortex

$$\alpha = \frac{Z}{R}. \quad (2.8)$$

Finally, we make use of expression (2.3c) to recover the scaling law for the vertical velocity W . Substituting the previous factors and density profile (2.1) in this equation without presence of diffusivity ($\kappa = 0$) yields the following balance

$$\left(\frac{W\rho_0 RN^2}{gU\rho^*} \right) u_z = \left(\frac{W}{U\alpha} \right) u_z \frac{\partial \rho_A}{\partial z}. \quad (2.9)$$

From expression (2.9), two distinct scaling laws are possible for the axial velocity W , namely $W \sim (gU\rho^*)/(\rho_0 RN^2)$ or $W \sim U\alpha$, depending on the regime considered (strong or weak stratification and rotation rate). We further introduce the horizontal Froude number (to quantify the influence of stratification) (Godoy-Diana and Chomaz, 2003; Godoy-Diana, Chomaz, and Billant, 2004; Bartello and Tobias, 2013) and the Rossby number (the ratio of inertial to Coriolis forces) (Yim, Stegner, and Billant, 2019) as, respectively,

$$F_h = \frac{U}{RN}, \quad Ro = \frac{U}{fR}. \quad (2.10)$$

In the following we assume a regime where the stratification is strong and the rotation rate is fast such that the ratio F_h^2/Ro is of order unity and thus, both scales for W are consistent whatever the value of α is (Eunok, Billant, and Menesguen, 2016). We therefore choose $W = \alpha U$ for the sake of simplifications in the equations of motion.

To complete the space of dimensionless parameters of consideration, we introduce the last two dimensionless numbers, namely the Schmidt and Ekman numbers

$$Sc = \frac{\nu}{\kappa} \quad \text{and} \quad Ek = \frac{Ro}{Re} = \frac{\nu}{fR^2}, \quad (2.11)$$

respectively, where $Re = UR/\nu$ is the Reynolds number.

Equations of motions (2.3) are expressed in their dimensionless form as

$$Ro \frac{d\mathbf{u}}{dt} + \mathbf{e}_z \times \mathbf{u} = -\nabla_\alpha P - \frac{\rho}{\alpha^2} \mathbf{e}_z + Ek \mathcal{D}\mathbf{u}, \quad (2.12a)$$

$$Ro \frac{d\rho}{dt} = \frac{Ek}{Sc} \mathcal{D}\rho, \quad (2.12b)$$

$$\nabla \cdot \mathbf{u} = 0, \quad (2.12c)$$

where $d/dt = \partial_t + (\mathbf{u} \cdot \nabla)$, $\mathcal{D} = \nabla_h^2 + \alpha^{-2} \partial_z^2$ and where we introduced the modified gradient operator $\nabla_\alpha = (\partial_r, r^{-1} \partial_\theta, \alpha^{-2} \partial_z)^T$

2.3 Steady state

The background velocity flow is assumed to be purely azimuthal

$$\mathbf{U} = [\mathbf{U}_h, U_z] = [U_r, U_\theta, U_z] = [0, r\Omega(r, z), 0], \quad (2.13)$$

where $\Omega(r, z) = (R/U)\tilde{\Omega}$ is the dimensionless angular velocity. Additionally, we assume the vortex profile to possess a Gaussian shape along both

radial and axial directions

$$\Omega(r, z) = e^{-(r^2+z^2)}. \quad (2.14)$$

The profile (2.14) represents a particular class of lenticular vortices, known as the *pancake* vortices (Eunok, Billant, and Menesguen, 2016; Yim, Stegner, and Billant, 2019; Godoy-Diana and Chomaz, 2003; Godoy-Diana, Chomaz, and Billant, 2004) and is believed to be the closest model of real oceanic Meddies (Orozco Estrada et al., 2020).

Consider the equilibrium governed by the stationary and inviscid form of (2.12a)

$$\frac{\partial P}{\partial r} = r\Omega(1 + Ro\Omega), \quad (2.15a)$$

$$\frac{\partial P}{\partial z} = -\rho, \quad (2.15b)$$

where ρ is the dimensionless version of the density profile (2.1)

$$\begin{aligned} \rho(r, z) &= \frac{g\alpha}{fU} - \left(\frac{g\alpha}{\rho_0 fU} \right) \rho_0 \frac{N^2}{g} Zz + \rho_A(r, z) \\ &= \frac{g\alpha}{fU} - \frac{\alpha^2 Ro}{F_h^2} z + \rho_A(r, z) \\ &= \frac{g\alpha}{fU} - \frac{Bu}{Ro} z + \rho_A(r, z) \end{aligned} \quad (2.16)$$

and Bu is the Burger number

$$Bu = \frac{\alpha^2 Ro^2}{F_h^2}. \quad (2.17)$$

Taking the radial derivative of expression (2.15b) and substituting expression (2.15a) in the result, we obtain the *gradient wind equation* (Eunok, Billant, and Menesguen, 2016) for the density profile (2.16) as

$$r \frac{\partial}{\partial z} [\Omega(1 + Ro\Omega)] = -\frac{\partial \rho_A}{\partial r}. \quad (2.18)$$

Making use of the angular velocity profile (2.14) in (2.18) and computing the axial derivative yields

$$2rz\Omega(1 + 2Ro\Omega) = \frac{\partial \rho_A}{\partial r}. \quad (2.19)$$

Integrating (2.19) over the radial coordinate returns an explicit expression for the density anomaly

$$\rho_A(r, z) = -z\Omega(1 + Ro\Omega). \quad (2.20)$$

Hence, in the *cyclogeostrophic balance* (Gula, Zeitlin, and Plougonven, 2009;

Buckingham, Gula, and Carton, 2021; Dritschel and Viúdez, 2003) between centrifugal, Coriolis and pressure forces

$$\rho(r, z) = \frac{g\alpha}{fU} - z \frac{Bu}{Ro} - z\Omega(1 + Ro\Omega). \quad (2.21)$$

2.4 Linearized equations of motion

We assume the background flow presented in the previous section to depart slightly from its original state, according to infinitesimal disturbances. Let thus introduce perturbations $(u'_r, u'_\theta, u'_z, p', \rho')$ of velocity, pressure and density to perform a linear stability analysis of this hydrodynamic model.

Linearizing equations (2.12) about the base state described in the previous section yields

$$Ro \left(\frac{d}{dt} + \mathcal{U} \right) \mathbf{u}' + e_z \times \mathbf{u}' + \nabla_\alpha p' + \frac{\rho'}{\alpha^2} e_z = Ek \mathcal{D} \mathbf{u}', \quad (2.22a)$$

$$Ro \left(\frac{d\rho'}{dt} + \mathcal{B}^T \mathbf{u}' \right) = u'_z Bu + \frac{Ek}{Sc} \mathcal{D} \rho', \quad (2.22b)$$

$$\nabla \cdot \mathbf{u}' = 0, \quad (2.22c)$$

where $d/dt = \partial_t + (\mathbf{U} \cdot \nabla)$, $\mathcal{U} = \nabla \mathbf{U}$ and $\mathcal{B} = \nabla \rho_A$ with

$$\mathcal{U} = \begin{pmatrix} 0 & -\Omega & 0 \\ \Omega + r\partial_r\Omega & 0 & r\partial_z\Omega \\ 0 & 0 & 0 \end{pmatrix}, \quad (2.23)$$

and

$$\mathcal{B} = \begin{pmatrix} -z \frac{\partial\Omega}{\partial r} (1 + 2Ro\Omega) \\ 0 \\ -z \frac{\partial\Omega}{\partial z} (1 + 2Ro\Omega) - \Omega (1 + Ro\Omega) \end{pmatrix}. \quad (2.24)$$

The system of equations (2.22) is solved with respect to the background states, along with the space of parameters defined from expressions (2.8), (2.10) and (2.11).

2.5 Geometrical optics approximation

Solutions of the linearized equations of motion (2.22) can be expanded in terms of a small parameter ϵ , such that $0 < \epsilon \ll 1$ (Kirillov, Stefani, and

Fukumoto, 2014; Kirillov and Mutabazi, 2017). Disturbances of the flow under such asymptotic expansion are written as

$$\mathbf{u}'(\mathbf{x}, t, \epsilon) = e^{i\epsilon^{-1}\phi(\mathbf{x}, t)} [\mathbf{u}^{(0)}(\mathbf{x}, t) + \epsilon \mathbf{u}^{(1)}(\mathbf{x}, t)] + \epsilon \mathbf{u}^{(r)}(\mathbf{x}, t, \epsilon), \quad (2.25a)$$

$$p'(\mathbf{x}, t, \epsilon) = e^{i\epsilon^{-1}\phi(\mathbf{x}, t)} [p^{(0)}(\mathbf{x}, t) + \epsilon p^{(1)}(\mathbf{x}, t)] + \epsilon p^{(r)}(\mathbf{x}, t, \epsilon), \quad (2.25b)$$

$$\rho'(\mathbf{x}, t, \epsilon) = e^{i\epsilon^{-1}\phi(\mathbf{x}, t)} [\rho^{(0)}(\mathbf{x}, t) + \epsilon \rho^{(1)}(\mathbf{x}, t)] + \epsilon \rho^{(r)}(\mathbf{x}, t, \epsilon), \quad (2.25c)$$

with ϕ being the phase of oscillations and \mathbf{x} a vector of coordinates. We further assume the residual terms $[\mathbf{u}^{(r)}, p^{(r)}, \rho^{(r)}]$ to be uniformly bounded in ϵ (Kirillov, Stefani, and Fukumoto, 2014; Kirillov and Mutabazi, 2017).

Substituting the series (2.25) in the isochoric condition (2.22c), and retaining only terms of orders ϵ^{-1} and ϵ^0 respectively, yields

$$\mathbf{u}^{(0)} \cdot \nabla \phi = 0, \quad (2.26)$$

$$\nabla \cdot \mathbf{u}^{(0)} + i \mathbf{u}^{(1)} \cdot \nabla \phi = 0. \quad (2.27)$$

Following the approach of (Kirillov, Stefani, and Fukumoto, 2014; Kirillov and Mutabazi, 2017), we assume that damping terms are quadratic in the small parameter ϵ and we therefore have $Ek = \epsilon^2 \widetilde{Ek}$. Using a similar analysis as for the expanded incompressibility conditions (2.26) and (2.27), we recover the Navier-Stokes equations (2.22a) along with the local conservation of density (2.22b) in terms of a linear system at order ϵ^{-1}

$$Ro \begin{pmatrix} \frac{\partial \phi}{\partial t} + (\mathbf{U} \cdot \nabla \phi) & 0 \\ 0 & \frac{\partial \phi}{\partial t} + (\mathbf{U} \cdot \nabla \phi) \end{pmatrix} \begin{pmatrix} \mathbf{u}^{(0)} \\ \rho^{(0)} \end{pmatrix} = -\nabla_\alpha \phi \begin{pmatrix} p^{(0)} \\ 0 \end{pmatrix}, \quad (2.28)$$

and at order ϵ^0

$$iRo \begin{pmatrix} \frac{\partial \phi}{\partial t} + (\mathbf{U} \cdot \nabla \phi) & 0 \\ 0 & \frac{\partial \phi}{\partial t} + (\mathbf{U} \cdot \nabla \phi) \end{pmatrix} \begin{pmatrix} \mathbf{u}^{(1)} \\ \rho^{(1)} \end{pmatrix} + \\ \left(Ro \begin{bmatrix} \frac{\partial}{\partial t} + \mathcal{U} + \mathbf{U} \cdot \nabla \\ Ro \mathcal{B}^T - \mathbf{e}_z^T \mathbf{B} \mathbf{u} \end{bmatrix} + \widetilde{Ek} (\nabla_\alpha \phi \cdot \nabla \phi) + \mathbf{e}_z \times \begin{bmatrix} \frac{\partial}{\partial t} + \mathbf{U} \cdot \nabla \\ Ro \mathcal{B}^T - \mathbf{e}_z^T \mathbf{B} \mathbf{u} \end{bmatrix} \right) \begin{pmatrix} \mathbf{u}^{(0)} \\ \rho^{(0)} \end{pmatrix} = \\ -i \nabla_\alpha \phi \begin{pmatrix} p^{(1)} \\ 0 \end{pmatrix} - \nabla_\alpha \begin{pmatrix} p^{(0)} \\ 0 \end{pmatrix} \quad (2.29)$$

Taking the dot product of the first equation in (2.28) with $\nabla \phi$ and applying the constraint (2.26) yields (Kirillov and Mutabazi, 2017)

$$p^{(0)} = 0. \quad (2.30)$$

Taking (2.30) into account in the linear system (2.28), while seeking for non-trivial solutions, we recover the Hamilton-Jacobi equation from the computation of its determinant (Kirillov and Mutabazi, 2017)

$$\frac{\partial \phi}{\partial t} + \mathbf{U} \cdot \nabla \phi = 0. \quad (2.31)$$

For the rest of this section we assume that $\nabla \phi = \mathbf{k}$ and $\nabla_\alpha \phi = \mathbf{k}_\alpha$, with $\mathbf{k} = (k_r, k_\theta, k_z)^T$ and $\mathbf{k}_\alpha = (k_r, k_\theta, k_z/\alpha^2)^T$. The application of the gradient operator ∇ on equation (2.31) yields the following eikonal equation (Kirillov, Stefani, and Fukumoto, 2014; Kirillov and Mutabazi, 2017)

$$\frac{d\mathbf{k}}{dt} = -\mathcal{U}^T \mathbf{k}, \quad (2.32)$$

where \mathcal{U} is defined from expression (2.23) and $d/dt = \partial_t + (\mathbf{U} \cdot \nabla)$.

Taking relations (2.30) and (2.31) into account within (2.29) results in the coupled equations

$$\left(Ro \left[\frac{d}{dt} + \mathcal{U} \right] + Ek + \mathbf{e}_z \times \right) \mathbf{u}^{(0)} + \frac{\rho^{(0)}}{\alpha^2} \mathbf{e}_z = -i\mathbf{k}_\alpha p^{(1)}, \quad (2.33)$$

$$\left(Ro \frac{d}{dt} + \frac{Ek}{Sc} \right) \rho^{(0)} + \left(Ro \mathcal{B}^T - \mathbf{e}_z^T B u \right) \mathbf{u}^{(0)} = 0, \quad (2.34)$$

where $Ek = \widetilde{Ek} |\mathbf{k}_\alpha^T \mathbf{k}|$.

Taking the dot product of (2.33) with \mathbf{k}^T from the left, in view of (2.26) we can isolate the first-order pressure term in the right-hand side and express it in terms of the zeroth-order terms as

$$p^{(1)} = \frac{i\mathbf{k}^T}{\mathbf{k}^T \mathbf{k}_\alpha} \left[\left(Ro \left[\frac{d}{dt} + \mathcal{U} \right] + \mathbf{e}_z \times \right) \mathbf{u}^{(0)} + \frac{\rho^{(0)}}{\alpha^2} \mathbf{e}_z \right]. \quad (2.35)$$

Differentiating (2.26) yields (Kirillov, Stefani, and Fukumoto, 2014; Kirillov and Mutabazi, 2017)

$$\frac{d}{dt} \left(\mathbf{k} \cdot \mathbf{u}^{(0)} \right) = \frac{d\mathbf{k}}{dt} \cdot \mathbf{u}^{(0)} + \mathbf{k} \cdot \frac{d\mathbf{u}^{(0)}}{dt} = 0.$$

With the identity (2.36) the expression (2.35) becomes

$$p^{(1)} = \frac{i\mathbf{k}^T}{\mathbf{k}^T \mathbf{k}_\alpha} \left[Ro \mathcal{U} \mathbf{u}^{(0)} + \mathbf{e}_z \times \mathbf{u}^{(0)} + \frac{\rho^{(0)}}{\alpha^2} \mathbf{e}_z \right] - \frac{iRo}{\mathbf{k}^T \mathbf{k}_\alpha} \frac{d\mathbf{k}}{dt} \cdot \mathbf{u}^{(0)}. \quad (2.36)$$

Re-writing (2.36) by means of the phase equation (2.32), we further obtain

$$p^{(1)} = \frac{i\mathbf{k}^T}{\beta^2} \left(\mathbf{e}_z \times \mathbf{u}^{(0)} + \frac{\rho^{(0)}}{\alpha^2} \mathbf{e}_z \right) + 2iRo \frac{\mathbf{k}^T \mathcal{U}}{\beta^2} \mathbf{u}^{(0)}, \quad (2.37)$$

where $\beta^2 = \mathbf{k}^T \mathbf{k}_\alpha = k_r^2 + k_\theta^2 + k_z^2/\alpha^2$.

Inserting expression (2.37) in (2.33) yields the transport equations

$$\begin{aligned} Ro \frac{du^{(0)}}{dt} &= -Ek\mathbf{u}^{(0)} - Ro \left(\mathcal{I} - 2\frac{\mathcal{K}}{\beta^2} \right) \mathcal{U}\mathbf{u}^{(0)} - \left(\mathcal{I} - \frac{\mathcal{K}}{\beta^2} \right) \mathbf{e}_z \times \mathbf{u}^{(0)} \\ &\quad - \left(\mathcal{I} - \frac{\mathcal{K}}{\beta^2} \right) \mathbf{e}_z \frac{\rho^{(0)}}{\alpha^2}, \\ Ro \frac{d\rho^{(0)}}{dt} &= -\frac{Ek}{Sc} \rho^{(0)} - \left(\mathcal{B}^T Ro - \mathbf{e}_z^T Bu \right) \mathbf{u}^{(0)}, \end{aligned} \quad (2.38)$$

where $\mathcal{K} = \mathbf{k}_\alpha \mathbf{k}^T$.

From the eikonal equation (2.32) we deduce that $k_r = k_z = const$ and $k_\theta = 0$ due to expression (2.23) (Kirillov, Stefani, and Fukumoto, 2014; Kirillov and Mutabazi, 2017). Introducing the scaled wavenumbers $q_r = k_r/\beta$ and $q_z = k_z/\beta$, we find $q_r = \sqrt{1 - q_z^2/\alpha^2}$. This allows us to write $\mathcal{K} = \mathbf{q}_\alpha \mathbf{q}^T$, where $\mathbf{q} = (q_r, 0, q_z)$ and $\mathbf{q}_\alpha = (q_r, 0, q_z/\alpha^2)$.

In the new notation the amplitude transport equations (2.38) for the perturbed velocity and density fields take the following explicit form

$$\left[Ro \left(\frac{\partial}{\partial t} + \Omega \frac{\partial}{\partial \theta} \right) + Ek \right] u_r^{(0)} - \frac{q_z^2}{\alpha^2} (1 + 2Ro\Omega) u_\theta^{(0)} - \frac{q_z q_r}{\alpha^2} \rho^{(0)} = 0, \quad (2.39a)$$

$$\left[Ro \left(\frac{\partial}{\partial t} + \Omega \frac{\partial}{\partial \theta} \right) + Ek \right] u_\theta^{(0)} + \left[1 + Ro \left(2\Omega + r \frac{\partial \Omega}{\partial r} \right) \right] u_r^{(0)} + rRo \frac{\partial \Omega}{\partial z} u_z^{(0)} = 0, \quad (2.39b)$$

$$\left[Ro \left(\frac{\partial}{\partial t} + \Omega \frac{\partial}{\partial \theta} \right) + Ek \right] u_z^{(0)} + \frac{q_z q_r}{\alpha^2} (1 + 2Ro\Omega) u_\theta^{(0)} + \frac{q_r^2}{\alpha^2} \rho^{(0)} = 0, \quad (2.39c)$$

$$\left[Ro \left(\frac{\partial}{\partial t} + \Omega \frac{\partial}{\partial \theta} \right) + \frac{Ek}{Sc} \right] \rho^{(0)} - u_z^{(0)} Bu + Ro \left(\frac{\partial \rho_A}{\partial r} u_r^{(0)} + \frac{\partial \rho_A}{\partial z} u_z^{(0)} \right) = 0, \quad (2.39d)$$

As one can notice, equations (2.39a) and (2.39c) coincide under the linear transformation $u_z^{(0)} = -(q_r/q_z)u_r^{(0)}$ and further reduces the degree of the system (2.39).

2.6 Dispersion relation

Introducing in (2.39) the growth rate λ and azimuthal wavenumber m from the ansatz

$$\left[u_r^{(0)}, u_\theta^{(0)}, u_z^{(0)}, \rho^{(0)} \right] = \left[\hat{u}_r^{(0)}, \hat{u}_\theta^{(0)}, \hat{u}_z^{(0)}, \hat{\rho}^{(0)} \right] \exp(\lambda t + im\theta), \quad (2.40)$$

and considering the system in the form of a linear eigenvalue problem $\mathcal{H}\xi = \hat{\lambda}\xi$, where $\xi = (\hat{u}_r^{(0)}, \hat{u}_\theta^{(0)}, \hat{\rho}^{(0)})^T$ and $\hat{\lambda} = Ro(\lambda + im\Omega) + Ek$, it yields the

3×3 matrix

$$\mathcal{H} = \begin{pmatrix} 0 & \frac{q_z^2}{\alpha^2} \frac{2j}{r^2} & \frac{q_r q_z}{\alpha^2} \\ -\frac{r^2 (q_z \kappa_r^2 - q_r \kappa_z^2)}{2q_z j} & 0 & 0 \\ -q_z^{-1} [Ro (q_z \partial_r \rho_A - q_r \partial_z \rho_A) + q_r Bu] & 0 & Ek \frac{Sc - 1}{Sc} \end{pmatrix}, \quad (2.41)$$

where $\partial_r \rho_A$ and $\partial_z \rho_A$ are given by (2.24), $j(r, z)$ is the angular momentum per unit mass

$$j = \frac{r^2}{2} (1 + 2Ro\Omega), \quad (2.42)$$

κ_r is the epicyclic frequency and κ_z is the frequency of vertical oscillations (Lyra and Umurhan, 2019)

$$\kappa_r^2 = r^{-3} \frac{\partial j^2}{\partial r}, \quad \kappa_z^2 = r^{-3} \frac{\partial j^2}{\partial z}. \quad (2.43)$$

As usual in such problems, the dispersion relation $\mathcal{D}(\hat{\lambda})$ of the system is obtained from

$$\mathcal{D}(\hat{\lambda}) = \det(\mathcal{H} - \hat{\lambda}\mathcal{I}), \quad (2.44)$$

where \mathcal{I} is the identity matrix and which in this case reduces to a third-order polynomial in $\hat{\lambda}$

$$\mathcal{D}(\hat{\lambda}) = \hat{\lambda}^3 + Ek \frac{1 - Sc}{Sc} \hat{\lambda}^2 + (\gamma_1 + \gamma_2) \hat{\lambda} + Ek \frac{1 - Sc}{Sc} \gamma_1 \quad (2.45)$$

where

$$\gamma_1 = \frac{q_z}{\alpha^2} (q_z \kappa_r^2 - q_r \kappa_z^2), \quad \gamma_2 = \frac{q_r}{\alpha^2} \left[Ro \left(q_z \frac{\partial \rho_A}{\partial r} - q_r \frac{\partial \rho_A}{\partial z} \right) + q_r Bu \right]. \quad (2.46)$$

It is worth mentioning that similar dispersion relations of third order were obtained earlier by McIntyre (McIntyre, 1970), who studied a baroclinic circular vortex in the presence of viscosity and a temperature gradient, and Singh and Mathur (Singh and Mathur, 2019) who studied a barotropic columnar vortex in a stratified ambient fluid in the non-rotating frame. In both of these works, the authors restricted their analyses to axisymmetric ($m = 0$) instabilities only.

Therefore, dispersion relation (2.45) with the coefficients (2.46) substantially generalizes those of the previous works as it takes into account rotation of the frame, azimuthal wavenumber m , diffusion of mass and momentum, both r - and z -dependence of the vortex angular velocity Ω via the Gaussian profile (2.14), radial and axial stratification of the vortex, its aspect ratio, and axial stratification of the ambient fluid. This implies that a shear parameter γ_1 related to differential rotation induced by the vortex and a buoyancy parameter γ_2 related to the density stratification of the ambient fluid influenced by the vortex, can take both positive and negative values.

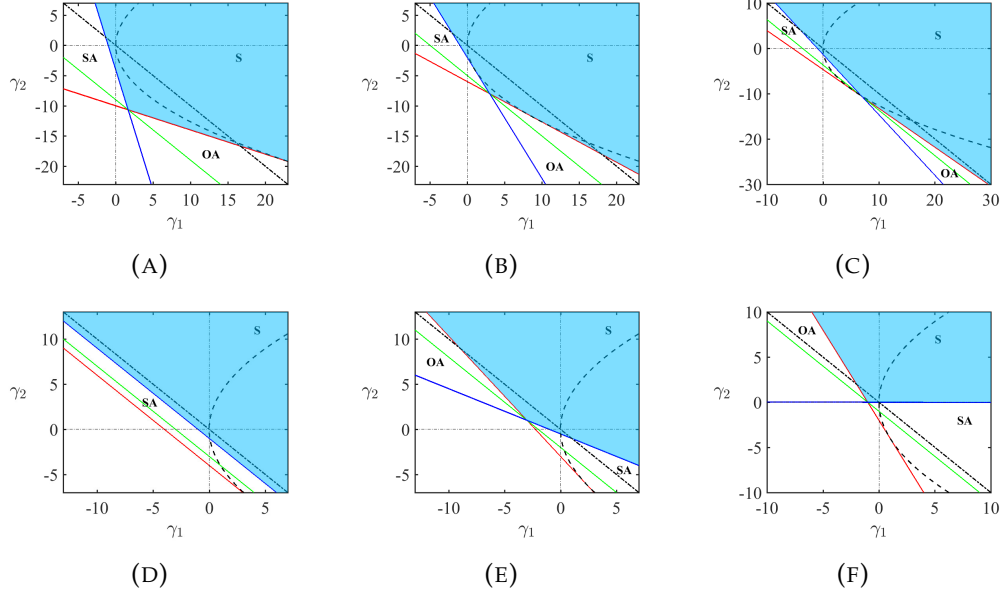


FIGURE 2.2: Stability maps with codimension-2 points (2.65) on the neutral stability curve for $Ek = 1$ and (a) $Sc = 0.25$, (b) $Sc = 0.5$, (c) $Sc = 0.75$, (d) $Sc = 1$, (e) $Sc = 2$, (f) $Sc \rightarrow +\infty$. The blue solid line stands for the boundary of the domain of stationary axisymmetric (SA) instability (2.64), the red solid line for that of the oscillatory axisymmetric (OA) instability (2.62), S stands for the stability domain. The dashed line is the envelope (2.69) and the dot-dashed line is the neutral stability boundary for the diffusionless system (2.48). The green solid line corresponds to the condition (2.63).

2.6.1 Diffusionless and $Sc = 1$ cases

Notice that at $Ek = 0$, as well as at $Sc = 1$, dispersion relation (2.45) factorizes into a product of quadratic and linear in $\hat{\lambda}$ polynomials and thus can be solved explicitly.

In these cases, the eigenvalues governing the centrifugal instability are recovered as

$$\lambda^\pm = -\frac{im\Omega}{Ro} \pm \frac{1}{Ro} \sqrt{-(\gamma_1 + \gamma_2)}, \quad (2.47)$$

which reads the instability condition

$$\gamma_1 + \gamma_2 < 0. \quad (2.48)$$

Centrifugal instability of a barotropic circular vortex

In the particular case of purely transverse perturbations ($q_r \rightarrow 0$), the eigenvalues (2.47) are

$$\lambda^\pm = -\frac{im\Omega}{Ro} \pm \frac{q_z}{\alpha Ro} \sqrt{-\kappa_r^2}, \quad (2.49)$$

which therefore yields an instability when $\kappa_r^2 < 0$. Notice that in the dimensional variables and parameters

$$\kappa_r^2 = f^{-2}(\partial_{\tilde{r}} \tilde{u}_z + \tilde{u}_z/\tilde{r} + f)(2\tilde{u}_z/\tilde{r} + f)$$

is nothing else but the generalized Rayleigh discriminant for a barotropic circular vortex (Yim, Stegner, and Billant, 2019). The inequality $\kappa_r^2 < 0$ is thus the well-known criterion for the centrifugal instability of columnar vortices (Yim, Stegner, and Billant, 2019).

Connection to Acheson and Gibbons Acheson and Gibbons, 1978

Let us compare our criterion for centrifugal instability (2.48) with the results derived previously by Acheson and Gibbons in the study of a magnetic and differentially rotating star (Acheson and Gibbons, 1978).

For this purpose, we first present their axisymmetric and diffusionless dispersion relation (without magnetic field) in its original form

$$\gamma \frac{s^2}{n^2} \omega^2 = \gamma r \Omega^2 \frac{\partial R}{\partial h} + G \frac{\partial E}{\partial h}, \quad (2.50)$$

where, in our notations, $n = k_z$ is the axial wavenumber, $s = |\mathbf{k}|$ is the norm of the wave vector, $\sigma = i\lambda$ is an eigenfrequency, $\omega = \sigma - m\Omega$ is the Doppler-shifted eigenfrequency, $R = \ln r^4 \Omega^2$ is the squared angular momentum, $E = \ln p \rho^{-\gamma}$ is a measure of entropy, $G = g_r - (k_r/k_z)g_z$ is a function containing gravitational effects and γ is the heat capacity ratio. The derivative operator in (2.50) is further defined (Acheson and Gibbons, 1978) as $\partial/\partial h = \partial/\partial r - (k_r/k_z)\partial/\partial z$.

Multiplying both sides of (2.50) by n^2/s^2 and introducing the wavenumbers $q_r = k_r/s$ and $q_z = k_z/s$, we first recover

$$(\lambda + im\Omega)^2 = -q_z^2 \left[\frac{\tilde{j}^2}{r^3} \frac{\partial_h \tilde{j}^2}{\tilde{j}^2} + \frac{G}{\gamma} \partial_h(p \rho^{-\gamma}) \right], \quad (2.51)$$

where $\tilde{j} = r^2 \Omega$ is a simplified version of the angular momentum (2.42) without the influence of the Coriolis force.

If the gravity is directed along the axial z -coordinate only (as it is in our setting), then using the correspondence $(g_r, g_z) = (0, \rho)$ within the function G in (2.51) yields

$$(\lambda + im\Omega)^2 = -q_z^2 \left[\frac{1}{r^3} \partial_h \tilde{j}^2 - \frac{q_r \rho}{q_z \gamma} \left(\frac{\partial_h p}{p} + \gamma \frac{\partial_h \rho}{\rho} \right) \right]. \quad (2.52)$$

As a consequence of the Newton-Laplace equation, the specific heat capacity ratio is related to the speed of sound c_s via the expression $c_s^2 = \gamma p / \rho$ and hence, tends to infinity in the case of incompressible flows (as it is in our case). Taking this limit in (2.52), we obtain

$$(\lambda + im\Omega)^2 = -q_z \left[\left(q_z \tilde{\kappa}_r^2 - q_r \tilde{\kappa}_z^2 \right) + \frac{q_r}{q_z} (q_z \partial_r \rho - q_r \partial_z \rho) \right], \quad (2.53)$$

with $\tilde{\kappa}_z = r^{-3}\partial_z\tilde{j}^2$ and $\tilde{\kappa}_r = r^{-3}\partial_r\tilde{j}^2$. Finally, the inviscid eigenfrequency of the work (Acheson and Gibbons, 1978) takes the form

$$\lambda^\pm = -im\Omega \pm \sqrt{-[q_z(q_z\tilde{\kappa}_r^2 - q_r\tilde{\kappa}_z^2) + q_r(q_z\partial_r\rho - q_r\partial_z\rho)]}. \quad (2.54)$$

Notice that the radicand in (2.54) has the same structure as our expressions (2.46) and (2.47), with the difference only in the factors α^{-2} and Ro and in the term containing the Burger number.

2.6.2 Particular cases when either $\gamma_1 = 0$ or $\gamma_2 = 0$

In these two particular cases the polynomial (2.45) factorizes, which allows us to find its roots explicitly.

For $\gamma_1 = 0$ the roots are

$$\begin{aligned} \lambda_{1,2} &= -im\Omega - \frac{Ek}{2Ro} \left\{ 1 + \frac{1}{Sc} \pm \sqrt{\frac{(Sc-1)^2}{Sc^2} - \frac{4\gamma_2}{Ek^2}} \right\}, \\ \lambda_3 &= -im\Omega - \frac{Ek}{Ro}. \end{aligned} \quad (2.55)$$

Recalling that $Ek/Ro = 1/Re > 0$, we see that in the limit $Sc \rightarrow +\infty$ the vortex is linearly stable if $\gamma_2 \geq 0$, see Fig. 2.2(f) and Fig. 2.6. In general, the condition for stability at $\gamma_1 = 0$ reads

$$\gamma_2 \geq -\frac{Ek^2}{Sc}. \quad (2.56)$$

In the particular case when $\gamma_2 = 0$ we have

$$\begin{aligned} \lambda_{1,2} &= -im\Omega - \frac{Ek}{Ro} \pm \frac{\sqrt{-\gamma_1}}{Ro}, \\ \lambda_3 &= -im\Omega - \frac{Ek}{RoSc}. \end{aligned} \quad (2.57)$$

According to (2.57), in the diffusionless case ($Ek = 0$) the vortex is linearly stable regardless of the sign of Ro , if and only if $\gamma_1 \geq 0$, which is similar to the generalized Rayleigh criterion $\kappa_r^2 - \kappa_z^2 \geq 0$ described in the literature (Yim, Stegner, and Billant, 2019), since $\gamma_2 = 0$ corresponds to the radial and axial density gradients compensating each other. When diffusivities of mass and momentum are taken into account, then with any $Sc > 0$ such vortices remain stable. Unstable diffusionless vortices ($\gamma_1 < 0$) can be stabilized for any $Sc > 0$, if $|\gamma_1| < Ek^2$. This is consistent with the results of McIntyre (McIntyre, 1970) and Singh and Mathur (Singh and Mathur, 2019), see Fig. 2.2.

2.7 General stability analysis

2.7.1 Bilharz algebraic criterion

Written with respect to λ the polynomial (2.45) has complex coefficients. Bilharz algebraic criterion (Bilharz, 1944; Kirillov, 2021) guarantees that all the roots of a complex polynomial of the form $p(\lambda) = (a_0 + ib_0)\lambda^3 + (a_1 + ib_1)\lambda^2 + (a_2 + ib_2)\lambda + (a_3 + ib_3)$ lie in the open left half of the complex λ -plane if and only if three determinants of even-order submatrices on the main diagonal of the following Bilharz matrix,

$$\mathcal{B} = \begin{pmatrix} a_3 & -b_3 & 0 & 0 & 0 & 0 \\ b_2 & a_2 & a_3 & -b_3 & 0 & 0 \\ -a_1 & b_1 & b_2 & a_2 & a_3 & -b_3 \\ -b_0 & -a_0 & -a_1 & b_1 & b_2 & a_2 \\ 0 & 0 & -b_0 & -a_0 & -a_1 & b_1 \\ 0 & 0 & 0 & 0 & -b_0 & -a_0 \end{pmatrix}, \quad (2.58)$$

are strictly positive. In view of $Ek/Ro = 1/Re > 0$, being applied to polynomial (2.45), the Bilharz criterion yields

$$\left\{ m^4 \Omega^4 Ro^4 Sc(2Sc + 1) + 6m^2 \Omega^2 Ro^2 Sc(Ek^2 + Sc\gamma_2 + \gamma_1) + (Ek^2 + Sc\gamma_2 + \gamma_1) \left[(Sc + 2)Ek^2 + Sc(\gamma_1 + \gamma_2) \right] \right\} \times \left[2(Sc + 1)^2 Ek^2 + Sc(2Sc\gamma_1 + Sc\gamma_2 + \gamma_2) \right] > 0, \quad (2.59)$$

$$m^2 Ro^2 \Omega^2 \left[2(Sc^2 + Sc + 1)Ek^2 + Sc(2\gamma_1 - \gamma_2)(Sc - 1) \right] + m^4 \Omega^4 Ro^4 Sc(2Sc + 1) + (Ek^2 + Sc\gamma_2 + \gamma_1) \left[(Sc + 2)Ek^2 + Sc(\gamma_1 + \gamma_2) \right] > 0, \quad (2.60)$$

$$Sc(Ek^2 + Sc\gamma_2 + \gamma_1) > 0. \quad (2.61)$$

In the following, we will use the inequalities (2.59)–(2.61) to examine stability and instabilities of the lenticular vortex in the presence of differential diffusion of mass and momentum.

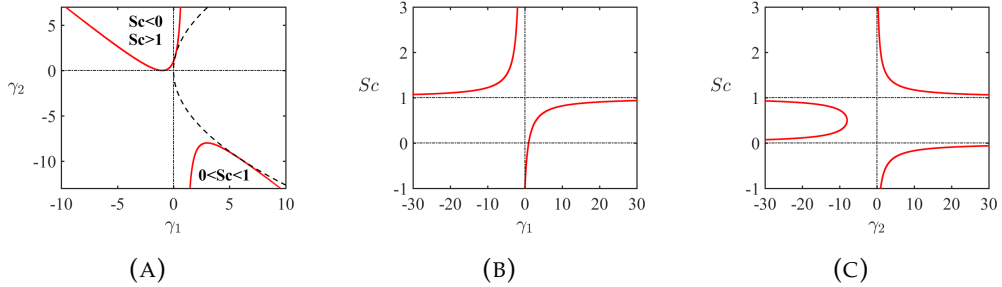


FIGURE 2.3: For $Ek = 1$ projections of the loci of the codimension-2 points onto different planes given by equations (2.65) and (2.66). The dashed curve is the envelope (2.69).

2.7.2 Stationary and oscillatory axisymmetric instabilities

A codimension-2 point on the neutral stability line

Setting $m = 0$ in (2.59)–(2.61) we find that for $Sc > 0$ the base flow is linearly stable if and only if the following three inequalities are fulfilled simultaneously

$$2(Sc + 1)^2 Ek^2 + Sc(2Sc\gamma_1 + \gamma_2(Sc + 1)) > 0, \quad (2.62)$$

$$(Sc + 2)Ek^2 + Sc(\gamma_1 + \gamma_2) > 0, \quad (2.63)$$

$$Ek^2 + Sc\gamma_2 + \gamma_1 > 0. \quad (2.64)$$

Although $Sc < 0$ might not look physically meaningful, we mention, for completeness, that in this case the inequality (2.62) remains the same whereas the inequalities (2.63) and (2.64) are reversed. It is worth to notice that continuation of stability diagrams to negative values of dissipation parameters can help in uncovering instability mechanisms (Kirillov, 2017; Kirillov, 2021).

The expressions in (2.62)–(2.64) are linear in γ_1 and γ_2 which makes it convenient to represent the criteria in the (γ_1, γ_2) -plane (Singh and Mathur, 2019), where the corresponding stability domain will be given by the intersection of the half-planes (2.62)–(2.64), see Fig. 2.2.

Equating to zero the left-hand sides of the expressions (2.62)–(2.64) and then solving the resulting equations with respect to γ_1 and γ_2 , we find that all the three straight lines intersect at one and the same point with the coordinates, cf. (Singh and Mathur, 2019)

$$\gamma_1 = Ek^2 \frac{1 + Sc}{1 - Sc}, \quad \gamma_2 = \frac{2Ek^2}{Sc(Sc - 1)}. \quad (2.65)$$

At a given value of Ek equations (2.65) define a spatial curve in the (γ_1, γ_2, Sc) -space, which projections are shown in Fig. 2.3. In particular, the projection onto the (γ_1, γ_2) -plane is

$$\gamma_2(Ek^2 - \gamma_1) - (Ek^2 + \gamma_1)^2 = 0. \quad (2.66)$$

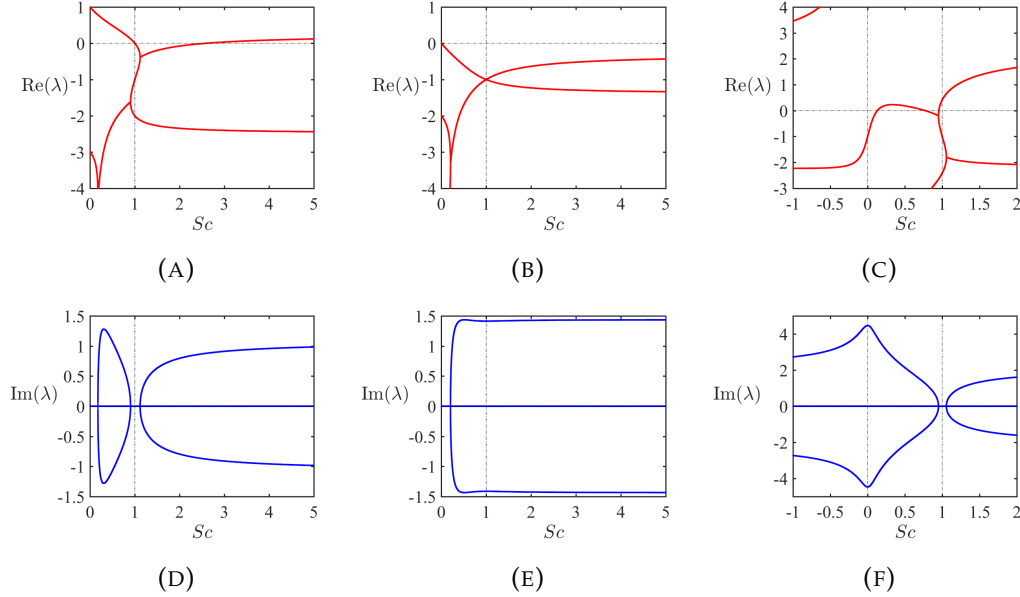


FIGURE 2.4: Growth rates and frequencies for $m = 0$, $Ek = 1$, $Ro = 1$, and (a,d) $\gamma_1 = -4$, $\gamma_2 = 3$ (b,e) $\gamma_1 = -1$, $\gamma_2 = 3$, (c,f) $\gamma_1 = 20$, $\gamma_2 = -22$, demonstrating exchange of stationary and oscillatory instabilities near $Sc = 1$, cf. Fig. 2.2.

At the common point (2.65) the slopes $d\gamma_2/d\gamma_1$ of straight lines (2.62), (2.63), and (2.64) are, respectively,

$$\sigma_1 = -\frac{2Sc}{Sc + 1}, \quad \sigma_2 = -1, \quad \sigma_3 = -\frac{1}{Sc}. \quad (2.67)$$

Notice the following relationships between the slopes:

$$\left. \begin{array}{l} -1 \geq \sigma_1 > -2 \\ \sigma_2 = -1 \\ -1 \leq \sigma_3 < 0 \end{array} \right\} \quad \text{if} \quad 1 \leq Sc < +\infty, \\ \left. \begin{array}{l} 0 > \sigma_1 > -1 \\ \sigma_2 = -1 \\ -\infty < \sigma_3 < -1 \end{array} \right\} \quad \text{if} \quad 0 < Sc < 1. \quad (2.68)$$

For $0 < Sc < 1$ we have $0 > \sigma_1 > \sigma_2 = -1 > \sigma_3$, meaning that the slope of the line (2.64) is steeper than the slope of (2.62), see Fig. 2.2(a-c). Therefore, the neutral stability lines forming the boundary of the stability domain intersect each other at the point (2.65) such that $\gamma_1 > 0$ and $\gamma_2 < 0$, see Fig. 2.3(a). This singular point on the stability boundary is widely known in the hydrodynamical literature as a *codimension-2 point* (Kirillov and Mutabazi, 2017) or Bogdanov-Takens bifurcation point (Tuckerman, 2001). Stability domain is therefore convex, with its edge lying in the domain of centrifugal instability of the diffusionless vortex, Fig. 2.2(a-c). On the other hand, difference of the slopes σ_1 and σ_3 from $\sigma_2 = -1$ allows for diffusive

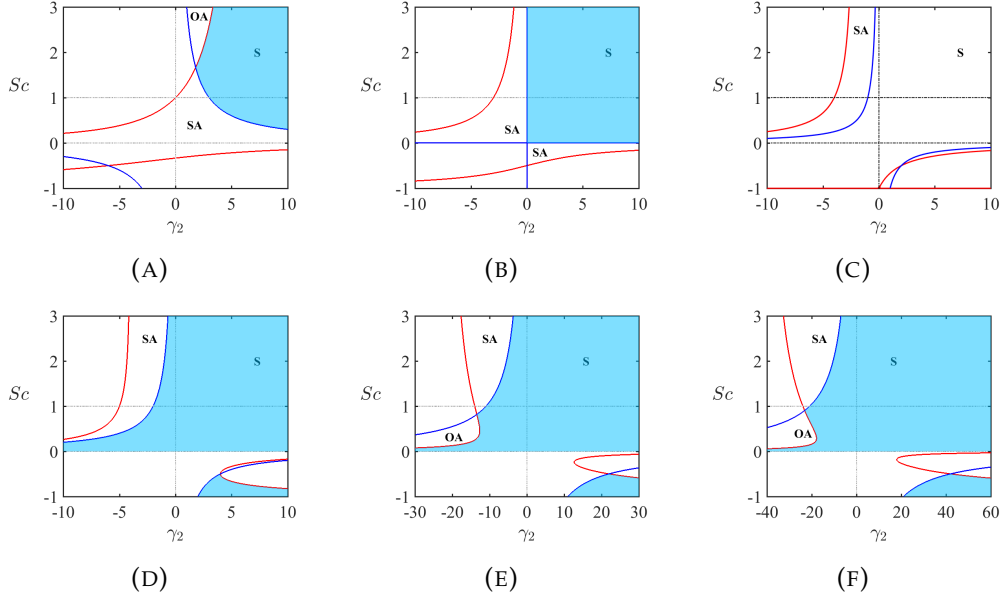


FIGURE 2.5: Stability maps for $Ek = 1$ and (a) $\gamma_1 = -4$, (b) $\gamma_1 = -1$, (c) $\gamma_1 = 0$, (d) $\gamma_1 = 1$, (e) $\gamma_1 = 10$, (f) $\gamma_1 = 20$ with the codimension-2 points at (a) $\gamma_2 = 9/5$ and $Sc = 5/3$, (e) $\gamma_2 = -121/9$ and $Sc = 9/11$, and (f) $\gamma_2 = -441/19$ and $Sc = 19/21$. At the codimension-2 point $Sc \rightarrow 1$ as $|\gamma_1| \rightarrow \infty$, in accordance with Fig. 2.3(b).

destabilization of centrifugally-stable vortices, if the absolute values of γ_1 and γ_2 are large enough, Fig. 2.2(a-c).

As Sc approaches 1, the difference between slopes (2.67) is decreased so that $\sigma_1 = \sigma_2 = \sigma_3 = -1$ at $Sc = 1$, Fig 2.2(d). This process is accompanied by the movement of the codimension-2 point on the lower branch of the curve (2.66) from $\gamma_2 \rightarrow -\infty$ along the asymptotic direction $\gamma_1 = Ek^2$ as Sc departs from zero to $\gamma_1 \rightarrow +\infty$ and $\gamma_2 \rightarrow -\infty$ along the asymptotic direction $\gamma_1 + \gamma_2 + 3Ek^2 = 0$ as $Sc \rightarrow 1$, Fig. 2.3.

At $Sc = 1$ the stability boundaries of the diffusionless system and the double-diffusive system exactly coincide in the limit of $Ek \rightarrow 0$. However, for $Ek \neq 0$, double diffusion can stabilize centrifugally unstable diffusionless vortices, quite in agreement with Lazar et al. (Lazar, Stegner, and Heifetz, 2013), Fig. 2.2(d).

As soon as the Schmidt number passes the threshold $Sc = 1$, the codimension-2 point reappears at infinity on the upper branch of the curve (2.66) and moves along the asymptotic direction $\gamma_1 + \gamma_2 + 3Ek^2 = 0$ until it reaches a minimum of this curve at $\gamma_1 = -Ek^2$ and $\gamma_2 = 0$ when $Sc \rightarrow +\infty$, Fig. 2.3. This qualitative change in location of the codimension-2 point (cf. Tuckerman (Tuckerman, 2001)) is accompanied by the exchange of the stability criteria: the condition (2.64) becomes dominating over (2.62) and vice versa, Fig. 2.2(e,f).

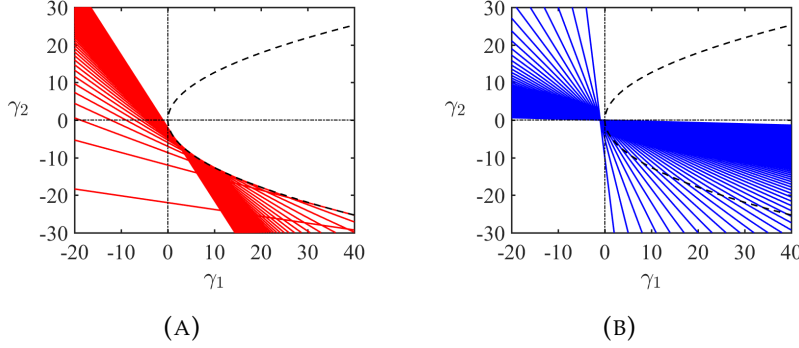


FIGURE 2.6: (Dashed) For $Ek = 1$ the parabolic envelope (2.69) of (solid, red) a family of straight lines (2.62), parameterized by $0 < Sc < 30$, that determine the boundary between the domain of stability and oscillatory axisymmetric instability. Inside the parabolic region there is no oscillatory axisymmetric instability for all $Sc > 0$. (Solid, blue) A family of straight lines (2.64) parameterized by $0 < Sc < 30$, that determine the boundary between the domain of stability and stationary axisymmetric instability; all the lines in this family have a common point at $\gamma_1 = -Ek^2$ and $\gamma_2 = 0$.

2.7.3 Exchange of stationary and oscillatory instabilities

Actually, reversed inequality (2.64) determines stationary axisymmetric (SA) instability, corresponding to a monotonically growing perturbation, while the reversed inequality (2.62) stands for oscillatory axisymmetric (OA) instability, i.e. growing oscillation.

Fig. 2.2 provides evidence that stability boundary consisting of two straight lines that intersect at a codimension-2 point in the (γ_1, γ_2) -plane exhibit a qualitative change at $Sc = 1$ such that for $Sc < 1$ ($Sc > 1$) the upper (lower) line corresponds to the onset of SA and the lower (upper) line to the onset of OA. Notice that, as described above, the location of the codimension-2 point changes with the change of Sc with a ‘jump’ at $Sc = 1$.

By the latter reason, the qualitative fact of exchange of stationary and oscillatory axisymmetric instabilities at $Sc = 1$, so evident in the (γ_1, γ_2) -plane, is obscured in the plots of growth rates and frequencies of the perturbation versus Sc .

Indeed, in Fig. 2.4(a,d) $\gamma_1 = -4$, exactly as in Fig. 2.5(a), where a codimension-2 point exists at $\gamma_2 = 9/5$ and $Sc = 5/3 > 1$, separating the boundaries of stationary ($Sc < 5/3$) and oscillatory ($Sc > 5/3$) axisymmetric instabilities. Although the growth rates and frequencies in Fig. 2.4(a,d) computed at $\gamma_2 = 3$ confirm the order of SA and OA, the exchange between these instabilities occurs not exactly at $Sc = 1$, but in a neighborhood of this value. According to Fig. 2.3(b) the critical value of $Sc \rightarrow 1$ as $\gamma_1 \rightarrow -\infty$.

Changing the sign of γ_1 from negative to positive leads to re-appearance of the codimension-2 point in the second quadrant in the (γ_2, Sc) -plane, Fig. 2.5(e,f). In particular, for $\gamma_1 = 20$ it is situated at $\gamma_2 = -441/19$ and $Sc = 19/21 < 1$. The codimension-2 point separates the boundaries of oscillatory ($Sc < 19/21$) and stationary ($Sc > 19/21$) axisymmetric instabilities that are in the reverse order with respect to the case of negative γ_1 . Again, growth rates

and frequencies computed in Fig. 2.4(c,f) for $\gamma_2 = -22$, confirm that transition from OA to SA occurs at a value of Sc in the vicinity of $Sc = 1$. The critical value of Sc tends to 1 as $\gamma_1 \rightarrow +\infty$ in agreement with Fig. 2.3(b).

We notice that according to (2.62)–(2.64), the described qualitative picture with destabilization of centrifugally stable vortices for $Sc \neq 1$, codimension-2 point, and exchange of instabilities is preserved even in the limit of vanishing dissipation, $Ek \rightarrow 0$, in accordance with the properties of the McIntyre instability (McIntyre, 1970), which are typical for a broad class of dissipation-induced instabilities (Kirillov and Verhulst, 2010; Kirillov, 2021).

2.7.4 OA as a genuine dissipation-induced instability

In Fig. 2.2 and Fig. 2.5 one can see that the codimension-2 point separates the boundaries of the regions of oscillatory and stationary axisymmetric instabilities. The existence of the codimension-2 point qualitatively distinguishes the diffusive case from the diffusionless one, where the onset of instability corresponds to the stationary axisymmetric centrifugal instability only.

The growth rate of the oscillatory instability is smaller than the growth rate of the centrifugal instability, Fig. 2.4. However, in contrast to McIntyre (McIntyre, 1970), who found such modes within the domain of centrifugal instability and concluded that they are not important with respect to centrifugally-unstable modes that are always destabilized first in his setting, we discovered the conditions when the oscillatory axisymmetric modes are destabilized first and thus determine the onset of instability.

Hence, the oscillatory axisymmetric instability is a genuine dissipation-induced instability (Kirillov and Verhulst, 2010; Kirillov, 2021) which is as important as the stationary axisymmetric one despite its relatively low growth rate, because in a large set of parameters the oscillatory axisymmetric modes are the first to be destabilized by the differential diffusion of mass and momentum.

2.7.5 Sufficient conditions for the vortex stability at any $Sc > 0$

Notice that the family of straight lines given by equating to zero the left-hand side of the inequality (2.62) and parameterized with Sc has a non-trivial envelope, see Fig. 2.6(a). To find it, we differentiate the left-hand side by Sc , express Sc from the result to substitute it back to (2.62). This yields the following parabola in the (γ_1, γ_2) -plane

$$\gamma_1 = \frac{\gamma_2^2}{16Ek^2}, \quad (2.69)$$

shown as a dashed curve in Fig. 2.2, Fig. 2.3, and Fig. 2.6. One can see that as Sc increases from 0 to infinity, the OA-boundaries are accumulating and ultimately tend to the line

$$\gamma_2 = -2(Ek^2 + \gamma_1) \quad (2.70)$$

that passes through the point $\gamma_1 = -Ek^2$ and $\gamma_2 = 0$ in the (γ_1, γ_2) -plane, see Fig. 2.6(a).

This implies that in all the points inside the parabolic envelope (2.69) the vortex cannot be destabilized via the oscillatory instability mechanism, no matter what is the value of $Sc > 0$. To the best of our knowledge this explicit result has never been reported in the literature.

On the other hand, the family of straight lines given by equating to zero the left-hand side of the inequality (2.64) varies between the line $\gamma_1 = -Ek^2$ at $Sc = 0$ and the line $\gamma_2 = 0$ at $Sc \rightarrow \infty$, Fig. 2.6(b). Therefore, the whole lower part of the parabola (2.69) can belong to the domain of stationary axisymmetric instability in the limit of infinite $Sc > 0$.

Consequently, the area in the (γ_1, γ_2) -plane, limited by the criteria

$$\gamma_1 \geq -Ek^2, \quad \gamma_2 \geq 0 \quad (2.71)$$

corresponds to the stability domain, no matter what is the value of $Sc > 0$. This is in agreement with the analysis of the case $\gamma_2 = 0$ based on the equations (2.57) and generalises the results of McIntyre (McIntyre, 1970) and Singh and Mathur (Singh and Mathur, 2019) due to more comprehensive structure of parameters γ_1 and γ_2 given by (2.46).

2.8 Conclusion

We considered a model of a baroclinic circular lenticular vortex with a Gaussian profile of angular velocity both in radial and axial directions, immersed in a vertically stratified viscous fluid in the presence of diffusion of a stratifying agent and rotation of the coordinate frame related to the ambient fluid. This setting is substantially more comprehensive than those of the previous works that, in particular, were limited by the assumption of barotropy, did not take into account rotation of the frame and diffusion of mass and momentum, or set the Schmidt number equal to unity.

We have derived an original dimensionless set of equations on the f -plane, describing the dynamics of the vortex immersed in a vertically stratified fluid and then linearized it about a base state that we have found explicitly. The linearized equations of motion were further expanded in terms of asymptotic series by means of the geometric optics approximation (Kirillov, Stefani, and Fukumoto, 2014; Kirillov and Mutabazi, 2017; Kirillov, 2017; Singh and Mathur, 2019; Vidal et al., 2019; Kirillov, 2021) to produce a set of the amplitude transport equations. The latter offered us an opportunity to derive an exhaustive but elegant third-order polynomial dispersion relation governing the local stability of the vortex.

In the diffusionless limit and in the case where magnitudes of both damping mechanisms are identical we obtained a generalized Rayleigh criterion for centrifugal instability in terms of the shear and buoyancy parameters γ_1 and γ_2 and shown that it reduces to the known in the literature particular cases.

Applying the algebraic Bilharz criterion to the complex dispersion relation we derived new rigorous stability criteria in terms of γ_1 and γ_2 as well as the Schmidt and Ekman numbers related to the differential diffusion of mass and momentum. We visualized these criteria in the (γ_1, γ_2) -plane and revealed a codimension-2 point splitting the boundaries of oscillatory and stationary axisymmetric instabilities that can affect both centrifugally stable and unstable diffusionless flows.

The oscillatory axisymmetric instability was found to be a genuine dissipation-induced instability because of its absence in the diffusionless case. Nevertheless, we have described explicitly a parabolic region in the (γ_1, γ_2) -plane that is free of oscillatory axisymmetric instabilities, no matter what the value of $Sc > 0$ is.

In contrast to the work of McIntyre (McIntyre, 1970) we found conditions when oscillatory axisymmetric modes are the first to be destabilized by the double diffusion and thus are dominant even despite the growth rate of the oscillatory instability is generally weaker than that of the centrifugal instability (Yim and Billant, 2016). Finally, we provided a sufficient condition for stability of a baroclinic vortex at arbitrary $Sc > 0$ that generalizes that of the previous works by McIntyre (McIntyre, 1970) and Singh and Mathur (Singh and Mathur, 2019).

This study conclusively proved the decisive role of the Schmidt number and therefore the differential diffusion of mass and momentum for the stability of lenticular vortices and, particularly, for excitation of the genuine dissipation-induced oscillatory instability. A codimension-2 point found on the neutral stability curve is proven to govern exchange of stationary and oscillatory instability as the Schmidt number transits through the unit value. All the results are preserved even in the limit of vanishing dissipation, which is a typical property of dissipation-induced instabilities (Kirillov and Verhulst, 2010; Kirillov, 2021).

We have thus developed new analytical criteria for an express-analysis of stability of baroclinic circular lenticular vortices for arbitrary parameter values that is believed to be an efficient tool for informing future numerical and experimental studies in this actively developing field.

Chapter 3

Double-diffusive instabilities in magnetohydrodynamic flows

“But the effect of her being on those around her was incalculably diffusive [...]”

George Eliot, *Middlemarch*

A famous example of dynamical systems subject to instabilities due to multiple diffusive mechanisms consists of the analysis of magnetohydrodynamic (MHD) flows, namely hydrodynamical flows of an electrically conducting fluid in the presence of a magnetic field. Such a system is well-known among the community of astrophysicists as it clearly describes the model of rotating stellar flows that are present, e.g., in plasmas or in accretion disks. Considering that the two equations of motion governing the structure of the velocity and magnetic fields in these systems correspond to the coupled Navier-Stokes and Maxwell equations, a seminal monograph on the stability of such systems has been published 60 years ago by Chandrasekhar (Chandrasekhar, 1961), see also modern monographs (Davidson, 2001; Goedbloed, Keppens, and Poedts, 2010). However, it still remains crucial to continue investigating the stability of MHD flows, as it has recently been shown that new types of instabilities might arise from the consideration of particular background fields. Indeed, the influence of an azimuthal magnetic field on the stability of a rotating MHD flow highly decreases the threshold for instability for the new azimuthal magnetorotational instability (AMRI) in terms of the Reynolds number Re (Hollerbach and Rüdiger, 2005; Liu et al., 2006; Kirillov and Stefani, 2013). Such instability can now be verified experimentally due to the tolerable critical Reynolds in experiments such as the magnetized Taylor-Couette flow, which has been confirmed shortly after in laboratory (Stefani et al., 2006; Stefani et al., 2009; Rüdiger et al., 2010; Seilmayer et al., 2014). We can further notice that similar instability phenomenon can be attributed to the onset of turbulence in accretion disks (Balbus and Hawley, 1992; Terquem and Papaloizou, 1996).

Afterwards, connection of the MRI in its general formulation with the notion of dissipation-induced instability has been made (Kirillov, Stefani, and Fukumoto, 2014; Kirillov, 2017; Kirillov, 2021) and similar behaviours as in

the double-diffusive CFS instability, presented in Chapter 1, have been observed. In a similar manner as in the CFS configuration with the parameter χ , the stability of resistive MHD flows is governed by the ratio of dissipative parameters, namely the magnetized Prandtl number Pm . Because of the low electric conductivity of the relevant physical applications (Rüdiger et al., 2014), we mainly consider the *inductionless* limit of the MHD equations, namely the case where Pm is vanishing. As for damped Maclaurin spheroids, the argument of small damping ratio in MHD does not asymptotically correspond to the undamped configuration, due to the intrinsic structure of this double-diffusive system (Kirillov, 2017). Much attention is therefore required to solve the dispersion relations associated with the different magnetorotational instabilities, and the consideration of new settings of methods to approximate the equations of motion are essential to enhance the previously known results. Our contribution directly supports this notion, and we intend to extend the already established stability domains to new unstable regions, by the formulation and analysis of an advanced differential equation. The approach presented below follows from the previous analysis of AMRI by means of the Hain-Lüst differential equation (Hain and Lüst, 1958) derived for the ideal (nondiffusive) MHD equations (Zou and Fukumoto, 2014) and extend to the case of resistive MHD flows.

Therefore, we consider a differentially rotating flow of an incompressible electrically conducting and viscous fluid subject to an external axial and azimuthal magnetic field. Starting with the derivation of this new differential equation from the original equations of motion, we perform a linear stability analysis of the newly derived dispersion relation by means of the Wentzel-Kramers-Brillouin (WKB) method. In particular, we find that the flow is subject to a long-wavelength instability that takes place even beyond the Liu limit (Liu et al., 2006), under the condition of vanishing magnetized Prandtl number Pm . We confirm this instability through the numerical solution of the boundary value problem associated with a magnetized Taylor-Couette flow, using a combined approach of pseudo-spectral collocation methods (Hollerbach, Teeluck, and Rüdiger, 2010; Deguchi, 2017). As it has been omitted in the original version of the published paper presented hereafter, we provide further information on the numerical parameters used in the numerical computation of the MHD Taylor-Couette flow. We used a truncature number N (as defined in the following article) with values ranging around 20, as it was enough to reach convergence and good agreement with the previous numerical studies (Hollerbach, Teeluck, and Rüdiger, 2010; Deguchi, 2017). Moreover, we emphasize that ζ is a parameter describing the ratio of inner to outer radii and hence, limits of $\zeta \rightarrow 0$ and $\zeta \rightarrow 1$ correspond respectively to wide and narrow gaps of the cylinders.

This chapter consists of a paper submitted and published in the peer-reviewed journal *Physical Review E* by R. Zou, O. N. Kirillov, Y. Fukumoto and myself (Zou et al., 2020). My original contribution is in the numerical simulation of a magnetized Taylor-Couette flow to confirm the new instability domain in the long-wavelength approximation, as theoretically predicted from the extended Hain-Lüst equation.

Analysis of azimuthal magnetorotational instability of rotating magnetohydrodynamic flows and Tayler instability via an extended Hain-Lüst equation

R. Zou *Zhejiang Normal University, 688 Yingbin Road, Jinhua, Zhejiang, 321004, China*J. Labarbe  and O. N. Kirillov **Northumbria University, Newcastle upon Tyne, NE1 8ST, United Kingdom*Y. Fukumoto *Institute of Mathematics for Industry, Kyushu University, Fukuoka, 819-0395, Japan*

(Received 11 July 2019; revised manuscript received 12 November 2019; published 3 January 2020)

We consider a differentially rotating flow of an incompressible electrically conducting and viscous fluid subject to an external axial magnetic field and to an azimuthal magnetic field that is allowed to be generated by a combination of an axial electric current external to the fluid and electrical currents in the fluid itself. In this setting we derive an extended version of the celebrated Hain-Lüst differential equation for the radial Lagrangian displacement that incorporates the effects of the axial and azimuthal magnetic fields, differential rotation, viscosity, and electrical resistivity. We apply the Wentzel-Kramers-Brillouin method to the extended Hain-Lüst equation and derive a comprehensive dispersion relation for the local stability analysis of the flow to three-dimensional disturbances. We confirm that in the limit of low magnetic Prandtl numbers, in which the ratio of the viscosity to the magnetic diffusivity is vanishing, the rotating flows with radial distributions of the angular velocity beyond the Liu limit, become unstable subject to a wide variety of the azimuthal magnetic fields, and so is the Keplerian flow. In the analysis of the dispersion relation we find evidence of a new long-wavelength instability which is caught also by the numerical solution of the boundary value problem for a magnetized Taylor-Couette flow.

DOI: [10.1103/PhysRevE.101.013201](https://doi.org/10.1103/PhysRevE.101.013201)

I. INTRODUCTION

A. Standard magnetorotational instability

Due to the rediscovery of Velikhov's [1] and Chandrasekhar's [2] pioneering results by Balbus and Hawley [3], the magnetorotational instability (MRI) has aroused strong interest in astrophysics as a promising mechanism for triggering turbulence in the flow of an accretion disk and for promoting outward transport of angular momentum, while the matter accretes to the center [4,5]. In magnetohydrodynamics (MHD) and plasma physics communities the MRI stimulated development of new experimental facilities for its detection in the magnetized Couette-Taylor flow of either liquid metal (sodium, gallium, and liquid eutectic alloy GaInSn) as in the Potsdam Rossendorf Magnetic Instability Experiment (PROMISE) or plasma as in the Madison plasma Couette flow experiment [6–9].

Let us introduce the cylindrical coordinates (r, θ, z) with the z axis along the axis of symmetry, along with \mathbf{e}_r , \mathbf{e}_θ , and \mathbf{e}_z being the unit vectors in the radial, azimuthal, and axial direction, respectively. For an accretion disk, the Keplerian flow, a cylindrically symmetric flow with the profile $U_\theta \propto r^{-1/2}$ of rotational velocity, satisfies the force balance: $U_\theta^2(r)/r = \Omega^2(r)r = -\nabla\Phi$; $\Phi \propto 1/r$. In general, a steady

rotating flow with the angular velocity $\Omega(r)\mathbf{e}_z$, parallel to the z axis can be considered as a base state. To quantify the differential rotation the Rossby number is defined as $\text{Ro} = 1/2(d \log \Omega / d \log r) = r\Omega'/(2\Omega)$, where the prime designates the derivative with respect to r and $\Omega > 0$ without loss of generality; see, e.g., Refs. [10,11].

For a nonmagnetized flow of an ideal incompressible fluid, Rayleigh's criterion states that the centrifugal instability with respect to axisymmetric disturbance occurs when the Rossby number, $\text{Ro} < -1$, which fails to include the Keplerian flow ($\text{Ro} = -3/4$).

According to Refs. [1–3], a combined effect of fluid rotation and the imposed axial magnetic field is able to raise the critical Rossby number from -1 to 0 and destabilize the Rayleigh-stable flows (including the Keplerian one) of an incompressible fluid, for which the viscosity and the electric resistivity are neglected. The instability caused by the magnetic field that has only the axial component $\mathbf{B} = B_z \mathbf{e}_z$ is known as the standard magnetorotational instability (SMRI) [10].

Already in Refs. [1,2] a counterintuitive Velikhov-Chandrasekhar paradox for SMRI has been pointed out. In the case of an ideal nonresistive flow, boundaries of the region of the magnetorotational instability are misplaced compared to the Rayleigh boundaries of the region of the centrifugal instability and do not converge to those in the limit of a negligibly small axial magnetic field [12]. Willis and Barenghi established that the convergence is possible in the presence

*Corresponding author: oleg.kirillov@northumbria.ac.uk

of viscosity and resistivity [13]. Actually, the transition is parameterized by the Lundquist number S , so that the highly conducting fluids characterized by high values of S have SMRI for $\text{Ro} < 0$ and more resistive fluids with low Lundquist numbers are Rayleigh-unstable for $\text{Ro} < -1$, see the short-wavelength analysis in Ref. [14] and its recent confirmation by asymptotic and numerical methods in Ref. [15].

B. Helical and azimuthal MRI and Tayler instability

Given an axial magnetic field at some instant, the radial component is seeded by perturbing the axial field. Once the radial component arises, with the magnetic field frozen into a perfectly conducting accretion disk, the radial component is tilted by the differential rotation to produce azimuthal component, and the latter component is constantly stretched with time, resulting in establishing a strong azimuthal component [16]. Three-dimensional numerical simulations demonstrated that the initial weak azimuthal magnetic field tends to be stretched out to become, at a later stage, dominant over the initial axial magnetic field [17,18].

Instabilities induced by azimuthal magnetic fields have been studied already in Refs. [19,20] for the accretion disks and in a more general setting for a differentially rotating flow of a perfectly conducting ideal fluid in Refs. [21,22]. A combined action of the azimuthal and the axial magnetic field, i.e., the helical field, on the stability of accretion disks in the ideal MHD setting was addressed in Ref. [23].

In a protoplanetary disk surrounding a young star, the ionization depends on the radiation from the x rays and cosmic rays [24], and the temperature of the disk. The midplane of the accretion disk receives fewer radiation and the cold region of the disk is only weakly ionized. For the cold and less radiated parts of the protoplanetary and accretion disks as well as for the experiments with liquid metals, the effects of both the viscosity ν and the magnetic diffusivity η are therefore not ignorable. Because of the low electric conductivity, the magnetic Prandtl number $\text{Pm} = \nu/\eta$ is very small [25] (e.g., $\text{Pm} \sim 10^{-5}$ for liquid sodium, $\text{Pm} \sim 10^{-6}$ for gallium and liquid eutectic alloy GaInSn). By contrast, in the hot parts of the accretion disks, because of the high electric conductivity, Pm can become very large; see, e.g., Ref. [26] where Pm ranges from 10^{-3} to 10^3 .

The case of $\text{Pm} = 0$ is referred to as the inductionless limit [8,27–29]. Viewing Pm as a ratio of the magnetic and hydrodynamics Reynolds numbers, $\text{Pm} = \text{Rm}/\text{Re}$, one can deduce that $\text{Pm} \sim 10^{-5}$ and $\text{Rm} > 1$ implies $\text{Re} > 10^5$ for the onset of SMRI that is governed by Rm and S and requires high values of these numbers for its excitation [30]. On the other hand, at $\text{Re} > 10^5$ it is hard to keep the base flow of a liquid metal laminar in an experimental Couette-Taylor setup, which explains why SMRI is still not observed in an experiment [4,5].

In 2005 Hollerbach and Rüdiger [31] demonstrated that the simultaneous application of an axial and an azimuthal magnetic field in the case of low Pm can significantly reduce the critical value of the hydrodynamic Reynolds number at the onset of MRI in the Couette-Taylor flow. The predicted in Ref. [31] axisymmetric helical MRI (HMRI) has been successfully detected in subsequent experiments on the PROMISE facility [32–34].

The azimuthal MRI (AMRI), for which the magnetic field has only the azimuthal component $\mathbf{B} = B_\theta(r)\mathbf{e}_\theta$, was predicted to be nonaxisymmetric and feasible for the parameters of the existing liquid-metal Couette-Taylor facilities in Ref. [35]. It was detected by PROMISE in 2014 for the azimuthal magnetic field created by an axial current external to the liquid metal [36]. We notice, however, that the domains of both AMRI and HMRI plotted in the (Ha, Re) plane typically have a finite size along the Re axis, which means that these instabilities can be inhibited at sufficiently large Reynolds numbers.

Both HMRI and AMRI observed in the liquid metal experiments were reported for the differential flows that are distant from the Keplerian one. Detection of HMRI and AMRI for the quasi-Keplerian Couette-Taylor flows is planned in the upcoming MRI-TI liquid metal experiment in the frame of the DRESDYN project [9]. This advancement is based on a stability analysis initiated in Ref. [37] and motivated by the work by Liu *et al.* [38] who, using a short wavelength approximation, identified critical steepnesses of the rotation profile, which prevent excitation of HMRI for $-0.828 \approx 2 - 2\sqrt{2} < \text{Ro} < 2 + 2\sqrt{2} \approx 4.828$. These “Liu limits” were derived in the assumption that the radial profile of the azimuthal magnetic field is $B_\theta(r) \propto r^{-1}$ and Pm is very low and thus excluded HMRI and AMRI of Keplerian flows, characterized by $\text{Ro} = -3/4$, in the liquid metal experiments where the azimuthal field is created by an isolated axial current (e.g., in PROMISE).

It is known, however, that the azimuthal magnetic field $B_\theta(r) \propto r$, corresponding to a homogeneous axial current density in a conducting fluid, may cause the kink-type Tayler instability (TI) [39–41], even if the fluid is at rest, as it was observed in a recent liquid metal experiment [42]. By combining the field of an external to the fluid current with the currents through the fluid itself one can create azimuthal fields with the radial distributions that interpolate between $B_\theta(r) \propto r^{-1}$ and $B_\theta(r) \propto r$. This is the idea behind the design of the new MRI-TI experimental setup [9].

In view of these considerations, a helical magnetic field with the arbitrary radial dependence of the azimuthal component has been considered in Ref. [37]. To characterize the magnetic shear, an appropriate *magnetic Rossby number*, $\text{Rb} = r^2(B_\theta/r)'/(2B_\theta)$, has been defined [37]. Then $\text{Rb} = -1$ corresponds to $B_\theta(r) \propto r^{-1}$ and $\text{Rb} = 0$ to $B_\theta(r) \propto r$. In the short wavelength approximation it was established that both the azimuthal and helical MRI are very sensitive to the parameter of the magnetic shear, Rb . In particular, it was discovered that, if the magnetic profile is made slightly shallower than $B_\theta \propto r^{-1}$, so as to satisfy the condition $\text{Rb} \geq -25/32$, the Keplerian flow invites both the AMRI and HMRI [30,37,43]. Later, these results were confirmed numerically by solving a boundary value problem for the Couette-Taylor flow with the internal and external currents [8,44]. Numerous previous studies, e.g., Refs. [10,21,22,27,28,31,35,38,45], overlooked this important result because they were restricted to the current-free field $B_\theta \propto r^{-1}$ with $\text{Rb} = -1$.

C. The Hain-Lüst equation and its extensions

The HMRI and the AMRI were addressed for axisymmetric and nonaxisymmetric perturbations in the

short-wavelength regime by the traditional Wentzel-Kramers-Brillouin (WKB) method [10,46] and within the geometrical optics [21] approximation [30,37,43,45,47,48]. The advantage of the latter is a possibility of a systematic derivation of asymptotic equations of different order controlled by a universal small parameter.

In Ref. [49] Hain and Lüst derived an ordinary differential equation of the Sturm-Liouville type [50] for the radial Lagrangian displacement to determine the growth rates of MHD instabilities with respect to isothermal perturbations in a diffuse linear pinch. Since then the Hain-Lüst equation (following from the Frieman-Rotenberg equation [51]) is widely used in the studies of local and global instabilities of cylindrical plasma equilibria [52–54]. In particular, it was established that the standard WKB analysis applied to the Hain-Lüst equation produces the correct local dispersion relation compared to that following from the WKB analysis of the original system of first order MHD equations; see, e.g., the discussion on page 103 in Ref. [53].

Motivated by this advantage Zou and Fukumoto [55] performed a rigorous derivation of the Hain-Lüst equation for a differentially rotating ideal MHD fluid in a cylindrical configuration and subjected to an azimuthal magnetic field. After the substitution of the WKB form of the radial solution into the result they found a new local dispersion relation that contained the dispersion relation of Refs. [21,22] as a particular case in the limit of short axial wavelengths.

Compared to Refs. [21,22], the dispersion relation by Zou and Fukumoto contained new terms affecting instabilities with respect to nonaxisymmetric perturbations [55]. By that reason, it is extremely interesting to apply this approximation scheme to the case of nonideal MHD and derive a comprehensive local dispersion relation allowing for differential rotation, viscosity and resistivity and thus applicable to the studies of HMRI, AMRI, and TI. This is the goal of the present paper. In it the extended Hain-Lüst equation serves as a basis for the linear stability analysis of AMRI, HMRI and TI both in the limit of $Pm \rightarrow 0$ and in the case of general Pm and Rb .

D. Overview of the article

In Sec. II we present the base state and the linearized MHD equations and derive our version of the Hain-Lüst differential equation for the incompressible fluid with allowance for differential rotation, viscosity, and electrical resistivity.

In Sec. III we apply the Wentzel-Kramers-Brillouin (WKB) method to the extended Hain-Lüst equation and obtain the comprehensive dispersion relation in the short radial wavelength limit.

In Sec. IV we check that our dispersion relation restores the known results for the SMRI and the HMRI, when restricted to axisymmetric disturbances.

In Sec. V we derive the dispersion relation for the case of purely azimuthal magnetic field and arbitrary Pm . Then we focus on the nonaxisymmetric AMRI at finite and vanishing magnetic Prandtl numbers. In the weak magnetic field limit we find that the Rayleigh criterion decides the instability. In the case of sufficiently strong azimuthal magnetic field we first deal exclusively with two extreme modes of $kr \rightarrow 0$ and $kr \rightarrow \infty$, being featured by the axial wave number k . For the

Keplerian flow, the short axial-wavelength mode ($kr \rightarrow \infty$) is excitable for $Rb > -25/32$, in accordance with the earlier works [30,37]. We find that the long axial-wavelength mode ($kr \rightarrow 0$) is excitable for $Rb < -1/4$ even when the flow is nonrotating. These findings are supported by computation of the growth rates optimized over radial and axial wavelengths and by presenting the evolution of the stability diagrams in the (Ro, Rb) plane as the radial wave number varies from small to large values.

In Sec. VI we find that in the limit of $kr \rightarrow 0$, an upper limit of the value of qr , where q is the radial wave number, is placed for the instability to occur. Then we analyze numerically our WKB dispersion relation with a reasonable restriction on the radial wave number q . This results in the stability diagrams well compared with that of the global numerical analysis of Ref. [56] and local analysis of Refs. [30,47] for various values of the magnetic Prandtl number.

Finally, in Sec. VII we complement the local stability analysis with the global stability analysis of the original MHD system equipped with boundary conditions that we solve by the pseudospectral method [57–59] to validate the theory.

II. EXTENDING THE HAIN-LÜST EQUATION

We consider the linear stability of a cylindrically symmetric rotating flow, of an *incompressible* viscous fluid with finite electric conductivity, to three-dimensional disturbances. The basic state is a rotating flow in equilibrium with the velocity field $\mathbf{U} = \mathbf{U}(r)$, characterized by the angular velocity $\Omega(r)$, in the steady magnetic field $\mathbf{B} = \mathbf{B}(r)$, of the same symmetry, with the azimuthal and the axial components $r\mu(r)$ and $B_z(r)$, respectively:

$$\mathbf{U} = r\Omega(r)\mathbf{e}_\theta, \quad \mathbf{B} = r\mu(r)\mathbf{e}_\theta + B_z\mathbf{e}_z. \quad (1)$$

The constant axial component of the magnetic field can be assumed to be externally imposed whereas the azimuthal component can be thought of as created by axial electric currents both external to the fluid and running through the fluid itself [29,44].

The velocity \mathbf{u} , the magnetic field \mathbf{b} , and the total pressure p are partitioned into the basic flow, and the disturbance as

$$\mathbf{u} = \mathbf{U} + \tilde{\mathbf{u}}, \quad \mathbf{b} = \mathbf{B} + \tilde{\mathbf{b}}, \quad p = P + \tilde{p}. \quad (2)$$

The Navier-Stokes and the induction equations linearized in the disturbance $(\tilde{\mathbf{u}}, \tilde{\mathbf{b}}, \tilde{p})$ are

$$\frac{\partial \tilde{\mathbf{u}}}{\partial t} + (\tilde{\mathbf{u}} \cdot \nabla) \mathbf{U} + (\mathbf{U} \cdot \nabla) \tilde{\mathbf{u}} = -\frac{1}{\rho} \nabla \tilde{p} + \frac{1}{\rho \mu_0} (\mathbf{B} \cdot \nabla) \tilde{\mathbf{b}} + \frac{1}{\rho \mu_0} (\tilde{\mathbf{b}} \cdot \nabla) \mathbf{B} + \nu \nabla^2 \tilde{\mathbf{u}}, \quad (3)$$

$$\frac{\partial \tilde{\mathbf{b}}}{\partial t} = \nabla \times (\mathbf{U} \times \tilde{\mathbf{b}}) + \nabla \times (\tilde{\mathbf{u}} \times \mathbf{B}) + \eta \nabla^2 \tilde{\mathbf{b}}, \quad (4)$$

$$\nabla \cdot \tilde{\mathbf{u}} = 0, \quad (5)$$

$$\nabla \cdot \tilde{\mathbf{b}} = 0, \quad (6)$$

where μ_0 , ν , and η represent the magnetic permeability, the kinematic viscosity, and the magnetic diffusivity, respectively. We assume that μ_0 , ν , and η are all constant [43].

Owing to the steadiness and to the symmetries with respect to translation along and rotation about the z axis, we pose the disturbances in the normal-mode form

$$\tilde{u}, \tilde{b}, \tilde{p} \propto \exp[\lambda t + i(m\theta + kz)]. \quad (7)$$

The azimuthal wave number m takes an integer value, the axial wave number k is taken to be a real number, and λ is the eigenvalue to be calculated. Substituting (7) into (3)–(6) yields a coupled system of eight ordinary differential equations for functions of r .

With a view to incorporate only the leading-order effect of short-wave radial disturbances under the assumption of v and η being small, we may simply replace $-\nabla^2$ with $|\mathbf{k}|^2 = k^2 + q^2 + m^2/r^2$, where $q(r)$ is the radial wave number. Indeed, if the disturbance is thought to be

$$\propto \exp[\lambda t + i(m\theta + kz)]c(r) \exp\left\{i \int q(r) dr\right\}$$

and L is the characteristic length, then $c'(r) \approx c(r)/L$ and $c''(r) \approx c(r)/L^2$, and $q'(r) \approx q(r)/L$. For $q(r)L \gg 1$, $c(r)q^2(r)$ becomes the leading-order term, and we can write

$$-\nabla^2 \approx q^2(r) + k^2 + m^2/r^2 \quad (8)$$

in the dissipation terms. This procedure amounts to discarding terms in the short wavelength regime, and should be justified *a posteriori*.

Within the assumptions made, we write the resulting equations in the matrix form for the vector function

$$\xi = (\tilde{u}_r, \tilde{u}_\theta, \tilde{u}_z, \tilde{b}_r, \tilde{b}_\theta, \tilde{b}_z, \tilde{p})$$

as

$$\mathbf{M}\xi = \mathbf{0} \quad (9)$$

with the matrix operator

$$\mathbf{M} = \begin{pmatrix} \tilde{\lambda}_v & -2\Omega & 0 & -\frac{iF}{\rho\mu_0} & \frac{2\mu}{\rho\mu_0} & 0 & \frac{1}{\rho} \frac{d}{dr} \\ \frac{1}{r} \frac{d}{dr} (r^2 \Omega) & \tilde{\lambda}_v & 0 & -\frac{2\mu + r \frac{d\mu}{dr}}{\rho\mu_0} & -\frac{iF}{\rho\mu_0} & 0 & \frac{1}{r\rho} im \\ 0 & 0 & \tilde{\lambda}_v & 0 & 0 & -\frac{iF}{\rho\mu_0} & \frac{1}{\rho} ik \\ -iF & 0 & 0 & \tilde{\lambda}_\eta & 0 & 0 & 0 \\ r \frac{d\mu}{dr} & -iF & 0 & -r \frac{d\Omega}{dr} & \tilde{\lambda}_\eta & 0 & 0 \\ 0 & 0 & -iF & 0 & 0 & \tilde{\lambda}_\eta & 0 \\ \frac{1}{r} + \frac{d}{dr} & \frac{im}{r} & ik & 0 & 0 & 0 & 0 \\ 0 & 0 & 0 & \frac{1}{r} + \frac{d}{dr} & \frac{im}{r} & ik & 0 \end{pmatrix}, \quad (10)$$

where $F = m\mu + B_z k$ [54],

$$\tilde{\lambda}_v = \lambda + im\Omega + \omega_v, \quad \tilde{\lambda}_\eta = \lambda + im\Omega + \omega_\eta \quad (11)$$

and $\omega_v = |\mathbf{k}|^2 v$, $\omega_\eta = |\mathbf{k}|^2 \eta$ [30].

The assumption (8) allows us to reduce the system (9) to a single ordinary differential equation of *second order*, governing the radial Lagrangian displacement of a fluid particle, an equivalent to the famous Hain-Lüst equation [49], which is a Sturm-Liouville equation with coefficients depending rationally on the eigenvalue parameter λ [50]. Note that without

(8) the resulting differential equation would be of order higher than 2.

For the ideal MHD, the magnetic field is frozen into the fluid and the Lagrangian variable helps to construct the iso-magnetovortical [60] perturbations, with respect to which the stability analysis is typically made. This is no longer true for the nonideal case. We find that, with v and η included, the following “quasi-” radial displacement $\xi_r = u_r/\tilde{\lambda}_\eta$, connected with the radial component \tilde{u}_r , is advantageous for simplifying the resulting equation. This differs from the radial Lagrangian displacement by the ω_η term in $\tilde{\lambda}_\eta$.

Therefore, we introduce a dependent variable $\chi = -ru_r/\tilde{\lambda}_\eta$, with the minus sign chosen for convenience, and the following notation:

$$\Lambda = \tilde{\lambda}_v + \frac{F^2}{\tilde{\lambda}_\eta \rho \mu_0}, \quad (12)$$

$$h^2 = k^2 + \frac{m^2}{r^2}. \quad (13)$$

With this, as we show in detail in Appendix A, the system (9) collapses into a single second-order ordinary differential equation for $\chi(r)$:

$$\frac{d}{dr} \left(f \frac{d\chi}{dr} \right) + s \frac{d\chi}{dr} - g\chi = 0, \quad (14)$$

where

$$\begin{aligned} f &= \frac{\tilde{\lambda}_\eta \Lambda}{h^2 r}, \quad s = \frac{im(\tilde{\lambda}_v - \tilde{\lambda}_\eta)}{h^2 r} \Omega', \\ g &= \frac{d}{dr} \left\{ \frac{im\tilde{\lambda}_\eta}{h^2 r^2} \left[\left(1 - \frac{\tilde{\lambda}_v}{\tilde{\lambda}_\eta} \right) r \Omega' + 2 \left(\Omega - \frac{iF\mu}{\rho\mu_0\tilde{\lambda}_\eta} \right) \right] \right\} \\ &\quad + \frac{E\tilde{\lambda}_\eta}{\Lambda r} - \left(\Omega - \frac{iF\mu}{\rho\mu_0\tilde{\lambda}_\eta} \right) \\ &\quad \times \frac{2m^2\tilde{\lambda}_\eta}{\Lambda h^2 r^3} \left[\left(1 - \frac{\tilde{\lambda}_v}{\tilde{\lambda}_\eta} \right) r \Omega' + 2 \left(\Omega - \frac{iF\mu}{\rho\mu_0\tilde{\lambda}_\eta} \right) \right], \end{aligned} \quad (15)$$

and the prime denotes the derivative with respect to r . The expression for the coefficient E is given by formula (A4) in Appendix A.

Equation (14) with the coefficients (15) is thought of as an alternative version of the Hain-Lüst equation [49,50] for the incompressible fluid extended with allowance for the effect of differential rotation, viscous dissipation, and magnetic diffusion. To the best of our knowledge in this generality it has not been previously reported in the literature. With $v = 0$ and $\eta = 0$, it reduces to the extended Hain-Lüst equation for the ideal incompressible MHD flow in differential rotation [55]. If, additionally, $\Omega = 0$, it exactly coincides with the classical Hain-Lüst equation for the nonrotating ideal incompressible MHD fluid in cylindrical configuration [52–54].

III. DISPERSION RELATION IN SHORT RADIAL WAVELENGTH APPROXIMATION

Following Refs. [52–54] we apply the WKB approximation to (14) by introducing the ansatz $\chi(r) = c(r) \exp[i \int q(r) dr]$ and assuming that the *radial* wavelength is very short, i.e., $q(r)L \gg 1$, where L is the length scale

for the radial inhomogeneity. This results in the algebraic dispersion relation

$$(h^2 + q^2)\tilde{\lambda}_\eta^2 \Lambda^2 + 4k^2 \left(\Omega \tilde{\lambda}_\eta - \frac{iF\mu}{\rho\mu_0} \right) \\ \times \left[\Omega \text{Ro}(\omega_\eta - \omega_v) + \left(\Omega \tilde{\lambda}_\eta - \frac{iF\mu}{\rho\mu_0} \right) \right] \\ + 4\Lambda h^2 \tilde{\lambda}_\eta \left\{ \left(\Omega^2 \text{Ro} - \frac{\mu^2}{\rho\mu_0} \text{Rb} \right) \right. \\ \left. + \frac{imr}{4} \frac{d}{dr} \left[\frac{2(\Omega \tilde{\lambda}_\eta - \frac{iF\mu}{\rho\mu_0}) + (\omega_\eta - \omega_v)r\Omega'}{h^2 r^2} \right] \right\} = 0, \quad (16)$$

where we have introduced the Rossby number Ro and the magnetic Rossby number Rb by [30,37,45]

$$\text{Ro} = \frac{1}{2} \frac{r}{\Omega} \Omega', \quad \text{Rb} = \frac{1}{2} \frac{r}{\mu} \mu'. \quad (17)$$

In the ideal case when $\omega_v = 0$ and $\omega_\eta = 0$ the dispersion relation (16) reduces to that of Ref. [55] that, in its turn, reduces to the ideal dispersion relation derived by Ogilvie and Pringle [22] and Friedlander and Vishik [21] as well as to the ideal versions of the dispersion relation of Refs. [30,37,46] in the limit of large axial wave numbers, $k \rightarrow \infty$.

Applying the WKB approximation to the extended Hain-Lütt equation for the radial Lagrangian displacement rather than to the coupled system of the ordinary differential equations (9) we obtain an additional term $\frac{imr}{4} \frac{d}{dr} \left[\frac{2(\Omega \tilde{\lambda}_\eta - \frac{iF\mu}{\rho\mu_0}) + (\omega_\eta - \omega_v)r\Omega'}{h^2 r^2} \right]$ in the resulting dispersion relation (16). We notice that the axisymmetric mode ($m = 0$) remains intact since this term is irrelevant. However, it can improve the prediction accuracy in the case of nonaxisymmetric perturbations with long axial wavelength.

For our purpose of stability analysis, it is expedient to define two kinds of Alfvén frequency ω_A and $\omega_{A\theta}$, along with their ratio β representing the helical geometry of the magnetic field, by [30]

$$\omega_A = \frac{kB_z}{\sqrt{\rho\mu_0}}, \quad \omega_{A\theta} = \frac{\mu}{\sqrt{\rho\mu_0}}, \quad \beta = \frac{\omega_{A\theta}}{\omega_A}. \quad (18)$$

In addition, we introduce three dimensionless parameters, namely, the magnetic Prandtl number Pm , the Reynolds number Re and the Hartmann number Ha by [30]

$$\text{Pm} = \frac{\omega_v}{\omega_\eta}, \quad \text{Re} = \frac{\Omega}{\omega_v}, \quad \text{Ha} = \frac{\omega_A}{\sqrt{\omega_v \omega_\eta}}. \quad (19)$$

The dispersion relation for nondimensional variables, with the derivative term in (16) being expanded out, leads to

$$(\Lambda_1 \Lambda_2 + \widehat{\text{Ha}}^2)^2 \\ + 4 \frac{\widehat{h}^2 (\Lambda_1 \Lambda_2 + \widehat{\text{Ha}}^2)}{\widehat{h}^2 + \widehat{q}^2} (\text{Re}^2 \text{Pm} \text{Ro} - \beta^2 \text{Ha}^2 \text{Rb}) \\ + \frac{4im(\Lambda_1 \Lambda_2 + \widehat{\text{Ha}}^2)}{\widehat{h}^2 + \widehat{q}^2} \left[\text{Re} \text{Ro} \sqrt{\text{Pm}} (\Lambda_2 + im \text{Re} \sqrt{\text{Pm}}) \right.$$

$$- i(2m\beta + 1)\beta \text{Ha}^2 \text{Rb} + (i\widehat{\text{Ha}}\beta \text{Ha} - \text{Re} \sqrt{\text{Pm}} \Lambda_2) \frac{\widehat{k}^2}{\widehat{h}^2} \\ + \text{Ro} \text{Re}(1 - \text{Pm}) \left(\text{Ro} - \frac{\widehat{k}^2}{\widehat{h}^2} \right) \\ + 4\alpha^2 \{ (\text{Re} \Lambda_2 \sqrt{\text{Pm}} - i\widehat{\text{Ha}}\beta \text{Ha}) [\text{Re} \Lambda_2 \sqrt{\text{Pm}} - i\widehat{\text{Ha}}\beta \text{Ha}] \\ + \text{Ro} \text{Re}(1 - \text{Pm}) \} = 0, \quad (20)$$

where

$$\Lambda_1 = \frac{\lambda}{\Omega} \text{Re} \sqrt{\text{Pm}} + im \text{Re} \sqrt{\text{Pm}} + \sqrt{\text{Pm}},$$

$$\Lambda_2 = \frac{\lambda}{\Omega} \text{Re} \sqrt{\text{Pm}} + im \text{Re} \sqrt{\text{Pm}} + \frac{1}{\sqrt{\text{Pm}}},$$

$$\widehat{\text{Ha}} = \text{Ha}(1 + m\beta),$$

$$\widehat{k} = kr, \quad \widehat{q} = qr, \quad \widehat{h} = hr, \quad \alpha^2 = \frac{\widehat{k}^2}{\widehat{h}^2 + \widehat{q}^2}. \quad (21)$$

In the rest of the paper, this form of the dispersion relation plays the decisive role for determining the instability criteria and for calculating the growth rates.

IV. AXISYMMETRIC PERTURBATIONS

To begin with, we confirm that (20) and (21) reproduce the known results in the axisymmetric case.

A. Standard MRI in the ideal MHD and beyond

For axisymmetric perturbations ($m = 0$) and purely axial magnetic field ($\beta = 0$) the dispersion relation (20) simplifies as follows:

$$\text{Pm}^2 \frac{\lambda^4}{\Omega^4} + 2 \frac{(\text{Pm} + 1)\text{Pm}}{\text{Re}} \frac{\lambda^3}{\Omega^3} \\ + \left[4\text{Pm}^2 \alpha^2 (\text{Ro} + 1) + \frac{2(\text{Ha}^2 + 1)\text{Pm} + (\text{Pm} + 1)^2}{\text{Re}^2} \right] \frac{\lambda^2}{\Omega^2} \\ + 2 \left[\frac{4\text{Pm}\alpha^2(\text{Ro} + 1)}{\text{Re}} + \frac{(\text{Ha}^2 + 1)(\text{Pm} + 1)}{\text{Re}^3} \right] \frac{\lambda}{\Omega} \\ + 4\alpha^2 \frac{\text{Ha}^2 \text{Pm} \text{Ro} + \text{Ro} + 1}{\text{Re}^2} + \frac{(\text{Ha}^2 + 1)^2}{\text{Re}^4}. \quad (22)$$

Expressing Ha , Re , and Pm in terms of the Alfvén, viscous, and resistive frequencies according to (19) and then setting $\omega_v = 0$ and $\omega_\eta = 0$ we arrive at the well-known dispersion relation of the standard MRI of the ideal MHD [3,11,55]:

$$\lambda^4 + 2[2\alpha^2 \Omega^2 (\text{Ro} + 1) + \omega_A^2] \lambda^2 + 4\alpha^2 \Omega^2 \text{Ro} \omega_A^2 + \omega_A^4 = 0, \quad (23)$$

from which $\text{Ro} < 0$ follows as a necessary condition for the standard magnetorotational instability, established first in Refs. [1,2], and $\text{Ro} < -1$ as a criterion for the Rayleigh centrifugal instability in the absence of the magnetic field. The Velikhov-Chandrasekhar paradox is that the exact criterion for SMRI produced by (23)

$$\text{Ro} < -\frac{\omega_A^2}{4\alpha^2 \Omega^2}$$

does not tend to the Rayleigh criterion as $\omega_A \rightarrow 0$, [11,12].

Willis and Barenghi [13] realized, using numerical computation, that viscosity and resistivity are necessary to connect the two criteria. To show this, we require negativity of the free term in the dispersion relation (22), which yields the generalized criterion for SMRI of the nonideal MHD [10,14]:

$$\text{Ro} < -\frac{1 + \frac{1}{4\alpha^2} \left(\frac{\text{Ha}^2}{\text{Re}} + \frac{1}{\text{Re}} \right)^2}{\text{Ha}^2 \text{Pm} + 1}.$$

Introducing the magnetic Reynolds number $\text{Rm} = \text{PmRe}$ and the Lundquist number $S^2 = \text{Ha}^2 \text{Pm}$ we rewrite it as

$$\text{Ro} < -\frac{1 + \frac{1}{4\alpha^2} \left(\frac{S^2}{\text{Rm}} + \frac{1}{\text{Re}} \right)^2}{S^2 + 1},$$

which in the limit of $\text{Re} \rightarrow \infty$ and $\text{Rm} \rightarrow \infty$ reduces to the condition [14]

$$\text{Ro} < -\frac{1}{S^2 + 1}, \quad (24)$$

recently confirmed by the asymptotic and numerical analysis of Deguchi [15]. At $S = 0$ the inequality (24) yields the Rayleigh criterion $\text{Ro} < -1$ whereas for $S \rightarrow \infty$ it restores the Velikhov-Chandrasekhar condition $\text{Ro} < 0$.

B. Helical MRI in the limit $\text{Pm} \rightarrow 0$

Now we revisit the axisymmetric ($m = 0$) HMRI occurring in the presence of both azimuthal and axial components of the magnetic field $\mathbf{B} = r\mu(r)\mathbf{e}_\theta + B_z\mathbf{e}_z$.

It is well known that [8] “AMRI, HMRI and TI survive also at low magnetic Prandtl numbers. One finds for their lines of neutral stability convergence in the (Ha/Re) coordinate plane for decreasing magnetic Prandtl number $\text{Pm} \rightarrow 0$, which can also be obtained with the inductionless approximation of the MHD equations for $\text{Pm} = 0$.”

By that reason we can consider (20) in the limit of $\text{Pm} \rightarrow 0$ and solve it for the eigenvalue as [30]

$$\begin{aligned} \frac{\lambda}{\Omega} &= -\frac{1}{\text{Re}} + \frac{\text{Ha}^2}{\text{Re}} (2\alpha^2\beta^2\text{Rb} - 1) \\ &\pm \frac{2\alpha}{\text{Re}} [\beta^2\text{Ha}^4 (1 + \alpha^2\beta^2\text{Rb}^2) - \text{Re}^2 (1 + \text{Ro}) \\ &+ i\beta\text{Ha}^2\text{Re}(2 + \text{Ro})]^{1/2}. \end{aligned} \quad (25)$$

At large values of Re , (25) is expanded as

$$\begin{aligned} \frac{\lambda}{\Omega} &\approx \pm 2i\alpha\sqrt{1 + \text{Ro}} + \left\{ -1 + \text{Ha}^2 \left[2\alpha^2\beta^2\text{Rb} - 1 \right. \right. \\ &\quad \left. \left. \pm \frac{(2 + \text{Ro})\alpha\beta}{\sqrt{1 + \text{Ro}}} \right] \right\} \frac{1}{\text{Re}}, \quad (\text{Ro} \neq -1), \\ \frac{\lambda}{\Omega} &\approx \pm 2\alpha\text{Ha}\sqrt{i\beta} \frac{1}{\sqrt{\text{Re}}} + (-1 - \text{Ha}^2 + 2\alpha^2\beta^2\text{Ha}^2\text{Rb}) \frac{1}{\text{Re}}, \\ &\quad (\text{Ro} = -1). \end{aligned} \quad (26)$$

From the zeroth-order term in (26), $\text{Ro} < -1$ is sufficient for instability and so is $\text{Ro} = -1$ unless $\text{Ha} = 0$ or $\beta = 0$. The remaining task is classification for the case of $\text{Ro} > -1$. Equation (26) tells that the growth rate, if it is positive, increases with $|\text{Ha}|$.

For $1 \ll \text{Ha} \ll \text{Re}$ and $\text{Ro} \neq -1$, (26) reads for the growth rates [30]

$$\frac{\Re(\lambda)}{\Omega} = \left(2\alpha^2\beta^2\text{Rb} - 1 \pm \alpha\beta \frac{\text{Ro} + 2}{\sqrt{1 + \text{Ro}}} \right) \text{N} - \frac{1}{\text{Re}}, \quad (27)$$

where $\text{N} = \text{Ha}^2/\text{Re}$ is known as the Elsasser number [30] and $\Re(\cdot)$ designates the real part. The coefficient at N is a quadratic equation with respect to $\alpha\beta$. Its discriminant is

$$D = 8\text{Rb} + \frac{(\text{Ro} + 2)^2}{\text{Ro} + 1}.$$

Therefore, for $\text{Rb} < 0$ the coefficient at N can be positive, if $D > 0$, which yields [30,37]

$$\text{Rb} > -\frac{1}{8} \frac{(\text{Ro} + 2)^2}{\text{Ro} + 1} \quad (28)$$

as a necessary condition for instability.

Note that when $\text{Rb} < 0$ and $\text{Re} \rightarrow \infty$ the maximum of the growth rate, as a function of $\alpha\beta$, turns out to be

$$\frac{\Re(\lambda)}{\Omega} = -\frac{DN}{8\text{Rb}}$$

and is attained at

$$\alpha\beta = \mp \frac{\text{Ro} + 2}{4\text{Rb}\sqrt{\text{Ro} + 1}}.$$

Correspondingly, when $\text{Rb} \leq -1/2$ the instability occurs in the region [30,37]

$$\text{Ro} \in [-1, 2(-\sqrt{2}\sqrt{2\text{Rb}^2 + \text{Rb}} - 1 - 2\text{Rb})]$$

$$\cup [2(\sqrt{2}\sqrt{2\text{Rb}^2 + \text{Rb}} - 1 - 2\text{Rb}), +\infty], \quad (29)$$

and when $-1/2 < \text{Rb} < 0$ the instability occurs in the region

$$\text{Ro} \in [-1, +\infty]. \quad (30)$$

In particular, for $\text{Rb} = -1$ the critical Rossby numbers are $\text{Ro}_c = 2(1 \pm \sqrt{2})$ at $\alpha\beta = \pm 1/\sqrt{2}$, and thus the upper and lower Liu limits are recovered [10,11,38].

V. NONAXISYMMETRIC PERTURBATIONS

Hereafter we limit ourselves to the magnetic field that has only the azimuthal component $\mathbf{B} = r\mu(r)\mathbf{e}_\theta$. Let

$$\text{Ha}_\theta = \frac{\omega_{A\theta}}{\sqrt{\omega_v\omega_\eta}} \quad (31)$$

be the azimuthal Hartmann number.

We first substitute $\beta = \text{Ha}_\theta/\text{Ha}$ into (20) and then take the limit $\text{Ha} \rightarrow 0$. As a result, we get the dimensionless dispersion relation of AMRI for arbitrary Pm :

$$\begin{aligned} &(\Lambda_1\Lambda_2 + m^2\text{Ha}_\theta^2)^2 \\ &+ 4 \frac{\widehat{h}^2(\Lambda_1\Lambda_2 + m^2\text{Ha}_\theta^2)}{\widehat{h}^2 + \widehat{q}^2} (\text{Re}^2\text{Pm}\text{Ro} - \text{Ha}_\theta^2\text{Rb}) \\ &+ \frac{4im(\Lambda_1\Lambda_2 + m^2\text{Ha}_\theta^2)}{\widehat{h}^2 + \widehat{q}^2} \left[\text{Re}\text{Ro}\sqrt{\text{Pm}}(\Lambda_2 + im\text{Re}\sqrt{\text{Pm}}) \right. \\ &\quad \left. - 2im\text{Ha}_\theta^2\text{Rb} + (im\text{Ha}_\theta^2 - \text{Re}\sqrt{\text{Pm}}\Lambda_2) \frac{\widehat{k}^2}{\widehat{h}^2} \right] \end{aligned}$$

$$\begin{aligned}
& + \text{RoRe}(1 - \text{Pm}) \left(\text{Ro} - \frac{\widehat{k}^2}{\widehat{h}^2} \right) \Big] \\
& + 4\alpha^2 \{ (\text{Re}\Lambda_2 \sqrt{\text{Pm}} - im\text{Ha}_\theta^2) [\text{Re}\Lambda_2 \sqrt{\text{Pm}} - im\text{Ha}_\theta^2 \\
& + \text{RoRe}(1 - \text{Pm})] \} = 0. \quad (32)
\end{aligned}$$

Taking the limit of $\text{Pm} \rightarrow 0$ in (32), we find

$$\begin{aligned}
\widehat{\lambda}^2 + \frac{4\widehat{\lambda}}{\widehat{h}^2 + \widehat{q}^2} \left[\text{Ha}_\theta^2 \left(2m^2 \text{Rb} - \widehat{h}^2 \text{Rb} - \frac{\widehat{k}^2 m^2}{\widehat{h}^2} \right) \right. \\
\left. + im\text{Re}(\text{Ro} + 1) \left(\text{Ro} - \frac{\widehat{k}^2}{\widehat{h}^2} \right) \right] \\
+ 4\alpha^2 (\text{Re} - im\text{Ha}_\theta^2) (\text{Re} - im\text{Ha}_\theta^2 + \text{ReRo}) = 0, \quad (33)
\end{aligned}$$

where

$$\widehat{\lambda} = 1 + \text{Ha}_\theta^2 m^2 + \frac{\lambda \text{Re}}{\Omega} + im\text{Re}.$$

A. Weak field

To examine the instability when magnetic field is weak, we express the solution of (33) in powers of small parameter Ha_θ . Then its leading-order term reads

$$\begin{aligned}
\frac{\lambda}{\Omega} = & -\frac{1}{\text{Re}} - im \left[1 + \frac{2(1 + \text{Ro})}{\widehat{h}^2 + \widehat{q}^2} \left(\text{Ro} - \frac{\widehat{k}^2}{\widehat{h}^2} \right) \right] \\
& \pm 2 \sqrt{-\alpha^2(1 + \text{Ro}) - \frac{m^2(1 + \text{Ro})^2}{(\widehat{h}^2 + \widehat{q}^2)^2} \left(\text{Ro} - \frac{\widehat{k}^2}{\widehat{h}^2} \right)^2} \\
& + O(\text{Ha}_\theta). \quad (34)
\end{aligned}$$

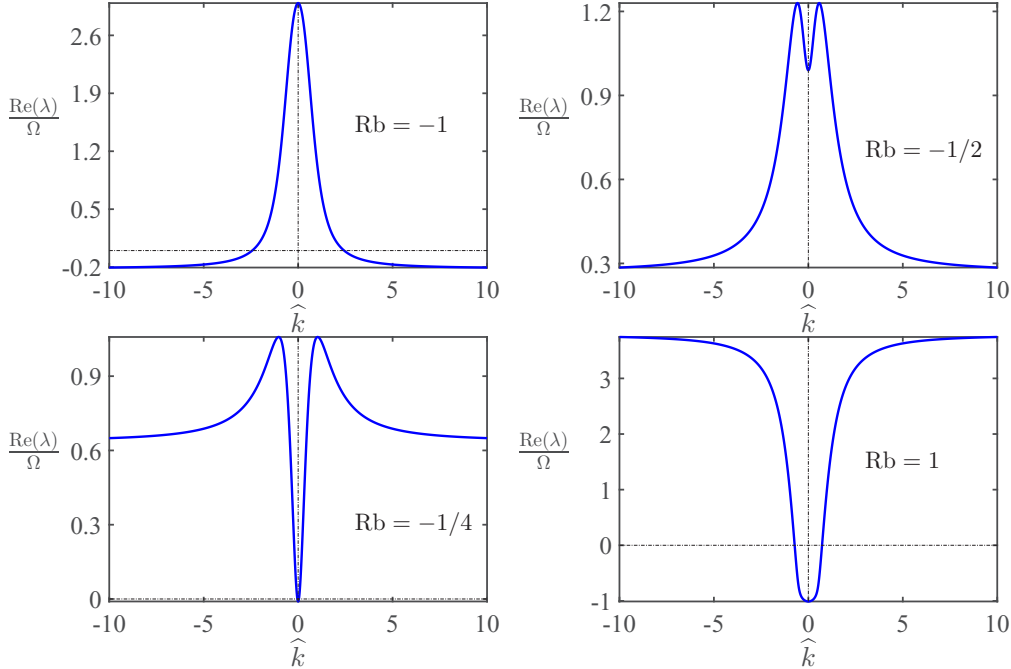


FIG. 1. The growth rate $\text{Re}(\lambda)/\Omega$ given by (33) versus the dimensionless axial wave number $\widehat{k} = kr$ for $\text{Re} = 100$, $\text{Ha}_\theta = 10$, $m = 1$, $\widehat{q} = 0$, $\text{Ro} = -3/4$. From upper left to lower right, Rb is varied from -1 to 1 . As Rb increases, the value of \widehat{k} corresponding to the maximum growth rate increases from $\widehat{k} = 0$ to finite but nonzero value and ultimately this $\widehat{k} \rightarrow \infty$.

The radicand should be positive in total for instability. The first term in the radicand $-\alpha^2(1 + \text{Ro})$ becomes positive for $\text{Ro} < -1$ and the second one is definitely nonpositive. This nonpositive term has the effect of decreasing the growth rate. In particular, setting $m = 0$ in (34) yields

$$\frac{\lambda}{\Omega} = \pm 2\alpha i \sqrt{1 + \text{Ro}} - \frac{1}{\text{Re}}. \quad (35)$$

From (35) it follows that instability requires [30]

$$\text{Ro} < \text{Ro}_c = -1 - \frac{1}{4\alpha^2 \text{Re}^2}.$$

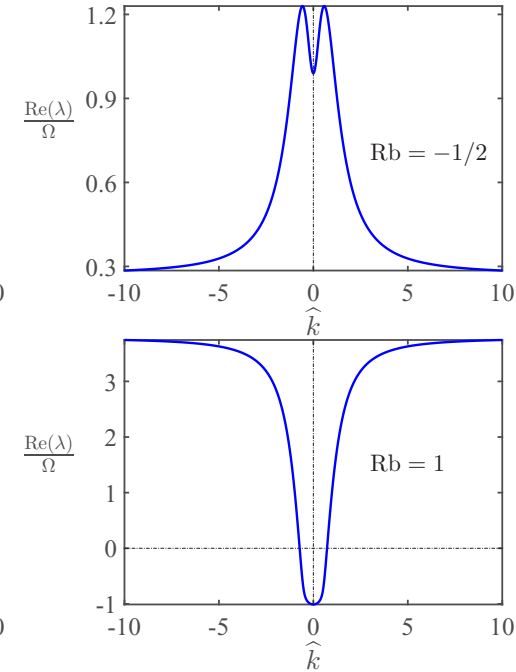
Compared with the ideal hydrodynamics, for which the critical Rossby number is $\text{Ro}_c = -1$, the critical Rossby number is lowered by $1/(4\alpha^2 \text{Re}^2)$ and the maximum growth rate is decreased by $1/\text{Re}$ due to viscosity.

When $\text{Ro} > -1$, to which the Keplerian flow ($\text{Ro} = -3/4$) belongs, the nonaxisymmetric as well as the axisymmetric modes decay as $\lambda/\Omega \approx -1/\text{Re}$.

B. Strong field

We turn to the case of a strong magnetic field. The Reynolds number is assumed to be large. The axial wave number \widehat{k} is an important parameter for determining the maximum growth rate and the instability region.

Figure 1 shows the growth rate given by Eq. (33) as a function of \widehat{k} for different values of Rb . We fix $m = 1$, $\text{Ro} = -3/4$, and $\widehat{q} = 0$, because numerically the modes of $\widehat{q} = 0$ exhibit the fastest growth. We observe that at around $\text{Rb} = -1/4$, there is some finite \widehat{k} at which the growth rate takes the maximum value. When Rb is smaller than $-1/4$, the fast growth rate gives way to the $\widehat{k} = 0$ mode at $\text{Rb} = -1$.



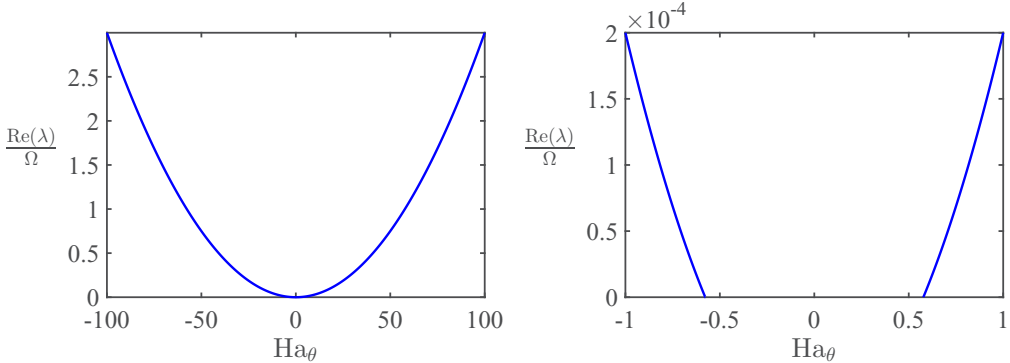


FIG. 2. The growth rate $\text{Re}(\lambda_2)$ of (36) versus Ha_θ when $\text{Re} = 10^4$, $m = 1$, $\hat{k} = \hat{q} = 0$, $\text{Ro} = -3/4$, and $\text{Rb} = -1$. The right panel is the close-up view of the left one near $\text{Ha}_\theta = 0$, demonstrating a certain strength of magnetic field needed for instability.

When Rb is increased above $-1/4$ by a certain amount, the maximum growth rate is attained in the limit of $\hat{k} \rightarrow \infty$.

1. The limit $\hat{k} \rightarrow 0$

The observations described above suggest us to examine closer the limit of $\hat{k} \rightarrow 0$, which means letting $\alpha \rightarrow 0$ and $\hat{h} \rightarrow m$ in (33). In this limit the roots of (33) at $\text{Re} \gg 1$ take the form

$$\begin{aligned}\frac{\lambda_1}{\Omega} &= -im - (1 + \text{Ha}_\theta^2 m^2) \frac{1}{\text{Re}}, \\ \frac{\lambda_2}{\Omega} &= -im \left[1 + \frac{4\text{Ro}(1 + \text{Ro})}{m^2 + \hat{q}^2} \right] \\ &\quad - \left[1 + \text{Ha}_\theta^2 m^2 \left(1 + \frac{4\text{Rb}}{m^2 + \hat{q}^2} \right) \right] \frac{1}{\text{Re}}.\end{aligned}\quad (36)$$

A glance at (36) shows that the axisymmetric mode ($m = 0$) is excluded from the unstable ones and the growth rate $\Re(\lambda_1)$ is always negative. The growth rate $\Re(\lambda_2)$ is positive provided that

$$\text{Rb} < -\frac{1}{4}(m^2 + \hat{q}^2) \text{ and } \text{Ha}_\theta^2 > \frac{1}{m^2 \left(\frac{4|\text{Rb}|}{m^2 + \hat{q}^2} - 1 \right)}. \quad (37)$$

Figure 2 displays the growth rate $\Re(\lambda_2)$ as a function of Ha_θ when $\text{Re} = 10^4$, $m = 1$, $\hat{k} = \hat{q} = 0$, $\text{Ro} = -3/4$, and $\text{Rb} = -1$. The left panel shows that the growth rate increases with Ha_θ ; the right panel is the close-up view near the origin. We recognize that the small but nonzero value $|\text{Ha}_\theta| = 1/\sqrt{3} \approx 0.5774$ is necessary for the onset of instability.

Note that rather than Ro , it is now Rb that is tied with the instability and the negative value of $d\mu/dr$ is required. The maximum growth rate is attained at $\hat{q} = 0$.

When $\text{Rb} = -1$, the $m = \pm 1$ modes are the only possible modes for instability.

When $m = \pm 1$ is fixed, $\text{Rb} < -1/4$ is necessary for the instability of the $\hat{k} = 0$ mode.

It is remarkable that the instability exists, beyond the restriction of the Liu limit, for arbitrary Rossby number Ro . However, we should be cautious about this result, because the modes of $\hat{q} = 0$ lie outside the regime of validity of the radial WKB approximation. Later in the article, we argue about the limitation on \hat{q} .

2. The limit $\hat{k} \rightarrow \infty$

In the limit $\hat{k} \rightarrow \infty$, where \hat{q}^2 is replaced by $\hat{k}^2/\alpha^2 - \hat{k}^2 - m^2$ ($0 \leq \alpha \leq 1$), the roots of (33) take the form [30,43]

$$\begin{aligned}\frac{\lambda_{1,2}}{\Omega} &= \text{N}_A(2\alpha^2\text{Rb} - m^2) - im - \frac{1}{\text{Re}} \\ &\quad \pm 2\alpha \left\{ \text{N}_A^2(m^2 + \alpha^2\text{Rb}^2) + im\text{N}_A(2 + \text{Ro}) - 1 - \text{Ro} \right\}^{\frac{1}{2}},\end{aligned}\quad (38)$$

where $\text{N}_A = \text{Ha}_\theta^2/\text{Re}$ is the Elsasser number for the azimuthal magnetic field [30,43].

By expanding the eigenvalues (38) to first order in $1/\text{Re}$ we get [28,30]

$$\begin{aligned}\frac{\lambda_{1,2}}{\Omega} &= -im \pm 2\alpha\sqrt{-(1 + \text{Ro})} \\ &\quad + \text{N}_A \left[2\alpha^2\text{Rb} - m^2 \pm \frac{\alpha m(2 + \text{Ro})}{\sqrt{1 + \text{Ro}}} \right] - \frac{1}{\text{Re}}.\end{aligned}\quad (39)$$

When $\text{Ro} < -1$, the instability occurs with the growth rate $\Re(\lambda)/\Omega \approx 2\alpha\sqrt{-(1 + \text{Ro})}$. This mode pertains to the classical Rayleigh instability since no magnetic field is required.

When $\text{Ro} > -1$, the instability criterion becomes

$$\begin{aligned}-n^2 + |n| \frac{2 + \text{Ro}}{\sqrt{1 + \text{Ro}}} + 2\text{Rb} &> 0, \\ \text{and } \alpha^2\text{Ha}_\theta^2 &> \frac{\sqrt{1 + \text{Ro}}}{(2\text{Rb} - n^2)\sqrt{1 + \text{Ro}} + |n|(2 + \text{Ro})},\end{aligned}\quad (40)$$

where $n = m/\alpha$. If we choose that, e.g., $\text{Rb} = 0$, $m = 1$, and $\alpha = 1$, then $|\text{Ha}_\theta| \approx 0.8165$ is the onset of AMRI at the Keplerian $\text{Ro} = -3/4$ as shown in Fig. 3.

The left-hand side of the first of the inequalities (40) is a quadratic polynomial with respect to the real-valued number m . Hence, the discriminant of this polynomial

$$D = \frac{(2 + \text{Ro})^2}{1 + \text{Ro}} + 8\text{Rb} > 0$$

in order that the polynomial can take positive values. This yields the familiar [30,37] necessary condition for instability (28). For instance, for Keplerian flow $\text{Ro} = -3/4$ in (28) the inequality $\text{Rb} > -25/32$ is necessary for instability [30,37].

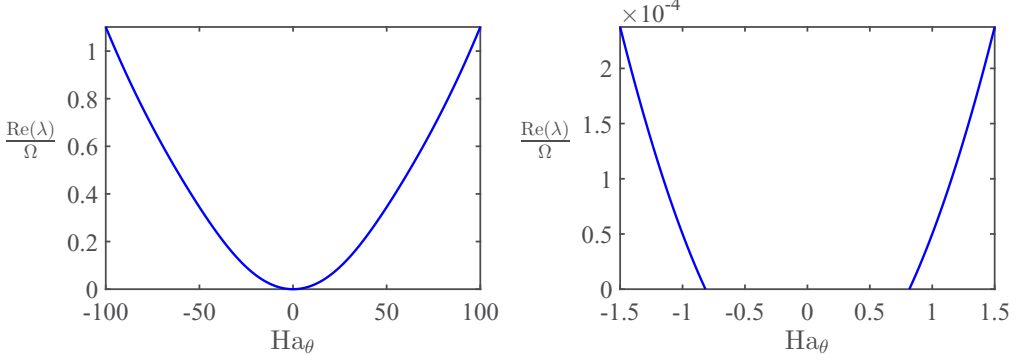


FIG. 3. The growth rate $\text{Re}(\lambda)$ to Ha_θ when $\text{Re} = 10^4$, $m = 1$, $\hat{k} \rightarrow \infty$, $\alpha = 1$, $\text{Ro} = -3/4$, and $\text{Rb} = 0$ according to (38). The left panel shows that large Ha_θ increase the growth rate, and the right panel is the amplification of the left one when Ha_θ is small, which demonstrates that a certain strength of magnetic field is needed for instability.

The first inequality in (40), when $\text{Rb} \leq n^2/2 - n$, is written for Ro as

$$\begin{aligned} -1 < \text{Ro} < -2 + \frac{n^2 - 2\text{Rb} - \sqrt{(n^2 - 2\text{Rb})^2 - 4n^2}}{2n^2(n^2 - 2\text{Rb})^{-1}} \\ \text{or } \text{Ro} > -2 + \frac{n^2 - 2\text{Rb} + \sqrt{(n^2 - 2\text{Rb})^2 - 4n^2}}{2n^2(n^2 - 2\text{Rb})^{-1}}, \end{aligned} \quad (41)$$

and when $\text{Rb} > n^2/2 - n$, as

$$\text{Ro} > -1. \quad (42)$$

When $n = \pm\sqrt{-2\text{Rb}}$, the domain (41) reduces to (29), which, at $\text{Rb} = -1$ takes the form

$$-1 < \text{Ro} < 2 - 2\sqrt{2} \quad \text{or} \quad \text{Ro} > 2 + 2\sqrt{2},$$

where $2 - 2\sqrt{2}$ and $2 + 2\sqrt{2}$ are the lower and the upper Liu limits, respectively [38].

3. Growth rate optimized by \hat{k} and \hat{q}

In the long-wavelength limit of $\hat{k} \rightarrow 0$, $\text{Rb} < -1/4$ is necessary for the instability of $m = 1$ mode as shown by (37), while in the short-wavelength limit of $\hat{k} \rightarrow \infty$, the condition $\text{Rb} > -\frac{1}{8}\frac{(\text{Ro}+2)^2}{\text{Ro}+1}$ given by (28) is necessary for the instability. Since the latter one overlaps with the former one, we conclude that for each value of Rb there exist wave numbers \hat{k} and \hat{q} such that the mode with $m = 1$ is unstable.

Either the mode of $\hat{k} \rightarrow 0$ or $\hat{k} \rightarrow \infty$ dominate in large range of Rb , and the maximum growth rate is attained at a finite value of \hat{k} for every particular value of the magnetic Rossby number, Rb , as illustrated in Fig. 4. In this figure the optimized with respect to \hat{k} growth rate is plotted against Rb for $\text{Re} = 10^4$, $\text{Ha}_\theta = 100$, $m = 1$, and $\text{Ro} = -3/4$ and $\hat{q} = 0$ (upper panel) and $\hat{q} = 1$ (lower panel). We observe the crossover of the $\hat{k} = 0$ mode and the $\hat{k} = \infty$ mode. The range of large negative values of Rb is dominated by the $\hat{k} = 0$ mode and the one of large positive values of Rb is dominated by the $\hat{k} \rightarrow \infty$ mode.

4. Evolution of AMRI region in the (Ro, Rb) plane with \hat{k}

In order to understand how the instability region evolves from that described by (37) at $\hat{k} \rightarrow 0$ to (41) at $\hat{k} \rightarrow \infty$ we plot the growth rate of the dispersion relation (32) in the

projection to the (Rb, Ro) plane; see Fig. 5. The results are presented over a growing set of axial wave number \hat{k} for $\text{Re} = 10^4$, $\text{Ha}_\theta = 10^2$, $\text{Pm} = 10^{-6}$, $\hat{q} = 1$, and $m = 1$.

It is clearly seen that already for $\hat{k} > 1.8$ the neutral stability curve bounding the stability domain (shown in white in Fig. 5) is close to $\text{Rb} = -\frac{1}{8}\frac{(\text{Ro}+2)^2}{\text{Ro}+1}$ corresponding to the limit of $\text{Pm} \rightarrow 0$. Equivalently, the instability domain is close to (41).

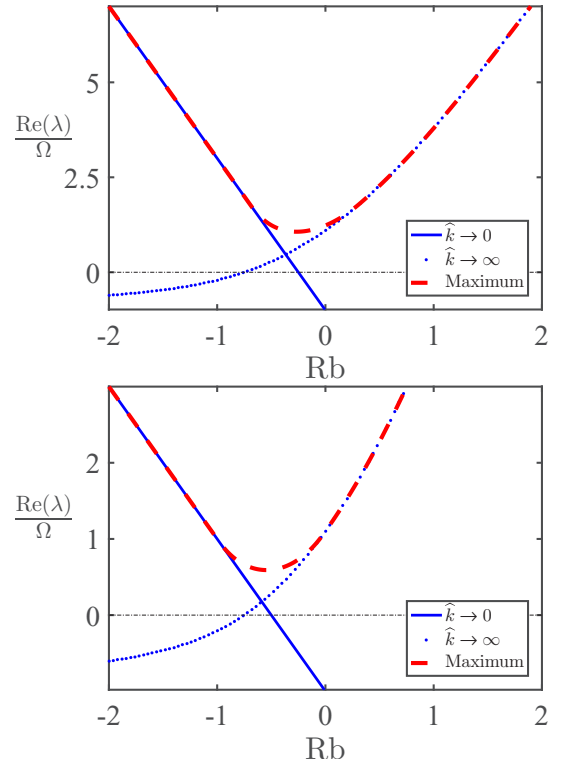


FIG. 4. The growth rate to magnetic Rossby number Rb for $\text{Re} = 10^4$, $\text{Ha}_\theta = 100$, $m = 1$, $\text{Ro} = -3/4$, and $\hat{q} = 0$ (upper panel) or $\hat{q} = 1$ (lower panel) according to (33). The solid line is $\hat{k} = 0$ mode, the dotted one is the $\hat{k} \rightarrow \infty$ mode, and the dashed line stands for the growth rate maximized over \hat{k} , whose left part tends to the $\hat{k} = 0$ mode and the right part tends to the $\hat{k} = \infty$, $\alpha = 1$ mode.

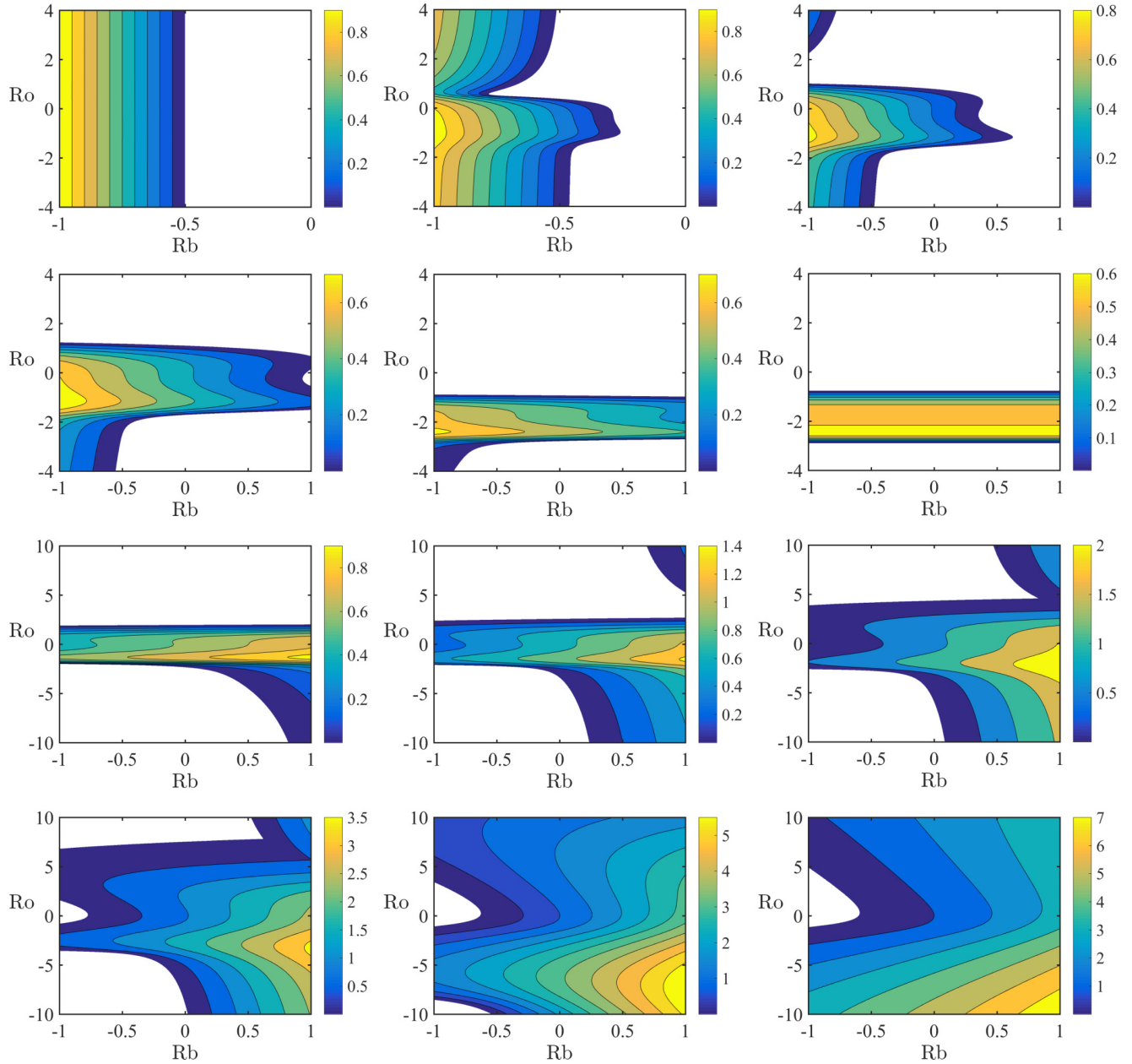


FIG. 5. Growth rate calculated with the use of the Hain-Lüst dispersion relation (32) in projection to the Rossby plane (Rb , Ro) for $Re = 10^4$, $Ha_\theta = 10^2$, $\hat{q} = 1$, $m = 1$, and (from upper-left to lower-right panel): $\hat{k} = 0.01, 0.4, 0.7, 0.8, 0.9, 1, 1.1, 1.3, 1.8, 2.5, 5$, and 10 . The white domains represent stability.

At the lower values of \hat{k} the instability domain splits into two parts, one of which becomes dominant at $\hat{k} = 1.3$ stretching along the Rb axis at $\hat{k} = 1$ and finally bifurcating into the instability domain corresponding to large negative values of Rb and practically not depending on Ro , in agreement with the criterion (37).

Below we demonstrate a similar transition for the domain of Tayler instability.

C. Tayler instability in the limit of $Pm \rightarrow 0$

Tayler [39,41] established that an ideal nonrotating perfectly conducting fluid in an azimuthal magnetic field is stable

against nonaxisymmetric perturbations with the azimuthal wave number $m = 1$ under the condition

$$\frac{d}{dr}[rB_\theta^2(r)] < 0. \quad (43)$$

Recalling the definition of the magnetic Rossby number (17) and taking into account that $B_\theta(r) = r\mu(r)$, the Tayler stability criterion for $m = 1$ takes the form

$$Rb < -\frac{3}{4}, \quad (44)$$

which means that the azimuthal magnetic field $B_\theta(r) \sim r$ created by a current passing through a conducting fluid and corresponding to $Rb = 0$ is unstable.

Reference [41] numerically predicted the Tayler instability (TI) caused by the field with $Rb = 0$ to exist also in the limit of $Pm \rightarrow 0$, which allowed for its recent observation in the experiments with liquid metals [42].

Using the geometrical optics stability analysis Kirillov *et al.* [30] extended the criterion for the onset of the Tayler instability to the case of arbitrary $m \geq 1$:

$$Rb > \frac{m^2}{4\alpha^2} - 1, \quad (45)$$

where $\alpha = \hat{k}^2/(\hat{k}^2 + \hat{q}^2)$. When $m = \pm 1$ and $\alpha = 1$, the criterion (45) yields $Rb > -3/4$ for instability, which includes the case of $Rb = 0$ observed in the experiment [42].

In order to explore the Tayler instability on the base of the dispersion relation (32), we assume $Re = 0$ in it and take into account the relation

$$\frac{\text{Re}\sqrt{Pm}}{\Omega} = \frac{Ha_\theta}{\omega_{A\theta}}. \quad (46)$$

This reduces (32) to

$$\begin{aligned} & \left[\left(\frac{\lambda Ha_\theta}{\omega_{A\theta}} + \sqrt{Pm} \right) \left(\frac{\lambda Ha_\theta}{\omega_{A\theta}} + \frac{1}{\sqrt{Pm}} \right) + Ha_\theta^2 m^2 \right]^2 (\hat{h}^2 + \hat{q}^2) \\ & - 4Ha_\theta^4 \hat{k}^2 m^2 - 4Ha_\theta^2 \left[(\hat{k}^2 - m^2) Rb + \frac{m^2 \hat{k}^2}{\hat{h}^2} \right] \\ & \times \left[\left(\frac{\lambda Ha_\theta}{\omega_{A\theta}} + \sqrt{Pm} \right) \left(\frac{\lambda Ha_\theta}{\omega_{A\theta}} + \frac{1}{\sqrt{Pm}} \right) + Ha_\theta^2 m^2 \right] = 0. \end{aligned} \quad (47)$$

We consider the limit where Pm is very small. Then the growth rate is of $O(\sqrt{Pm})$, and we can renormalize the eigenvalue as

$$\lambda = \lambda_0 \sqrt{Pm}. \quad (48)$$

Then the leading-order terms of (48) are

$$\begin{aligned} & \left(1 + \frac{\lambda_0}{\omega_{A\theta}} Ha_\theta + Ha_\theta^2 m^2 \right)^2 (\hat{h}^2 + \hat{q}^2) \\ & - 4Ha_\theta^4 \hat{k}^2 m^2 - 4Ha_\theta^2 \left[(\hat{k}^2 - m^2) Rb + \frac{m^2 \hat{k}^2}{\hat{h}^2} \right] \\ & \times \left(1 + \frac{\lambda_0}{\omega_{A\theta}} Ha_\theta + Ha_\theta^2 m^2 \right) = 0. \end{aligned} \quad (49)$$

For very large magnetic field we have $Ha_\theta \gg 1$ and can further renormalize the eigenvalue as

$$\lambda_0 = \lambda_a Ha_\theta \quad (50)$$

and solve (49) for λ_a , to the leading order in Ha_θ^{-1} , as

$$\begin{aligned} \frac{\lambda_a}{\omega_{A\theta}} = & -m^2 + \frac{2}{\hat{h}^2 + \hat{q}^2} \left\{ (\hat{k}^2 - m^2) Rb + \frac{m^2 \hat{k}^2}{\hat{h}^2} \right. \\ & \left. \pm \sqrt{\left[(\hat{k}^2 - m^2) Rb + \frac{m^2 \hat{k}^2}{\hat{h}^2} \right]^2 + m^2 \hat{k}^2 (\hat{h}^2 + \hat{q}^2)} \right\}. \end{aligned} \quad (51)$$

In the limit of $\hat{k} \rightarrow 0$, Eq. (51) yields

$$\frac{\lambda_a}{\omega_{A\theta}} = \frac{\pm 2m^2 Rb - m^2 (\hat{q}^2 + m^2 + 2Rb)}{\hat{q}^2 + m^2}. \quad (52)$$

One of the roots (52) is equal to $-m^2$, whereas another one becomes positive if

$$Rb < -\frac{1}{4}(m^2 + \hat{q}^2) \quad (53)$$

reproducing the first of the inequalities (37).

In the limit of $\hat{k} \rightarrow \infty$ and $\alpha \rightarrow 1$, Eq. (51) reduces to

$$\begin{aligned} \frac{\lambda_a^\pm}{\omega_{A\theta}} = & 2Rb - m^2 \pm 2\sqrt{Rb^2 + m^2} \\ = & (1 + Rb)^2 - (1 \mp \sqrt{Rb^2 + m^2})^2. \end{aligned} \quad (54)$$

The root $\lambda_a^-/\omega_{A\theta}$ in (54) is always negative. The other,

$$\frac{\lambda_a^+}{\omega_{A\theta}} = (Rb + \sqrt{Rb^2 + m^2})(2 + Rb - \sqrt{Rb^2 + m^2}),$$

is a product of two expressions, the first of which is always positive, whereas $2 + Rb - \sqrt{Rb^2 + m^2}$ is positive if

$$Rb > \frac{m^2}{4} - 1 \quad (55)$$

in accordance with (45), where $\alpha = 1$. Therefore in the short axial wavelength approximation we reproduce the result [30]. Note that Ogilvie and Pringle [22] established criterion (55) for the case of ideal MHD.

In general, setting the right-hand side of (51) to zero, we get the critical Rb at the neutral stability surface

$$Rb = \frac{1}{4} \left\{ \frac{\hat{q}^2 m^2}{\hat{k}^2 - m^2} + \frac{\hat{k}^2 (m^2 - 4)(\hat{k}^2 + 2m^2) + m^6}{\hat{k}^4 - m^4} \right\}. \quad (56)$$

For $\hat{k} = 0$ the expression (56) yields the critical value of the criterion (53) and for $\hat{k} \rightarrow \infty$ the critical value of the criterion (55).

Figure 6 illustrates the transition from the criterion (55) to the criterion (53) as \hat{k} varies from 100 to 0 at the fixed $\hat{q} = 0$, based on the expression (56). At the value

$$\hat{k} = \sqrt{3 - \frac{1}{2}\hat{q}^2} \quad (57)$$

(equal to $\sqrt{3}$ for $\hat{q} = 0$ in Fig. 6) there are two saddle points at

$$Rb = \frac{1}{8}\hat{q}^2 - 2 \quad \text{and} \quad m = \pm\sqrt{3 - \frac{1}{2}\hat{q}^2}, \quad (58)$$

corresponding to $Rb = -2$ and $m = \pm\sqrt{3}$ in Fig. 6. The saddle points are formed by the straight lines $m = \pm\sqrt{3 - \frac{1}{2}\hat{q}^2}$

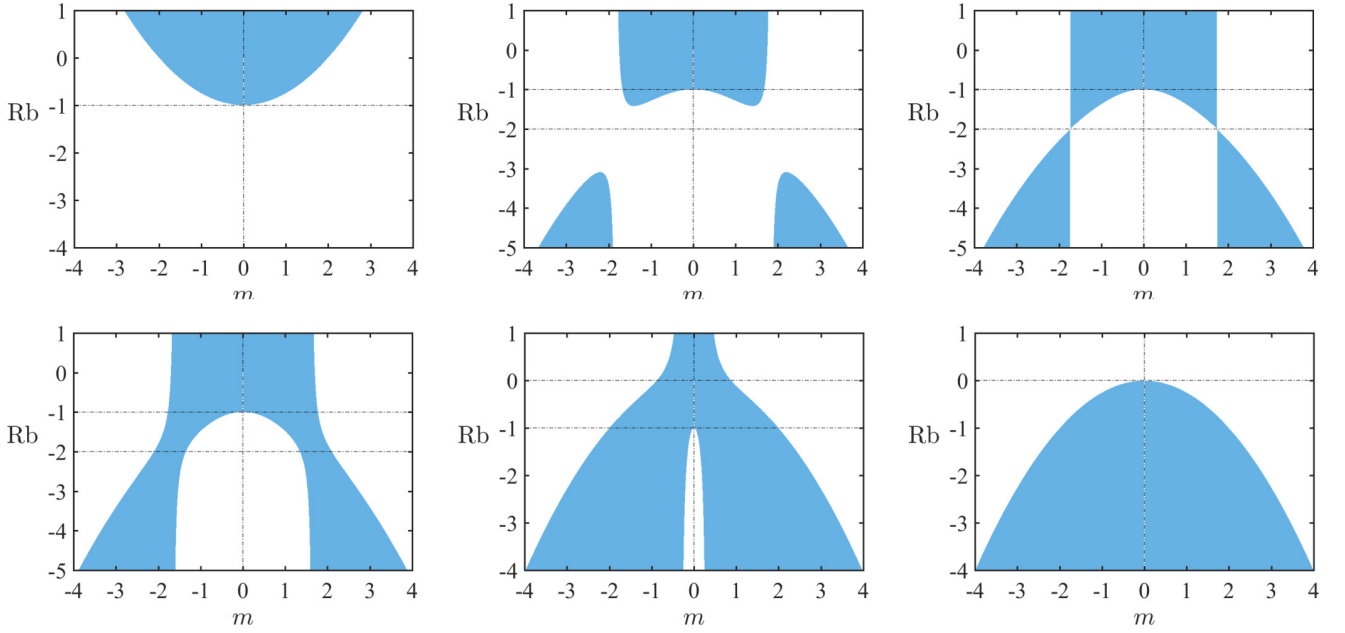


FIG. 6. The regions of the Tayler instability (blue) with the boundary (56) for $\hat{q} = 0$ and (top row from left to right) $\hat{k} = 100$, $\hat{k} = \sqrt{3} + 0.1$, and $\hat{k} = \sqrt{3}$ and (bottom row from left to right) $\hat{k} = \sqrt{3} - 0.1$, $\hat{k} = 0.3$, and $\hat{k} \rightarrow 0$.

intersecting with the curve

$$Rb = \frac{2m^4 + (18 - \hat{q}^2)m^2 - 4\hat{q}^2 + 24}{4(\hat{q}^2 - 2m^2 - 6)}.$$

Note that (58) implies an upper bound on the value of \hat{q} : $|\hat{q}| < \sqrt{6}$. In these conditions the bifurcation value (57) for the parameter \hat{k} sharply separates the cases of the short-axial-wavelength (55) and long-axial-wavelength (53) Tayler instability in the limit of vanishing Pm . However, in the case $|\hat{q}| > \sqrt{6}$ the saddle point is absent and the transition scenario simplifies; see Fig. 7.

VI. AMRI AND TAYLER INSTABILITY AT FINITE Pm

The magnetorotational instability is, by definition, caused by the cooperative effect of rotating flow field and magnetic field. The cooperative action comes into play for a differential rotation. Assuming the expansion of the solution in terms of Re as $\lambda^\pm/\omega_{A\theta} = a_0 Re + a_1 + a_2 Re^{-1} + a_3 Re^{-2} + \dots$, we expand the dispersion relation (32) with respect to $1/Re$ and solve the leading-order term to obtain a_0 . We repeat the

process to find the coefficient a_1 from the next-order term resulting in the following representation for the critical roots at large Re :

$$\begin{aligned} \frac{\lambda_{1,2}}{\omega_{A\theta}} &= -im \frac{\text{Re}\sqrt{Pm}}{\text{Ha}_\theta} - \frac{1}{\text{Ha}_\theta\sqrt{Pm}} \pm m \frac{\sqrt{-\text{Ro}(\text{Ro}+1)}}{\text{Ro}+1} \\ &\quad + O\left(\frac{1}{\text{Re}}\right), \\ \frac{\lambda_{3,4}}{\omega_{A\theta}} &= \frac{-i\text{Re}\sqrt{Pm}}{\text{Ha}_\theta\hat{h}^2(\hat{q}^2 + \hat{h}^2)} \{m[\hat{k}^2(\hat{k}^2 + \hat{q}^2 + 2\text{Ro} - 2) \\ &\quad + m^4 + m^2(2\hat{k}^2 + \hat{q}^2 + 2\text{Ro})] \pm 2i\sqrt{c_2}\} \\ &\quad + c_3 + O\left(\frac{1}{\text{Re}}\right), \end{aligned} \quad (59)$$

where

$$\begin{aligned} c_1 &= \hat{h}^2\text{Ro} - \hat{k}^2, \\ c_2 &= -\text{Ha}_\theta^2 Pm [\hat{k}^2 \hat{h}^4 (\hat{h}^2 + \hat{q}^2)(1 + \text{Ro}) + m^2 c_1^2], \end{aligned}$$

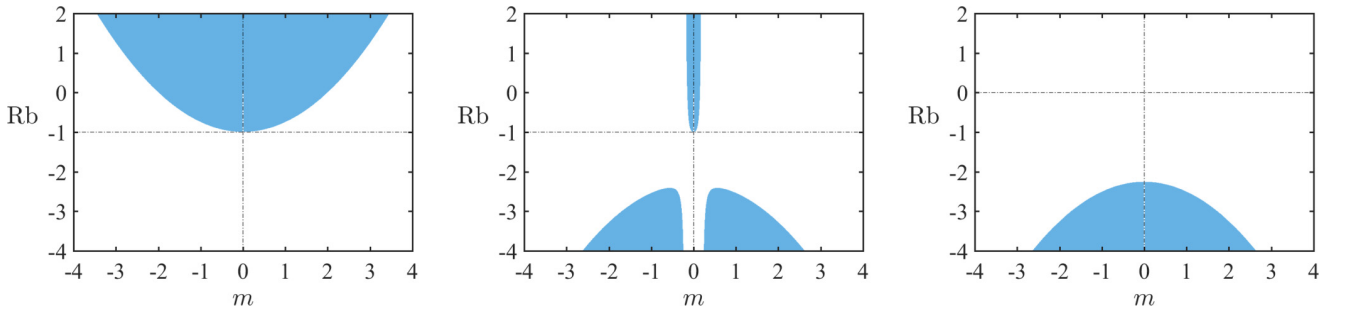


FIG. 7. The regions of the Tayler instability (blue) with the boundary (56) for $\hat{q} = 3$ and (from left to right) $\hat{k} = 100$, $\hat{k} = 0.2$, and $\hat{k} \rightarrow 0$.

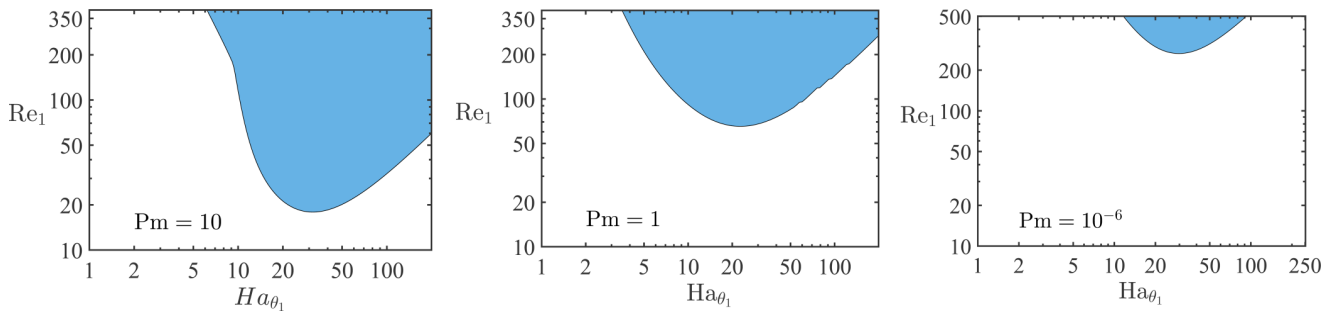


FIG. 8. AMRI regions (above the neutral stability curves) in the (Ha_{θ_1}, Re_1) plane for $Rb = Ro = -1$, $m = 1$, $q = 3r_0^{-1}$, $r = 1.5r_0$ and (left to right) $Pm = 10$, $Pm = 1$, and $Pm = 10^{-6}$ found with the use of the growth rates maximized over k of the roots of the dispersion relation (32) with the parameters specified by (62).

$$c_3 = -\frac{\sqrt{Pm}}{Ha_\theta} - \frac{(1 - Pm)c_1Ro(-m^2c_1Ha_\theta\sqrt{Pm} \pm im\sqrt{c_2})}{c_2 \pm imc_1\sqrt{c_2}Ha_\theta\sqrt{Pm}}.$$

The growing wave $\Re(\lambda) > 0$ corresponding to $\lambda_{1,2}$ for the particular case of Keplerian flow ($Ro = -3/4$) with $m = 1$ is admitted for

$$Ha_\theta > \frac{1}{\sqrt{3Pm}}. \quad (60)$$

For $\lambda_{3,4}$, numerically we find that a growing wave is permitted for small Pm and finite \hat{k} . For example, for the Keplerian flow ($Ro = -3/4$) and $m = \hat{k} = Ha_\theta = 1$, $Pm = 0.01$, $\hat{q} = 10$, the zeroth-order growth rate $c_3 \approx 1.68$.

In the PROMISE laboratory facility [36], the experimental setup is a Taylor-Couette flow between two corotating cylinders of finite axial size. The inner cylinder is set with the radius $r_{in} = 40$ mm and the outer cylinder is with $r_{out} = 2r_{in} = 80$ mm. The gap between the cylinders is $d = r_{out} - r_{in} = r_{in}$. By that reason, in this section we assume $r_{in} = d = r_0$. Recalling (17), we can write

$$\Omega(r_{in}) = \Omega(r) \left(\frac{r_0}{r} \right)^{2Ro}, \quad \mu(r_{in}) = \mu(r) \left(\frac{r_0}{r} \right)^{2Rb}. \quad (61)$$

This allows us to redefine the Reynolds and Hartmann numbers as follows:

$$Re_1 = \frac{\Omega(r_{in})d^2}{v} = Re|\mathbf{k}|^2r_0^2 \left(\frac{r_0}{r} \right)^{2Ro},$$

$$Ha_{\theta_1} = \frac{\mu(r_{in})d^2}{\sqrt{\rho\mu_0v\eta}} = Ha_\theta|\mathbf{k}|^2r_0^2 \left(\frac{r_0}{r} \right)^{2Rb}, \quad (62)$$

where $|\mathbf{k}|^2 = k^2 + q^2 + m^2/r^2$ and Re and Ha_θ are given by (19). These Reynolds and Hartmann numbers (62) match those of the numerical and experimental works [25, 36, 56].

The critical Reynolds number at the onset of instability is crucial for the experimental realization of the MRI. The liquid metals used in the experiments have $Pm \sim 10^{-6}$, and the standard MRI which scales with the magnetic Reynolds number and the Lundquist number corresponds to the Reynolds numbers of order 10^6 . Therefore it is hard to maintain the basic flow undisturbed before the onset of SMRI [4, 5].

The helical and the azimuthal MRI scale with the Reynolds and Hartmann numbers and thus require moderate ranges of the Reynolds numbers compared to SMRI [31]. By that reason both HMRI and AMRI were detected in the laboratory experiments [8, 9, 33, 34, 36] for rotation which is a little bit shallower than the Rayleigh value $\Omega \sim r^{-1.9}$ and for the current-free azimuthal magnetic field corresponding to $Rb = -1$. In [37, 43] it was theoretically shown that the inductionless HMRI and AMRI for the Keplerian flow with $Ro = -3/4$ exist when the radial dependence of the azimuthal magnetic field is shallower than that of the current-free type: $Rb > -\frac{1}{8}\frac{(Ro+2)^2}{Ro+1}$. In Sec. V we have verified this result for large axial wave numbers, $k \gg 1$. The planned MRI-TI experiment in the frame of the new DRESDYN facility [8, 9] creates the azimuthal magnetic field both due to currents isolated of the liquid metal and passing directly through the metal thus allowing for variable Rb including those satisfying the instability criterion (28).

On the other hand, in Sec. V we have found that for small axial wave numbers, $k \ll 1$, the inductionless AMRI of the Keplerian flow may occur at $Rb < -1/4$, which includes the current-free azimuthal magnetic field with $Rb = -1$ used in the existing PROMISE experiment; see Fig. 4. Using the redefined Reynolds and Hartmann numbers (62) in this section we compare our WKB analysis with the results from the global analysis [35, 56] for arbitrary Pm and discuss the implications for the experimental detection of the long-axial-wavelength instability. In view of the recent discovery of a long-wavelength linear instability of a hydrodynamical Taylor-Couette flow [59] this direction is worth pursuing.

A. Case of $Ro = Rb = -1$ and $m = 1$ with $q = 3r_0^{-1}$

Since the Taylor-Couette experimental apparatus is radially bounded, we limit q from below and choose, e.g., $q = 3r_0^{-1}$, which is reasonable when the radial velocity disturbance should be zero on the boundary and the width between the two cylinders is r_0 . In Fig. 8 we present the instability region in the (Ha_{θ_1}, Re_1) plane. To find it, we numerically calculate the maximum growth rate at every meshing point in the (Ha_{θ_1}, Re_1) plane for a wide range of k . Zero growth rates correspond to the neutral stability curve. The calculation is performed locally at $r = 1.5r_0$, the average of $r_{in} = r_0$ and $r_{out} = 2r_0$. Notice that the Tayler instability is excluded in this parameter regime by (53) and (55). We can see that Fig. 8 is similar to Fig. 1 of Hollerbach *et al.* [35] and Fig. 1 of Rüdiger

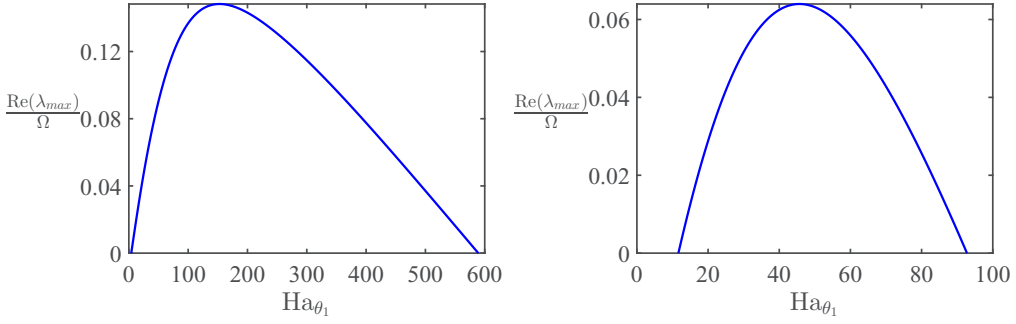


FIG. 9. The maximized over k growth rate $Re(\lambda_{\max})$ in the units of Ω versus Ha_{θ_1} according to Eq. (32) with the parameters (62) for the flow with $Ro = -1$, $Rb = -1$, $Pm = 10^{-6}$, $m = 1$, $q = 3r_0^{-1}$, and $r = 1.5r_0$ when (left) $Re_1 = 3000$ and (right) $Re_1 = 500$.

et al. [25]. The instability is invited when the Reynolds number is of the order 10^2 when $Pm \ll 1$ and of the order 10 when $Pm \approx 1$, 10. When $Pm = 10^{-6}$, the critical Reynolds number is $Re_1 \approx 265$, which is attained at $Ha_{\theta_1} \approx 30$, $k = 3.4727r_0^{-1}$, and $q = 3r_0^{-1}$. Note, however, that in Refs. [25,35] the instability domains have a finite size along the Re axis, which yields the existence of the second critical Reynolds number by exceeding which the AMRI vanishes. The neutral stability curves based on our local dispersion relation do not catch this upper critical Reynolds number.

The left panel of Fig. 9 shows that for $Re_1 = 3000$ and $Pm = 10^{-6}$, the instability occurs when $Ha_{\theta_1} \in (4, 590)$. The growth rate has its extremum $\Re(\lambda_{\max})/\Omega_{\text{in}} \approx 0.1483$ at $Ha_{\theta_1} \approx 153$ with the extremizer $k \approx 7.43r_0^{-1}$. In the right panel of Fig. 9 corresponding to $Re_1 = 500$, the instability occurs for $Ha_{\theta_1} \in (12, 93)$. The growth rate reaches its ex-

tremum $\Re(\lambda_{\max})/\Omega_{\text{in}} \approx 0.06397$ at $Ha_{\theta_1} \approx 46$ with the extremizer $k \approx 4.35r_0^{-1}$. We see that in both cases no instability occurs when the magnetic field is sufficiently weak in agreement with the argument in Sec. V A.

B. Case of $Ro = Rb = -1/2$ and $m = 1$ with $q = 3r_0^{-1}$

The magnetic Rossby number $Rb = -1/2$ and the azimuthal wave number $m = 1$ lie inside the range (55) and thus allow for the emergence of Tayler instability [39,56]. Figure 10 displays the variation of the instability regions in (Ha_{θ_1}, Re_1) plane when the magnetic Prandtl number Pm changes from 100 to 0.1. This result compares well with Fig. 3 of Rüdiger *et al.* [56]. We notice that there are two types of instabilities, with the lower part originating from the Tayler instability occurring without rotation in the basic

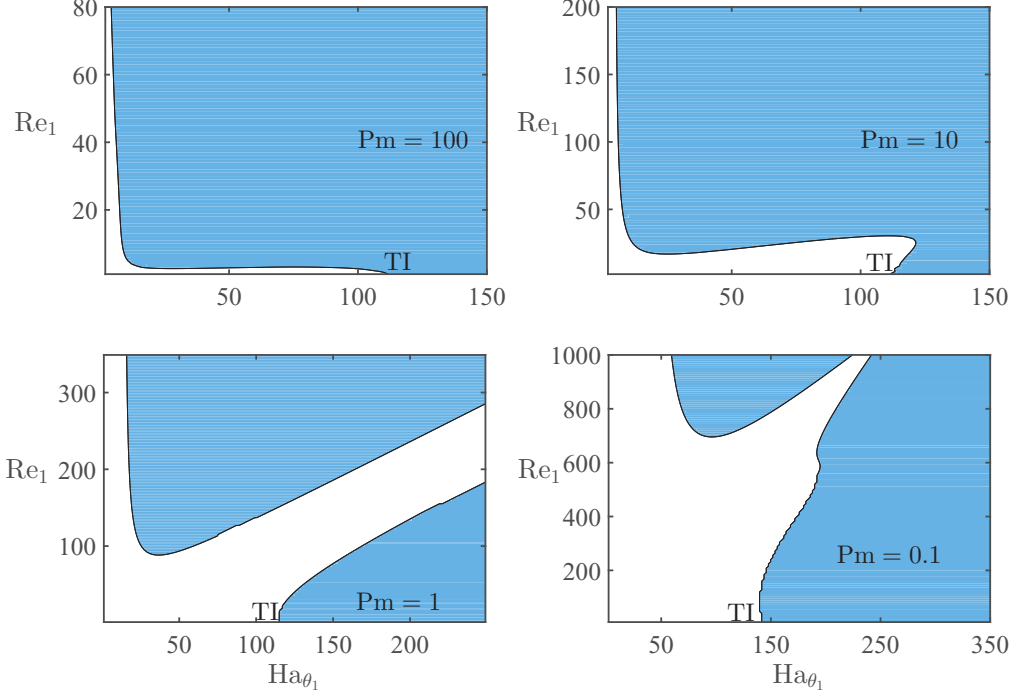


FIG. 10. The instability region in the (Re_1, Ha_{θ_1}) plane for $Ro = -1/2$, $Rb = -1/2$, $m = 1$, $q = 3r_0^{-1}$, $r = 1.5r_0$, and $Pm = 100$, $Pm = 10$, $Pm = 1$, and $Pm = 0.1$. The instability domains represented in blue are found with the use of the growth rates maximized over k of the roots of Eq. (32) with the parameters (62).

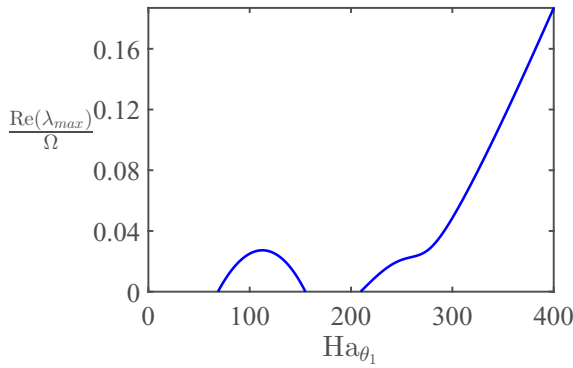


FIG. 11. The optimized over k growth rate versus the Hartmann number Ha_{θ_1} according to Eq. (32) with the parameters (62). The parameters chosen are $\text{Re}_1 = 800$, $\text{Rb} = -1/2$, $\text{Ro} = -1/2$, and $\text{Pm} = 0.1$ with $m = 1$, $q = 3r_0^{-1}$, and $r = 1.5r_0$.

state, and with the upper part originating from the AMRI. As Pm decreases, the critical Reynolds number becomes larger for the AMRI and the AMRI region shrinks to a seemingly separate upper region. The critical Hartmann number for the Tayler instability turns out to be insensitive to Pm . Figure 10 exhibits marked contrast with Fig. 8 where TI is excluded by the criteria (53) and (55).

Closer to the experimental condition is the case of $\text{Pm} = 0.1$ in Fig. 10. Fixing $\text{Pm} = 0.1$ and $\text{Re}_1 = 800$, we draw the optimized over k growth rate as a function of Ha_{θ_1} in Fig. 11. There are two instability intervals $\text{Ha}_{\theta_1} \in (69, 155) \cup (210, \infty)$. In the first one a local extremum is attained at $\text{Ha}_{\theta_1} \approx 112$ with the wave numbers $k = 2.7493r_0^{-1}$ and $q = 3r_0^{-1}$. The growth rate increases monotonically with Ha_{θ_1} for $\text{Ha}_{\theta_1} > 195$.

C. Case of $\text{Ro} = -3/4$, $\text{Rb} = -1$, and $m = 1$ with $q = 3r_0^{-1}$

According to the instability condition (28) the Keplerian rotation with $\text{Ro} = -3/4$ cannot be destabilized by the current-free azimuthal magnetic field with $\text{Rb} = -1$ in the inductionless limit of $\text{Pm} = 0$. Instead, the criterion (28) suggests shallower radial profiles for the magnetic field with

$\text{Rb} > -25/32$. Does this change for small but finite Pm ? The work [30] predicted regions of HMRI existing at such values of the magnetic Prandtl number. What can we say about AMRI?

Here we demonstrate that, for $\text{Ro} = -3/4$ and $\text{Rb} = -1$, there is a minimum value of the magnetic Prandtl number Pm , below which the instability is ruled out. Let us choose $r = 1.5r_0$ and search for the critical Pm for instability. For the flow with $\text{Re}_1 = 10^4$, the left panel of Fig. 12 shows that the instability necessitates $\text{Pm} > 0.0046$, with the critical value of Pm corresponding to $\text{Ha}_{\theta_1} \approx 400$. For $\text{Re}_1 = 10^3$, the critical value is raised to $\text{Pm} \approx 0.048$ which is attained at $\text{Ha}_{\theta_1} \approx 127$ as shown by the right panel of Fig. 12.

As Re_1 is increased, the critical value of Pm is decreased, which yields a larger strength of magnetic field according to (60). Large Reynolds numbers mean turbulence in practice so that $\text{Pm} \gtrsim 10^{-3}$ is at least necessary for experimental realization of the AMRI. However the liquid eutectic alloy GaInSn has $\text{Pm} = 1.4 \times 10^{-6}$ making the AMRI of a Keplerian flow virtually impossible for the experimental setup with the current-free azimuthal magnetic field [36]. Indeed, Fig. 13 shows that as Pm decreases, the instability region becomes smaller and smaller.

However, as Fig. 4 demonstrates, in the limit ($\text{Pm} \rightarrow 0$), the $k \rightarrow 0$ mode has positive growth rate. To approach this instability, we set $r_{\text{out}} = r_0$ as the characteristic length but set r to vary freely toward $r = 0$. By setting $\tilde{k} = 0$ in (33), we find its roots in the following form:

$$\begin{aligned} \frac{\lambda_1}{\Omega} &= -\sqrt{\frac{r_0}{r}} \frac{1}{1 + (qr)^2} \frac{\text{Ha}_{\theta_1}^2}{\text{Re}_1} - \sqrt{\frac{r_0}{r}} \frac{1 + (qr)^2}{\text{Re}_1} - i, \\ \frac{\lambda_2}{\Omega} &= \sqrt{\frac{r_0}{r}} \frac{3 - (qr)^2}{(1 + (qr)^2)^2} \frac{\text{Ha}_{\theta_1}^2}{\text{Re}_1} - \sqrt{\frac{r_0}{r}} \frac{1 + (qr)^2}{\text{Re}_1} - i \frac{1 + 4q^2r^2}{4 + 4q^2r^2}. \end{aligned} \quad (63)$$

The first root has $\Re(\lambda_1) < 0$ and corresponds to a stable mode. The second one indicates that, for large values of Ha_{θ_1} , the instability occurs when

$$(qr)^2 < 3. \quad (64)$$

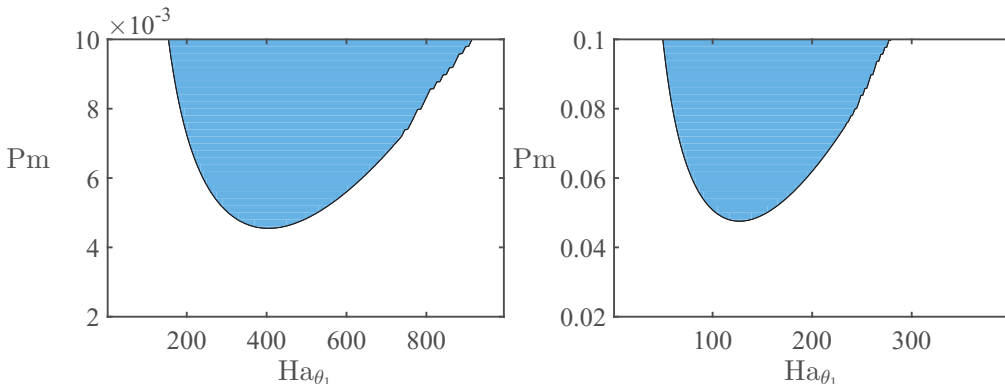


FIG. 12. The region of AMRI (above the critical lines) in the $(\text{Ha}_{\theta_1}, \text{Pm})$ plane when $\text{Rb} = -1$, $\text{Ro} = -3/4$ and (left) $\text{Re}_1 = 10^4$ and (right) $\text{Re}_1 = 10^3$ according to Eq. (32) with the parameters (62). In the former case the instability occurs when $\text{Pm} > 0.0046$ with the smallest Pm corresponding to $\text{Ha}_{\theta_1} \approx 400$, whereas in the latter when $\text{Pm} > 0.048$ with the lowest Pm corresponding to $\text{Ha}_{\theta_1} \approx 127$.

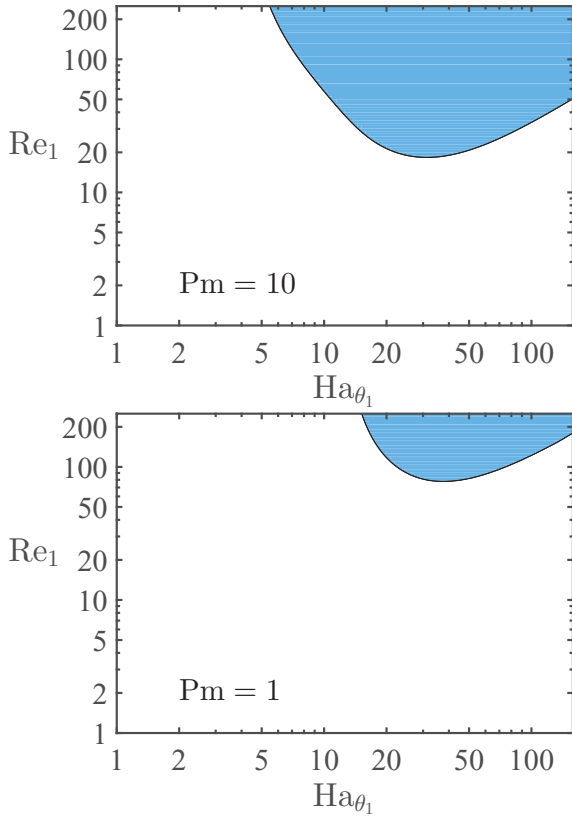


FIG. 13. The region of AMRI in the $(\text{Ha}_{\theta_1}, \text{Re}_1)$ plane when $\text{Ro} = -3/4$ and $\text{Rb} = -1$, $m = 1$, $q = 3r_0^{-1}$, and $r = 1.5r_0$. The neutral stability curve is obtained by maximizing the growth rate over k for $\text{Pm} = 10$ and $\text{Pm} = 1$ with the use of Eq. (32) with the parameters (62).

In addition, the radial wave number is bounded so as to satisfy the boundary conditions at the cylinders of $r = r_{\text{in}}$ and r_{out} , indicating

$$q(r_{\text{out}} - r_{\text{in}}) > \pi > 3. \quad (65)$$

Combining (64) and (65), we obtain

$$\frac{r}{r_{\text{out}} - r_{\text{in}}} < \frac{1}{\sqrt{3}}. \quad (66)$$

Setting $r = (r_{\text{in}} + r_{\text{out}})/2$, we obtain an estimate for $r_{\text{in}}/r_{\text{out}}$ as

$$\frac{r_{\text{in}}}{r_{\text{out}}} < \frac{2 - \sqrt{3}}{2 + \sqrt{3}} \approx 0.0718. \quad (67)$$

This crude argument suggests that the experimental setups with $r_{\text{in}}/r_{\text{out}} = 1/2$ might need to be modified to have a wider gap in order to be able to capture the mode of $k = 0$ for a Keplerian flow subject to the current-free magnetic field.

VII. GLOBAL STABILITY ANALYSIS

In order to provide a numerical validation of the analytical results based on the Hain-Lüst dispersion relation (32), in the following we consider the cylindrical Taylor-Couette flow as described in Sec. VI. We will decompose the magnetic and velocity fields into toroidal and poloidal parts and after that

reduce the original MHD system (3)–(6) to a one-dimensional boundary eigenvalue problem [35,44] by expanding the solution in the Heinrichs basis [15,58,61].

We assume a finite radial gap $d := |r_{\text{out}} - r_{\text{in}}|$ and a radius ratio $\zeta := r_{\text{in}}/r_{\text{out}}$ that both define the geometry of the setup. Our numerical method is based on the pseudospectral expansion of the solution in terms of normal modes before collocating at the Chebyshev-Gauss nodes. The code we have developed has been benchmarked against several well-established results of similar stability analyses for either insulating or conducting boundary conditions with excellent agreement.

For the sake of clarity, we first render the problem (3)–(6) in a dimensionless form following the notations in Child *et al.* [44] except for the background velocity field where we follow the work of Deguchi [15]. This can be summarized by scaling length with d , time with the viscous timescale d^2/ν , velocities with ν/d , pressure with $\rho\nu^2/d^2$, and magnetic fields with B_0 .

A. Background fields and Rossby numbers

The scaling introduced before leads to the following set of equations:

$$\begin{aligned} \frac{\partial \hat{\mathbf{u}}}{\partial \hat{t}} &= -(\hat{\mathbf{u}} \cdot \hat{\nabla}) \hat{\mathbf{U}} - (\hat{\mathbf{U}} \cdot \hat{\nabla}) \hat{\mathbf{u}} - \hat{\nabla} \hat{P} + \hat{\nabla}^2 \hat{\mathbf{u}} \\ &\quad + \frac{\text{Ha}_\theta^2}{\text{Pm}} [(\hat{\mathbf{b}} \cdot \hat{\nabla}) \hat{\mathbf{B}} + (\hat{\mathbf{B}} \cdot \hat{\nabla}) \hat{\mathbf{b}}], \\ \frac{\partial \hat{\mathbf{b}}}{\partial \hat{t}} &= \hat{\nabla} \times (\hat{\mathbf{U}} \times \hat{\mathbf{b}}) + \hat{\nabla} \times (\hat{\mathbf{u}} \times \hat{\mathbf{B}}) + \frac{1}{\text{Pm}} \hat{\nabla}^2 \hat{\mathbf{b}}, \\ \hat{\nabla} \cdot \hat{\mathbf{u}} &= 0, \quad \hat{\nabla} \cdot \hat{\mathbf{b}} = 0, \end{aligned} \quad (68)$$

where $\text{Ha}_\theta = B_0 d / \sqrt{\rho \mu_0 \nu \eta}$ is the azimuthal Hartmann number and $\text{Pm} = \nu/\eta$ is the magnetic Prandtl number.

This dimensionless MHD system is therefore solved regarding to no-slip boundary conditions for the velocity field, which in the cylindrical coordinates (r, θ, z) lead to [59]

$$\begin{aligned} \hat{U}_\theta(r_{\text{in}}, \theta, z) &= \frac{\Omega_{\text{in}} r_{\text{in}} d}{\nu} =: \text{Re}_{\text{in}}, \\ \hat{U}_\theta(r_{\text{out}}, \theta, z) &= \kappa \text{Re}_{\text{in}}/\zeta =: \text{Re}_{\text{out}}, \end{aligned} \quad (69)$$

where \hat{U}_θ is the azimuthal component of the fluid velocity, $\kappa := \Omega_{\text{out}}/\Omega_{\text{in}}$ is the ratio between the angular velocities, and the inner and outer radii can be defined according to the Taylor-Couette parameters as $r_{\text{in}} := d\zeta/(1 - \zeta)$ and $r_{\text{out}} := d/(1 - \zeta)$.

A fundamental solution for this system and the boundary conditions is the well-known Couette profile $\hat{\mathbf{U}} = \hat{r}\Omega(\hat{r})\mathbf{e}_\theta$, given by

$$\Omega(\hat{r}) = \frac{\text{Re}_{\text{in}}}{1 + \zeta} \left[\left(\frac{\kappa}{\zeta} - \zeta \right) + \frac{\zeta(1 - \kappa)}{(1 - \zeta)^2} \frac{1}{\hat{r}^2} \right], \quad (70)$$

where $\hat{r} = rd^{-1}$ is the dimensionless radial coordinate.

The background magnetic field we consider here is purely azimuthal $\hat{\mathbf{B}} = \hat{B}_\phi(\hat{r})\mathbf{e}_\theta$ and given by

$$\hat{B}_\phi(\hat{r}) = \frac{\zeta(\tau - \zeta)}{1 - \zeta^2} \hat{r} + \frac{1 - \tau\zeta}{1 - \zeta^2} \frac{1}{\hat{r}}, \quad (71)$$

where $\tau := B_{\text{out}}/B_{\text{in}}$ is the ratio between the outer and the inner azimuthal magnetic fields [32].

Using (61) and (71) we can write

$$\kappa = \zeta^{-2\text{Ro}}, \quad \tau = \zeta^{-(2\text{Rb}+1)}. \quad (72)$$

Then the solid-body rotation ($\text{Ro} = 0$) corresponds to $\kappa = 1$ and the Keplerian flow ($\text{Ro} = -3/4$) to $\kappa = \zeta^{3/2}$.

In the following, we will specify the basic state of the magnetized flow via Ro , Rb , ζ , Re_{in} , Pm , and Ha_{θ} defined earlier.

B. Pseudospectral expansion

We seek for a solution to linearized MHD equations decomposed into toroidal and poloidal parts as follows:

$$\tilde{\mathbf{u}} = \nabla \times (\psi \mathbf{e}_r) + \nabla \times \nabla \times (\phi \mathbf{e}_r), \quad (73)$$

$$\tilde{\mathbf{b}} = \nabla \times (\Psi \mathbf{e}_r) + \nabla \times \nabla \times (\Phi \mathbf{e}_r). \quad (74)$$

The disturbance fields (ψ, ϕ, Ψ, Φ) in (73) and (74) are expanded in terms of normal modes according to the pseudospectral Fourier method. In it, each variable is expressed with respect to Heinrichs basis [15,58,61] for the radial direction and to Fourier basis for the axial and azimuthal directions. Such expansion can be represented for an arbitrary field \mathcal{L} as

$$\mathcal{L}(x, t, \theta, z) := \sum_{n=0}^{\infty} [\mathcal{H}(x) T_n(x)] \exp[\lambda t + i(m\theta + kz)], \quad (75)$$

where $T_n(x)$ is a Chebyshev polynomial, $\mathcal{H}(x)$ is the Heinrichs factor, which depends on the boundary conditions considered, λ is an eigenvalue, (m, k) are the azimuthal and axial wave numbers, respectively, and x is the length coordinate.

In order for the method to be computable, the infinite series are truncated at the N th order and the mapping of the radial interval $[r_{\text{in}}, r_{\text{out}}]$ to the Chebyshev interval $[-1, 1]$ comes from the linear transformation [58] $x = 2(r - r_m)d^{-1}$ with $r_m = d(1 + \zeta)/[2(1 - \zeta)]$ being the mean radius. Finally, the series are evaluated at the Chebyshev-Gauss collocation points

$$x_i = \pm \cos\left(\pi \frac{i+1}{N+2}\right), \quad i = 0, \dots, N.$$

The decomposition (75) allows us to express the differential operators as functions of the wave numbers and parameters of the system. Details of this method and coefficients of the boundary value problem can be found, e.g., in Child *et al.* [44] and Hollerbach *et al.* [35]. The set of equations we obtain is solved regarding the boundary conditions considered, i.e., no-slip conditions for the velocity field and perfectly conducting for the magnetic field. Assuming the expansion in terms of normal modes for each variables, these conditions can be written in the following form [62]:

$$\psi = \phi = \partial_r \phi = 0, \quad (76)$$

$$\Phi = 0, \quad (77)$$

$$ik\partial_r \Psi + ikr^{-1}\Psi + imr^{-1}\partial_{rr}\Phi - imr^{-2}\partial_r \Phi = 0. \quad (78)$$

The system is therefore reduced to a generalised eigenvalue problem of the form $A\xi = \lambda B\xi$, where λ is an eigenvalue and ξ an eigenvector.

C. Numerical results

For a fixed set of boundary conditions, the boundary value problem is solved and leads to the computation of the eigenvalues λ of the magnetized Taylor-Couette flow. The global stability analysis is therefore conducted over similar sets of parameters from the previous sections of this paper in order to validate a large part of the results.

In Fig. 14 we compare growth rates given by the boundary value problem, the Hain-Lüst dispersion relation (32) and the original WKB approximation [30]. The latter solution is given according to our notations as follows:

$$\frac{\Re(\lambda)}{\Omega_{\text{in}}} = N_{\theta} \left(2\text{Rb} - \frac{m}{\alpha_1} \right) - \frac{1}{\text{Re}} \pm \sqrt{2X + 2\sqrt{X^2 + Y^2}}, \quad (79)$$

where $N_{\theta} = \text{Ha}_{\theta}^2/\text{Re}$, $\alpha_1 = k/\sqrt{k^2 + q^2}$ and

$$X = N_{\theta}^2 \left(\text{Rb}^2 + \frac{m}{\alpha_1} \right) - (\text{Ro} + 1),$$

$$Y = N_{\theta}(\text{Ro} + 2) \frac{m}{\alpha_1}.$$

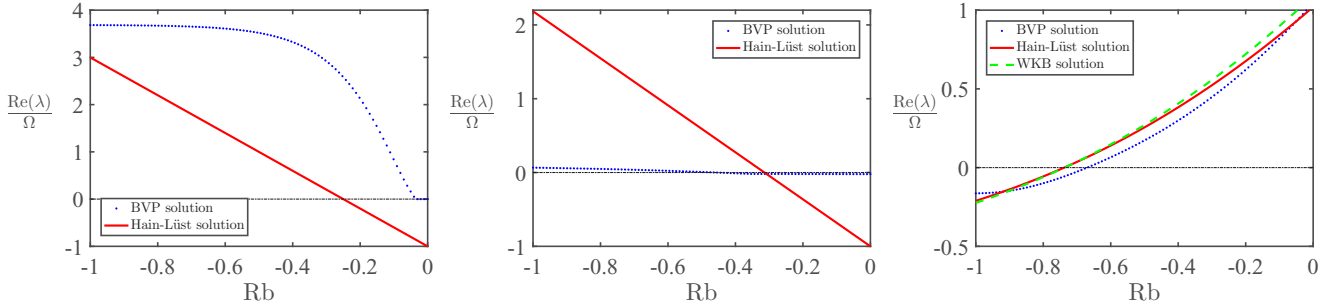


FIG. 14. The growth rate $\text{Re}(\lambda)$ in units of Ω_{in} over a range of magnetic Rossby number Rb for the Keplerian ($\text{Ro} = -3/4$) flow with $\text{Re}_{\text{in}} = 10^4$, $\text{Ha}_{\theta} = 10^2$, $\text{Pm} = 0$, and $m = 1$, in the case of the long axial wavelength ($\zeta = 0.02/\zeta = 0.336$ and $k = 10^{-4}d^{-1}$, left/middle panels) and short axial wavelength ($\zeta = 0.98$ and $k = 3.5d^{-1}$, right panel). The dotted blue line comes from the dimensionless Taylor-Couette boundary value problem with the boundary conditions corresponding to the perfectly conducting walls. The red and dashed green lines correspond to the Hain-Lüst dispersion relation (33) and the WKB approximation (79). The radial wave number is set to be $\hat{q} = \zeta/(1 - \zeta)$.

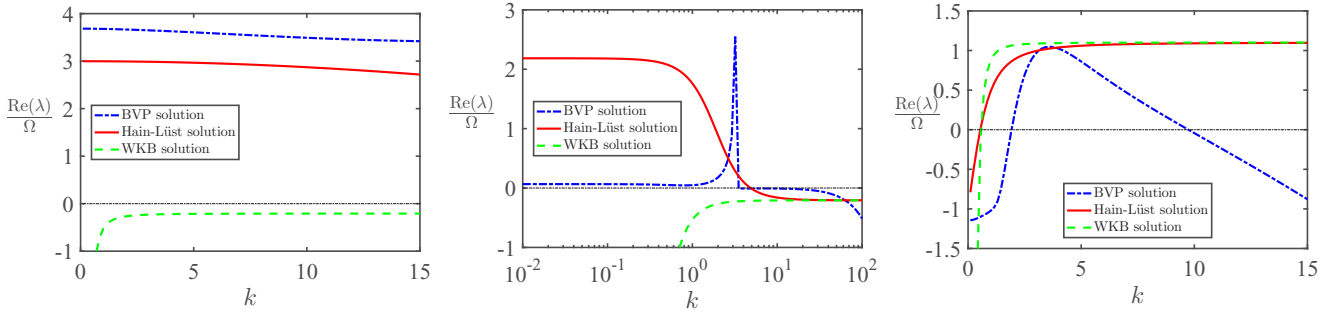


FIG. 15. The growth rate $\text{Re}(\lambda)$ in the units of Ω_{in} from BVP (dash-dotted blue), WKB approximation (dashed green), and Hain-Lüst (red) versus the axial wave number k (in units of d^{-1}) for perfectly conducting boundaries. We set $R_b = -1$ with $\zeta = 0.02$ (left) and $\zeta = 0.366$ (middle) and $R_b = 0$ with $\zeta = 0.98$ (right). The parameter space is the same as in Fig. 14.

The eigenvalues are both scaled with the inner angular velocity Ω_{in} and the stability analysis has been conducted for different but finite radial gaps over different values of R_b in Fig. 14. In the interest of reaching the $k \rightarrow 0$ mode, we have fixed a wide radial gap in order to have a small radial wave number. We chose an arbitrary value for the gap between both cylinders $\zeta = 0.02$ and according to this geometry, we manage to find a similar behavior for the growth rate of the long-wavelength domain but with nevertheless a discrepancy for the threshold of instability. Not surprisingly, the WKB solution (79) in the long-wavelength approximation is diverging at such value of k and therefore cannot be represented in this plot. In a similar way, if we decrease the gap between both cylinders until the limit that Eq. (67) predict, the numerical solution still behaves as the analytical result with nevertheless a worst accuracy in the magnitude. Nevertheless, while the WKB solution (79) is not able to catch such limit, it appears that our extended version of the Hain-Lüst dispersion

relation can. Regarding the short-wavelength domain, we used a narrow-gap $\zeta = 0.98$ and a larger wave number k and the growth rates from the BVP, the WKB solution and our dispersion relations are as expected in good agreement.

The dependence of the growth rate on the axial wave number k in our numerical scheme is represented in Fig. 15 where we observe that for the long-wavelength domain the growth rate reaches its maximum for $k \rightarrow 0$ as expected. For the short-wavelength approximation, we are limited to a smaller interval of k for which the growth rate is positive in the BVP solution, but it still remains sufficient to produce smooth and correct comparisons with the analytic. It is interesting to notice that in the middle panel for $\zeta = 0.366$, the numeric is predicting a peak between both domains. A similar behavior has been observed in the second figure of Bodo *et al.* [63] and is analyzed by the authors as a localized state of MRI. As we can notice, the WKB and the Hain-Lüst solutions are both asymptotically converging to the same value as k is increasing

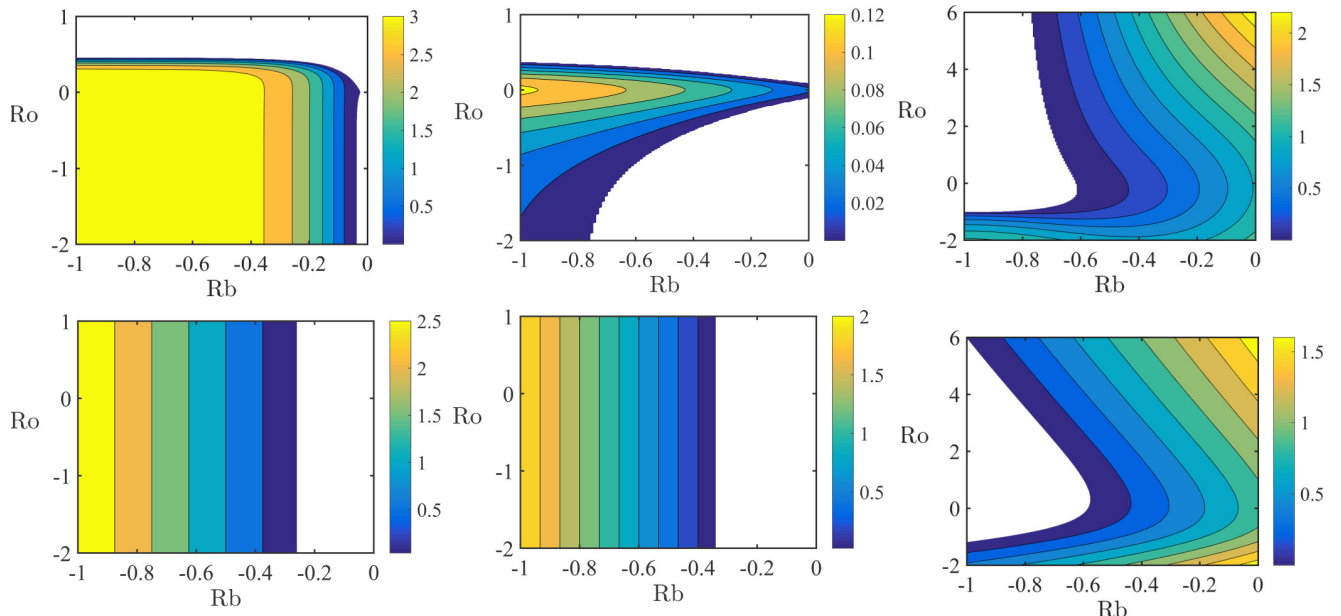


FIG. 16. Growth rate magnitude in the Rossby plane (R_b , Ro) from the boundary value problem with perfectly conducting boundaries for the upper panels and from Hain-Lüst dispersion relation (32) for the lower panels. The geometry correspond to $\zeta = 0.02$, $k = 10^{-4}d^{-1}$ (left column), $\zeta = 0.366$, $k = 10^{-4}d^{-1}$ (middle column), and $\zeta = 0.98$, $k = 3.5d^{-1}$ (right column). The parameter space is the same as in Fig. 14, and stability is represented in white.

(tending therefore to the short-axial-wavelength limit) only when the radial gap between both cylinder is not too large.

The last computation presents the stability domains in the (Rb, Ro) plane as in the previous Sec. V-B-4. This case is presented in Fig. 16 where the growth rate magnitude from the BVP and from the dispersion relation (32) is computed. The left and middle column panels show the long-wavelength instability domains with $\zeta = 0.02$, $\zeta = 0.366$, and $k = 10^{-4}d^{-1}$ and despite the difference in the neutral stability boundaries, the shape of both domains are in agreement with the analytical results of Fig. 16. When increasing the value of k as in the right column of Fig. 16, we also notice that the numerics is fitting well with our solution.

VIII. CONCLUSION

We have explored the AMRI and the Tayler instability of a rotating MHD flow, augmented by viscosity and electrical resistivity, with respect to the axisymmetric as well as nonaxisymmetric perturbations. We have derived the extended Hain-Lüst equation to include the viscosity and electrical resistivity. This is a second-order ordinary differential equation for the radial Lagrangian displacement.

We then applied the WKB approximation to it to derive a dispersion relation, valid in the regime of short wavelengths in the radial direction but allowing for arbitrary azimuthal and axial wave numbers.

By that reason, the extended Hain-Lüst dispersion relation contains the previously known dispersion relations derived by different methods, including the geometrical optics approximation.

On the other hand, the additional terms in it enable more accurate treatment of the nonaxisymmetric perturbations with large axial wavelength.

While being in the limit of short axial wavelength we restored the well-known results of the inductionless approximation, including the necessary condition (28) for both HMRI and AMRI, and the generalized Tayler instability condition (55), in the limit of long axial wavelength we discovered instability that works both in the rotating and in the nonmoving fluid.

We found a limitation on the radial wavelength providing an estimate for the gap in a Taylor-Couette setup which is necessary for detection of the instability. Finally, we combined the numerical methods of Deguchi and Nagata [58,59] and Child *et al.* [44] to validate the analytical findings, based on the Hain-Lüst dispersion relation, using global stability analysis.

ACKNOWLEDGMENTS

R.Z. was supported by a Ph.D. Studentship from the China Scholarship Council and by the Zhejiang Provincial Natural Science Foundation of China (Grant No. LQ20A020004). J.L. was supported by a Ph.D. Scholarship from Northumbria University. Y.F. was supported in part by a Grant-in-Aid for Scientific Research from the Japan Society for the Promotion of Science (Grant No. 19K03672).

APPENDIX A: DERIVATION OF EQ. (14)

In this Appendix we derive the extended Hain-Lüst equation (14). The lines 4–6 in (10) allow us to express the magnetic field disturbance \tilde{b}_r , \tilde{b}_θ , and \tilde{b}_z in terms of the other variables. By eliminating the magnetic field disturbances, we can reduce (10) to equations for $\xi_1 = (\tilde{u}_r, \tilde{u}_\theta, \tilde{u}_z, \tilde{p})$ as

$$\mathbf{M}_1 \xi_1 = \mathbf{0}, \quad (\text{A1})$$

where, with use of (12),

$$\mathbf{M}_1 = \begin{pmatrix} \Lambda + \frac{2\mu r}{\rho\mu_0\tilde{\lambda}_\eta} \left(\frac{iF}{\tilde{\lambda}_\eta} \Omega' - \mu' \right) & -2\Omega + \frac{2iF\mu}{\rho\mu_0\tilde{\lambda}_\eta} & 0 & \frac{1}{\rho} \frac{d}{dr} \\ 2\Omega + r\Omega' \left(1 + \frac{F^2}{\rho\mu_0\tilde{\lambda}_\eta^2} \right) - \frac{2iF\mu}{\rho\mu_0\tilde{\lambda}_\eta} & \Lambda & 0 & \frac{1}{r\rho} im \\ 0 & 0 & \Lambda & \frac{1}{\rho} ik \\ \frac{im}{r} & ik & 0 & \end{pmatrix}, \quad (\text{A2})$$

and the prime denotes the derivative with respect to r .

We then combine all the equations into a single second-order differential equation for the radial component of the Lagrangian displacement field. As an intermediate step, we solve algebraic equations (A1) and express $(\tilde{u}_r, \tilde{u}_\theta, \tilde{u}_z)$ in terms of \tilde{p} as

$$\begin{aligned} \tilde{u}_r &= -\frac{\Lambda}{E\rho} \frac{d\tilde{p}}{dr} + \frac{im}{E\rho r} \left(\frac{2iF\mu}{\tilde{\lambda}_\eta\rho\mu_0} - 2\Omega \right) \tilde{p}, \\ \tilde{u}_\theta &= \frac{1}{E\rho} \left[2\Omega + r\Omega' \left(1 + \frac{F^2}{\rho\mu_0\tilde{\lambda}_\eta^2} \right) - \frac{2iF\mu}{\rho\mu_0\tilde{\lambda}_\eta} \right] \frac{d\tilde{p}}{dr} \\ &\quad - \frac{im}{E\rho} \left[\Lambda + \frac{2\mu r}{\rho\mu_0\tilde{\lambda}_\eta} \left(\frac{iF}{\tilde{\lambda}_\eta} \Omega' - \mu' \right) \right] \tilde{p}, \end{aligned}$$

$$\tilde{u}_z = -\frac{ik}{\rho\Lambda} \tilde{p}, \quad (\text{A3})$$

where

$$\begin{aligned} E &= \Lambda^2 + \frac{2\Lambda\mu r}{\tilde{\lambda}_\eta\rho\mu_0} \left(\frac{iF}{\tilde{\lambda}_\eta} \Omega' - \mu' \right) + 2 \left(\Omega - \frac{i\mu F}{\tilde{\lambda}_\eta\rho\mu_0} \right) \\ &\quad \times \left[2\Omega + \left(1 + \frac{F^2}{\tilde{\lambda}_\eta^2\rho\mu_0} \right) r\Omega' - \frac{2i\mu F}{\tilde{\lambda}_\eta\rho\mu_0} \right]. \end{aligned} \quad (\text{A4})$$

Upon substitution from (A3) for \tilde{u}_r , \tilde{u}_θ , the continuity equation (5) produces a second-order differential equation

for \tilde{p} :

$$\begin{aligned} \frac{d}{dr} \left(\frac{\Lambda}{\rho E} \frac{d\tilde{p}}{dr} \right) + \left[\frac{\Lambda}{rE\rho} - \frac{im}{E\rho} \left(1 + \frac{F^2}{\rho\mu_0\tilde{\lambda}_\eta^2} \right) \Omega' \right] \frac{d\tilde{p}}{dr} \\ + \frac{2im}{Er^2\rho} \left(\Omega - \frac{iF\mu}{\rho\mu_0\tilde{\lambda}_\eta} \right) \tilde{p} + \frac{d}{dr} \left[\frac{2im}{Er\rho} \left(\Omega - \frac{iF\mu}{\rho\mu_0\tilde{\lambda}_\eta} \right) \right] \tilde{p} \\ - \frac{2m^2}{Er^2\rho} \left[\frac{\Lambda}{2} + \frac{\mu r}{\rho\mu_0\tilde{\lambda}_\eta} \left(\frac{iF}{\tilde{\lambda}_\eta} \Omega' - \mu' \right) \right] \tilde{p} - \frac{k^2}{\Lambda\rho} \tilde{p} = 0. \end{aligned} \quad (\text{A5})$$

The first of Eqs. (A3) yields an expression for $\chi = -r\tilde{u}_r/\tilde{\lambda}_\eta$ in terms of \tilde{p} and $d\tilde{p}/dr$:

$$\chi = \frac{\Lambda r}{\tilde{\lambda}_\eta E \rho} \frac{d\tilde{p}}{dr} + \frac{2im}{E\rho\tilde{\lambda}_\eta} \left(\Omega - \frac{iF\mu}{\rho\mu_0\tilde{\lambda}_\eta} \right) \tilde{p}. \quad (\text{A6})$$

In order to derive the equation for χ , first we take the radial derivative of (A6), and eliminate the second derivative of \tilde{p} , with the help of (A5), leaving

$$\begin{aligned} \frac{d\chi}{dr} = \frac{im}{E\rho\tilde{\lambda}_\eta} \left[\left(1 - \frac{\tilde{\lambda}_v}{\tilde{\lambda}_\eta} \right) r\Omega' + 2 \left(\Omega - \frac{iF\mu}{\rho\mu_0\tilde{\lambda}_\eta} \right) \right] \frac{d\tilde{p}}{dr} \\ + \frac{2m^2}{E\rho\tilde{\lambda}_\eta^2} \left(\Omega - \frac{iF\mu}{\rho\mu_0\tilde{\lambda}_\eta} \right) \Omega' \tilde{p} \\ + \frac{h^2 r}{\Lambda E \rho \tilde{\lambda}_\eta} \left[\Lambda^2 + \frac{2\mu r}{\tilde{\lambda}_\eta \rho \mu_0} \Lambda \left(\frac{iF}{\tilde{\lambda}_\eta} \Omega' - \mu' \right) \right] \tilde{p} \\ + \frac{2k^2 r}{\Lambda E \rho \tilde{\lambda}_\eta} \left[2\Omega + \left(1 + \frac{F^2}{\tilde{\lambda}_\eta^2 \rho \mu_0} \right) r\Omega' - \frac{2i\mu F}{\tilde{\lambda}_\eta \rho \mu_0} \right] \\ \times \left(\Omega - \frac{i\mu F}{\tilde{\lambda}_\eta \rho \mu_0} \right) \tilde{p}, \end{aligned} \quad (\text{A7})$$

where h is defined by (13).

A combination of (A6) and (A7) brings the expression for $d\tilde{p}/dr$ in terms of χ and $d\chi/dr$:

$$\begin{aligned} \frac{d\tilde{p}}{dr} = -\frac{2ipm\tilde{\lambda}_\eta}{h^2r^2} \left(\Omega - \frac{iF\mu}{\rho\mu_0\tilde{\lambda}_\eta} \right) \frac{d\chi}{dr} + \frac{\rho\tilde{\lambda}_\eta E}{\Lambda r} \chi \\ - \frac{2pm^2\tilde{\lambda}_\eta}{h^2r^3\Lambda} \left(\Omega - \frac{iF\mu}{\rho\mu_0\tilde{\lambda}_\eta} \right) \left[\left(1 - \frac{\tilde{\lambda}_v}{\tilde{\lambda}_\eta} \right) r\Omega' \right. \\ \left. + 2 \left(\Omega - \frac{iF\mu}{\rho\mu_0\tilde{\lambda}_\eta} \right) \right] \chi. \end{aligned} \quad (\text{A8})$$

This helps us to rule out $d\tilde{p}/dr$ from (A7) and obtain

$$\begin{aligned} \Lambda r \frac{d\chi}{dr} - im \left[\left(1 - \frac{\tilde{\lambda}_v}{\tilde{\lambda}_\eta} \right) r\Omega' + 2 \left(\Omega - \frac{iF\mu}{\rho\mu_0\tilde{\lambda}_\eta} \right) \right] \chi \\ = \frac{h^2 r^2}{\rho\tilde{\lambda}_\eta} \tilde{p}. \end{aligned} \quad (\text{A9})$$

Multiplying both sides of (A9) by $\rho\tilde{\lambda}_\eta/(h^2r^2)$, taking the derivative in r and then substituting from (A8) for $d\tilde{p}/dr$ expressed in terms of χ and $d\chi/dr$, we eventually arrive at

the extended Hain-Lüst equation (14):

$$\frac{d}{dr} \left(f \frac{d\chi}{dr} \right) + s \frac{d\chi}{dr} - g\chi = 0, \quad (\text{A10})$$

supplemented by (15).

APPENDIX B: CONNECTION TO REF. [43]

We write again the dispersion relation (16), which we deduced from the extended Hain-Lüst equation (14):

$$\begin{aligned} & \tilde{\lambda}_\eta^2 \Lambda^2 + 4\alpha^2 \left(\Omega \tilde{\lambda}_\eta - \frac{iF\mu}{\rho\mu_0} \right) \\ & \times \left[\Omega \text{Ro}(\omega_\eta - \omega_v) + \left(\Omega \tilde{\lambda}_\eta - \frac{iF\mu}{\rho\mu_0} \right) \right] \\ & + \frac{4\Lambda h^2 \tilde{\lambda}_\eta}{h^2 + q^2} \left\{ \left(\Omega^2 \text{Ro} - \frac{\mu^2}{\rho\mu_0} \text{Rb} \right) \right. \\ & \left. + \frac{imr}{4} \frac{d}{dr} \left[\frac{2 \left(\Omega \tilde{\lambda}_\eta - \frac{i\mu F}{\rho\mu_0} \right) + (\omega_\eta - \omega_v)r\Omega'}{h^2 r^2} \right] \right\} = 0, \end{aligned} \quad (\text{B1})$$

where $\Lambda = \tilde{\lambda}_v + \frac{F^2}{\tilde{\lambda}_\eta \rho \mu_0}$ and $\alpha^2 = \frac{k^2}{h^2 + q^2}$. The dispersion relation in Ref. [43] differs from (B1) only by the term

$$\frac{\Lambda h^2 \tilde{\lambda}_\eta imr}{h^2 + q^2} \frac{d}{dr} \left[\frac{2 \left(\Omega \tilde{\lambda}_\eta - \frac{i\mu F}{\rho\mu_0} \right) + (\omega_\eta - \omega_v)r\Omega'}{h^2 r^2} \right]. \quad (\text{B2})$$

We illustrate the difference by calculating the growth rates given by the two dispersion relations for $\text{Ro} = -1/2$, $\text{Rb} = -1/2$, $m = 1$, and $\text{Pm} = 1$. We define α_1 by $\alpha_1^2 = k^2/(k^2 + q^2)$. Expanding the growth rates at large values of Ha_θ for (B1) with and without the term (B2), we find

$$\frac{\Re(\lambda)}{\Omega} = a_H \text{Ha}_\theta + O(\text{Ha}_\theta^0), \quad \frac{\Re(\lambda)}{\Omega} = a_K \text{Ha}_\theta + O(\text{Ha}_\theta^0), \quad (\text{B3})$$

respectively, where

$$\begin{aligned} a_H &= \frac{1}{\text{Re} \sqrt{[1 + (rk)^2][\alpha_1^2 + (rk)^2]}} \\ &\times ((\alpha_1^2 - 1)(rk)^2 - (1 + \alpha_1^2)(rk)^4 \\ &+ \alpha_1 \{4(rk)^4 [1 + (rk)^2]^2 + \alpha_1^2 (1 + 8(rk)^2 \\ &+ 10(rk)^4 + (rk)^8]\}^{\frac{1}{2}})^{\frac{1}{2}}, \\ a_K &= \frac{1}{\text{Re} \sqrt{\sqrt{\alpha_1^2 (4 + \alpha_1^2)} - (1 + \alpha_1^2)}}. \end{aligned} \quad (\text{B4})$$

The relation between a_H and a_K becomes clear, if we expand a_H in power of $1/k$ at large values of $|k|$ leaving

$$\begin{aligned} a_H = & \frac{1}{\text{Re}} \sqrt{\sqrt{\alpha_1^2(4 + \alpha_1^2)} - (1 + \alpha_1^2)} \\ & + \frac{[(3 + \alpha_1^2)\sqrt{\alpha_1^2(4 + \alpha_1^2)} - \alpha_1^2(5 + \alpha_1^2)]\sqrt{\alpha_1^2}}{2\sqrt{\alpha_1^2 + 4}\sqrt{\sqrt{\alpha_1^2(4 + \alpha_1^2)} - 1 - \alpha_1^2\text{Re}}} \frac{1}{k^2 r^2} \\ & + O\left(\frac{1}{k^4}\right). \end{aligned} \quad (\text{B5})$$

We find that the leading-order term is a_K .

APPENDIX C: CONNECTION TO REF. [63]

Bodo *et al.* [63] consider compressible MHD without viscosity and electrical resistivity in contrast to our setting, which is an incompressible MHD with viscosity and electrical resistivity. Here we demonstrate that in the limit of infinite speed of sound ($c_s \rightarrow \infty$) the differential equation (35) of Ref. [63] yields the same version of the Hain-Lüst equation for the Lagrangian displacement as our Eq. (14) does for $v = 0$ and $\eta = 0$.

Indeed, the differential equation (35) in Ref. [63] is

$$\begin{aligned} \frac{d^2}{dr^2}(r\xi_r) + \frac{d}{dr} \ln\left(\frac{\Delta}{rC_2}\right) \frac{d}{dr}(r\xi_r) \\ + \left[\frac{C_2 C_3 - C_1^2}{\Delta^2} - \frac{rC_2}{\Delta} \frac{d}{dr}\left(\frac{C_1}{rC_2}\right) \right](r\xi_r) = 0, \end{aligned} \quad (\text{C1})$$

which can be transformed to

$$\frac{d}{dr} \left[\frac{\Delta}{rC_2} \frac{d}{dr}(r\xi_r) \right] + \left[\frac{C_2 C_3 - C_1^2}{r\Delta C_2} - \frac{d}{dr}\left(\frac{C_1}{rC_2}\right) \right](r\xi_r) = 0. \quad (\text{C2})$$

The coefficients Δ , C_1 , C_2 , and C_3 are defined in Ref. [63] by Eqs. (27)–(30) that contain the sound speed c_s . Retaining only the leading-order terms in c_s in the assumption that $c_s \gg 1$,

we write these coefficients as

$$\begin{aligned} \Delta &= c_s^2(\rho\tilde{\omega}^2 - k_B^2), \\ C_1 &= -\frac{2mc_s^2}{r^2}(kB_\phi + \rho v_\phi \tilde{\omega})(\rho\tilde{\omega}^2 - k_B^2), \\ C_2 &= -c_s^2\left(k^2 + \frac{m^2}{r^2}\right)(\rho\tilde{\omega}^2 - k_B^2), \\ C_3 &= c_s^2(\rho\tilde{\omega}^2 - k_B^2)^2 \left[\rho\tilde{\omega}^2 - k_B^2 + r \frac{d}{dr} \left(\frac{B_\phi^2 - \rho v_\phi^2}{r^2} \right) \right] \\ &\quad - \frac{4c_s^2}{r^2}(\rho\tilde{\omega}^2 - k_B^2)(kB_\phi + \rho v_\phi \tilde{\omega})^2, \end{aligned} \quad (\text{C3})$$

where we omit the subscript 0 that was used in Ref. [63] to denote the equilibrium.

In Ref. [63] $k_B = \frac{m}{r}B_\phi + kB_z$ and $\tilde{\omega} = \omega - \frac{m}{r}v_\phi - kv_z$.

In our notation before Appendix C, $\phi = \theta$ and m, k are defined with opposite sign. Hence, comparing with our notation we have $k_B = -F$, $B_\phi = \mu r$, $v_\phi = r\Omega$, $v_z = 0$, and $\omega = -i\lambda$. Now, using (C3), we can write

$$\begin{aligned} \frac{\Delta}{rC_2} &= -\frac{\rho\tilde{\omega}^2 - k_B^2}{r(k^2 + \frac{m^2}{r^2})}, \\ \frac{C_2 C_3 - C_1^2}{r\Delta C_2} - \frac{d}{dr}\left(\frac{C_1}{rC_2}\right) &= \frac{1}{r}(\rho\tilde{\omega}^2 - k_B^2) + \frac{d}{dr}(\mu^2 - \rho\Omega^2) - \frac{4(k_B\mu + \rho\tilde{\omega}\Omega)^2}{r(\rho\tilde{\omega}^2 - k_B^2)} \\ &\quad + \frac{4m^2(k_B\mu + \rho\tilde{\omega}\Omega)^2}{r^3(k^2 + \frac{m^2}{r^2})(\rho\tilde{\omega}^2 - k_B^2)} - \frac{d}{dr} \left[\frac{2m(k_B\mu + \rho\tilde{\omega}\Omega)}{k^2 r^2 + m^2} \right]. \end{aligned} \quad (\text{C4})$$

Substituting (C4) into (C2), then dividing both sides of the resulting equation by a constant ρ , and noticing that in our notation $\chi = -ru_r/\tilde{\lambda} = -r\xi_r$, we arrive at the same Hain-Lüst equation (14) that is derived in our paper and in which one needs to set $v = 0$ and $\eta = 0$; see also Ref. [55].

We notice also that the dispersion relation (37) in Ref. [63], which is a sixth-degree polynomial derived in the assumption $c_s = 0$, totally differs from our dispersion relation (16) corresponding to the incompressible limit $c_s \rightarrow \infty$.

-
- [1] E. P. Velikhov, J. Exp. Theor. Phys. (USSR) **36**, 1398 (1959).
 - [2] S. Chandrasekhar, Proc. Natl. Acad. Sci. USA **46**, 253 (1960).
 - [3] A. Balbus and J. F. Hawley, Astrophys. J. **376**, 214 (1991).
 - [4] S. A. Balbus, Nature (London) **470**, 475 (2011).
 - [5] H. Ji and S. Balbus, Phys. Today **66**, 27 (2013).
 - [6] F. Stefani, A. Gailitis, and G. Gerbeth, Z. Angew. Math. Mech. **88**, 930 (2008).
 - [7] F. Ebrahimi *et al.*, Phys. Plasmas **18**, 062904 (2011).
 - [8] G. Rüdiger *et al.*, Phys. Rep. **741**, 1 (2018).
 - [9] F. Stefani *et al.*, Geophys. Astrophys. Fluid Dyn. **113**, 51 (2019).
 - [10] O. N. Kirillov and F. Stefani, Astrophys. J. **712**, 52 (2010).
 - [11] O. N. Kirillov and F. Stefani, Acta Appl. Math. **120**, 177 (2012).
 - [12] O. N. Kirillov, D. E. Pelinovsky, and G. Schneider, Phys. Rev. E **84**, 065301(R) (2011).
 - [13] A. P. Willis and C. F. Barenghi, Astron. Astroph. **388**, 688 (2002).
 - [14] O. N. Kirillov and F. Stefani, Phys. Rev. E **84**, 036304 (2011).
 - [15] K. Deguchi, J. Fluid Mech. **865**, 492 (2019).
 - [16] S. J. Desch, Astrophys. J. **608**, 509 (2004).
 - [17] J. C. B. Papaloizou and C. Terquem, Mon. Not. R. Astron. Soc. **287**, 771 (1997).
 - [18] A. Brandenburg *et al.*, Astrophys. J. **446**, 741 (1995).
 - [19] A. Balbus and J. F. Hawley, Astrophys. J. **400**, 610 (1992).
 - [20] C. Terquem and J. C. B. Papaloizou, Mon. Not. R. Astron. Soc. **279**, 767 (1996).

- [21] S. Friedlander and M. M. Vishik, *Chaos* **5**, 416 (1995).
- [22] G. I. Ogilvie and J. E. Pringle, *Mon. Not. R. Astron. Soc.* **279**, 152 (1996).
- [23] C. Curry and R. E. Pudritz, *Mon. Not. R. Astron. Soc.* **281**, 119 (1996).
- [24] R. Salmeron and M. Wardle, *Mon. Not. R. Astron. Soc.* **345**, 992 (2003).
- [25] G. Rüdiger *et al.*, *Mon. Not. R. Astron. Soc.* **438**, 271 (2014).
- [26] A. Balbus and P. Henri, *Astrophys. J.* **674**, 408 (2008).
- [27] J. Priede, I. Grants, and G. Gerbeth, *Phys. Rev. E* **75**, 047303 (2007).
- [28] J. Priede, *Phys. Rev. E* **84**, 066314 (2011).
- [29] J. Priede, *Phys. Rev. E* **91**, 033014 (2015).
- [30] O. N. Kirillov, F. Stefani, and Y. Fukumoto, *J. Fluid Mech.* **760**, 591 (2014).
- [31] R. Hollerbach and G. Rüdiger, *Phys. Rev. Lett.* **95**, 124501 (2005).
- [32] G. Rüdiger *et al.*, *Phys. Rev. E* **82**, 016319 (2010).
- [33] F. Stefani, T. Gundrum, G. Gerbeth, G. Rüdiger, M. Schultz, J. Szklarski, and R. Hollerbach, *Phys. Rev. Lett.* **97**, 184502 (2006).
- [34] F. Stefani, G. Gerbeth, T. Gundrum, R. Hollerbach, J. Priede, G. Rüdiger, and J. Szklarski, *Phys. Rev. E* **80**, 066303 (2009).
- [35] R. Hollerbach, V. Teeluck, and G. Rüdiger, *Phys. Rev. Lett.* **104**, 044502 (2010).
- [36] M. Seilmayer, V. Galindo, G. Gerbeth, T. Gundrum, F. Stefani, M. Gellert, G. Rüdiger, M. Schultz, and R. Hollerbach, *Phys. Rev. Lett.* **113**, 024505 (2014).
- [37] O. N. Kirillov and F. Stefani, *Phys. Rev. Lett.* **111**, 061103 (2013).
- [38] W. Liu, J. Goodman, I. Herron, and H. Ji, *Phys. Rev. E* **74**, 056302 (2006).
- [39] R. J. Tayler, *Mon. Not. R. Astron. Soc.* **161**, 365 (1973).
- [40] R. J. Tayler, *Mon. Not. R. Astron. Soc.* **191**, 151 (1980).
- [41] G. Rüdiger and M. Schultz, *Astron. Nachr.* **331**, 121 (2010).
- [42] M. Seilmayer, F. Stefani, T. Gundrum, T. Weier, G. Gerbeth, M. Gellert, and G. Rüdiger, *Phys. Rev. Lett.* **108**, 244501 (2012).
- [43] O. N. Kirillov, F. Stefani, and Y. Fukumoto, *Fluid Dyn. Res.* **46**, 031403 (2014).
- [44] A. Child, E. Kersalé, and R. Hollerbach, *Phys. Rev. E* **92**, 033011 (2015).
- [45] O. N. Kirillov, F. Stefani, and Y. Fukumoto, *Astrophys. J.* **756**, 83 (2012).
- [46] J. Squire and A. Bhattacharjee, *Phys. Rev. Lett.* **113**, 025006 (2014).
- [47] F. Stefani and O. N. Kirillov, *Phys. Rev. E* **92**, 051001(R) (2015).
- [48] O. N. Kirillov, *Proc. R. Soc. A* **473**, 20170344 (2017).
- [49] K. Hain and R. Lüst, *Z. Naturforsch.* **13**, 936 (1958).
- [50] S. Hassi, M. Möller, and H. de Snoo, *Math. Nachr.* **291**, 652 (2017).
- [51] E. Frieman and M. Rotenberg, *Rev. Mod. Phys.* **32**, 898 (1960).
- [52] J. P. Goedbloed and S. Poedts, *Principles of Magnetohydrodynamics* (Cambridge University Press. Cambridge, 2004).
- [53] J. P. Goedbloed, R. Keppens, and S. Poedts, *Advanced Magnetohydrodynamics* (Cambridge University Press. Cambridge, 2010).
- [54] J. P. Goedbloed, R. Keppens, and S. Poedts, *Magnetohydrodynamics of Laboratory and Astrophysical Plasmas* (Cambridge University Press. Cambridge, 2019).
- [55] R. Zou and Y. Fukumoto, *Prog. Theor. Exp. Phys.* **2014**, 113J01 (2014).
- [56] G. Rüdiger *et al.*, *Mon. Not. R. Astron. Soc.* **377**, 1481 (2007).
- [57] R. Hollerbach, *Int. J. Num. Methods in Fluids* **32**, 773 (2000).
- [58] K. Deguchi and M. Nagata, *J. Fluid Mech.* **678**, 156 (2011).
- [59] K. Deguchi, *Phys. Rev. E* **95**, 021102(R) (2017).
- [60] V. A. Vladimirov, H. K. Moffatt, and K. I. Il'in, *J. Fluid Mech.* **390**, 127 (1999).
- [61] W. Heinrichs, *Math. Comput.* **53**, 103 (1989).
- [62] A. Guseva *et al.*, *New J. Phys.* **17**, 093018 (2015).
- [63] G. Bodo *et al.*, *Mon. Not. R. Astron. Soc.* **462**, 3031 (2016).

Part II

Radiation-induced instabilities in flow-structure interactions

Chapter 4

Radiative instability of an infinite Nemtsov membrane

“The heart of man is very much like the sea, it has its storms, it has its tides and in its depths it has its pearls too.”

Vincent Van Gogh, *The Letters of Vincent Van Gogh*

Flutter of membranes has been a classical subject for at least seven decades. Membranes submerged in a compressible gas flow and their flutter at supersonic speeds have been considered already in the works of Benjamin, 1963 and Bolotin, 1963. Recent works on the membrane flutter are motivated by such diverse applications as stability of membrane roofs in civil engineering (Sygulski, 2007), flutter of traveling paper webs (Banichuk et al., 2019), aerodynamics of sails, and membrane wings of natural flyers (Newman and Paidoussis, 1991; Tiomkin and Raveh, 2017).

Surface gravity waves on a motionless fluid of finite depth is a classical subject as well, going back to the seminal studies of Russell and Kelvin (Russell, 1844; Thomson, 1887; Carusotto and Rousseaux, 2013). Numerous generalizations are known taking into account, for instance, a uniform or a shear flow and surface tension (Maissa, Rousseaux, and Stepanyants, 2016), flexible bottom or a flexible plate resting on a free surface (Das, Sahoo, and Meylan, 2018). The latter setting has a straightforward motivation in dynamics of sea ice and a less obvious application in analogue gravity experiments (Carusotto and Rousseaux, 2013).

Remarkably, another phenomenon that is being analysed from the analogue gravity perspective is super-radiance (Carusotto and Rousseaux, 2013) and its particular form, discovered by Ginzburg and Frank (Ginzburg and Frank, 1947), known as the anomalous Doppler effect (ADE) (Bekenstein and Schiffer, 1998; Nezlin, 1976). In electrodynamics, the ADE manifests itself when an electrically neutral overall particle, endowed with an internal structure, becomes excited and emits a photon during its uniform but superluminal motion through a medium, even if it started the motion in its ground state; the energy source is the bulk motion of the particle (Bekenstein and Schiffer, 1998).

Anomalous Doppler effect in hydrodynamics was demonstrated for a mechanical oscillator with one degree of freedom, moving parallel to the boundary between two incompressible fluids of different densities (Gaponov-Grekhov, Dolina, and Ostrovskii, 1983). It was shown that the oscillator becomes excited due to radiation of internal gravity waves if it moves sufficiently fast. In Abramovich, Mareev, and Nemtsov, 1986 the ADE for such an oscillator was demonstrated due to radiation of surface gravity waves in a layer of an incompressible fluid.

Nemtsov (Nemtsov, 1985) was the first who considered flutter of an elastic membrane being on the bottom of a uniform horizontal flow of an inviscid and incompressible fluid as an anomalous Doppler effect due to emission of long surface gravity waves. In the shallow water approximation, he investigated both the case of a membrane that spreads infinitely far in both horizontal directions and the case when the chord of the membrane in the direction of the flow is finite whereas the span in the perpendicular direction is infinite. Nevertheless, the case of the flow of arbitrary depth has not been studied in (Nemtsov, 1985), as well as no numerical computation supporting the asymptotical results has been performed. Another issue that has not been addressed in (Nemtsov, 1985) is the relation of stability domains for the membrane of the finite chord-length to that for the membrane of the infinite extension.

Vedeneev (Vedeneev, 2016) studied flutter of an elastic plate of finite and infinite widths on the bottom of a uniform horizontal flow of a compressible gas occupying the upper semi-space. He performed analysis of the relation of stability conditions for the finite plate with that for the infinite plate using the method of global stability analysis by Kulikovskii (Doaré and Langre, 2006; Vedeneev, 2016). However, no connection has been made to the ADE and the concept of negative energy waves.

In the present work (Labarbe and Kirillov, 2020) we reconsider the setting of Nemtsov in order to address the finite height of the fluid layer. We managed in that setting to derive a full dispersion relation for the case of infinite membrane and find the flutter domains in the parameter space. Using perturbation of multiple roots of the dispersion relation, we analyze the character of the instability to determine the wave motion due to flutter of the membrane. We also investigate dependence of the flutter onset on the width of the membrane, and we seek relations with the infinite membrane case by using a numerical model developed in (Vedeneev, 2012) and new expressions for the pressure and the potential of the fluid derived in this work. Finally, we will explain the instabilities via the interaction of positive and negative energy waves by finding explicit formulations of kinetic and potential energy of the flow and relate these results to the anomalous Doppler effect. The membrane of finite-chord length, due to its inherent mathematical complexity, will be presented as a separated article in Chapter 5. Significant connections between this chapter and the following will be highlighted, as some expressions for the infinite membrane appear within the dispersion relation of the membrane with finite extension.

This chapter is presented in the form of an article written by O.N. Kirillov and I, published in the peer-reviewed journal *Journal of Fluid Mechanics* (Labarbe and Kirillov, 2020). My contribution is equally shared with O.N. Kirillov, as we jointly worked on the different sections side-by-side.

Membrane flutter induced by radiation of surface gravity waves on a uniform flow

Joris Labarbe¹ and Oleg N. Kirillov^{1,†}

¹Northumbria University, Newcastle upon Tyne NE1 8ST, UK

(Received 23 April 2020; revised 13 June 2020; accepted 26 June 2020)

We consider the stability of an elastic membrane on the bottom of a uniform horizontal flow of an inviscid and incompressible fluid of finite depth with free surface. The membrane is simply supported at the leading and the trailing edges which attach it to the two parts of the horizontal rigid floor. The membrane has an infinite span in the direction perpendicular to the direction of the flow and a finite length in the direction of the flow. For the membrane of infinite length we derive a full dispersion relation that is valid for arbitrary depth of the fluid layer and find conditions for the flutter of the membrane due to emission of surface gravity waves. We describe this radiation-induced instability by means of the perturbation theory of the roots of the dispersion relation and the concept of negative energy waves and discuss its relation to the anomalous Doppler effect.

Key words: flow–structure interactions

1. Introduction

Flutter of membranes has been a classical subject for at least seven decades. Membranes submerged in a compressible gas flow occupying a space or a semi-space and their flutter at supersonic speeds have been considered already in the works by Miles (1947, 1956), Goland & Luke (1954), Benjamin (1963) and Bolotin (1963).

Bolotin (1963), Spriggs, Messiter & Anderson (1969), Dowell & Ventres (1970) and Kornecki, Dowell & O'Brien (1976) addressed the problem of the so-called membrane flutter paradox regarding the relation of stability criteria for an elastic plate to those for a membrane. Gislason (1971) demonstrated both theoretically and experimentally that a membrane or elastic plate with a finite chord develops not only flutter but also a divergence instability.

Dowell (1966), when critically appraising the study by Miles (1956) of an infinitely long, infinitely wide panel in a compressible flow occupying the upper semi-space, pointed out that the critical wavelength predicted in this study was infinite and the flutter velocity was zero, which was not physically meaningful. This observation has led him to the conclusion that the finite dimension of a membrane or a plate in the flow or a span direction is critical to the physically meaningful prediction of the instability (Dowell 1966). A similar effect

† Email address for correspondence: oleg.kirillov@northumbria.ac.uk

of an elastic foundation was shown both theoretically and experimentally by Dugundji, Dowell & Perkin (1963).

Absolute and convective hydroelastic instabilities of slender elastic structures submerged in a uniform flow were discussed by Triantafyllou (1992). A comprehensive monograph by Dowell (2015) is a standard reference in the field.

Recent works on membrane flutter are motivated by such diverse applications as stability of membrane roofs in civil engineering (Sygulski 2007), flutter of travelling paper webs (Banichuk *et al.* 2010, 2019), aerodynamics of sails and membrane wings of natural flyers (Newman & Paidoussis 1991; Tiomkin & Raveh 2017), as well as the design of piezoaeroelastic systems for energy harvesting (Mavroyiakoumou & Alben 2020).

Surface gravity waves on a motionless fluid of finite depth are a classical subject as well, going back to the seminal studies of Russell and Kelvin (Carusotto & Rousseaux 2013). Numerous generalizations are known taking into account, for instance, a uniform or a shear flow and surface tension (Maissa, Rousseaux & Stepanyants 2016), submerged solids (Smorodin 1972; Arzhannikov & Kotelnikov 2016) and hydrofoils (Faltinsen & Semenov 2008), a flexible bottom (Mohapatra & Sahoo 2011) or a flexible plate resting on a free surface (Greenhill 1886; Schulkes, Hosking & Sneyd 1987; Bochkarev, Lekomtsev & Matveenko 2016; Das, Sahoo & Meylan 2018a,b; Das *et al.* 2018). The latter setting has a straightforward motivation in the dynamics of sea ice and a less obvious application in the analogue gravity experiments (Barcelo, Liberati & Visser 2011; Weinfurtner *et al.* 2011; Carusotto & Rousseaux 2013). Recent work (Robertson & Rousseaux 2018) discusses the effects of viscous dissipation of surface gravity waves to the analogue gravity.

Remarkably, another phenomenon that is analysed from the analogue gravity perspective is super-radiance (Barcelo *et al.* 2011; Carusotto & Rousseaux 2013; Brito, Cardoso & Pani 2015) and its particular form, discovered by Ginzburg & Frank (1947) and Ginzburg (1996), known as the anomalous Doppler effect (ADE) (Nezlin 1976; Nemtsov & Eidman 1987; Bekenstein & Schiffer 1998). In electrodynamics, the ADE manifests itself when an electrically neutral overall particle, endowed with an internal structure, becomes excited and emits a photon during its uniform but superluminal motion through a medium, even if it started the motion in its ground state; the energy source is the bulk motion of the particle (Bekenstein & Schiffer 1998).

The anomalous Doppler effect in hydrodynamics was demonstrated for a mechanical oscillator with one degree of freedom, moving parallel to the border between two incompressible fluids of different densities (Gaponov-Grekhov, Dolina & Ostrovskii 1983). It was shown that the oscillator becomes excited due to radiation of internal gravity waves if it moves sufficiently fast. In Abramovich, Mareev & Nemtsov (1986) the ADE for such an oscillator was demonstrated due to radiation of surface gravity waves in a layer of an incompressible fluid.

Nemtsov (1985) was the first who considered flutter of an elastic membrane resting at the bottom of a uniform horizontal flow of an inviscid and incompressible fluid as an anomalous Doppler effect due to emission of long surface gravity waves. In the shallow water approximation, he investigated both the case of a membrane that spreads infinitely far in both horizontal directions and the case when the length of the membrane in the direction of the flow (or the chord length) is finite whereas the span in the perpendicular direction is infinite. Nevertheless, the case of flow of arbitrary depth has not been studied in Nemtsov (1985), and no numerical computation supporting the asymptotic results has been performed. Another issue that has not been addressed in Nemtsov (1985) is the relation of stability domains for the membrane of finite length to those for the membrane of infinite length.

Vedeneev (2004) studied flutter of an elastic plate of finite and infinite length at the bottom of a uniform horizontal flow of a compressible gas occupying the upper semi-space. He performed an analysis of the relation of the stability conditions for the finite plate to those for the infinite plate using the method of global stability analysis of Kulikovskii (Doaré & de Langre 2006; Vedeneev 2016). A single-mode high-frequency flutter due to a negative aerodynamic damping and a binary flutter have been identified in Vedeneev (2016). However, no connection has been made to the ADE and the concept of negative energy waves.

In the present work we reconsider the setting of Nemtsov in order to address the finite depth of the fluid layer, find flutter domains in the parameter space, analyse them using perturbation of multiple roots of the dispersion relation and investigate the flutter onset for the membrane of infinite chord length. We will explain the radiative instabilities via the interaction of positive and negative energy waves using an explicit expression for the averaged total energy derived rigorously from physical considerations and relate them to the anomalous Doppler effect. We believe that the Nemtsov membrane is as important for understanding the phenomenon of radiation-induced instabilities (Hagerty, Bloch & Weinstein 2003) as the famous Lamb oscillator coupled to a semi-infinite string was for understanding the radiative damping (Lamb 1900; Barbone & Crighton 1994).

2. Model of a membrane interacting with a free surface

2.1. Physical system

In a Cartesian coordinate system $OXYZ$, consider an inextensible elastic rectangular membrane strip of constant thickness h and density ρ_m , of infinite span in the Y -direction, held at $Z = 0$ at the leading edge ($X = 0$) and at the trailing edge ($X = L$) by simple supports, figure 1.

The membrane is initially still and flat, immersed in a layer of inviscid, incompressible fluid of constant density ρ , with free surface at the height $Z = H$. The two-dimensional flow in the layer is supposed to be irrotational and moving steadily with velocity v in the positive X -direction. The bottom of the fluid layer at $Z = 0$ is supposed to be rigid and flat for $X \in (-\infty, 0] \cup [L, +\infty)$.

Nemtsov (1985) assumed that a vacuum exists below the membrane. In the present study we prefer to consider that a motionless incompressible medium of the same density ρ is present below the membrane with a pressure that is the same as the unperturbed pressure of the fluid (Vedeneev 2004, 2016).

Assuming small vertical displacement of the membrane $w(X, t)$, where t is time, a constant tension T along the membrane profile and neglecting viscous forces, we write the dimensional membrane dynamic equation as (Tiomkin & Raveh 2017)

$$\rho_m h \partial_t^2 w = T \partial_X^2 w - \Delta P, \quad X \in [0, L], \quad Z = 0, \quad (2.1)$$

where $\Delta P(X, t)$ is the pressure difference across the interface $Z = 0$. The simply supported boundary conditions for the membrane are

$$w(0) = w(L) = 0 \quad \text{at } Z = 0. \quad (2.2)$$

In general, to recover the pressure $P(X, Z, t)$ of the fluid we write the Euler equation for the vorticity-free flow (Carusotto & Rousseaux 2013; Maissa *et al.* 2016)

$$\partial_t \mathbf{v} + \nabla \left(\frac{\mathbf{v} \cdot \mathbf{v}}{2} + \frac{P}{\rho} + gZ \right) = 0 \quad (2.3)$$

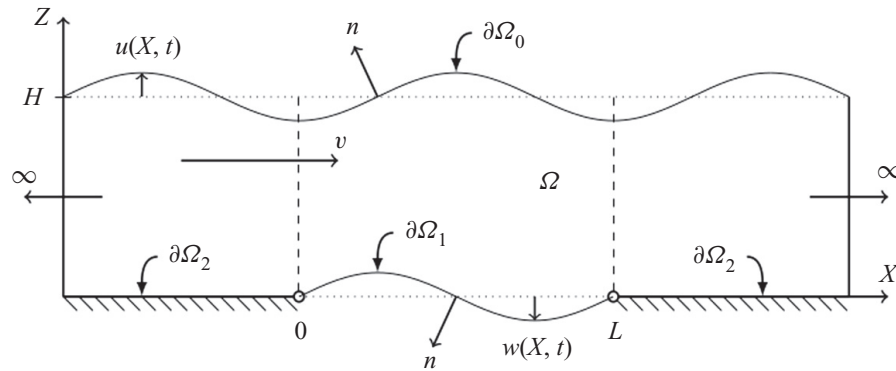


FIGURE 1. An elastic membrane with chord of length L attached to two rigid walls along its leading ($X = 0$) and trailing ($X = L$) edges on the bottom of a fluid layer of depth H moving with the velocity v . Ω is the fluid domain and $\partial\Omega_0$, $\partial\Omega_1$ and $\partial\Omega_2$ are respectively the free surface, membrane and rigid wall boundaries.

with $\mathbf{v} = v\mathbf{e}_X + \nabla\varphi$, where $\varphi(X, Z, t)$ is the potential of the fluid, \mathbf{e}_X is the unit vector in the X -direction and g stands for the gravitational acceleration. This yields the integral of Bernoulli

$$\frac{P}{\rho} + (\partial_t + v\partial_X)\varphi + \frac{1}{2}\nabla\varphi \cdot \nabla\varphi + gZ = \text{const.} \quad (2.4)$$

The incompressibility condition takes the form

$$\nabla^2\varphi = 0. \quad (2.5)$$

From (2.4) it follows that, in the case when a motionless medium of density ρ is present below the membrane with its pressure equal to the unperturbed pressure of the fluid above the membrane, the linear in φ expression for the pressure difference, $\Delta P(X, t)$, is

$$\Delta P(X, t) = -\rho(\partial_t + v\partial_X)\varphi(X, 0, t). \quad (2.6)$$

For the sake of completeness, we present also the analogous expression for the pressure difference for the case when there is a vacuum below the membrane (Nemtsov 1985)

$$\Delta P(X, t) = -\rho(\partial_t + v\partial_X)\varphi(X, 0, t) - \rho gw(X, t). \quad (2.7)$$

Impermeability of the rigid bottom implies the condition

$$\nabla\varphi \cdot \mathbf{n} = 0 \quad \text{at } Z = 0, X \in (-\infty, 0] \cup [L, +\infty). \quad (2.8)$$

The prescription of the normal velocity at the boundaries of moving surfaces allows us to express the kinematic condition for the membrane

$$\nabla\varphi \cdot \mathbf{n} = -(\partial_t + v\partial_X)w \quad \text{at } Z = 0, X \in [0, L], \quad (2.9)$$

and to specify the same condition at the free surface

$$\nabla\varphi \cdot \mathbf{n} = (\partial_t + v\partial_X)u, \quad (2.10)$$

where $u(X, t)$ is the free surface elevation and \mathbf{n} is the vector of the outward normal to a surface. This implies that the projection of the vector $\nabla\varphi$ to the normal will coincide with the positive z -direction for the free surface and have the opposite direction for the membrane, see figure 1.

Using the Bernoulli integral (2.4) at the free surface where $P = 0$ and retaining only linear in φ terms, we find

$$gu = -(\partial_t + v\partial_x)\varphi. \quad (2.11)$$

Taking u from (2.11) and substituting it into (2.10) we obtain the boundary condition at the free surface of the liquid that reads

$$\nabla\varphi \cdot \mathbf{n} = -\frac{1}{g}(\partial_t + v\partial_x)^2\varphi \quad \text{at } Z = H. \quad (2.12)$$

2.2. Dimensionless mathematical model

Let us choose the height of the fluid layer, H , as a length scale, and ω_0^{-1} , where $\omega_0 = \sqrt{g/H}$, as a time scale. Then, we can introduce the dimensionless time and coordinates

$$\tau = t\omega_0, \quad x = \frac{X}{H}, \quad y = \frac{Y}{H}, \quad z = \frac{Z}{H}, \quad (2.13a-d)$$

the dimensionless variables

$$\xi = \frac{w}{H}, \quad \eta = \frac{u}{H}, \quad \phi = \frac{\omega_0}{gH}\varphi, \quad (2.14a-c)$$

the dimensionless parameters of the added mass ratio (Minami 1998) and membrane chord length

$$\alpha = \frac{\rho H}{\rho_m h}, \quad \Gamma = \frac{L}{H}, \quad (2.15a,b)$$

and the two Mach numbers (Vedeneev 2004, 2016)

$$M_w = \frac{c}{\sqrt{gH}}, \quad M = \frac{v}{\sqrt{gH}}, \quad (2.16a,b)$$

where $c^2 = T/(\rho_m h)$ is the squared speed of propagation of elastic waves in the membrane and \sqrt{gH} is the speed of propagation of long surface gravity waves in the shallow water approximation. The added mass ratio α is the ratio of the fluid to solid mass contained in the volume delimited by the dashed lines in figure 1 and in the membrane (Minami 1998). In figure 1, Ω denotes the fluid domain and $\partial\Omega_0$, $\partial\Omega_1$ and $\partial\Omega_2$ stand, respectively, for the free surface, membrane and solid wall borders.

The dimensionless wave equation (2.1) is therefore

$$\partial_\tau^2\xi - M_w^2\partial_x^2\xi = -\alpha\frac{\Delta P}{\rho gH}, \quad x \in [0, \Gamma], \quad z = 0. \quad (2.17)$$

Supplementing it with the expression (2.6), which in the dimensionless time and coordinates has the form

$$\frac{\Delta P}{\rho} = -\left(\omega_0\partial_\tau + \frac{v}{H}\partial_x\right)\varphi, \quad (2.18)$$

we find

$$\begin{aligned} \partial_\tau^2\xi - M_w^2\partial_x^2\xi &= \alpha\left(\partial_\tau + \frac{v}{\omega_0 H}\partial_x\right)\frac{\omega_0}{gH}\varphi \\ &= \alpha(\partial_\tau + M\partial_x)\phi. \end{aligned} \quad (2.19)$$

The dimensionless boundary condition (2.9) is

$$\nabla\phi \cdot \mathbf{n} = -(\partial_\tau + M\partial_x)\xi \quad \text{at } z = 0, \quad x \in [0, \Gamma], \quad (2.20)$$

whereas the boundary condition (2.12) at the free surface in dimensionless form becomes

$$\nabla\phi \cdot \mathbf{n} = -(\partial_\tau + M\partial_x)^2\phi \quad \text{at } z = 1. \quad (2.21)$$

Collecting together (2.19)–(2.21) and the obvious dimensionless versions of (2.5) and (2.8) and assuming a time dependence in the form of $\phi, \xi \sim e^{-i\omega\tau}$ results in the following dimensionless set of equations and the boundary conditions for the case when a motionless medium is present below the membrane:

$$\nabla^2\phi = 0, \quad \text{in } \Omega, \quad (2.22a)$$

$$\nabla\phi \cdot \mathbf{n} = -(-i\omega + M\partial_x)^2\phi, \quad \text{on } \partial\Omega_0, \quad (2.22b)$$

$$\nabla\phi \cdot \mathbf{n} = V(x), \quad \text{on } \partial\Omega_1, \quad (2.22c)$$

$$\nabla\phi \cdot \mathbf{n} = 0, \quad \text{on } \partial\Omega_2, \quad (2.22d)$$

$$[\omega^2 + M_w^2\partial_x^2]\xi = -\alpha(-i\omega + M\partial_x)\phi, \quad \text{on } \partial\Omega_1, \quad (2.22e)$$

$$\xi(0) = \xi(\Gamma) = 0, \quad \text{on } \partial\Omega_1, \quad (2.22f)$$

where $V(x) = (i\omega - M\partial_x)\xi(x)$, $x \in [0, \Gamma]$ is the impermeability condition for the membrane. For simplicity, we retain the same notation for the membrane displacement and the fluid potential after the separation of time.

Therefore, due to the irrotational, incompressible and inviscid character of the fluid, our mathematical model (2.22) consists of the Laplace equation for the fluid potential (2.22a), supplemented by the kinematic conditions for the free surface (2.22b) and the membrane (2.22c). The pressure at the surface of the fluid is also prescribed as a dynamic condition and therefore closes the system of equations for the fluid in this model: the motion of the membrane is described by a non-homogeneous wave equation (2.22e) with the pressure of the fluid (recovered through the Bernoulli principle) as a source term. The membrane is supposed to be simply supported at its extremities as in (2.22f).

3. Methods and results

3.1. Membrane of infinite chord length

Our ultimate goal is to understand the fundamentals of the phenomenon of radiation-induced instabilities in the model (2.22) that we see as a reasonable analytically treatable substitute for the famous Lamb system (Lamb 1900; Barbone & Crighton 1994; Hagerty *et al.* 2003). In this paper, as a first natural step, we analyse the case when the chord of the membrane is infinite, i.e. when the membrane extends from $-\infty$ to $+\infty$ in the x -direction.

The extension of the Nemytsov model to the case where the fluid layer presents a finite depth is our main concern. In the following we will show that even in the limit of infinite chord length the model (2.22) demonstrates physically meaningful radiation-induced flutter that sets in at finite values of the dimensionless flow velocity $M > M_w > 0$, no matter what the values of the wavenumber κ and the added mass ratio α are, in contrast to other known models discussed, e.g. in Miles (1956) and Dowell (1966).

3.1.1. Dispersion relation for the fluid layer of arbitrary depth

Since the motion of the fluid is two-dimensional in the (x, z) -plane and the horizontal extension of the fluid layer is infinite in the x -direction too, we can represent the potential of the fluid ϕ in the physical space by means of the inverse Fourier transform of the potential $\hat{\phi}$ in the wavenumber space as

$$\phi(x, z, \omega) = \frac{1}{2\pi} \int_{-\infty}^{+\infty} \hat{\phi}(\kappa, z, \omega) e^{ikx} d\kappa, \quad (3.1)$$

where κ is the wavenumber and

$$\hat{\phi}(\kappa, z, \omega) = \int_{-\infty}^{+\infty} \phi(x, z, \omega) e^{-ikx} dx, \quad (3.2)$$

under the standard assumption that both $\phi(x)$ and $\hat{\phi}(\kappa)$ are absolutely integrable functions, implying they vanish at infinity.

Assuming that $\partial_x \phi$ is also absolutely integrable, which allows us to use twice the property $\widehat{\partial_x \phi} = ik\hat{\phi}$, we find the Fourier transform of the Laplace equation (2.22a)

$$\partial_z^2 \hat{\phi} - \kappa^2 \hat{\phi} = 0. \quad (3.3)$$

The general solution to (3.3) is

$$\hat{\phi}(\kappa, z, \omega) = A(\kappa, \omega) e^{\kappa z} + B(\kappa, \omega) e^{-\kappa z}, \quad (3.4)$$

where $A(\kappa, \omega)$ and $B(\kappa, \omega)$ are yet to be determined from the Fourier-transformed boundary conditions.

The boundary condition (2.22c), expressing the impermeability of the membrane at $z = 0$, takes the form

$$-\partial_z \phi = V, \quad (3.5)$$

because the outward direction of the normal vector \mathbf{n} to the surface of the membrane is opposite to the positive z -direction, see figure 1. The Fourier transform of (3.5) reads

$$\partial_z \hat{\phi} = -\hat{V}(\kappa, \omega), \quad (3.6)$$

where

$$\begin{aligned} \hat{V}(\kappa, \omega) &= \int_{-\infty}^{+\infty} (i\omega\xi(s) - M\partial_s \xi(s)) e^{-ik s} ds \\ &= i(\omega - \kappa M) \hat{\xi}. \end{aligned} \quad (3.7)$$

Substituting (3.4) into (3.6) yields at $z = 0$

$$\kappa(A - B) = -i(\omega - \kappa M) \hat{\xi}. \quad (3.8)$$

Similarly transforming the boundary condition (2.22b) at the free surface we find

$$\partial_z \hat{\phi} = (\omega - \kappa M)^2 \hat{\phi}. \quad (3.9)$$

Substituting (3.4) into (3.9) yields at $z = 1$

$$\kappa(Ae^\kappa - Be^{-\kappa}) = (\omega - \kappa M)^2(Ae^\kappa + Be^{-\kappa}). \quad (3.10)$$

Solving (3.8) and (3.10) simultaneously with respect to A and B , we obtain

$$\left. \begin{aligned} A(\kappa, \omega) &= \frac{-i\hat{\xi}[(\omega - \kappa M)^2 + \kappa](\omega - \kappa M)}{\kappa[(\omega - \kappa M)^2 - \kappa]e^{2\kappa} + \kappa[(\omega - \kappa M)^2 + \kappa]}, \\ B(\kappa, \omega) &= \frac{i\hat{\xi}[(\omega - \kappa M)^2 - \kappa](\omega - \kappa M)}{\kappa[(\omega - \kappa M)^2 - \kappa] + \kappa[(\omega - \kappa M)^2 + \kappa]e^{-2\kappa}}. \end{aligned} \right\} \quad (3.11)$$

The Fourier transform of the non-homogeneous wave equation (2.22e) for the membrane displacement evaluated at $z = 0$ reads

$$(\omega^2 - \kappa^2 M_w^2)\hat{\xi} - i\alpha(\omega - \kappa M)\hat{\phi}(\kappa, 0, \omega) = 0. \quad (3.12)$$

Inserting expression (3.4) for $\hat{\phi}$ with the coefficients (3.11) into (3.12), discarding $\hat{\xi}$ in the result and introducing new parameters, namely the phase velocity

$$\sigma = \frac{\omega}{\kappa}, \quad (3.13)$$

and the coupling parameter

$$\beta = \frac{\alpha}{\kappa^2}, \quad (3.14)$$

we obtain the following dispersion equation in the case where a medium with constant pressure is present below the membrane

$$\beta = \frac{(M_w^2 - \sigma^2)[\kappa(\sigma - M)^2 - \tanh \kappa]}{\kappa(\sigma - M)^2[\kappa(\sigma - M)^2 \tanh \kappa - 1]}. \quad (3.15)$$

It is instructive to show another way of deriving the dispersion equation (3.15). For this, we notice that (3.6) and (3.7) allow us to express $\hat{\xi}$ by means of $\partial_z \hat{\phi}$. Using the result in (3.12), we can obtain a boundary condition for $\hat{\phi}(z)$ at $z = 0$. This new boundary condition together with boundary condition (3.9) and equation (3.3) produce a closed-form boundary value problem for the Laplace equation with the Robin boundary conditions

$$\left. \begin{aligned} \partial_z^2 \hat{\phi} - \kappa^2 \hat{\phi} &= 0, \\ \partial_z \hat{\phi}(\omega^2 - \kappa^2 M_w^2) - \alpha(\omega - \kappa M)^2 \hat{\phi} &= 0, \quad z = 0, \\ \partial_z \hat{\phi} - (\omega - \kappa M)^2 \hat{\phi} &= 0, \quad z = 1. \end{aligned} \right\} \quad (3.16)$$

Substituting the general solution (3.4) into the boundary conditions of the problem (3.16) results in the system of two linear equations with respect to A and B ,

$$\left. \begin{aligned} \kappa(A - B)(\omega^2 - \kappa^2 M_w^2) - \alpha(\omega - \kappa M)^2(A + B) &= 0, \\ \kappa(Ae^\kappa - Be^{-\kappa}) - (\omega - \kappa M)^2(Ae^\kappa + Be^{-\kappa}) &= 0. \end{aligned} \right\} \quad (3.17)$$

This system can be written in matrix form as

$$(\omega^2 M_1 + \omega M_2 + M_3) \mathbf{f} = 0, \quad \mathbf{f} := \begin{pmatrix} A \\ B \end{pmatrix}, \quad (3.18)$$

where the 2×2 matrices involved are

$$\left. \begin{aligned} M_1 &= -\begin{pmatrix} \alpha - \kappa & \alpha + \kappa \\ e^\kappa & e^{-\kappa} \end{pmatrix}, \\ M_2 &= 2\kappa M \begin{pmatrix} \alpha & \alpha \\ e^\kappa & e^{-\kappa} \end{pmatrix}, \\ M_3 &= -\begin{pmatrix} \kappa^2(M^2\alpha + M_w^2\kappa) & \kappa^2(M^2\alpha - M_w^2\kappa) \\ \kappa e^\kappa(M^2\kappa - 1) & \kappa e^{-\kappa}(M^2\kappa + 1) \end{pmatrix}. \end{aligned} \right\} \quad (3.19)$$

Computing the determinant of the matrix polynomial we arrive at the dispersion equation

$$\begin{aligned} D(\omega, \kappa) &= \det(\omega^2 M_1 + \omega M_2 + M_3) \\ &= -\alpha(M\kappa - \omega)^2[(M\kappa - \omega)^2 \tanh \kappa - \kappa] + \kappa(M_w^2\kappa^2 - \omega^2)[(M\kappa - \omega)^2 - \kappa \tanh \kappa] \\ &= 0, \end{aligned} \quad (3.20)$$

which, with the notation $\sigma = \omega/\kappa$ and $\beta = \alpha/\kappa^2$, transforms exactly to (3.15).

For the sake of completeness we present also the dispersion relation for the system with a vacuum below the membrane

$$\beta = \frac{(M_w^2 - \sigma^2) [\kappa(\sigma - M)^2 - \tanh \kappa]}{[\kappa^2(\sigma - M)^4 - 1] \tanh \kappa}. \quad (3.21)$$

In the shallow water approximation corresponding to the limit $\kappa \rightarrow 0$, the expression (3.21) reduces to

$$\beta = (\sigma^2 - M_w^2) ((\sigma - M)^2 - 1), \quad (3.22)$$

which is nothing else but the shallow water dispersion relation derived by Nemtsov (1985).

In order to get the dispersion relation (3.21), one must take the pressure difference (2.7), make it non-dimensional and use in the expression (2.17) which then reads as

$$\partial_\tau^2 \xi - M_w^2 \partial_x^2 \xi - \alpha \xi = \alpha(\partial_\tau + M \partial_x) \phi. \quad (3.23)$$

After separation of time it reduces to the analogue of boundary condition (2.22e),

$$[-\omega^2 - M_w^2 \partial_x^2 - \alpha] \xi - \alpha(-i\omega + M \partial_x) \phi(x, 0, t) = 0, \quad (3.24)$$

which has the following Fourier transform

$$[\omega^2 - \kappa^2 M_w^2 + \alpha] \hat{\xi} - i\alpha(\omega - \kappa M) \hat{\phi}(\kappa, 0, \omega) = 0. \quad (3.25)$$

Inserting the expression (3.4) for $\hat{\phi}$ with the coefficients (3.11) into (3.25) results, after familiar algebraic manipulations, in the dispersion relation (3.21).

3.1.2. Analysis of the dispersion equation

In the absence of coupling between the free surface and the membrane, i.e. for $\beta = 0$, both the dispersion relation (3.15) and the dispersion relation (3.21) reduce to

$$(\sigma^2 - M_w^2)[\kappa(\sigma - M)^2 - \tanh \kappa] = 0, \quad (3.26)$$

which yields the dispersion relation of the elastic waves in the free membrane $\sigma^2 = M_w^2$ and that of the surface gravity waves on a uniform flow: $\kappa(\sigma - M)^2 = \tanh \kappa$. The latter

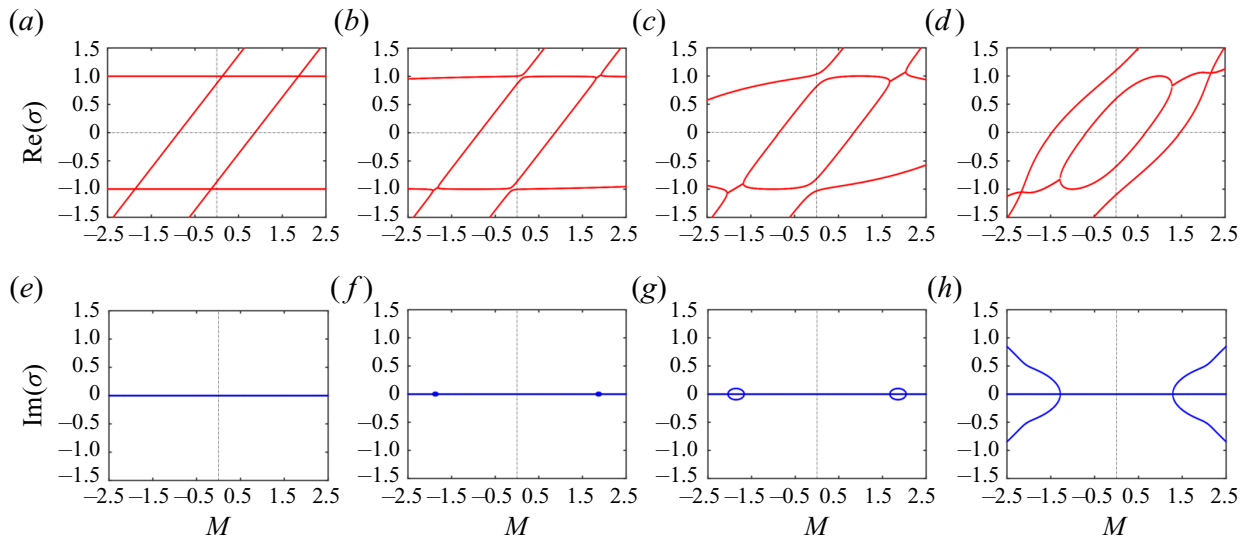


FIGURE 2. Real (red, *a–d*) and imaginary (blue, *e–h*) parts of the roots of the dispersion relation (3.15) over the Mach number M for $M_w = 1$, $\kappa = 1$ and (*a,e*) $\beta = 0$, (*b,f*) $\beta = 0.01$, (*c,g*) $\beta = 0.1$ and (*d,h*) $\beta = 1$.

acquires a more familiar traditional form (Maissa *et al.* 2016)

$$(\omega - \kappa Fr)^2 = \kappa \tanh \kappa \quad (3.27)$$

after taking into account that $\sigma = \omega/\kappa$ and that M , as defined in (2.16*a,b*), can also be interpreted as the Froude number, Fr .

The roots of the decoupled dispersion equation (3.26) are real

$$\sigma_1^\pm = \pm M_w, \quad \sigma_2^\pm = M \pm \sqrt{\frac{\tanh \kappa}{\kappa}}. \quad (3.28a,b)$$

If we consider the roots (3.28*a,b*) as functions of the fluid Mach number, M , we find that σ_1^\pm are two horizontal straight lines and σ_2^\pm are two straight lines with the slope equal to 1, see figure 2(*a*). One can see that at $\beta = 0$ the root branches intersect at four points forming the double roots $\sigma_0 = M_w$ at

$$M_0^\pm = M_w \pm \sqrt{\frac{\tanh \kappa}{\kappa}} \quad (3.29)$$

and the double roots $-\sigma_0$ at $-M_0^\pm$. The relation $M_w = M_0^+ - \sqrt{(\tanh \kappa)/\kappa} = \sigma_2^- = \sigma_1^+ = \sigma_0$ following from (3.29) and (3.28*a,b*) is the condition of ‘phase synchronism’ for the case of an arbitrary height of the fluid layer that extends the corresponding result obtained in Nemytsov (1985) in the shallow water limit, $\kappa \rightarrow 0$.

With the increase in β the roots $\pm\sigma_0$ situated at $M = \pm M_0^-$ split into simple real ones and this split is accompanied by unfolding of the crossings into avoided crossings, figure 2.

Quite in contrast, the roots $\pm\sigma_0$ situated at $M = \pm M_0^+$ split into complex-conjugate pairs that form bubbles of instability at moderate values of β that open up with the increase in β to develop disconnected complex branches, as is seen in figure 2(*d,h*).

Let us re-write the dispersion relation (3.15) as follows

$$\begin{aligned} D(\sigma, M, \beta) := & \beta \kappa (\sigma - M)^2 [\kappa (\sigma - M)^2 \tanh \kappa - 1] \\ & - (M_w^2 - \sigma^2) [\kappa (\sigma - M)^2 - \tanh \kappa] = 0. \end{aligned} \quad (3.30)$$

Then, we can apply to it the perturbation theory derived in [appendix A](#).

Consider the double root σ_0 at $M = M_0^+$ and $\beta = \beta_0 = 0$. Adapt the approximate equation ([A 18](#)) to our model

$$\begin{aligned} \Delta\sigma (\partial_{\sigma M}^2 D \Delta M + \partial_{\sigma \beta}^2 D \Delta \beta) + \frac{1}{2} [\partial_M^2 D (\Delta M)^2 + 2\partial_{M\beta}^2 D \Delta M \Delta \beta + \partial_\beta^2 D (\Delta \beta)^2] \\ + \frac{1}{2} \partial_\sigma^2 D (\Delta \sigma)^2 + \partial_M D \Delta M + \partial_\beta D \Delta \beta = 0, \end{aligned} \quad (3.31)$$

where $\Delta\sigma = \sigma - \sigma_0$, $\Delta M = M - M_0^+$ and $\Delta\beta = \beta$. Calculating the partial derivatives at $\sigma = \sigma_0$, $M = M_0^+$, and $\beta = \beta_0 = 0$, we find

$$\left. \begin{aligned} \partial_\sigma^2 D &= -8M_w \kappa \sqrt{\frac{\tanh \kappa}{\kappa}}, & \partial_{\sigma M}^2 D &= 4M_w \kappa \sqrt{\frac{\tanh \kappa}{\kappa}}, \\ \partial_M^2 D &= 0, & \partial_{M\beta}^2 D &= -\partial_\beta^2 D = 2\kappa (2(\tanh \kappa)^2 - 1) \sqrt{\frac{\tanh \kappa}{\kappa}}, & \partial_\beta^2 D &= 0, \\ \partial_M D &= 0, & \partial_\beta D &= (\tanh \kappa)^3 - \tanh \kappa. \end{aligned} \right\} \quad (3.32)$$

With the derivatives (3.32) the approximation (3.31) to the dispersion equation (3.30) near the crossing takes the form

$$(\sigma - M_w) \left[\sigma - M + \sqrt{\frac{\tanh \kappa}{\kappa}} \right] = \beta \sqrt{\frac{\tanh \kappa}{\kappa}} \frac{(\tanh \kappa)^2 - 1}{4M_w}. \quad (3.33)$$

For any $\beta > 0$ the crossing of the real roots σ at $M = M_0^+$ unfolds into two hyperbolic branches of the real roots

$$\begin{aligned} \beta \sqrt{\frac{\tanh \kappa}{\kappa}} \frac{[1 - (\tanh \kappa)^2]}{4M_w} &= \frac{1}{4} \left(M - M_w - \sqrt{\frac{\tanh \kappa}{\kappa}} \right)^2 \\ &- \left(\operatorname{Re} \sigma - \frac{M_w + M}{2} + \frac{1}{2} \sqrt{\frac{\tanh \kappa}{\kappa}} \right)^2, \quad \operatorname{Im} \sigma = 0, \end{aligned} \quad (3.34a,b)$$

that are connected to the ‘bubble’ of complex eigenvalues with the real parts $\operatorname{Re} \sigma = \frac{1}{2}(M + M_w - \sqrt{(\tanh \kappa)/\kappa})$ and with the imaginary parts that form an ellipse in the $(M, \operatorname{Im} \sigma)$ -plane

$$(\operatorname{Im} \sigma)^2 + \frac{1}{4} \left(M - M_w - \sqrt{\frac{\tanh \kappa}{\kappa}} \right)^2 = \beta \sqrt{\frac{\tanh \kappa}{\kappa}} \frac{[1 - (\tanh \kappa)^2]}{4M_w}, \quad (3.35)$$

see [figure 3](#). Equating to zero the discriminant of the quadratic in σ in equation (3.33), we arrive at the following quadratic approximation to the neutral stability curve at the crossing

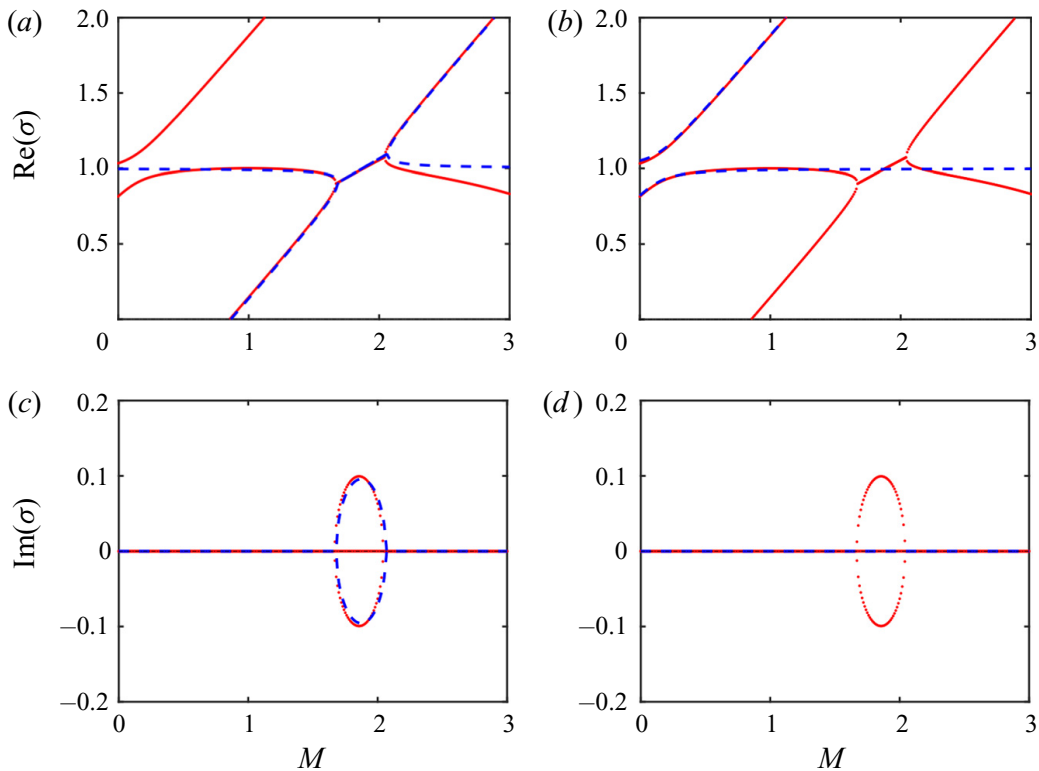


FIGURE 3. Real and imaginary parts of the roots of the dispersion relation for $M_w = 1$, $\kappa = 1$ and $\beta = 0.1$: (red) (3.15) and (blue, dashed) their approximations by (3.33) and (3.37) near the crossing points that exist at $\beta = 0$, $M = M_0^\pm$, $\sigma = \sigma_0$. Notice an avoided crossing above the line $\text{Re}(\sigma) = M$ and the bubble of instability below this line.

point $M = M_0^+$

$$\beta = M_w \frac{(M - M_w - \sqrt{(\tanh \kappa)/\kappa})^2}{(1 - (\tanh \kappa)^2)\sqrt{(\tanh \kappa)/\kappa}}. \quad (3.36)$$

The bubble of instability (3.35) corresponds to the inner points of the instability domain bounded by (3.36).

Using the same methodology to approximate the avoided crossing close to $M = M_0^-$, $\sigma = \sigma_0$ and $\beta = \beta_0$ by (3.31), we obtain

$$(\sigma - M_w) \left[\sigma - M - \sqrt{\frac{\tanh \kappa}{\kappa}} \right] = -\beta \sqrt{\frac{\tanh \kappa}{\kappa}} \frac{(\tanh \kappa)^2 - 1}{4M_w}. \quad (3.37)$$

Separating real and imaginary parts of σ in (3.37) similarly to how it has been done in the previous case, one can see that the bubble of instability does not originate for $\beta > 0$ in the unfolding of the crossing at $M = M_0^-$, see figure 3.

In figure 4 we show that the exact neutral stability boundaries obtained from equating the discriminant of the fourth-order polynomial (3.30) in σ to zero and their approximation (3.36) calculated at the crossing point at $M = M_0^+$ are in a very good agreement.

It is instructive to change the point of view and to look at the critical values of parameters as functions of the Mach number M_w of elastic waves in the membrane. In figure 5 we present stability maps of the dispersion equation (3.30) given by its discriminant in the (M_w, β) -plane for the fixed value of $M = M_0 = 2$ and increasing values of κ . We see that for all κ the instability is possible only in the interval $|M_w| < M_0 = 2$, which agrees

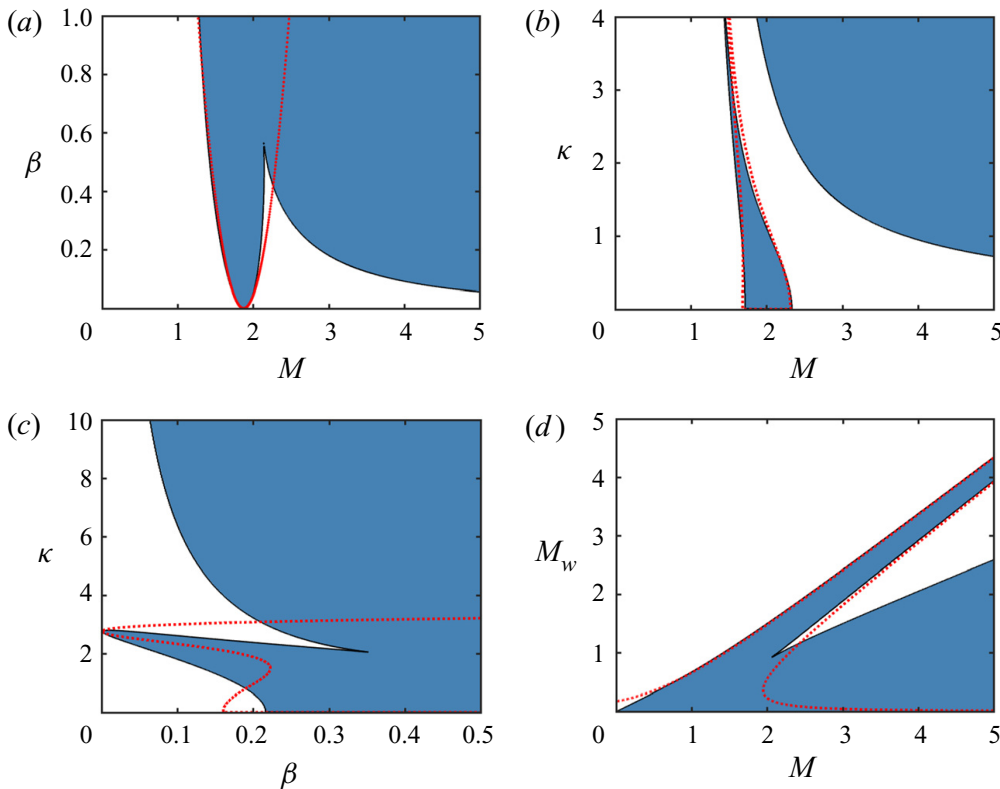


FIGURE 4. Stability maps of the dispersion equation (3.30) given by its discriminant for (a) $M_w = 1$ and $\kappa = 1$, (b) $M_w = 1$ and $\beta = 0.1$, (c) $M_w = 1$ and $M = 1.6$ and (d) $\beta = 0.5$ and $\kappa = 1$. The regions of real phase speed σ are shown in white (stability) and those of the complex σ (temporal instability) in blue. The red dotted curve is the approximation (3.36). Notice the absence of instabilities for $M_w > M$ in panel (d).

with figure 4. For $\beta = 0$, the instability domain touches the M_w -axis at the points $M_w = M_0 - \sqrt{(\tanh \kappa)/\kappa}$ and $M_w = -M_0 + \sqrt{(\tanh \kappa)/\kappa}$. In the limit $\kappa \rightarrow 0$, the touching occurs at $M_w = M_0 - 1 = 1$ and $M_w = -M_0 + 1 = -1$.

A qualitative change happens when $\kappa \geq \kappa_0$ where $\kappa_0 > 0$ is uniquely determined by $M_0 > 0$ from the equation

$$\kappa_0 \tanh \kappa_0 = \frac{1}{M_0^2}. \quad (3.38)$$

For instance, $M_0 = 2$ yields $\kappa_0 \approx 0.5218134478$. At $\kappa = \kappa_0$ a new, isolated, domain of instability originates that touches the M_w -axis at $\beta = 0$ and grows when κ is further increased, figure 5. At some value of κ the two domains touch each other and then form a unified domain. At $\kappa \rightarrow \infty$ the central part of the unified domain dominates over its side parts corresponding to the instability found by Nemtsov in the shallow water approximation when $\kappa \rightarrow 0$ and the coupling β is weak, figure 5.

To understand the origin of the new instability, we plot the real and imaginary values of σ as functions of M_w in figure 6 for a given $M = M_0 = 2$. The central panel of figure 6 corresponding to $\beta = 0$ and $\kappa = \kappa_0$ shows four straight lines intersecting at five points, including the origin. The upper horizontal line corresponds to the fast surface gravity wave with $\sigma = M_0 + \sqrt{(\tanh \kappa_0)/\kappa_0} \approx 3$, whereas the lower horizontal line to the slow surface gravity wave (Nemtsov 1985) with $\sigma = M_0 - \sqrt{(\tanh \kappa_0)/\kappa_0} \approx 1$. The two inclined lines correspond to the forward and backward elastic waves in the membrane with $\sigma = \pm M_w$. When β and κ depart respectively from zero and κ_0 , all the five crossings unfold either into

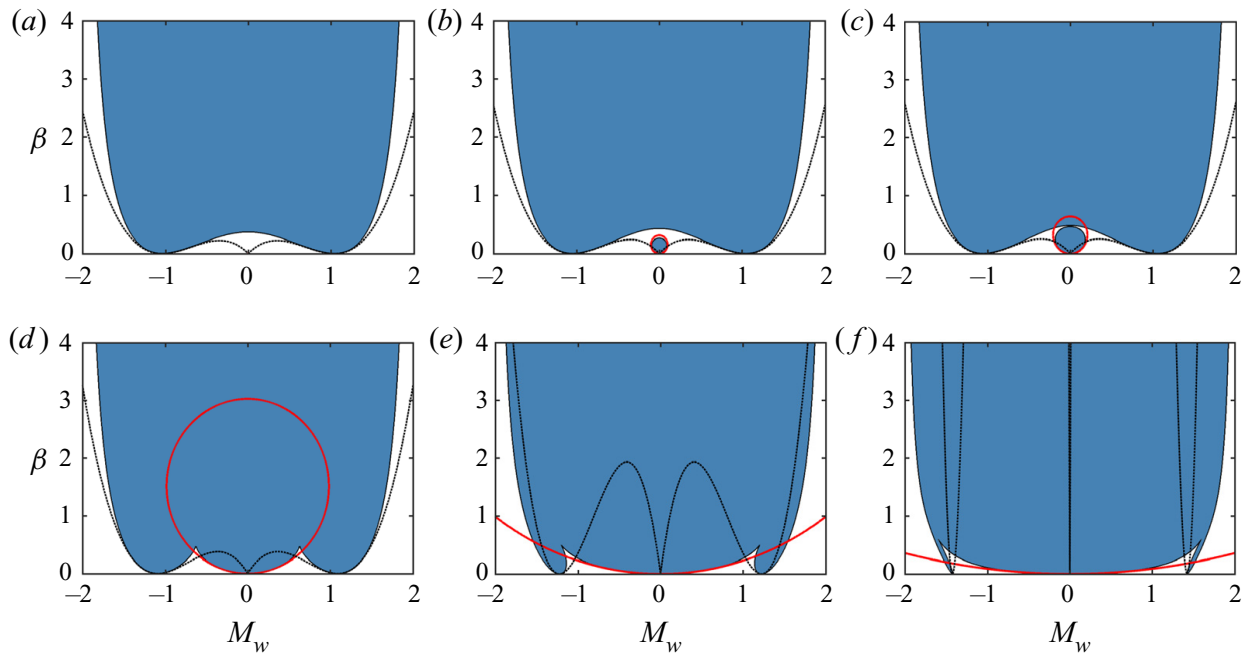


FIGURE 5. Stability maps of the dispersion equation (3.30) given by its discriminant for $M = M_0 = 2$ and: (a) $\kappa = 0.5$, (b) $\kappa = 0.55$, (c) $\kappa = 0.58$, (d) $\kappa = 0.8$, (e) $\kappa = 1.5$, (f) $\kappa = 3$. The regions of real phase speed σ are shown in white (stability) and those of the complex σ (temporal instability) in blue. The black dotted curve is the approximation (3.36) and the solid red ellipse is the conical approximation (3.43). When $\kappa \rightarrow \infty$, the central part of the instability domain approximated by (3.43) dominates over the side parts of the domain. Notice the absence of instabilities for $M_w > M_0$.

avoided crossings (as elastic and fast surface gravity waves) or into bubbles of instability (as elastic and slow surface gravity waves) resulting in the high-frequency flutter due to radiation of long surface gravity waves. For $\beta > 0$ the crossing at the origin transforms into an avoided crossing at $\kappa < \kappa_0$ or into the bubble of instability at $\kappa > \kappa_0$, which yields low-frequency flutter at short wavelengths κ .

Figure 7(a) allows us to track the evolution of the flutter domains as κ varies from zero to infinity at $M_0 = 2$ and $\beta = 0.03$. Nemtsov's radiation-induced flutter domain is the widest in the shallow water limit and evolves along the curves (shown as black solid lines in figure 7b)

$$(M_0 \pm M_w)^2 = \frac{\tanh \kappa}{\kappa}, \quad (3.39)$$

to which the Nemtsov domains degenerate at $\beta = 0$. Note that the Nemtsov flutter domain is perfectly approximated by formula (3.36) obtained from the unfolding of the eigenvalue crossing corresponding to the slow surface gravity wave and the elastic wave (dotted lines in figure 7a).

To understand the central instability domain shown in figure 7(a) for a given β we plot it in the (M_w, κ, β) -space in figure 7(b), given $M = M_0$. One can see that the domain is symmetric with respect to the plane $M_w = 0$ and has a pronounced conical singularity at $\kappa = \kappa_0$ determined by (3.38) when $\beta = 0$ and $M_w = 0$. Equation (3.38) follows from the discriminant of the dispersion equation (3.30) at $\beta = 0$ and $M_w = 0$. The conical singularity of the stability boundary therefore exactly corresponds to the crossing of the eigenvalue curves at the origin in figure 6(b). Usually, the conical singularity of the stability boundary is associated with a double semi-simple eigenvalue with two linearly

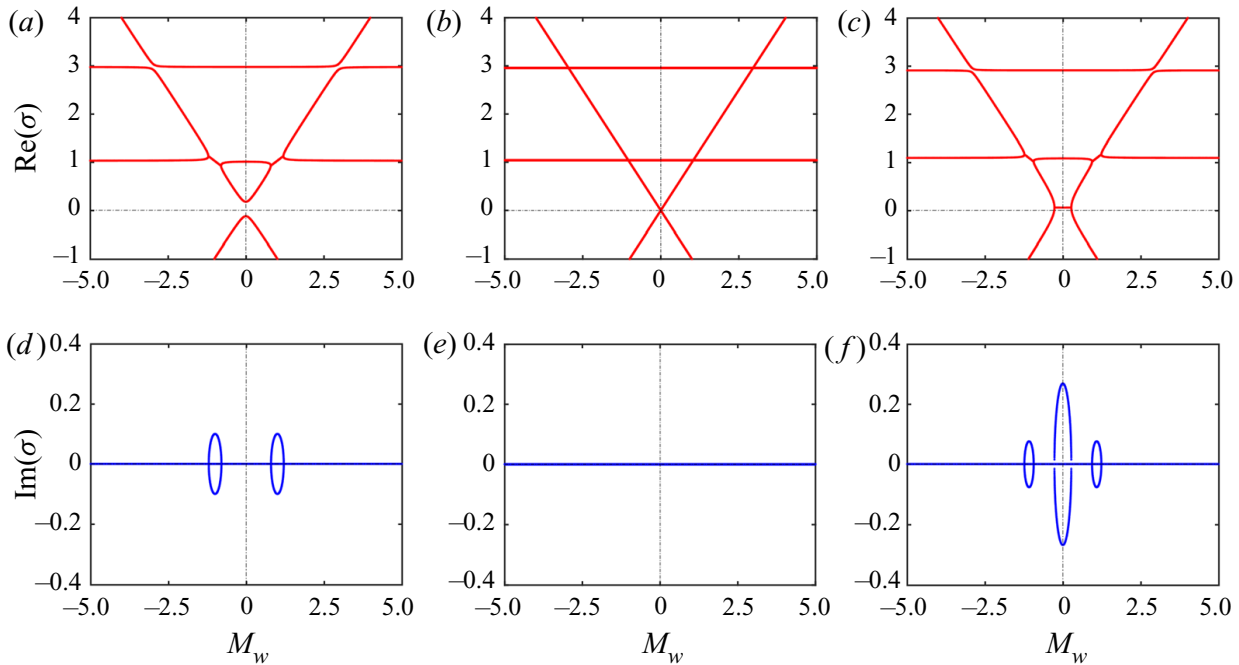


FIGURE 6. Real (upper panels) and imaginary (lower panels) parts of the roots of the dispersion equation (3.30) for $M = M_0 = 2$ and: (a,d) $\beta = 0.05$ and $\kappa = \kappa_0 - 0.1$, (b,e) $\beta = 0$ and $\kappa = \kappa_0 \approx 0.5218134478$, (c,f) $\beta = 0.05$ and $\kappa = \kappa_0 + 0.3$. Notice that the bubbles of instability develop only for $\text{Re}(\sigma) < M_0 = 2$.

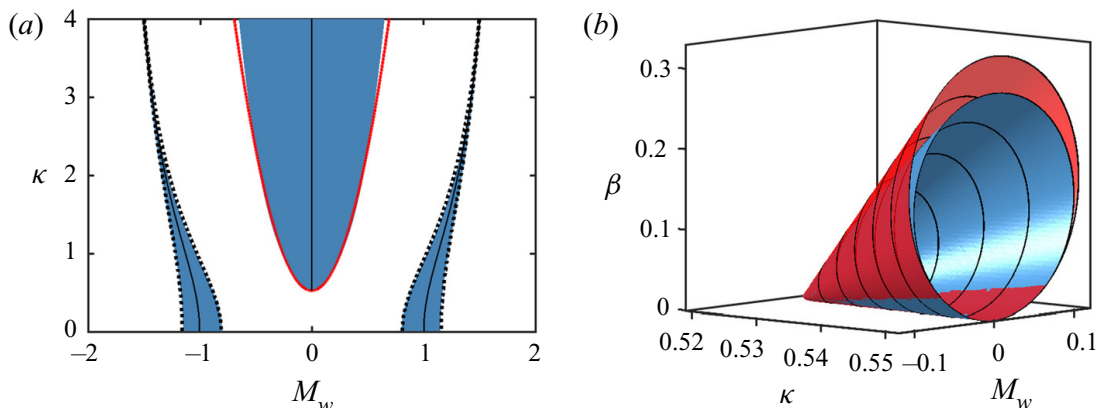


FIGURE 7. (a) Stability map of the dispersion equation (3.30) given by its discriminant for $M = M_0 = 2$ and $\beta = 0.03$. The regions of real phase speed σ are shown in white (stability) and those of the complex σ (temporal instability) in blue. The black dotted curves correspond to the approximation (3.36) and the solid red line is the conical approximation (3.43). When $\beta = 0$, the blue instability domains degenerate (central) to the ray $\kappa \geq \kappa_0 \approx 0.5218134478$ and (sides) to the curves (3.39) shown as solid black lines. (b) Stability boundary with the conical singularity at $\kappa = \kappa_0$, $\beta = 0$ and $M_w = 0$, according to (blue, internal surface) the discriminant of the dispersion equation (3.30) and (red, external surface) to the approximation of the cone (3.43).

independent eigenvectors (Kirillov & Seyranian 2004; Guenther & Kirillov 2006; Kirillov 2009, 2010, 2013; Kirillov, Guenther & Stefani 2009).

For this reason, we apply the perturbation theory of double eigenvalues presented in appendix A to the double zero eigenvalue $\sigma = \sigma_0 = 0$ at the crossing shown in figure 6(b) and corresponding to the values of parameters $\beta = \beta_0 = 0$, $\kappa = \kappa_0$, $M = M_0$,

$M_w = M_{w,0} = 0$. A natural extension of the approximation formula (A 18) to the case of four parameters β , κ , M_w and M yields

$$\begin{aligned} & (\Delta\sigma)^2 \frac{1}{2} \partial_\sigma^2 D + \Delta\sigma (\partial_{\sigma\beta}^2 D \Delta\beta + \partial_{\sigma\kappa}^2 D \Delta\kappa + \partial_{\sigma M}^2 D \Delta M + \partial_{\sigma M_w}^2 D \Delta M_w) + \partial_{\beta\kappa}^2 D \Delta\beta \Delta\kappa \\ & + \frac{1}{2} [\partial_\beta^2 D (\Delta\beta)^2 + \partial_\kappa^2 D (\Delta\kappa)^2 + \partial_M^2 D (\Delta M)^2 + \partial_{M_w}^2 D (\Delta M_w)^2] + \partial_{M\kappa}^2 D \Delta M \Delta\kappa \\ & + \partial_{M_w\kappa}^2 D \Delta M_w \Delta\kappa + \partial_{\beta M}^2 D \Delta\beta \Delta M + \partial_{\beta M_w}^2 D \Delta\beta \Delta M_w + \partial_{\beta M}^2 D \Delta M_w \Delta M \\ & + \partial_\beta D \Delta\beta + \partial_\kappa D \Delta\kappa + \partial_M D \Delta M + \partial_{M_w} D \Delta M_w = 0. \end{aligned} \quad (3.40)$$

Computing the corresponding partial derivatives of the left part of the dispersion equation (3.30), and evaluating them at $\beta = \beta_0 = 0$, $\kappa = \kappa_0$, $M = M_0$, $M_w = M_{w,0} = 0$, where M_0 and κ_0 are related by (3.38), we find that the only non-zero derivatives are

$$\left. \begin{aligned} \partial_\sigma^2 D &= -\partial_{M_w}^2 D = 2\kappa_0 M_0^2 - \frac{2}{\kappa_0 M_0^2}, & \partial_{M\beta}^2 D &= -\partial_{\sigma\beta}^2 D = 2\kappa_0 M_0, \\ \partial_{\kappa\beta}^2 D &= M_0^4 \kappa_0^2 + M_0^2 - 1. \end{aligned} \right\} \quad (3.41)$$

Taking this into account in (3.40), we find a simple approximation describing the unfolding of the double zero eigenvalue

$$\begin{aligned} & (M_0^4 \kappa_0^2 - 1)(\sigma^2 - M_w^2) - 2\kappa_0^2 M_0^3 \sigma \beta + \kappa_0 M_0^2 (M_0^4 \kappa_0^2 + M_0^2 - 1)(\kappa - \kappa_0) \beta \\ & + 2\kappa_0^2 M_0^3 (M - M_0) \beta = 0. \end{aligned} \quad (3.42)$$

Let us further assume that $M = M_0$ is fixed. Then the last term in (3.42) vanishes, and the discriminant of the resulting quadratic polynomial in σ produces the equation of a cone with the apex at $\kappa = \kappa_0$, $M_w = 0$ and $\beta = 0$

$$M_0^6 \kappa_0^4 \beta^2 - M_0^2 \kappa_0 (M_0^4 \kappa_0^2 + M_0^2 - 1) (M_0^4 \kappa_0^2 - 1) (\kappa - \kappa_0) \beta + M_w^2 (M_0^4 \kappa_0^2 - 1)^2 = 0. \quad (3.43)$$

The cone (3.43) is shown in red in figure 7(b). With $\beta = 0.03$, $M_0 = 2$ and κ_0 computed by means of (3.38), the approximation (3.43) fits the boundary of the exact instability domain with remarkable precision, as is evident in figure 7(a).

It is easy to see that in the plane $M_w = 0$ the cone (3.43) defines the two lines

$$\beta = \frac{(M_0^4 \kappa_0^2 - 1)(M_0^4 \kappa_0^2 + M_0^2 - 1)}{M_0^4 \kappa_0^3} (\kappa - \kappa_0), \quad \beta = 0, \quad (3.44)$$

that approximate the instability domain near $\kappa = \kappa_0$, see figure 8(b). As soon as M_w deviates from zero, the cone (3.43) again provides a very good fit to the actual stability boundary, figure 8(c). In the plane

$$\beta = \frac{(M_0^4 \kappa_0^2 - 1)(M_0^4 \kappa_0^2 + M_0^2 - 1)}{2M_0^4 \kappa_0^3} (\kappa - \kappa_0), \quad (3.45)$$

the cross-section of the cone (3.43) is described by the two lines

$$\kappa = \kappa_0 \pm M_w \frac{2\kappa_0 M_0}{M_0^4 \kappa_0^2 + M_0^2 - 1}, \quad (3.46)$$

that constitute a linear approximation to the stability boundary shown in figure 8(a).

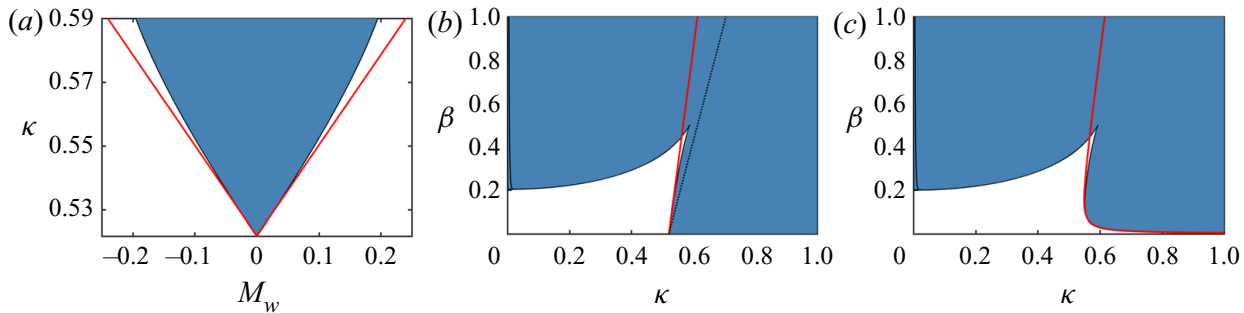


FIGURE 8. For $M = M_0 = 2$ (a) cross-section of the instability domain with the conical singularity shown in figure 7(b) in the plane (3.45). The regions of real phase speed σ are shown in white (stability) and those of the complex σ (temporal instability) in blue. The red lines crossing at the apex of the cone at $\kappa = \kappa_0 \approx 0.5218134478$ are linear approximations given by (3.46). (b) Cross-section in the plane $M_w = 0$ of the instability domain and (red line) its linear approximation (3.44) at the conical point $\kappa = \kappa_0$. The black dotted line is given by (3.45). (c) Similar cross-section in the plane $M_w = 0.1$ where the red curve is the approximation (3.43).

3.1.3. Wave energy of the Nemtsov system for membrane of infinite chord length

Let us use physical considerations to derive the expression for the averaged over the wave period energy of the Nemtsov system with the membrane of infinite chord length, by combining the approaches of the works by Maissa *et al.* (2016) and Schulkes *et al.* (1987).

In the linear wave theory, the energy is a function of the squared wave amplitude (Maissa *et al.* 2016). Therefore, the total energy per surface area of the membrane resulting both from the wave velocity of the structure and the elastic energy due to its tension is

$$\mathcal{E}_m = \mathcal{K}_m + \mathcal{P}_m = \frac{1}{2}(\text{Re}[\partial_\tau \xi(x, \tau)])^2 + \frac{1}{2}M_w^2(\text{Re}[\partial_x \xi(x, \tau)])^2, \quad (3.47)$$

where Re stands for the real part of the vibration amplitude that is complex valued because of the assumed plane wave solution

$$[\phi(x, z, \tau), \eta(x, \tau), \xi(x, \tau)] \sim [\hat{\phi}(z), \hat{\eta}, \hat{\xi}] e^{i(\kappa x - \omega \tau)}. \quad (3.48)$$

Recall that $\hat{\phi}(z)$ is determined by the expression (3.4) with the coefficients (3.11) and $\hat{\eta}, \hat{\xi}$ are, respectively, displacement amplitudes of the free surface and the membrane.

The energy of the fluid depends on whether we assume a vacuum below the membrane (Nemtsov 1985) or a quiescent medium of the same density as the fluid above the membrane and with a pressure equal to the pressure of the unperturbed fluid (Vedeneev 2004, 2016). The gravitational potential energy of the free surface is the only term contributing to the total potential energy of the fluid in the latter context. Therefore,

$$\mathcal{P}_f = \frac{1}{2}\alpha(\text{Re}[\eta(x, \tau)])^2. \quad (3.49)$$

The kinetic energy of the flow per unit area is determined by the velocity field $\mathbf{u} = \nabla\phi + M\mathbf{e}_x$, where $\mathbf{u} = \mathbf{v}/\sqrt{gH}$, that needs to be directly integrated within the limits given

by the surface of the membrane and the free surface of the fluid,

$$\begin{aligned}\mathcal{K}_f &= \frac{1}{2}\alpha \int_{\text{Re } \xi}^{\text{Re } \eta} ||\text{Re}(\mathbf{u})||^2 dz = \frac{1}{2}\alpha \int_{\text{Re } \xi}^{\text{Re } \eta} [(\text{Re}[\nabla \phi])^2 + 2M\text{Re}[\partial_x \phi] + M^2] dz \\ &= \frac{1}{2}\alpha \int_{\text{Re } \xi}^{\text{Re } \eta} [(\text{Re}[\partial_x \phi])^2 + (\text{Re}[\partial_z \phi])^2] dz \\ &\quad + \alpha M \int_{\text{Re } \xi}^{\text{Re } \eta} \left[\text{Re}[\partial_x \phi] + \frac{M}{2} \right] dz.\end{aligned}\quad (3.50)$$

From assumption (3.48) and the explicit form of the complex amplitude $\hat{\phi}(z)$ determined by (3.4) with the coefficients (3.11), it follows that

$$\left. \begin{aligned}\text{Re}[\partial_x \phi] &= i\kappa \hat{\phi}(z) \cos(\kappa x - \omega\tau), & \text{Re}[\partial_z \phi] &= i\partial_z \hat{\phi}(z) \sin(\kappa x - \omega\tau), \\ \text{Re } \xi &= \hat{\xi} \cos(\kappa x - \omega\tau), & \text{Re } \eta &= \hat{\eta} \cos(\kappa x - \omega\tau).\end{aligned}\right\} \quad (3.51)$$

Taking into account the expressions (3.51) in (3.50), we find

$$\int_{\text{Re } \xi}^{\text{Re } \eta} (\text{Re}[\partial_x \phi])^2 dz = -\kappa^2 \cos^2(\kappa x - \omega\tau) \int_{\text{Re } \xi}^{\text{Re } \eta} \hat{\phi}(z)^2 dz. \quad (3.52)$$

Similarly, with the help of integration by parts, the Laplace equation (3.3), and expressions (3.51), we obtain

$$\begin{aligned}\int_{\text{Re } \xi}^{\text{Re } \eta} (\text{Re}[\partial_z \phi])^2 dz &= -\sin^2(\kappa x - \omega\tau) \left\{ [\hat{\phi} \partial_z \hat{\phi}]_{\text{Re } \xi}^{\text{Re } \eta} - \int_{\text{Re } \xi}^{\text{Re } \eta} \hat{\phi} (\partial_z^2 \hat{\phi}) dz \right\} \\ &= -\sin^2(\kappa x - \omega\tau) \left\{ [\hat{\phi} \partial_z \hat{\phi}]_{\text{Re } \xi}^{\text{Re } \eta} - \kappa^2 \int_{\text{Re } \xi}^{\text{Re } \eta} \hat{\phi}(z)^2 dz \right\}.\end{aligned}\quad (3.53)$$

Finally, following Maissa *et al.* (2016), we evaluate the last integral term in (3.50) with the help of the Lagrange mean value theorem, which is justified by the assumption that η and ξ are infinitesimally small perturbations of the surface boundaries $\partial\Omega_0$ and $\partial\Omega_1$. Performing this procedure, and then taking into account expressions (3.51), we obtain

$$\begin{aligned}&\int_{\text{Re } \xi}^{\text{Re } \eta} \left[\text{Re}[\partial_x \phi] + \frac{M}{2} \right] dz \\ &= \int_{\text{Re } \xi}^0 \text{Re}[\partial_x \phi] dz + \int_0^1 \text{Re}[\partial_x \phi] dz + \int_1^{\text{Re } \eta} \text{Re}[\partial_x \phi] dz + \frac{1}{2} \int_{\text{Re } \xi}^{\text{Re } \eta} M dz \\ &= \text{Re } \eta \text{Re}[\partial_x \phi]|_{z=1} - \text{Re } \xi \text{Re}[\partial_x \phi]|_{z=0} + \int_0^1 \text{Re}[\partial_x \phi] dz + \frac{M}{2} \text{Re}(\eta - \xi) \\ &= i\kappa [\hat{\eta} \hat{\phi}(1) - \hat{\xi} \hat{\phi}(0)] \cos^2(\kappa x - \omega\tau) + \left[i\kappa \int_0^1 \hat{\phi}(z) dz + \frac{M}{2} (\hat{\eta} - \hat{\xi}) \right] \cos(\kappa x - \omega\tau).\end{aligned}\quad (3.54)$$

Note that the right-hand sides in the expressions (3.52)–(3.54) are T -periodic functions of time, where $T = 2\pi/\omega$. Averaging these expressions over the wave period T according to

the rule

$$\langle f(\tau) \rangle = \frac{1}{T} \int_0^T f(\tau) d\tau, \quad (3.55)$$

we deduce the mean kinetic energy of the fluid

$$\langle \mathcal{K}_f \rangle = \frac{1}{4} \alpha \{ -[\hat{\phi} \partial_z \hat{\phi}]_{\partial \Omega_1}^{\partial \Omega_0} + 2i\kappa M [\hat{\eta} \hat{\phi}(1) - \hat{\xi} \hat{\phi}(0)] \}. \quad (3.56)$$

The term $\hat{\phi} \partial_z \hat{\phi}$ in (3.56) is evaluated with the help of the Bernoulli principle (2.11) and the free surface kinematic condition (2.10) at $\partial \Omega_0$, and the wave equation (2.22e) with the impermeability condition (2.22c) at $\partial \Omega_1$. This yields, respectively,

$$\left. \begin{aligned} \hat{\phi}|_{\partial \Omega_0} &= \frac{\hat{\eta}}{i(\omega - \kappa M)}, & \hat{\phi}|_{\partial \Omega_1} &= \frac{\omega^2 - \kappa^2 M_w^2}{i\alpha(\omega - \kappa M)} \hat{\xi}, \\ \partial_z \hat{\phi}|_{\partial \Omega_0} &= -i(\omega - \kappa M) \hat{\eta}, & \partial_z \hat{\phi}|_{\partial \Omega_1} &= -i(\omega - \kappa M) \hat{\xi}. \end{aligned} \right\} \quad (3.57)$$

Substituting expressions (3.57) into (3.56) we obtain the final expression for the mean kinetic energy of the fluid

$$\langle \mathcal{K}_f \rangle = \frac{1}{4} \{ \alpha \hat{\eta}^2 - (\omega^2 - \kappa^2 M_w^2) \hat{\xi}^2 + 2i\alpha\kappa M [\hat{\eta} \hat{\phi}(1) - \hat{\xi} \hat{\phi}(0)] \}. \quad (3.58)$$

The other energies of the system, after taking into account (3.51) and time averaging (3.55), become

$$\langle \mathcal{P}_m \rangle = \frac{1}{4} \kappa^2 M_w^2 \hat{\xi}^2, \quad \langle \mathcal{K}_m \rangle = \frac{1}{4} \omega^2 \hat{\xi}^2, \quad \langle \mathcal{P}_f \rangle = \frac{1}{4} \alpha \hat{\eta}^2. \quad (3.59a-c)$$

Notice that in the absence of the background flow ($M = 0$) the system respects the equipartition of energy

$$\langle \mathcal{P}_f \rangle + \langle \mathcal{P}_m \rangle = \langle \mathcal{K}_f \rangle + \langle \mathcal{K}_m \rangle, \quad (3.60)$$

in accordance with the virial theorem (Landau & Lifschitz 1987), because the flow is irrotational and thus derived from a fluid potential (Schulkes *et al.* 1987).

After summing up all the different terms given by (3.58) and (3.59a–c) we obtain the total averaged energy

$$\langle \mathcal{E} \rangle = \frac{1}{2} \left\{ \kappa^2 M_w^2 \hat{\xi}^2 + \alpha \hat{\eta}^2 + i\alpha\kappa M [\hat{\eta} \hat{\phi}(1) - \hat{\xi} \hat{\phi}(0)] \right\}, \quad (3.61)$$

thus providing an extension to the case when the velocity field contains a background flow ($M \neq 0$).

A more suitable expression for the mean total energy can be obtained by expressing the different amplitudes of the system in (3.61) in terms of a unique one, for instance, $\hat{\xi}$. From the kinematic condition (2.10) on the free surface with the plane wave solution (3.48) and

the coefficients (3.11), it is straightforward to express the surface amplitude $\hat{\eta}$ as

$$\hat{\eta} = \frac{i\kappa}{\omega - \kappa M} [Ae^\kappa - Be^{-\kappa}] = \frac{(\omega - \kappa M)^2 \hat{\xi}}{(\omega - \kappa M)^2 \cosh \kappa - \kappa \sinh \kappa}. \quad (3.62)$$

Substituting (3.62) into (3.61) and using the complex amplitude $\hat{\phi}(z)$ recovered from the boundary value problem (3.16), we find

$$\begin{aligned} \langle \mathcal{E} \rangle &= \frac{\hat{\xi}^2}{2} \left\{ \kappa^2 M_w^2 + \alpha \frac{(\omega - \kappa M)^4 (1 - (\tanh \kappa)^2)}{[(\omega - \kappa M)^2 - \kappa \tanh \kappa]^2} \right. \\ &\quad \left. + \alpha M(\omega - \kappa M) \frac{[(\omega - \kappa M)^4 + \kappa^2] \tanh \kappa - 2\kappa(\omega - \kappa M)^2 (\tanh \kappa)^2}{[(\omega - \kappa M)^2 - \kappa \tanh \kappa]^2} \right\}. \end{aligned} \quad (3.63)$$

Next, expressing the term $\kappa^2 M_w^2$ by means of the dispersion relation (3.20) and substituting the result into (3.63) yields a more compact formula for the total energy

$$\langle \mathcal{E} \rangle = \frac{1}{4} \omega \left\{ 2\omega + \frac{\alpha}{\kappa} \frac{2(\omega - \kappa M) \tanh \kappa [(\omega - \kappa M)^4 + \kappa^2 - 2\kappa(\omega - \kappa M)^2 \tanh \kappa]}{[(\omega - \kappa M)^2 - \kappa \tanh \kappa]^2} \right\} \hat{\xi}^2. \quad (3.64)$$

Notice that the term in the braces in (3.64) is nothing else but the partial derivative $\partial \mathcal{D}/\partial \omega$ of the dispersion relation (3.20) written in the following equivalent form

$$\mathcal{D}(\omega, \kappa) := \mathcal{D}_m(\omega, \kappa) + \frac{\alpha}{\kappa} \frac{(\omega - \kappa M)^2 [(\omega - \kappa M)^2 \tanh \kappa - \kappa]}{\mathcal{D}_f(\omega, \kappa)} = 0, \quad (3.65)$$

where $\mathcal{D}_m = \omega^2 - \kappa^2 M_w^2$ and $\mathcal{D}_f = [(\omega - \kappa M)^2 - \kappa \tanh \kappa]$ stand for the dispersion relation of, respectively, the free membrane and the free surface flow with a rigid boundary at the bottom. This proves that our total energy per unit area, averaged over the wave period, possesses the following simple representation in terms of the dispersion relation

$$\langle \mathcal{E} \rangle = \frac{1}{4} \omega \frac{\partial \mathcal{D}}{\partial \omega} \hat{\xi}^2. \quad (3.66)$$

The representation (3.66) can be found, e.g. in Cairns (1979), and can be derived in the frame of the general Lagrangian variational approach (Ostrovskii, Rybak & Tsimring 1986; Whitham 1999), see also the recent work by Fukumoto, Hirota & Mie (2014) for historical notes and application to stability of vortices. Notice that according to (3.66) the energy vanishes at the points where $\omega = 0$ or $\partial \mathcal{D}/\partial \omega = 0$, the latter condition corresponding to the existence of multiple roots of the dispersion relation. Correspondingly, the ratio $\langle \mathcal{E} \rangle/\omega$, which is the averaged wave action $\langle \mathcal{A} \rangle$ (Whitham 1999; Zhang *et al.* 2016), vanishes only at the locations of the multiple eigenvalues, cf. figures 2 and 9. In the latter figure as well as in figure 10 we show several computations of the averaged wave energy and wave action over the fluid Mach number M , and, respectively, the membrane Mach number M_w , where ω is calculated with the use of the dispersion relation (3.20).

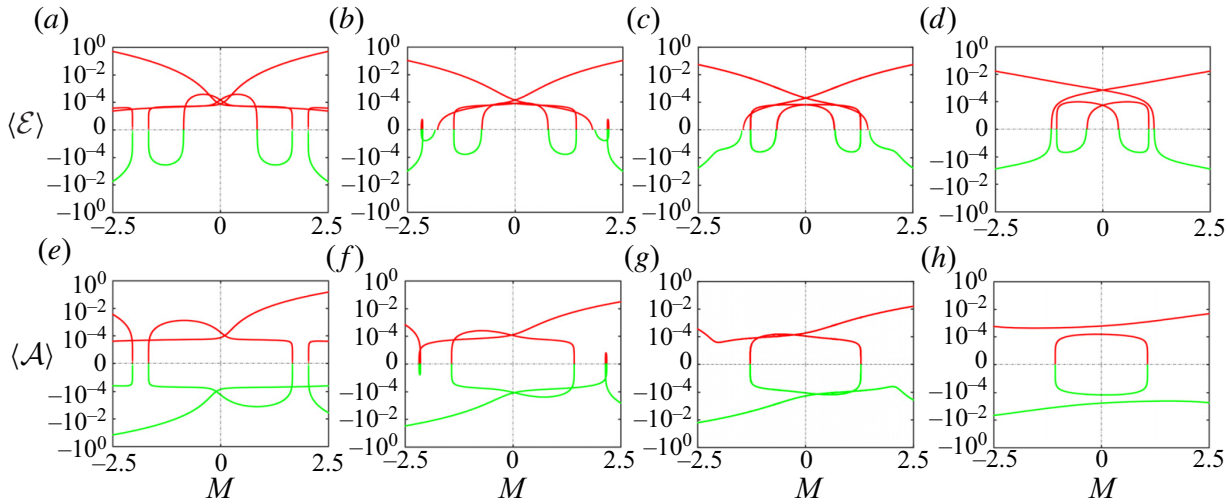


FIGURE 9. The averaged wave energy (a–d) $\langle \mathcal{E} \rangle$ given by the expression (3.64) and the action (e–h) $\langle \mathcal{A} \rangle = \langle \mathcal{E} \rangle / \omega$ over the Mach number M evaluated for $M_w = 1$, $\kappa = 1$, $\hat{\xi} = 0.01$ and: (a,e) $\alpha = 0.1$, (b,f) $\alpha = 0.5$, (c,g) $\alpha = 1$ and (d,h) $\alpha = 5$. Positive (respectively negative) energy/action is represented in red (respectively green).

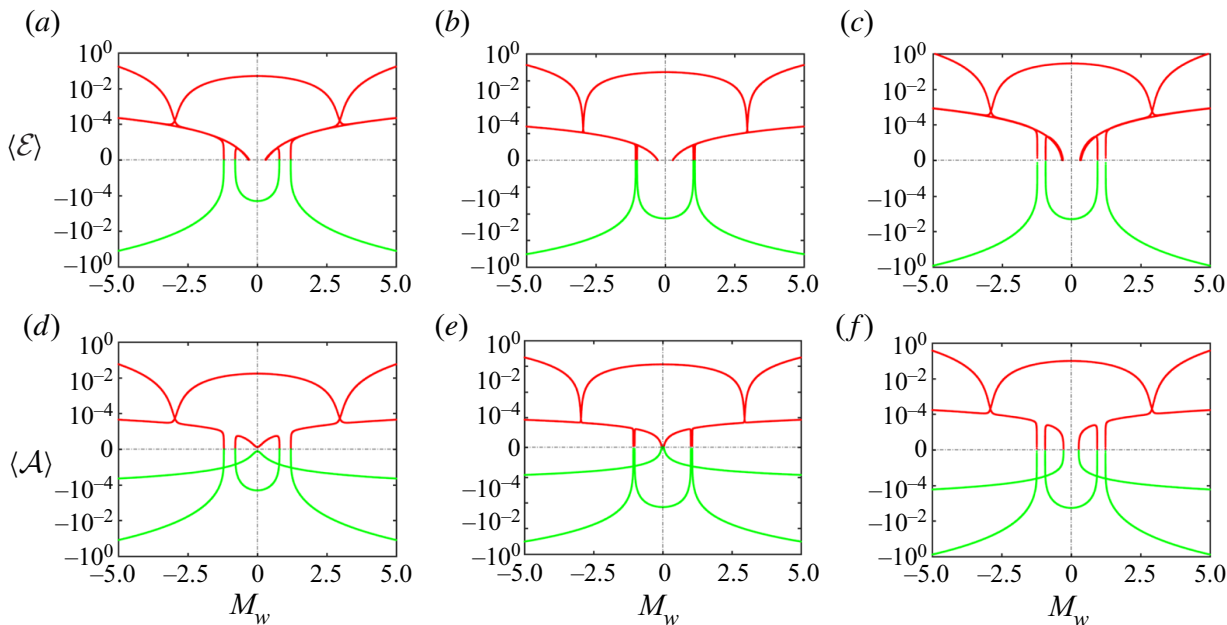


FIGURE 10. The averaged wave energy (upper panels) $\langle \mathcal{E} \rangle$ given by the expression (3.64) and the action (lower panels) $\langle \mathcal{A} \rangle = \langle \mathcal{E} \rangle / \omega$ over the Mach number M_w for $\hat{\xi} = 0.01$, $M = M_0 = 2$, and (a,d) $\beta = 0.05$ and $\kappa = \kappa_0 - 0.1$, (b,e) $\beta = 10^{-3}$ and $\kappa = \kappa_0 \approx 0.5218134478$, (c,f) $\beta = 0.05$ and $\kappa = \kappa_0 + 0.3$.

4. Discussion

Comparing the eigenvalue plots of figures 2 and 6 with the averaged wave energy and wave action of each branch that are shown in figures 9 and 10, respectively, we notice that flutter instability is necessarily accompanied with the interaction of waves of opposite sign of energy/action. In contrast to the action, the energy changes sign also at the points where the phase velocity σ changes sign, quite in accordance with (3.66).

Looking now at the roots (3.28a,b) of the decoupled dispersion equation (3.26), we conclude that the elastic waves $\sigma_1^\pm = \pm M_w$ propagating in the membrane always have

positive energy whereas among the surface gravity waves $\sigma_2^\pm = M \pm \sqrt{(\tanh \kappa)/\kappa}$ it is the energy of the slow wave σ_2^- that becomes negative for $M > 0$ as soon as $M > \sqrt{(\tanh \kappa)/\kappa}$. Therefore at the crossing (3.29) corresponding to $M_0^+ = M_w + \sqrt{(\tanh \kappa)/\kappa}$ the positive energy/action elastic wave meets the slow surface gravity wave that carries negative energy/action (Nemtsov 1985).

With β increasing from zero, the crossing unfolds causing the eigenvalue branches to merge on the interval bounded by the points where $\partial_\omega D = 0$. At these exceptional points (Kirillov 2013) both the energy and the action change sign, see figures 9 and 10. On the interval the roots are complex and form the bubble of instability, see figures 2 and 6.

Since the fast surface gravity wave carries positive energy, one needs to add energy to the flow in order to excite this wave on the flow. In contrast, in order for the slow surface gravity wave carrying negative energy to build up on the flow, the energy must be extracted from the flow (Nezlin 1976) via some mechanism for dissipation of its energy. In the Nemtsov problem, such a mechanism is the energy transfer from the slow surface gravity wave to an elastic wave associated with the membrane, which is a stationary medium and therefore has positive energy (Nezlin 1976). One can say that this transferred energy yields flutter of the membrane due to emission of the slow surface gravity wave carrying negative energy.

In figures 2 and 6 as well as in figures 9 and 10 we observe that the flutter instability of the membrane occurs only if the velocity of the flow is higher than the phase velocity of the oscillations on the surface of the flow, $\sigma < M$, i.e. the flow moves faster than the waves it can excite (Nezlin 1976; Nemtsov & Eidman 1987). The condition $\omega = M\kappa$ or $\sigma = M$ is known as the Cerenkov condition for emission of radiation by a moving source (Ginzburg & Frank 1947; Nezlin 1976; Ginzburg 1996; Bekenstein & Schiffer 1998; Carusotto & Rousseaux 2013). Substituted into a dispersion relation, the Cerenkov condition transforms the former into an expression defining a surface in the space of wavenumbers that determines the wake pattern behind the source (Schulkes *et al.* 1987; Carusotto & Rousseaux 2013). For the supercritical velocities $M > \sigma$ the surface in the space of wavenumbers develops a conical singularity known as the Cerenkov cone (Nemtsov 1985; Carusotto & Rousseaux 2013) with the angular aperture

$$2 \arccos \left(\frac{\sigma}{M} \right). \quad (4.1)$$

The anomalous Doppler effect (ADE) is the change in the sign of the field frequency radiated into the Cerenkov cone as compared with the field radiated outside this cone (Nezlin 1976; Gaponov-Grekhov *et al.* 1983; Nemtsov 1985; Abramovich *et al.* 1986; Carusotto & Rousseaux 2013). It is exactly the slow surface gravity wave that satisfies this condition

$$\sigma_2^- - M = -\sqrt{\frac{\tanh \kappa}{\kappa}} < 0. \quad (4.2)$$

Hence, for the one-dimensional or, more precisely, plane two-dimensional waves, both the negative energy waves and the ADE correspond simply to waves with phase velocity lower than the flow velocity and wave vector pointing in the same direction as the flow (Nemtsov 1985; Ostrovskii *et al.* 1986). In our case, the radiated slow gravity wave increases the energy of oscillations of the membrane at the expense of the energy of the flow that supports this wave.

Finally, we plot the dispersion curves $\omega(\kappa)$ in figure 11, which show that the slow surface gravity wave branch and the membrane branch interact under the line $\text{Re}(\omega) = \kappa M$, if $\kappa > 0$. Substituting the Cerenkov condition in the dispersion relation (3.20) we reduce

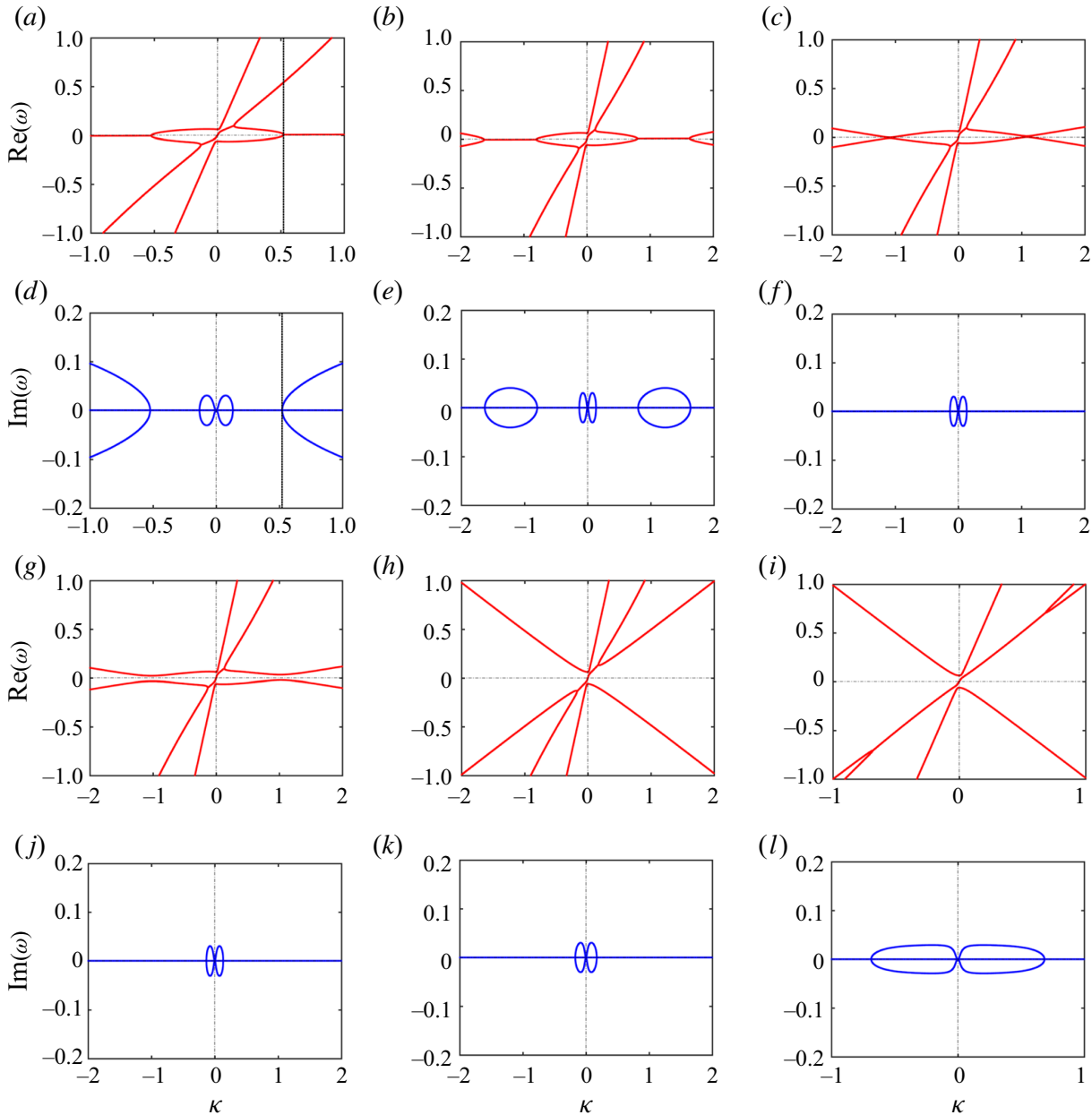


FIGURE 11. Dispersion curves ((red) real and (blue) imaginary parts of the roots ω of the dispersion relation (3.20)) for $M = 2$, $\alpha \approx 0.0036725648$ and (a,d) $M_w = 0$, (b,e) $M_w = 0.09$, (c,f) $M_w = 0.0967$, (g,j) $M_w = 0.1$, (h,k) $M_w = 0.5$, (i,l) $M_w = 1$. Vertical dashed lines in the panels (a,d) correspond to $\kappa = \kappa_0 \approx 0.5218134478$ and mark the onset of instability corresponding to the central instability zone in figure 7(a) and the conical instability zone in figure 7(b).

it to $(M_w^2 - M^2) \tanh \kappa = 0$, thus providing a rationale for the absence of instabilities for $M_w^2 > M^2$ that is evident in all our stability diagrams.

5. Conclusion

Through the revival of a classical hydrodynamical model performed in this work, we have been able to extend the stability analysis and to enhance knowledge of the underlying physics by making connections with the fundamental concepts such as negative energy waves and the ADE, supported by advanced mathematical tools.

Our continuation of Nemtsov's investigation of the radiation-induced flutter of a membrane in a uniform flow with the new derivation of the dispersion relation for a fluid layer of arbitrary depth and membrane of infinite chord length has led to a significant improvement in the computation of stability diagrams without any limitation on the range of the system parameters.

An exhaustive stability analysis has been performed using the original perturbation theory of multiple roots of the dispersion relation to compare with the exact stability domains, and both computations are proven to be in excellent agreement. More precisely, the crossings and avoided crossings of the dispersion curves are very well approximated by the simplified expressions for the phase speed of the membrane and fluid modes derived with the perturbation approach.

After computing the discriminant of the full dispersion relation, we have identified a new instability domain arising from a conical singularity in the parameter space that was not present in the early study of Nemtsov. This new domain is associated with a low-frequency flutter for short wavelengths and corresponds to the case when the velocity of propagation of elastic waves in the membrane is much smaller than the velocity of the flow.

Moreover, following the procedures used in previous studies on simplified hydrodynamical systems to calculate the averaged wave energy and after developing the method further to take into account the coupling between the free surface of the flow and the elastic membrane on the bottom, we have obtained an elegant and applicable expression for the total averaged energy. We have verified that, in the absence of the background flow, the system respects the equipartition of energy in accordance with the virial theorem, thus confirming that the existence of the negative energy waves can only be possible when the fluid is in motion.

We have shown that the formula for the total averaged energy recovered in our work by means of the direct integration of different physical fields is expressed via the derivative of the dispersion relation with respect to the frequency of oscillations and reduces exactly to the form described by Cairns (1979).

The ADE is a direct consequence of the relative motion of an oscillator in a medium and more precisely, it occurs when the internal energy of the system increases due to the emission of negative energy waves (NEW). In our context, while the system is composed of a fluid layer and a membrane, such a phenomenon has been proved by Nemtsov to exist only when the conditions of phase synchronism and NEW emission are satisfied. The criterion for the phase synchronism in the system is easily identified in the computations of the dispersion curves as the crossings of the different branches that lead to the onset of positive growth rate and therefore to temporal instability. The latter phenomenon is a natural consequence of the highly excited state of energy that the system transits to due to the dominance of NEW over the waves carrying positive energy. Indeed, NEW emission is known as a process that increases the total energy of an oscillatory system while radiating energy away from the oscillator and, only when this gain in internal energy exceeds the losses from the contribution of positive energy modes, the total energy of the system starts growing in amplitude. Hence, it requires to have waves carrying energy of opposite signs that interact for the instability to develop.

Our expressions for the action and energy of the Nemtsov system demonstrated as expected the collision of waves carrying positive and negative energy as the onset for the radiative instability and the flutter of the membrane. Such a phenomenon is well known in the community of dynamical systems, but in this context, it is associated with the emission of NEW in the region of ADE. Hence, in addition to improving the stability analysis of the Nemtsov system and computing the averaged wave energy, our study provides a further, more detailed, examination of the ADE in hydrodynamics. Despite our problem being

restricted to the study of planar waves, with the latter being emitted only in the horizontal direction, it is still sufficient for exploring the connection between the ADE and flutter theory.

An extension of this work to the case of a membrane with a chord of finite size, as described by the system of (2.22), is a promising necessary next step requiring asymptotic methods for the global stability analysis and numerical computations that we leave for future work.

Acknowledgements

We thank an anonymous referee for bringing important early works to our attention. We are grateful to Professor T.J. Bridges for helpful discussions. J.L. was supported by a PhD Scholarship from Northumbria University.

Declaration of interests

The authors report no conflict of interest.

Appendix A. Sensitivity analysis of dispersion equations

In contrast to other works on frequency coalescence, e.g. Triantafyllou & Triantafyllou (1991), we adapt a more systematic multiparameter sensitivity analysis that can be found, e.g. in Kirillov & Seyranian (2002), Kirillov & Seyranian (2004), Kirillov (2007a), Kirillov (2007b), Kirillov (2009), Kirillov *et al.* (2009), Kirillov (2010) and Kirillov (2013).

Let us consider the dispersion equation

$$D(\omega, p, q) = 0, \quad (\text{A } 1)$$

where D is a smooth function of scalar arguments ω , p and q . Assume that $D(\omega)$ is a polynomial of degree n in ω .

A.1. Sensitivity of simple roots

Let at $p = p_0$ and $q = q_0$ (A 1) have a simple root ω_0 such that

$$D_0 := D(\omega_0, p_0, q_0) = 0, \quad (\text{A } 2)$$

where we use the symbol $:=$ to indicate a definition.

Following Kirillov & Seyranian (2002), Kirillov & Seyranian (2004), Kirillov (2007a), Kirillov (2007b), Kirillov (2010) and Kirillov (2013), we assume that $p = p(\varepsilon)$ and $q = q(\varepsilon)$. For $|\varepsilon|$ sufficiently small we can represent these functions as Taylor series

$$\left. \begin{aligned} p(\varepsilon) &= p_0 + \varepsilon \frac{dp}{d\varepsilon} + \frac{\varepsilon^2}{2} \frac{d^2p}{d\varepsilon^2} + o(\varepsilon^2), \\ q(\varepsilon) &= q_0 + \varepsilon \frac{dq}{d\varepsilon} + \frac{\varepsilon^2}{2} \frac{d^2q}{d\varepsilon^2} + o(\varepsilon^2), \end{aligned} \right\} \quad (\text{A } 3)$$

with the derivatives evaluated at $\varepsilon = 0$, and $p_0 := p(0)$ and $q_0 := q(0)$. Then, $\omega = \omega(\varepsilon)$ is also a root of (A 1), i.e. it satisfies the equation

$$D_\varepsilon := D(\omega(\varepsilon), p(\varepsilon), q(\varepsilon)) = 0. \quad (\text{A } 4)$$

Differentiating (A 4), we find

$$\frac{d}{d\varepsilon}D_\varepsilon = \partial_\omega D \frac{d\omega}{d\varepsilon} + \partial_p D \frac{dp}{d\varepsilon} + \partial_q D \frac{dq}{d\varepsilon} = 0, \quad (\text{A } 5)$$

where the partial derivatives are evaluated at $\omega = \omega_0$, $q = q_0$, $p = p_0$.

Denoting $\Delta\omega = \varepsilon(d\omega/d\varepsilon) \approx \omega - \omega_0$, $\Delta q = \varepsilon(dq/d\varepsilon) \approx q - q_0$ and $\Delta p = \varepsilon(dp/d\varepsilon) \approx p - p_0$, we find the expression for the increment of the simple root ω_0 of (A 1) when the parameters depart from the values q_0 and p_0

$$\Delta\omega = -\frac{\partial_p D}{\partial_\omega D} \Delta p - \frac{\partial_q D}{\partial_\omega D} \Delta q + o(|\Delta p|, |\Delta q|). \quad (\text{A } 6)$$

A.2. Double root of the dispersion relation: generic case

Let at $p = p_0$ and $q = q_0$ the dispersion equation (A 1) have a double root ω_0 , which implies

$$\left. \begin{aligned} D_0 &= 0, \\ \partial_\omega D_0 &:= \partial_\omega D(\omega_0, p_0, q_0) = 0. \end{aligned} \right\} \quad (\text{A } 7)$$

Assume that the perturbation of the parameters (A 3) causes splitting of the double root ω_0 which generically is described by the Newton–Puiseux series (Kirillov & Seyranian 2002, 2004; Kirillov 2007a,b, 2010, 2013)

$$\omega(\varepsilon) = \omega_0 + \omega_1 \varepsilon^{1/2} + \omega_2 \varepsilon + \omega_3 \varepsilon^{3/2} + \omega_4 \varepsilon^2 + o(\varepsilon^2). \quad (\text{A } 8)$$

Expanding D_ε as

$$D_\varepsilon = \sum_{s=0}^n \frac{(\omega(\varepsilon) - \omega_0)^s}{s!} (\partial_\omega^s D + \varepsilon \partial_\omega^s D_1 + \varepsilon^2 \partial_\omega^s D_2 + o(\varepsilon^2)), \quad (\text{A } 9)$$

where

$$\left. \begin{aligned} D_1 &:= \partial_p D \frac{dp}{d\varepsilon} + \partial_q D \frac{dq}{d\varepsilon}, \\ D_2 &:= \frac{1}{2} \partial_p D \frac{d^2 p}{d\varepsilon^2} + \frac{1}{2} \partial_q D \frac{d^2 q}{d\varepsilon^2} + \frac{1}{2} \left(\partial_p^2 D \frac{d^2 p}{d\varepsilon^2} + 2\partial_{pq}^2 D \frac{dp}{d\varepsilon} \frac{dq}{d\varepsilon} + \partial_q^2 D \frac{d^2 q}{d\varepsilon^2} \right), \end{aligned} \right\} \quad (\text{A } 10)$$

substituting expansion (A 8) into (A 9) and collecting the coefficients at the same powers of ε , we find

$$\left. \begin{aligned} D_0 &= 0, \\ \omega_1 \partial_\omega D_0 &= 0, \\ D_1 + \omega_1^2 \frac{1}{2} \partial_\omega^2 D + \omega_2 \partial_\omega D_0 &= 0. \end{aligned} \right\} \quad (\text{A } 11)$$

Looking for the coefficient $\omega_1 \neq 0$, we see that the first two equations of (A 11) are satisfied in view of the fact that ω_0 is a double root of the dispersion equation (A 1). Taking this

into account, the last of (A 11) yields the expression for the coefficient ω_1 in the expansion (A 8)

$$\omega_1^2 = -D_1 \left(\frac{1}{2} \partial_\omega^2 D \right)^{-1}, \quad (\text{A } 12)$$

where all the partial derivatives are calculated at $p = p_0$, $q = q_0$, $\omega = \omega_0$.

Therefore, if $D_1 \neq 0$, the double root ω_0 splits under variation of parameters (A 3) according to the formula

$$\omega = \omega_0 \pm \sqrt{-\varepsilon D_1 \left(\frac{1}{2} \partial_\omega^2 D \right)^{-1}} + o(|\varepsilon|^{1/2}). \quad (\text{A } 13)$$

In terms of the increments of the parameters, we can re-write (A 13) as

$$\Delta\omega = \pm \sqrt{-(\partial_p D \Delta p + \partial_q D \Delta q) \left(\frac{1}{2} \partial_\omega^2 D \right)^{-1}} + o(|\Delta p|^{1/2}, |\Delta q|^{1/2}). \quad (\text{A } 14)$$

A.3. Double root of the dispersion relation: degenerate case

The case $D_1 = 0$ is degenerate, because the leading term in (A 13) of order $\varepsilon^{1/2}$ vanishes and the expansion (A 8) is no longer valid, see e.g. Kirillov & Seyranian (2004). Substituting expansion (A 13) with $\omega_1 = 0$ into (A 9) and collecting coefficients of the same powers of ε , we obtain

$$\left. \begin{aligned} D_1 + \omega_2 \partial_\omega D_0 &= 0, \\ \omega_3 \partial_\omega D_0 &= 0, \\ D_2 + \omega_2^2 \frac{1}{2} \partial_\omega^2 D + \omega_2 \partial_\omega D_1 + \omega_4 \partial_\omega D_0 &= 0. \end{aligned} \right\} \quad (\text{A } 15)$$

Taking into account that $\partial_\omega D_0 = 0$ since ω_0 is the double root and that $D_1 = 0$ due to our assumption, we conclude that the first two of (A 15) hold automatically. The third one simplifies as follows:

$$\omega_2^2 \frac{1}{2} \partial_\omega^2 D + \omega_2 \partial_\omega D_1 + D_2 = 0, \quad (\text{A } 16)$$

where all the derivatives are calculated at $\omega = \omega_0$, $p = p_0$ and $q = q_0$.

Therefore, the degeneracy, $D_1 = 0$, implies that the double root ω_0 splits according to the formula

$$\omega = \omega_0 + \omega_2 \varepsilon + o(\varepsilon), \quad (\text{A } 17)$$

where the coefficient ω_2 is a root of the polynomial (A 16).

In combination with (A 10) and (A 17) the polynomial (A 16) transforms into

$$\begin{aligned} (\Delta\omega)^2 \frac{1}{2} \partial_\omega^2 D + \Delta\omega (\partial_{\omega p}^2 D \Delta p + \partial_{\omega q}^2 D \Delta q) + \frac{1}{2} [\partial_p^2 D (\Delta p)^2 + 2\partial_{pq}^2 D \Delta p \Delta q + \partial_q^2 D (\Delta q)^2] \\ + \partial_p D \Delta p + \partial_q D \Delta q = 0. \end{aligned} \quad (\text{A } 18)$$

Extension to the case of more than two parameters is straightforward, see e.g. Kirillov & Seyranian (2002), Kirillov & Seyranian (2004), Kirillov (2007a), Kirillov (2007b), Kirillov (2009), Kirillov *et al.* (2009), Kirillov (2010) and Kirillov (2013).

REFERENCES

- ABRAMOVICH, B. S., MAREEV, E. A. & NEMTSOV, B. E. 1986 Instability in the oscillations of a moving oscillator while it radiates surface and internal waves. *Fluid Dyn.* **21** (1), 147–149.
- ARZHANNIKOV, A. V. & KOTELNIKOV, I. A. 2016 Excitation of ship waves by a submerged object: new solution to the classical problem. *Phys. Rev. E* **94**, 023103.
- BANICHUK, N., BARSUK, A., JERONEN, J., TUOVINEN, T. & NEITTAANMÄKI, P. 2019 *Stability of Axially Moving Materials*, Solid Mechanics and Its Applications, vol. 259. Springer.
- BANICHUK, N., JERONEN, J., NEITTAANMÄKI, P. & TUOVINEN, T. 2010 Static instability analysis for travelling membranes and plates interacting with axially moving ideal fluid. *J. Fluids Struct.* **26**, 274–291.
- BARBONE, P. E. & CRIGHTON, D. G. 1994 Vibrational modes of submerged elastic bodies. *Appl. Acoust.* **43**, 295–317.
- BARCELÓ, C., LIBERATI, S. & VISSER, M. 2011 Analogue gravity. *Living Rev. Relativ.* **14**, 3.
- BEKENSTEIN, J. D. & SCHIFFER, M. 1998 The many faces of superradiance. *Phys. Rev. D* **58**, 064014.
- BENJAMIN, T. B. 1963 The threefold classification of unstable disturbances in flexible surfaces bounding inviscid flows. *J. Fluid Mech.* **16**, 436–450.
- BOCHKAREV, S. A., LEKOMTSEV, S. V. & MATVEENKO, V. P. 2016 Hydroelastic stability of a rectangular plate interacting with a layer of ideal flowing fluid. *Fluid Dyn.* **51** (6), 821–833.
- BOLOTIN, V. V. 1963 *Nonconservative Problems of the Theory of Elastic Stability*. Pergamon Press.
- BRITO, R., CARDOSO, V. & PANI, P. 2015 *Superradiance*, Lecture Notes in Physics, vol. 906. Springer.
- CAIRNS, R. A. 1979 The role of negative energy waves in some instabilities of parallel flows. *J. Fluid Mech.* **92**, 1–14.
- CARUSOTTO, I. & ROUSSEAU, G. 2013 The Cerenkov effect revisited: from swimming ducks to zero modes in gravitational analogues. In *Analogue Gravity Phenomenology* (ed. D. Faccio, F. Belgiorno, S. Cacciatori, V. Gorini, S. Liberati & U. Moschella), Lecture Notes in Physics, vol. 870. Springer.
- DAS, S., KAR, P., SAHOO, T. & MEYLAN, M. H. 2018 Flexural-gravity wave motion in the presence of shear current: wave blocking and negative energy waves. *Phys. Fluids* **30**, 106606.
- DAS, S., SAHOO, T. & MEYLAN, M. H. 2018a Dynamics of flexural gravity waves: from sea ice to Hawking radiation and analogue gravity. *Proc. R. Soc. A* **474**, 20170223.
- DAS, S., SAHOO, T. & MEYLAN, M. H. 2018b Flexural-gravity wave dynamics in two-layer fluid: blocking and dead water analogue. *J. Fluid Mech.* **854**, 121–145.
- DOARÉ, O. & DE LANGRE, E. 2006 The role of boundary conditions in the instability of one-dimensional systems. *Eur. J. Mech. (B/Fluids)* **25**, 948–959.
- DOWELL, E. H. 1966 Flutter of infinitely long plates and shells. Part 1. Plate. *AIAA J.* **4**, 1370–1377.
- DOWELL, E. H. 2015 *A Modern Course in Aeroelasticity*, 5th Revised and Enlarged edn. Solid Mechanics and Its Applications, vol. 217. Springer.
- DOWELL, E. H. & VENTRES, C. S. 1970 On the flutter of low aspect ratio plates. *AIAA J.* **8**, 1162–1164.
- DUGUNDJI, J., DOWELL, E. & PERKIN, B. 1963 Subsonic flutter of panels on a continuous elastic foundation. *AIAA J.* **1**, 1146–1154.
- FALTINSEN, O. M. & SEMENOV, Y. A. 2008 The effect of gravity and cavitation on a hydrofoil near the free surface. *J. Fluid Mech.* **597**, 371–394.
- FUKUMOTO, Y., HIROTA, M. & MIE, Y. 2014 Representation of wave energy of a rotating flow in terms of the dispersion relation. In *Nonlinear Physical Systems: Spectral Analysis, Stability and Bifurcations* (ed. O. N. Kirillov & D. E. Pelinovsky). Wiley-ISTE.
- GAPONOV-GREKHOV, A. V., DOLINA, I. S. & OSTROVSKII, L. A. 1983 The anomalous Doppler effect and the radiation instability of oscillator motion in hydrodynamics. *Dokl. Akad. Nauk SSSR* **268** (4), 827–831. In Russian.
- GINZBURG, V. L. 1996 Radiation by uniformly moving sources (Vavilov–Cherenkov effect, transition radiation, and other phenomena). *Phys.-Uspekhi* **39** (10), 973–982.
- GINZBURG, V. L. & FRANK, I. M. 1947 On the Doppler effect at the superluminal velocity. *Dokl. Akad. Nauk SSSR* **56**, 583–586.
- GISLASON, T. JR. 1971 An experimental investigation of panel divergence at subsonic speeds. *AIAA J.* **9**, 2252–2258.

- GOLAND, M. & LUKE, Y. L. 1954 An exact solution for two-dimensional linear panel flutter at supersonic speeds. *J. Aeronaut. Sci.* **21** (4), 275–276.
- GREENHILL, A. G. 1886 Wave motion in hydrodynamics. *Am. J. Maths* **9** (1), 62–96.
- GUENTHER, U. & KIRILLOV, O. N. 2006 A Krein space related perturbation theory for MHD α^2 -dynamos and resonant unfolding of diabolical points. *J. Phys. A: Math. Gen.* **39**, 10057–10076.
- HAGERTY, P., BLOCH, A. M. & WEINSTEIN, M. I. 2003 Radiation induced instability. *SIAM J. Appl. Math.* **64** (2), 484–524.
- KIRILLOV, O. N. 2007a Bifurcation of the roots of the characteristic polynomial and destabilization paradox in friction induced oscillations. *Theor. Appl. Mech.* **34** (2), 87–109.
- KIRILLOV, O. N. 2007b On the stability of nonconservative systems with small dissipation. *J. Math. Sci.* **145** (5), 5260–5270.
- KIRILLOV, O. N. 2009 Campbell diagrams of weakly anisotropic flexible rotors. *Proc. R. Soc. A* **465** (2109), 2703–2723.
- KIRILLOV, O. N. 2010 Eigenvalue bifurcation in multiparameter families of non-self-adjoint operator matrices. *Z. Angew. Math. Phys.* **61** (2), 221–234.
- KIRILLOV, O. N. 2013 *Nonconservative Stability Problems of Modern Physics*, De Gruyter Studies in Mathematical Physics, vol. 14. De Gruyter.
- KIRILLOV, O. N., GUENTHER, U. & STEFANI, F. 2009 Determining role of Krein signature for three dimensional Arnold tongues of oscillatory dynamos. *Phys. Rev. E* **79** (1), 016205.
- KIRILLOV, O. N. & SEYRANIAN, A. P. 2002 Metamorphoses of characteristic curves in circulatory systems. *J. Appl. Math. Mech.* **66** (3), 371–385.
- KIRILLOV, O. N. & SEYRANIAN, A. P. 2004 Collapse of the Keldysh chains and stability of continuous non-conservative systems. *SIAM J. Appl. Math.* **64** (4), 1383–1407.
- KORNECKI, A., DOWELL, E. H. & O'BRIEN, J. 1976 On the aeroelastic instability of two-dimensional panels in uniform incompressible flow. *J. Sound Vibr.* **47**, 163–178.
- LAMB, H. 1900 On a peculiarity of the wave-system due to the free vibrations of a nucleus in an extended medium. *Proc. Lond. Math. Soc.* **s1-32** (1), 208–213.
- LANDAU, L. D. & LIFSHITZ, E. M. 1987 *Fluid Mechanics*, 2nd edn. Pergamon Press.
- MAISSA, P., ROUSSEAU, G. & STEPANYANTS, Y. 2016 Negative energy waves in a shear flow with a linear profile. *Eur. J. Mech. (B/Fluids)* **56**, 192–199.
- MAVROYIAKOUMOU, C. & ALBEN, S. 2020 Large-amplitude membrane flutter in inviscid flow. *J. Fluid Mech.* **891**, A23–1–24.
- MILES, J. W. 1947 The aerodynamic forces on an oscillating air foil at supersonic speeds. *J. Aeronaut. Sci.* **14** (6), 351–358.
- MILES, J. W. 1956 On the aerodynamic stability of thin panels. *J. Aeronaut. Sci.* **23**, 771–780.
- MINAMI, H. 1998 Added mass of a membrane vibrating at finite amplitude. *J. Fluids Struct.* **12**, 919–932.
- MOHAPATRA, S. C. & SAHOO, T. 2011 Surface gravity wave interaction with elastic bottom. *Appl. Ocean Res.* **33**, 31–40.
- NEMTSOV, B. E. 1985 Flutter effect and emission in the region of anomalous and normal Doppler effects. *Radiophys. Quantum Electron.* **28** (12), 1076–1079.
- NEMTSOV, B. E. & EIDMAN, V. Y. 1987 Hyperlight biresonant radiation (review). *Radiophys. Quantum Electron.* **30**, 171–188.
- NEWMAN, B. G. & PAIDOUSSIS, M. P. 1991 The stability of two-dimensional membranes in streaming flow. *J. Fluids Struct.* **5**, 443–454.
- NEZLIN, M. V. 1976 Negative-energy waves and the anomalous Doppler effect. *Sov. Phys. Uspekhi* **19**, 946–954.
- OSTROVSKII, L. A., RYBAK, S. A. & TSIMRING, L. SH. 1986 Negative energy waves in hydrodynamics. *Sov. Phys. Uspekhi* **29** (11), 1040–1052.
- ROBERTSON, S. & ROUSSEAU, G. 2018 Viscous dissipation of surface waves and its relevance to analogue gravity experiments. arXiv:1706.05255v3.
- SCHULKES, R. M. S. M., HOSKING, R. J. & SNEYD, A. D. 1987 Waves due to a steadily moving source on a floating ice plate. Part 2. *J. Fluid Mech.* **180**, 297–318.
- SMORODIN, A. I. 1972 Waves at the fluid surface during the motion of a submerged ellipsoid of revolution. *J. Appl. Math. Mech.* **36** (1), 137–141.

- SPRIGGS, J. H., MESSITER, A. F. & ANDERSON, W. J. 1969 Membrane flutter paradox – an explanation by singular-perturbation methods. *AIAA J.* **7** (9), 1704–1709.
- SYGULSKI, R. 2007 Stability of membrane in low subsonic flow. *Intl J. Non-Linear Mech.* **42** (1), 196–202.
- TIOMKIN, S. & RAVEH, D. E. 2017 On the stability of two-dimensional membrane wings. *J. Fluids Struct.* **71**, 143–163.
- TRIANTAFYLLOU, G. S. 1992 Physical condition for absolute instability in inviscid hydroelastic coupling. *Phys. Fluids A* **4**, 544–552.
- TRIANTAFYLLOU, M. S. & TRIANTAFYLLOU, G. S. 1991 Frequency coalescence and mode localization phenomena: a geometric theory. *J. Sound Vib.* **150** (3), 485–500.
- VEDENEEV, V. V. 2004 Instability of an unbounded elastic plate in a gas flow. *Fluid Dyn.* **39** (4), 526–533.
- VEDENEEV, V. V. 2016 On the application of the asymptotic method of global instability in aeroelasticity problems. *Proc. Steklov Inst. Math.* **295**, 274–301.
- WEINFURTNER, S., TEDFORD, E. W., PENRICE, M. C. J., UNRUH, W. G. & LAWRENCE, G. A. 2011 Measurement of stimulated Hawking emission in an analogue system. *Phys. Rev. Lett.* **106**, 021302.
- WHITHAM, G. B. 1999 *Linear and Nonlinear Waves*. John Wiley & Sons.
- ZHANG, R., QIN, H., DAVIDSON, R. C., LIU, J. & XIAO, J. 2016 On the structure of the two-stream instability-complex G-Hamiltonian structure and Krein collisions between positive- and negative-action modes. *Phys. Plasmas* **23**, 072111.

Chapter 5

Radiative instability of a finite Nemtsov membrane

*"A Cat may look at a King, and a
swaynes eye hath as high a reach as a
Lords looke."*

Robert Greene, *Never too Late*

In contrast with Chapter 4 where a membrane with infinite extension in the direction of the flow has been analyzed (Labarbe and Kirillov, 2020), we investigate hereafter the case of the finite chord length. Although Nemtsov himself already considered this particular system, he did not provide many details on the calculations nor on the interpretation of his results and restricted his analysis to the limit of shallow water (Nemtsov, 1985). For that reason, we decided to investigate further from his original ideas by first, providing an exhaustive derivation and comprehension of the shallow water approximation and then, extending this study to the general settings of a finite membrane submerged in a finite depth layer. However, as shown in detail below, this general treatment is highly challenging to solve due to its inherent mathematical structure and requires thus to develop new analytical and numerical methods.

The main idea in reviving Nemtsov problem for us was to provide a paradigmatic example of the classical Lamb oscillator problem and its connection to the notion of damping due to radiation (Lamb, 1900), but for the understanding of radiation-induced instabilities (Hagerty, Bloch, and Weinstein, 2003). It has indeed been proven that a dynamical system coupled with a radiator, described thus through a wave-like equation, can exhibit instability in the form of oscillatory motions, or flutter once the gyroscopic stabilization of such system is destroyed (Bloch et al., 2004). In that sense, Nemtsov membrane provides an excellent model for the understanding of this phenomenon, as it includes an elastic structure with infinitely many modes of vibrations that is coupled with a free surface flow continuum, propagating thus dispersive surface gravity waves.

In addition to the previous interpretation, an interesting feature of this classical problem relates to the notion of anomalous Doppler effect, a well-known phenomenon in plasma physics that corresponds to a radiation of energy inside the Cherenkov cone (Ginzburg and Frank, 1947; Tamm, 1960).

Originally, this famous effect has been observed and examined in the context of relativistic charged particles travelling with a superluminal motion through a dielectric non-dispersive medium (Ginzburg and Frank, 1947). The electromagnetic radiation resulting from this motion describes a universal mechanism of emission of negative energy waves (Nezlin, 1976; Abramovich, Mareev, and Nemtsov, 1986; Gaponov-Grekhov, Dolina, and Ostrovskii, 1983), in the sense that kinetic energy of the source supplies both the kinetic energy of the particle and the increase in the internal energy of the source (Ginzburg, 1996; Shi et al., 2018). We therefore interpret the case where the motion of the fluid particles in Nemtsov system exceeds the speed of propagation of waves along the membrane, as an illustration of this fundamental phenomenon. Moreover, we use this argument to predict the location of instability domains in the parameter space associated with both elastic waves and flow velocities (Metrikin, 1994).

The difficulty in considering the finite size of the Nemtsov membrane is due to the use of inverse Fourier transform to recover the velocity potential of the flow from the original boundary value problem (Nemtsov, 1985; Labarbe and Kirillov, 2020). Consequently, this potential is expressed as an improper integral that is highly nonlinear in the eigenfrequency considered. We present the derivation of an integro-differential equation following from this analysis and apply the same treatment as Nemtsov to solve it in the shallow water limit, namely by applying the Laplace transform on the equation (Nemtsov, 1985). In the shallow water approximation, the improper integral simplifies and analytic expressions can be obtained. Surprisingly, we obtain the dispersion relation governing the stability of the finite system in terms of the dispersion relation of the membrane with infinite extension. From the application of perturbation theory on this expression (Kirillov, 2021), we recover explicit forms of growth rate and frequency with respect to the added mass ratio parameter and residue calculus. It is interesting to notice the presence of intertwining instability pockets in the plane of flow velocity versus the speed of propagation of elastic waves reminding a similar characteristic inherent to the stability maps of some forms of the Hill equation (Broer and Levi, 1995). To compare with a recent work on the splitting of the domain inside the Cherenkov cone into two distinct sub-domains, corresponding respectively to the superlight (superluminal) normal and inverse Doppler effect (Shi et al., 2018), we derive an integral expression for the surface displacement of the flow. This expression allows us to explore the fluid dynamic analogue of this new phenomenon and to establish a global criterion for the predominance of one of the domains inside the Cherenkov cone, from a natural argument of '*phase synchronism*' (Nemtsov, 1985; Metrikin, 1994).

To complete our analysis in the more global but challenging configuration of Nemtsov system, we assume the fluid layer to possess a finite depth, along with the argument of finite chord length for the membrane. This configuration has not been considered by Nemtsov because of its complexity, mainly due to the non-polynomial and nonlinear character of the boundary eigenvalue problem. Although non-polynomial eigenvalue problems arise frequently in problems of fluid-structure interactions (Cho and Kim,

1998; Alben, 2008; Shelley and Zhang, 2011), they are notoriously hard to solve even numerically (Magri, 2019). We therefore present an original approach developed for this purpose, combining a Galerkin decomposition of the eigenfunctions (Vedeneev, 2012; Mougel and Michelin, 2020), a complex analysis of the locations of the poles in the integrand of the improper integral (Bindel and Hood, 2015) and a numerical application of Cauchy residue theorem to solve the algebraic nonlinear eigenvalue problem. Applying finally a Newton-like method on the matrix eigenvalue pencil (Mehrmann and Voss, 2004; Güttel and Tisseur, 2017; Magri, 2019), we recover with great accuracy the eigenfrequencies of the finite system in the limit of small coupling parameter (Mensah, Orchini, and Moeck, 2020). From the interpretation of these unprecedented results, we observe an asymptotic convergence of the finite depth solution with the previously derived shallow water solutions in the limit of large aspect ratio, corresponding thus to a long membrane and a thin layer. In addition, new patterns of instability can be noticed in the parameter spaces associated with the membrane chord length, in agreement with the analytical predictions of shallow- and deep water approximations. To the best of our knowledge, the procedure established along this study remains original and can easily be extended to various applications involving similar equations of motion.

This chapter is presented in the form of a draft that has been written by O.N. Kirillov and I (Labarbe and Kirillov, 2021), submitted to the peer-reviewed journal '*Communications in Nonlinear Science and Numerical Simulation*'. As previously, the contributions of both authors are equally shared within the entire article.

Radiation-induced instability of a finite-chord Nemtsov membrane

Joris Labarbe, Oleg N. Kirillov

Northumbria University, Newcastle upon Tyne, NE1 8ST, UK

Abstract

We consider a problem of stability of a membrane of an infinite span and a finite chord length that is submerged in a uniform flow of finite depth with free surface. In the shallow water approximation, Nemtsov (1985) has shown that an infinite-chord membrane is susceptible to flutter instability due to excitation of long gravity waves on the free surface if the velocity of the flow exceeds the phase velocity of the waves and placed this phenomenon into the general physical context of the anomalous Doppler effect. In the present work we derive a full nonlinear eigenvalue problem for an integro-differential equation in the case of the finite-chord Nemtsov membrane in the finite-depth flow. In the shallow- and deep water limits we develop a perturbation theory in the small added mass ratio parameter acting as an effective dissipation parameter in the system, to find explicit analytical expressions for the frequencies and the growth rates of the membrane modes coupled to the surface waves. This result reveals a new intricate pattern of instability pockets in the parameter space and allows for its analytical description. The case of an arbitrary depth flow with free surface requires numerical solution of a new non-polynomial nonlinear eigenvalue problem. We propose an original approach combining methods of complex analysis and residue calculus, Galerkin discretization, Newton method and parallelization techniques implemented in MATLAB to produce high-accuracy stability diagrams within an unprecedentedly wide range of system's parameters. We believe that the Nemtsov membrane appears to play the same paradigmatic role for understanding radiation-induced instabilities as the famous Lamb oscillator coupled to a string has played for understanding radiation damping.

Keywords: radiation-induced instabilities, dissipation through dispersion, radiation damping, anomalous Doppler effect, flow-structure interaction, nonlinear eigenvalue problem

2010 MSC: 70K50, 76E17, 35P30, 65N30

1. Introduction

Exactly 120 years ago Lamb (1900) had proposed a model of a one-dimensional harmonic oscillator without damping constrained to move in the vertical direction and coupled to a horizontally taut semi-infinite elastic string [1]. Quite surprisingly, he had found that the emission of traveling waves in the continuum by the oscillating mass contributes an effective Rayleigh damping correction term to the oscillator equation yielding decay of its vertical motion [1]. In the course of time the radiating *Lamb oscillator* became paradigmatic for understanding the *radiation damping* in open and damped subsystems of closed conservative systems and gave rise to a number of abstract models of dispersion of energy from a ‘small’, usually finite-dimensional, subsystem to a ‘large’, infinite-dimensional wave field [2, 3, 4, 5, 6, 7, 8, 9, 10, 11, 12, 13].

Remarkably, deep understanding of the radiation damping (including Lamb's model) involves Lax-Phillips scattering theory [3, 4, 5, 7, 13, 14] and the concept of resonance, quasimode or metastable (Gamow) state in the context of open systems [5, 8, 9, 11, 15]. Resonant interaction of bound states (eigenfunctions) and radiation (continuous spectral modes), leading to energy transfer from the discrete to continuum modes,

Email addresses: joris.labarbe@northumbria.ac.uk (Joris Labarbe), oleg.kirillov@northumbria.ac.uk (Oleg N. Kirillov)

is a universal mechanism describing even asymptotic stability of solitary type solutions, when radiation going away from the solitons to infinity leaves them to move freely [8, 9, 11].

To illustrate radiating vibratory motions in dimensions higher than one Love (1904) presented several extensions of Lamb's model that included decay of electromagnetic oscillations of a perfectly conducting spherical antenna due to emission of electromagnetic waves and decay of mechanical vibrations of an elastic sphere emitting acoustic waves [2, 3]. In [4, 7] in the frame of the resonant scattering theory an important question of interaction between the vibrational modes of a submerged solid and the scattering functions in the fluid for both light and heavy fluid loading has been discussed. It was established that modes of the fluid-solid system at zero fluid-loading can be identified with the solid whereas at infinite fluid-loading they correspond to scattering frequencies of the fluid alone with a soft boundary condition. The intermediate values of the fluid-loading parameter appear to be the most complicated as it is impossible to label the mode of the fluid-solid system as corresponding solely to a 'solid mode' or a 'fluid mode' [7].

In [16, 17] gyroscopic versions of the Lamb model were proposed, rather artificial however, such as the spherical pendulum and a rigid body with internal rotors, coupled either to the classical non-dispersive wave equation or to a dispersive equation of Klein-Gordon form. In such systems, the gyroscopic Lamb oscillator is susceptible to instabilities induced by wave emission (the *radiation-induced instabilities*), to which such physically important effects belong as the famous Chandrasekhar-Friedman-Schutz (CFS) instability of rotating stars caused by emission of gravitational waves [18, 19, 20, 21, 22], acoustic version of CFS instability [23], and the instability of vortices in a stratified rotating fluid due to emission of internal gravity waves [24] as it happens, e.g., in the events of coalescence of lenticular vortices observed in recent experiments [25].

In a recent work [26] attention was paid to an overlooked classical model that appears to be a perfect candidate for the role of the Lamb oscillator in the field of radiation-induced instabilities. This is the model, proposed by Nemtsov in 1985, of an elastic membrane resting on the bottom of a uniformly flowing fluid layer of finite depth and loosing its stability due to emission of surface gravity waves [27]. Nemtsov's membrane having infinitely many modes of free vibrations plays the role of a 'small' subsystem, the fluid with the free surface is the 'large' continuum supporting propagation of dispersive surface gravity waves, and the motion of the flow can contribute to a gyroscopic coupling [28].

We remark that scattering of surface gravity waves even by rigid horizontal submerged plates already has numerous applications in marine and coastal engineering such as submerged breakwaters or underwater wave lenses that allow exchange of water and hardly disturb horizontal currents [29, 30, 31]. The need for light, inexpensive and rapidly deployable wave barriers requires taking into consideration submerged horizontal flexible plates and membranes [31, 32]. Recent applications in energy harvesting exploit fluid-structure interaction, leading to the excitation (flutter) of an elastic plate or membrane, usually referred to as a flag [33, 34], due to radiation of surface gravity waves when immersed in a moving flow with a free surface [35]. Another relevant setting comes from the problem of turbulent friction reduction in a boundary layer by using compliant coatings. In particular, it involves studying propagation of waves in a layer of a viscoelastic material of finite thickness when a layer of an ideal incompressible fluid is moving over it [36].

The scattering theory formalism is efficient for analytical derivation of such important quantities as the reflection and transmission coefficients and displacement of the free surface of the flow [31]. However, investigation of stability of a radiating object requires different methods. In a related set of problems on the stability of oscillations of moving wave emitters (e.g. radiation of elastic waves in rails by high-speed trains [37] and emission of internal or surface gravity waves by a spherical body on an elastic spring moving parallel to the interface of two liquids [38, 39]), the theory of Cherenkov radiation for structureless particles [10, 40] and its extension by Ginzburg and Frank [41] to the particles having internal degrees of freedom, provides important clues both for derivation of necessary and sufficient criteria for instability and for better understanding radiation-induced instabilities in the general physical context [42].

Originally, Cherenkov radiation has been the name for the phenomenon that a charged particle, moving relativistically through a dielectric non-dispersive medium at constant speed v higher than the phase velocity of light $v_p < c$ in the medium, becomes a source of electromagnetic radiation [10, 43, 44, 45, 46]. If the source has a natural frequency ω_0 in its own static frame, then in the observer static frame one receives the far-field angular distribution of radiation with frequency $\omega = \omega_0 \gamma^{-1} / (1 - vv_p^{-1} \cos \theta)$, where γ is the Lorentz factor, that turns out to be concentrated in the forward direction on a conical surface making an angle θ

with the velocity vector [45, 46]. The angle $\theta_{ch} = \arccos(v_p/v)$, which is possible only if $\omega_0 = 0$, defines the *Cherenkov cone* with the angular aperture $2\theta_{ch}$, i.e. a locus in the space of wavenumbers of resonant modes into which the Cherenkov radiation from the structureless particle occurs [43, 45, 46]. In this case, the radiated electromagnetic field is spatially concentrated on a wave front forming a Mach cone with the angular aperture $\pi - 2\theta_{ch}$ behind the source, which is the apex of the cone [40, 45].

A source oscillating with the natural frequency $\omega_0 > 0$ and moving at a velocity $v < v_p$ or at a superluminal velocity $v > v_p$ but emitting outside the Cherenkov cone, i.e. under the condition $\cos \theta < v_p/v$, experiences conventional Doppler effect with the increase in $\omega > 0$ while approaching the observer [45, 46]. If the superluminal oscillator emits inside the Cherenkov cone then the condition $\cos \theta > v_p/v$ implies $\omega < 0$, which means that the source becomes excited by passing from a lower energy level to an upper one during the emission process [40, 41]. That is, the kinetic energy of the source supplies both the energy of the emitted photon and the positive increase in the internal energy of the source [43, 46]. Radiation inside the Cherenkov cone is known as the *anomalous Doppler effect* [40, 41, 42, 44]. Recent work [46] further distinguishes between the range $v_p/v < \cos \theta < 2v_p/v$ and the range $\cos \theta > 2v_p/v$ inside the Cherenkov cone as resulting in the superlight (superluminal) normal and inverse Doppler shift, respectively. It turns out that the major part of the change in the kinetic energy of the source contributes to a positive increase in the internal energy of the source (photon) for the superlight inverse (normal) Doppler effect [46].

The same basic process of generalized Cherenkov emission is characteristic of all the emission processes that take place when a uniformly moving source is coupled to some excitation field, even in the presence of dispersion that provides an individual Cherenkov cone for each frequency [40]: as soon as the source velocity exceeds the phase velocity of some mode of the field, the latter becomes continuously excited [45]. For the sources having internal degrees of freedom, this serves also as a necessary condition for the presence in the space of parameters of a domain of instability of the source due to the anomalous Doppler effect [37]. A sufficient condition for the radiation-induced instability is the prevalence of reaction of waves emitted inside the Cherenkov cone over those emitted outside it [37]. Therefore, it is not surprising that already Tamm in his Nobel lecture foresaw application of the anomalous Doppler effect to describe “self-excitation of some particular modes of vibrations of a supersonic airplane” [40, 43].

In [27] Nemtsov considered stability of the membrane under the surface of the uniform flow in the limits of (i) shallow water and (ii) vanishing added mass ratio [47] that measures coupling between the membrane and the flow and serves as an effective damping parameter. Since the surface gravity waves are *non-dispersive* in the shallow water approximation, the formalism of Cherenkov radiation and anomalous Doppler effect applied to the infinite-chord-length Nemtsov membrane predicts its instability in the range where the velocity of the flow is exceeding the phase velocity of the surface gravity waves (as a consequence, they appear to be traveling backward in the frame moving with the flow) and exactly when the phase of the induced surface gravity wave is equal to the phase of the elastic wave propagating in the membrane [27]. However, Nemtsov’s shallow water result, being effective in uncovering fundamental physical reasons for the membrane destabilization, could not answer to a question of practical importance, namely, what is the domain of instability when the parameters of the system are allowed to take arbitrary values?

In [26] we extended analysis of Nemtsov’s membrane with infinite chord to the case of *dispersive* surface gravity waves by allowing the fluid layer to have arbitrary depth and the added mass ratio parameter to take arbitrary non-negative values. New complete dispersion relation has been derived and analyzed with the perturbation theory for multiple roots of polynomials [48] to obtain an explicit analytical approximation to the critical flutter velocity that is in excellent agreement with the numerical computation of the full stability map. Moreover, we have identified in [26] a new instability domain arising from a conical singularity in the parameter space that could not be detected in the restrictive assumptions of [27]. This new domain is associated with a low-frequency flutter for short wavelengths and corresponds to the case when the velocity of propagation of elastic waves in the membrane is much smaller than the velocity of the flow. Finally, an elegant and applicable explicit expression for the total averaged energy has been derived by means of the direct integration and its reduction to the Cairns form involving the derivatives of the dispersion relation with respect to the frequency of oscillations has been proven. It was demonstrated that the radiation-induced instability of the membrane is the result of collision of modes of positive and negative energy and can be interpreted in terms of wave emission in the domain of the anomalous Doppler effect [26].

In the present work, we consider a model of Nemtsov's membrane in its entirety, with a flow of finite depth and a membrane of finite chord. We formulate the dimensionless boundary value problem for this system and by means of Fourier analysis recover an explicit expression for the velocity potential in the form of an improper integral. Determining the domain of dependence from the Cherenkov condition written for dispersive surface gravity waves, we extract an integro-differential equation for the membrane displacement in the presence of the flow, which is our main object of investigation.

Following [27] we first present a rigorous general treatment of the integro-differential equation in the shallow-water limit by means of the Laplace transform and complex analysis. We obtain an integral eigenvalue relation and develop a systematic procedure for its analysis based on the perturbation theory with respect to the small added mass ratio parameter and residue calculus. As a result, we find explicit expressions for the frequencies and growth rates of membrane's modes coupled to the free surface as a series in the small parameter. Analysing the first-order approximation we can treat membrane's destabilization as a classical dissipation-induced instability [48, 49, 50, 51, 52]. Plotting neutral stability curves in the plane of velocity of the flow versus the speed of propagation of elastic waves along the membrane we uncover a new and intricate pattern of self-intersecting instability pockets reminding a similar phenomenon characteristic of some forms of the Hill equation [53] and describe it explicitly in an analytical form. We derive an integral expression for the free surface of the flow which allows us to find and explore the fluid dynamical analogue to the superlight normal and inverse Doppler effects [46].

The case of the finite depth of the fluid layer requires numerical solution of the boundary eigenvalue problem for the original integro-differential equation. This investigation involves a thorough treatment of the improper integral using complex analysis with the subsequent Galerkin decomposition of the solution to generate an algebraic nonlinear and non-polynomial in the eigenvalue parameter eigenvalue problem. The non-polynomial dependence on the eigenvalue parameter arises in the coupling term with the added mass ratio parameter as a factor. Setting the latter parameter to zero, we obtain a standard quadratic eigenvalue problem determining the free membrane modes. Once taken into consideration, the coupling term 'turns on' the radiative instability mechanism tending to excite the flutter of the membrane.

We notice that non-polynomial eigenvalue problems frequently occur in the studies of fluid-structure interactions, see e.g. [33, 54], and are notoriously hard to solve even numerically. The methods for their solution are a hot topic in modern numerical mathematics and linear algebra communities, see e.g. [55, 56, 57, 58], where a broad range of approaches is discussed. Most of the methods presented are either based on Newton-Raphson iterative process or on contour integration and we are restricting ourselves to the former.

In order to reach an acceptable convergence rate of the Newton method, we derive the Jacobian in an analytical form using residue calculus and complex analysis instead of approximating it numerically. Since the domain of integration in our problem is one-dimensional and we intend to keep high accuracy of our numerical scheme, we use the Legendre-Gauss-Lobatto quadrature rule to approximate the integrals in the Galerkin discretization. Nodes and weights of this spectral collocation method are recovered using the Golub-Welsch algorithm [59], which is based on the inversion of a linear system obtained from the three-term recurrence relation for Legendre polynomials. The computed eigenvalues correspond to the quadrature points, while the eigenvectors are used to recover the weights. This spectral quadrature is able to reach computer accuracy with less than 20 nodes of discretization and is used all over our code that has been fully implemented and parallelized in MATLAB using the Parallel Computing Toolbox available from the software and run on the High Performance Cluster at Northumbria University.

To the best of our knowledge, the approach developed in our work is original and making use of it, we are able to recover the eigenfrequencies of the complete system and hence, to perform an exhaustive stability analysis of the finite-chord Nemtsov membrane. From the numerically found growth rates we recover stability maps for the finite-chord membrane in the finite depth layer and compare with the shallow water approximation. We show that in the limit of infinite chord length the neutral stability boundaries perfectly correspond to the shallow water boundaries found in [26]. We establish that there is a critical chord length such that the shorter membranes cannot be destabilized. The most intriguing finding is, however, the chains of intertwining instability pockets, which our method is able to resolve, thus confirming its excellent convergence and accuracy. We believe that our procedure is applicable to a broad class of fluid-structure interaction problems that require solving nonlinear eigenvalue problems.

2. Mathematical formulation

Following [26], in a Cartesian coordinate system $OXYZ$, we consider an inextensible elastic rectangular membrane strip of constant thickness h , density ρ_m , and tension T along the membrane chord in the X -direction. The membrane has infinite span in the Y -direction and is held at $Z = 0$ at the leading edge ($X = 0$) and at the trailing edge ($X = L$) by simple supports.

The membrane is initially still and flat, immersed in a layer of inviscid, incompressible fluid of constant density ρ , with free surface at the height $Z = H$. The two-dimensional flow in the layer is supposed to be irrotational and moving steadily with velocity v in the positive X -direction. Therefore, the system is solved under the potential theory as it is the case in the original paper by Nemtsov [27]. The bottom of the fluid layer at $Z = 0$ is supposed to be rigid and flat for $X \in (-\infty, 0] \cup [L, +\infty)$.

In contrast to Nemtsov [27] who assumed that vacuum exists below the membrane, we suppose that a motionless incompressible medium of the same density ρ is present below the membrane with a pressure that is the same as the unperturbed pressure of the fluid [26]. The system is in a uniform gravity field acting in the negative Z -direction with g standing for the gravity acceleration.

Let $w(X, t)$, where t is time, be a small vertical displacement of the membrane, $u(X, t)$ the free surface elevation, and $\varphi(X, Z, t)$ the potential of the fluid.

Following [26] we choose the height of the fluid layer, H , as a length scale, and ω_0^{-1} , where $\omega_0 = \sqrt{g/H}$, as a time scale to introduce the dimensionless time and coordinates

$$\tau = t\omega_0, \quad x = \frac{X}{H}, \quad y = \frac{Y}{H}, \quad z = \frac{Z}{H}, \quad (1)$$

the dimensionless variables

$$\xi = \frac{w}{H}, \quad \eta = \frac{u}{H}, \quad \phi = \frac{\omega_0}{gH}\varphi, \quad (2)$$

the dimensionless parameters of the added mass ratio [47] and membrane chord length

$$\alpha = \frac{\rho H}{\rho_m h}, \quad \Gamma = \frac{L}{H}, \quad (3)$$

and two dimensionless numbers

$$M_w = \frac{c}{\sqrt{gH}}, \quad M = \frac{v}{\sqrt{gH}}, \quad (4)$$

where $c^2 = T/(\rho_m h)$ is the squared speed of propagation of elastic waves in the membrane and \sqrt{gH} is the speed of propagation of long surface gravity waves in the shallow water approximation. The chosen scale for the velocity explains our choice of notation in (4) because the Froude number $\frac{v}{\sqrt{gH}}$ can be treated as a Mach number in the non-dispersive shallow water limit which simplifies comparison of our results with that of the supersonic aerodynamics [54].

Denoting the fluid domain by Ω , the free surface, membrane, and rigid wall borders by $\partial\Omega_0$, $\partial\Omega_1$, and $\partial\Omega_2$, respectively, and assuming the time dependence for the velocity potential ϕ and the membrane displacement ξ in the form of $e^{-i\omega\tau}$ we arrive at the dimensionless boundary value problem [26]

$$\nabla^2\phi = 0, \quad \text{in } \Omega \quad (5a)$$

$$\nabla\phi \cdot \mathbf{n} + (-i\omega + M\partial_x)^2\phi = 0, \quad \text{on } \partial\Omega_0 \quad (5b)$$

$$\nabla\phi \cdot \mathbf{n} + (-i\omega + M\partial_x)\xi = 0, \quad \text{on } \partial\Omega_1 \quad (5c)$$

$$\nabla\phi \cdot \mathbf{n} = 0, \quad \text{on } \partial\Omega_2 \quad (5d)$$

$$\omega^2\xi + M_w^2\partial_x^2\xi + \alpha(-i\omega + M\partial_x)\phi = 0, \quad \text{on } \partial\Omega_1 \quad (5e)$$

$$\xi(0) = \xi(\Gamma) = 0, \quad \text{on } \partial\Omega_1 \quad (5f)$$

where \mathbf{n} is the vector of the outward normal to a surface and, for simplicity, we retain the same notation for the membrane displacement and the fluid potential after the separation of time.

As one can notice, the Laplace equation (5a) is supplemented with a combination of dynamic and kinematic free surface conditions (5b) and the impermeability conditions for the membrane (5c) and the walls (5d). The nonhomogeneous wave equation (5e) describes the physics along the membrane and is solved with the rigid boundary conditions (5f). This set of equations represents a boundary eigenvalue problem for the complex eigenfrequency ω and will be used for the stability analysis of the finite-chord Nemtsov membrane.

2.1. Velocity potential via inverse Fourier transform

As in the previous study [26], since the fluid layer is assumed to have an infinite extension in the x -direction, we can write, respectively, the Fourier transform of the velocity potential ϕ and its inverse

$$\hat{\phi}(\kappa, z, \omega) = \int_{-\infty}^{+\infty} \phi(x, z, \omega) e^{-i\kappa x} dx, \quad \phi(x, z, \omega) = \frac{1}{2\pi} \int_{-\infty}^{+\infty} \hat{\phi}(\kappa, z, \omega) e^{i\kappa x} d\kappa, \quad (6)$$

where κ is the dimensionless wavenumber.

With (6) taken into account, the Laplace problem (5a–5c) yields the boundary value problem for $\hat{\phi}$ in the Fourier space

$$\partial_z^2 \hat{\phi} - \kappa^2 \hat{\phi} = 0, \quad \text{in } \Omega \quad (7a)$$

$$\partial_z \hat{\phi} - (\omega - \kappa M)^2 \hat{\phi} = 0, \quad \text{on } \partial\Omega_0 \quad (7b)$$

$$\partial_z \hat{\phi} + \int_0^\Gamma (i\omega \xi(x') - M \partial_{x'} \xi(x')) e^{-i\kappa x'} dx' = 0, \quad \text{on } \partial\Omega_1 \quad (7c)$$

where x' is a curvilinear abscissa along the membrane. Expression (7c) is the Fourier transform of the impermeability condition (5c).

The general solution to equation (7a) is known to be

$$\hat{\phi}(\kappa, z, \omega) = A(\kappa, \omega) e^{\kappa z} + B(\kappa, \omega) e^{-\kappa z}, \quad (8)$$

where the functions A and B are to be determined from the boundary conditions (7b) and (7c). This yields an expression for $\hat{\phi}$ at $z = 0$

$$\hat{\phi}(\kappa, 0, \omega) = \frac{\kappa - (\omega - \kappa M)^2 \tanh \kappa}{\kappa[(\omega - \kappa M)^2 - \kappa \tanh \kappa]} \int_0^\Gamma (-i\omega + M \partial_{x'}) \xi(x') e^{-i\kappa x'} dx'. \quad (9)$$

Returning to the physical space by means of the inverse Fourier transform (6) we recover an explicit form for the potential disturbance

$$\phi(x, 0, \omega) = \frac{1}{2\pi} \int_0^\Gamma (-i\omega + M \partial_{x'}) \xi(x') \int_{-\infty}^{+\infty} \frac{\kappa - (\omega - \kappa M)^2 \tanh \kappa}{\kappa[(\omega - \kappa M)^2 - \kappa \tanh \kappa]} e^{i\kappa(x-x')} d\kappa dx'. \quad (10)$$

2.2. Integro-differential equation for membrane's deflection

Surface gravity waves on a non-moving finite-depth layer are in general dispersive with the phase speed $\sigma(\kappa) = \sqrt{\kappa \tanh \kappa / \kappa}$, which is varying between $\sigma_{DW} = 0$ when $\kappa \rightarrow +\infty$ (deep water) and $\sigma_{SW} = 1$ when $\kappa \rightarrow 0$ (shallow water) [26]. Suppose we have a uniform flow in the positive x -direction with the supercritical speed $M > \sigma(\kappa)$ as shown in Fig.1. Perturbation with the wavenumber κ of the flow surface from a point (x, y, ξ) of the membrane will spread from that point along concentric circles in the (x, y) plane with the phase speed $\sigma(\kappa)$, which are washed downstream as $M > \sigma(\kappa)$ [60, 61]. The point obstacle therefore affects only the flow pattern in the conical domain of influence [62]. The boundary of this downstream half of the Mach cone is the envelope of the moving and expanding circles centred at the points with the horizontal coordinates $x' \geq x$ [60, 61]. The presence of the point obstacle at x does not make itself felt at the points upstream ($x' < x$) and outside of the half-cone [60, 61].

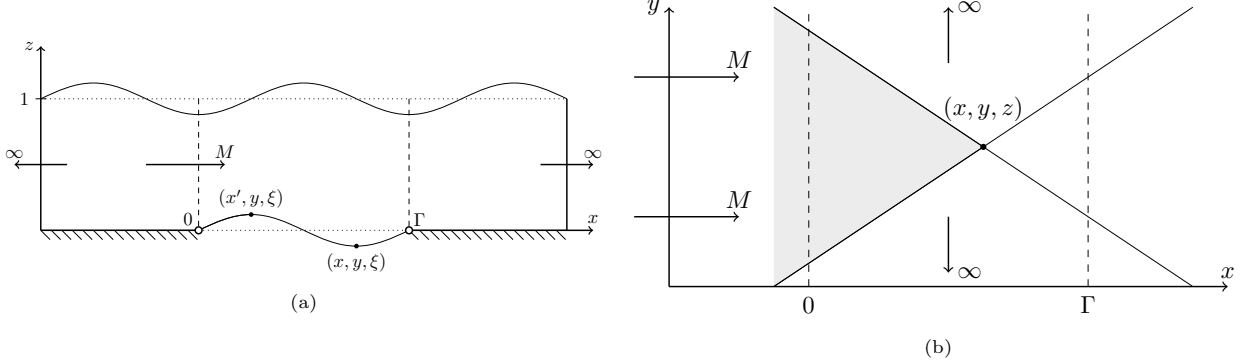


Figure 1: (a) Sketch of the Nemtsov system in the (x, z) -plane. (b) View of the system from above in the (x, y) -plane. A point obstacle at a position (x, y, ξ) in a uniform flow moving in the positive x -direction with a velocity $M > \sigma(\kappa)$ affects only the pattern of the surface gravity waves with the wavenumber κ in the (white) downstream Mach cone representing the domain of influence [60, 61, 62]. The (gray) upstream half of the Mach cone is the domain of dependence [60, 61, 62] at the point (x, y, z) .

On the other hand, the flow at the point (x, y, z) depends only on the flow in the upstream half of the same Mach cone (domain of dependence [62]), see Fig. 1(b) [60, 61]. Therefore, for $M > \sigma(\kappa)$ the perturbed potential (10) along the membrane with the finite chord length Γ at a given y is composed of all the single sources with coordinates (x', ξ) where $x' \in [0, x]$ as shown in Fig. 1(a). Hence, the interval of integration in the first integral in (10) can be truncated from $x' \in [0, \Gamma]$ to $x' \in [0, x]$ to match the domain of dependence. Inserting the modified in this manner expression (10) into (5e) yields the following integro-differential equation for the membrane displacement ξ

$$\omega^2 \xi + M_w^2 \partial_x^2 \xi = \frac{\alpha}{2\pi} (i\omega - M \partial_x) \int_0^x (-i\omega + M \partial_{x'}) \xi(x') \int_{-\infty}^{+\infty} \frac{\kappa - (\omega - \kappa M)^2 \tanh \kappa}{\kappa[(\omega - \kappa M)^2 - \kappa \tanh \kappa]} e^{i\kappa(x-x')} d\kappa dx'. \quad (11)$$

The equation (11) has to be solved with respect to the eigenfrequency ω as a nonlinear eigenvalue problem, which is generally a highly challenging task due to the presence of an improper integral. By this reason, in the next section we begin the analysis of (11) in the shallow water limit that will allow us to apply perturbation theory and derive explicit approximation of the flutter domain. With the guidance provided by the analytical solutions in the shallow- and deep-water limits we finally present a numerical method that eventually results in the solution of the full problem.

3. Shallow water analysis of the finite-chord Nemtsov membrane

The goal of this section is to extend the result of [27] by presenting a rigorous and general treatment of expression (11) in the shallow water approximation and provide new physical interpretation of the instability mechanism for a membrane of the finite chord in the finite-depth flow.

3.1. Velocity potential in the shallow water limit

Introducing the phase speed $\sigma = \omega/\kappa$ and re-writing the factor at $e^{i\kappa(x-x')}$ in the integrand of the improper integral in (11) as

$$\frac{1}{\kappa^2} \frac{1 - \kappa(\sigma - M)^2 \tanh \kappa}{[(\sigma - M)^2 - \frac{\tanh \kappa}{\kappa}]} = \frac{1}{\kappa^2} \left(\frac{1}{(\sigma - M)^2 - 1} + O(\kappa^2) \right) = \frac{1}{(\omega - \kappa M)^2 - \kappa^2} + O(1) \quad (12)$$

we find that in the long-wavelength (shallow-water) limit, $\kappa \rightarrow 0$, the velocity potential simplifies

$$\phi_{SW}(x) = \frac{1}{2\pi} \int_0^x (-i\omega + M \partial_{x'}) \xi(x') \int_{-\infty}^{+\infty} \frac{e^{i\kappa(x-x')}}{(\omega - \kappa M)^2 - \kappa^2} d\kappa dx' \quad (13)$$

and, after factorizing the denominator in the integrand, it can be further expressed in the equivalent form

$$\int_{-\infty}^{+\infty} \frac{e^{i\kappa(x-x')}\mathrm{d}\kappa}{(\omega - \kappa M)^2 - \kappa^2} = \frac{1}{M^2 - 1} \int_{-\infty}^{+\infty} \frac{e^{i\kappa(x-x')}}{(\kappa - p_1)(\kappa - p_2)} \mathrm{d}\kappa, \quad (14)$$

where the pole $p_1 = \omega/(M + 1)$ corresponds to the wave travelling forward along the membrane and $p_2 = \omega/(M - 1)$ to the wave travelling backward.

3.2. Explicit form of the velocity potential by means of residue calculus

For $M > 1$ the denominator in the expressions for the poles $p_{1,2}(\omega)$ always remains real and positive, only the (complex, in general) frequencies ω define the location of the poles in the complex κ -plane. In this configuration, we shall focus on the frequencies with positive imaginary parts ($\text{Im}(\omega) > 0$) to define a contour in the upper-half plane and integrate the expression (14).

We define the contour of integration \mathcal{C} as a semi-circular and positively oriented curve, of radius R , closed with a segment along the real axis as follows

$$\mathcal{C} = [-R, R] \cup \Delta_R, \quad \Delta_R = \{Re^{it}, 0 \leq t \leq \pi\}. \quad (15)$$

Applying the Cauchy residue theorem around the contour (15) yields [63]

$$\oint_{\mathcal{C}} F(z) \mathrm{d}z = \int_{-R}^R F(z) \mathrm{d}z + \int_{\Delta_R} F(z) \mathrm{d}z = 2\pi i \sum_{j=1}^2 \text{res}(F(z), p_j), \quad (16)$$

where $F(z) = f(z)e^{iz(x-x')}$ and $f(z) = [(\omega - zM)^2 - z^2]^{-1}$.

According to Jordan's lemma, since the function $f(z)$ is continuous for any $z \in \mathcal{C}$, except at the poles $p_{1,2}(\omega)$, and that we have $\lim_{R \rightarrow +\infty} |f(Re^{i\theta})| = 0$ for $\theta \in [0, \pi]$, the integral over Δ_R vanishes as we enlarge the radius. Therefore, the improper integral (14) reduces to [63]

$$\lim_{R \rightarrow +\infty} \int_{-R}^R F(\kappa) \mathrm{d}\kappa = \int_{-\infty}^{+\infty} F(\kappa) \mathrm{d}\kappa = 2\pi i \sum_{j=1}^2 \text{res}(F(\kappa), p_j). \quad (17)$$

In general, the residue $\text{res}(g(z), p)$ of a meromorphic function $g(z)$ having a simple pole p and a factorized denominator for this pole, can be found as $\text{res}(g(z), p) = \lim_{z \rightarrow p} (z - p)g(z)$. Hence, for $p_1 = \omega/(M + 1)$, $p_2 = \omega/(M - 1)$ and $F(\kappa)$ in the form of (14), we have [63]

$$\begin{aligned} \text{res}(F(\kappa), p_1) &= \lim_{\kappa \rightarrow p_1} \frac{1}{(M^2 - 1)} \frac{e^{i\kappa(x-x')}}{(\kappa - p_2)} = \frac{1}{(M^2 - 1)} \frac{e^{ip_1(x-x')}}{(p_1 - p_2)} = \frac{-e^{ip_1(x-x')}}{2\omega}, \\ \text{res}(F(\kappa), p_2) &= \lim_{\kappa \rightarrow p_2} \frac{1}{(M^2 - 1)} \frac{e^{i\kappa(x-x')}}{(\kappa - p_1)} = \frac{1}{(M^2 - 1)} \frac{e^{ip_2(x-x')}}{(p_2 - p_1)} = \frac{e^{ip_2(x-x')}}{2\omega}. \end{aligned} \quad (18)$$

With the residues (18) in the expression (17), the velocity potential (13) takes an explicit form

$$\begin{aligned} \phi_{SW}(x) &= \int_0^x (\omega + iM\partial_{x'}) \xi(x') \sum_{j=1}^2 \text{res}(F(\kappa), p_j) \mathrm{d}x', \\ &= \frac{1}{2\omega} \int_0^x (\omega + iM\partial_{x'}) \xi(x') \left[e^{ip_2(x-x')} - e^{ip_1(x-x')} \right] \mathrm{d}x', \\ &= \frac{-i}{2\omega} \int_0^x V(x') \left[e^{ip_1(x-x')} - e^{ip_2(x-x')} \right] \mathrm{d}x', \end{aligned} \quad (19)$$

which reproduces the result by Nemtsov, if we denote $V(x) = (-i\omega + M\partial_x)\xi(x)$ [27]. Note that the term $e^{ip_1(x-x')}$ corresponds to the normal Doppler effect due to emission of surface gravity waves of positive energy whereas the term $e^{ip_2(x-x')}$ to the anomalous Doppler effect due to emission of surface gravity waves of negative energy.

3.3. Explicit expression for the membrane displacement by means of Laplace transform

Substituting solution (19) with $u(x) = -iV(x)$ and $v(x) = e^{ip_2x} - e^{ip_1x}$ into the problem (11) yields

$$\omega^2 \xi(x) + M_w^2 \partial_x^2 \xi(x) + \frac{\alpha}{2\omega} (-i\omega + M\partial_x) \int_0^x u(x')v(x-x') dx' = 0, \quad (20)$$

which can be written as

$$\omega^2 \xi(x) + M_w^2 \partial_x^2 \xi(x) + \frac{\alpha}{2\omega} (-i\omega + M\partial_x) (u * v)(x) = 0, \quad (21)$$

where the symbol $*$ denotes the operator of convolution of two functions supported on the interval $[0, \infty)$.

Equation (21) supplemented with the boundary conditions (5e) for the displacement $\xi(x)$ is suitable to solve by the Laplace method. We recall that in the general case, the Laplace transform \mathcal{L} of an arbitrary function $g(x)$ is given as follows

$$\bar{g}(s) \equiv \mathcal{L}[g(x)] = \int_0^{+\infty} g(x)e^{-sx} dx, \quad s \in \mathbb{C}. \quad (22)$$

Also recall that if $h(x)$ is a convolution

$$h(x) = (u * v)(x) = \int_0^x u(x')v(x-x')dx',$$

then

$$\mathcal{L}[h(x)] = \bar{u}(s)\bar{v}(s). \quad (23)$$

Using Leibniz integral rule

$$\frac{d}{dx} h(x) = \frac{d}{dx} \int_0^x u(x')v(x-x')dx' = v(0)u(x) + \int_0^x \frac{dv(x-x')}{dx} u(x')dx', \quad (24)$$

we find the Laplace transform of the derivative of the convolution to be

$$\mathcal{L}[dh/dx] = \bar{u}(s)v(0) + \bar{u}(s)(s\bar{v}(s) - v(0)) = s\bar{u}(s)\bar{v}(s). \quad (25)$$

Following the definition in (22), applying the standard differentiation and integration properties of the Laplace transform to (21) and taking into account (23) and (25), we find

$$\omega^2 \bar{\xi}(s) + M_w^2 [s^2 \bar{\xi}(s) - s\xi(0) - \xi'(0)] - \frac{i\alpha}{2\omega} \bar{u}(s)\bar{v}(s)(\omega + isM) = 0, \quad (26)$$

where

$$\begin{aligned} \bar{u}(s) &= \omega \bar{\xi}(s) + iM [\bar{s}\bar{\xi}(s) - \xi(0)], \\ \bar{v}(s) &= \frac{1}{s-ip_2} - \frac{1}{s-ip_1} = \frac{i(p_2-p_1)}{(s-ip_1)(s-ip_2)} = -\frac{2i\omega}{(\omega+isM)^2+s^2}. \end{aligned} \quad (27)$$

Applying the boundary condition $\xi(0) = 0$ to the expressions (26) and (27) yields

$$(\omega^2 + s^2 M_w^2) \bar{\xi}(s) - \alpha \frac{(\omega + isM)^2}{(\omega + isM)^2 + s^2} \bar{\xi}(s) = M_w^2 \xi'(0). \quad (28)$$

Since the equation (28) is linear in $\bar{\xi}(s)$, we can isolate this term and invert the whole expression by means of Mellin's inverse formula to finally obtain

$$\xi(x) \equiv \mathcal{L}^{-1}[\bar{\xi}(p)] = \frac{1}{2\pi i} \lim_{T \rightarrow \infty} \int_{-T-i\nu}^{T-i\nu} \frac{M_w^2 \xi'(0)[(\omega - pM)^2 - p^2] e^{ipx}}{(\omega^2 - p^2 M_w^2)[(\omega - pM)^2 - p^2] - \alpha(\omega - pM)^2} dp, \quad (29)$$

where $p = -is$ and ν is a real number greater than the imaginary part of all the poles. The bounds in integral (29) define a line in the complex plane that is usually closed with a portion of a circle, thus delimiting a closed contour \mathcal{C}_B (commonly known as the Bromwich contour [63]). Using the same argument of Jordan's lemma as for (16), we prove that contribution of the circular integral is negligible in the limit of infinite radius. Then, another application of the Cauchy residue theorem to the contour integral allows an explicit computation of the inverse.

3.4. Integral eigenfrequency relation

Requiring $\xi(x)$ in the expression (29) to vanish at $x = \Gamma$ in accordance with (5e), we obtain the following eigenfrequency relation

$$\xi(\Gamma) = \frac{M_w^2 \xi'(0)}{2\pi i} \oint_{\mathcal{C}_B} \frac{[(\omega - pM)^2 - p^2] e^{ip\Gamma}}{(\omega^2 - p^2 M_w^2)[(\omega - pM)^2 - p^2] - \alpha(\omega - pM)^2} dp = 0, \quad (30)$$

which can be written as follows

$$\xi(\Gamma) = \frac{M_w^2 \xi'(0)}{2\pi i} D(\omega, \alpha) = 0, \quad (31)$$

where

$$D(\omega, \alpha) = \oint_{\mathcal{C}_B} \frac{e^{ip\Gamma}}{\mathcal{D}(\omega, \alpha, p)} dp, \quad (32)$$

and

$$\mathcal{D}(\omega, \alpha, p) = \omega^2 - p^2 M_w^2 - \alpha \frac{(\omega - pM)^2}{(\omega - pM)^2 - p^2}, \quad (33)$$

is nothing else but the shallow water dispersion relation of the membrane of the *infinite* chord length in the case of a medium with constant pressure and the same density as that of the fluid being present below the membrane [26].

An expression similar to (31), derived earlier by Nemtsov for the membrane of the finite chord length with vacuum below the membrane [27], naturally has the corresponding shallow water dispersion relation in the denominator of the integrand, which slightly differs from ours.

3.5. Perturbation of eigenfrequencies

In the case of $\alpha = 0$, the eigenvalue relation (31) reduces to

$$D(\omega, 0) = \oint_{\mathcal{C}_B} \frac{e^{ip\Gamma}}{\mathcal{D}(\omega, 0, p)} dp = \frac{1}{M_w^2} \oint_{\mathcal{C}_B} \frac{-e^{ip\Gamma}}{p^2 - p_0^2} dp = 0, \quad (34)$$

where $p_0 = \omega/M_w$. Applying the residue theorem to the last integral in (34), we find

$$D(\omega, 0) = \frac{1}{\omega M_w} \sin \left(\frac{\Gamma \omega}{M_w} \right) = 0,$$

which yields frequencies of the free (decoupled from the flow) membrane

$$\omega_n = \pi n \frac{M_w}{\Gamma} \neq 0, \quad n \in \mathbb{N}. \quad (35)$$

In contrast to Nemtsov, we develop a systematic approach based on the perturbation theory of simple eigenvalues ω_n to find how they are affected by a weak coupling to the flow with free surface [50, 51, 52]. Then, simple roots $\omega(\alpha)$ of the equation $D(\omega, \alpha) = 0$ can be represented as a series in α , $0 < \alpha \ll 1$, as follows [26, 48, 58, 64]

$$\omega = \omega_n - \alpha \frac{\partial_\alpha D}{\partial_\omega D} + o(\alpha), \quad \omega(0) = \omega_n. \quad (36)$$

Computing the partial derivatives and evaluating them at $\alpha = 0$ yields

$$\begin{aligned} \partial_\alpha D &= \frac{1}{M_w^2(M^2 - 1)} \oint_{\mathcal{C}_B} \frac{e^{ip\Gamma} (\omega_n - pM)^2}{(p^2 - p_{0,n}^2)^2 (p - p_{1,n})(p - p_{2,n})} dp, \\ \partial_\omega D &= -\frac{2\omega_n}{M_w^4} \oint_{\mathcal{C}_B} \frac{e^{ip\Gamma}}{(p^2 - p_{0,n}^2)^2} dp, \end{aligned} \quad (37)$$

where

$$p_{0,n} = \frac{\pi n}{\Gamma}, \quad p_{1,n} = \frac{\pi n}{\Gamma} \frac{M_w}{M+1}, \quad p_{2,n} = \frac{\pi n}{\Gamma} \frac{M_w}{M-1}.$$

Applying the residue theorem to the integrals in (37), we find

$$\begin{aligned} \partial_\omega D &= \frac{-i\Gamma^2}{n\pi M_w^3} (-1)^n, \\ \partial_\alpha D &= (-1)^n \frac{i\Gamma^3}{2\pi^2 n^2 M_w^4} \frac{(M_w^2 - M^2)^2 - M_w^2 - M^2}{(M_w^2 - M^2 - 1)^2 - 4M^2} \\ &\quad + \frac{i\Gamma^3}{2\pi^3 n^3 M_w^3} \left\{ \frac{(M-1)^2 \sin\left(\frac{\pi n M_w}{M-1}\right)}{(M_w^2 - (M-1)^2)^2} - \frac{(M+1)^2 \sin\left(\frac{\pi n M_w}{M+1}\right)}{(M_w^2 - (M+1)^2)^2} \right\} \\ &\quad + \frac{-\Gamma^3}{2\pi^3 n^3 M_w^3} \left\{ \frac{(M-1)^2 \left[(-1)^n - \cos\left(\frac{\pi n M_w}{M-1}\right)\right]}{(M_w^2 - (M-1)^2)^2} - \frac{(M+1)^2 \left[(-1)^n - \cos\left(\frac{\pi n M_w}{M+1}\right)\right]}{(M_w^2 - (M+1)^2)^2} \right\}. \end{aligned} \quad (38)$$

With the derivatives (38) the series expansion (36) takes the form

$$\begin{aligned} \omega &= \omega_n + \frac{\alpha}{2\omega_n} \frac{(M_w^2 - M^2)^2 - M_w^2 - M^2}{(M_w^2 - M^2 - 1)^2 - 4M^2} \\ &\quad + (-1)^n \frac{\alpha\Gamma}{2\pi^2 n^2} \left\{ \frac{(M-1)^2 \sin\left(\frac{\pi n M_w}{M-1}\right)}{(M_w^2 - (M-1)^2)^2} - \frac{(M+1)^2 \sin\left(\frac{\pi n M_w}{M+1}\right)}{(M_w^2 - (M+1)^2)^2} \right\} \\ &\quad + \frac{i\alpha\Gamma}{2\pi^2 n^2} \left\{ \frac{(M-1)^2 \left[1 - (-1)^n \cos\left(\frac{\pi n M_w}{M-1}\right)\right]}{(M_w^2 - (M-1)^2)^2} - \frac{(M+1)^2 \left[1 - (-1)^n \cos\left(\frac{\pi n M_w}{M+1}\right)\right]}{(M_w^2 - (M+1)^2)^2} \right\} + o(\alpha). \end{aligned} \quad (39)$$

In particular, from (39) we easily obtain the growth rate of the perturbed simple real eigenvalue ω_n

$$\text{Im}(\omega) = \frac{\alpha\Gamma}{2\pi^2 n^2} \left\{ \frac{(M-1)^2 \left[1 - (-1)^n \cos\left(\pi n \frac{M_w}{M-1}\right)\right]}{(M_w^2 - (M-1)^2)^2} - \frac{(M+1)^2 \left[1 - (-1)^n \cos\left(\pi n \frac{M_w}{M+1}\right)\right]}{(M_w^2 - (M+1)^2)^2} \right\}, \quad (40)$$

which, if re-written as follows

$$\text{Im}(\omega) = \frac{\alpha}{2\Gamma M_w^2} \left\{ \frac{p_{2,n}^2 [1 - (-1)^n \cos(p_{2,n}\Gamma)]}{(p_{2,n}^2 - p_{0,n}^2)^2} - \frac{p_{1,n}^2 [1 - (-1)^n \cos(p_{1,n}\Gamma)]}{(p_{1,n}^2 - p_{0,n}^2)^2} \right\}, \quad (41)$$

exactly reproduces the growth rate derived earlier by Nemtsov [27].

3.6. Stability diagrams in the shallow water limit

Setting to zero the linear in α approximation to the growth rate (41) of the n -th mode of the membrane, we can find an approximation to the neutral stability curve for this mode that subdivides the plane of parameters M and M_w into the domains of stability and flutter instability, Fig. 2.

First of all we observe a cluster of instability domains grouped in the region $M > M_w$ in Fig. 2. The threshold $M = M_w$ is visible in Fig. 2(c,d) as a black dotted line. For the Nemtsov membrane of infinite chord length the physical meaning of this threshold is the equality of the velocity of the flow to the phase speed of elastic waves propagating along the membrane, which is a consequence of the Cherenkov condition [26, 27]. However, in contrast to the infinite-chord membrane's stability map reported in [26], there are

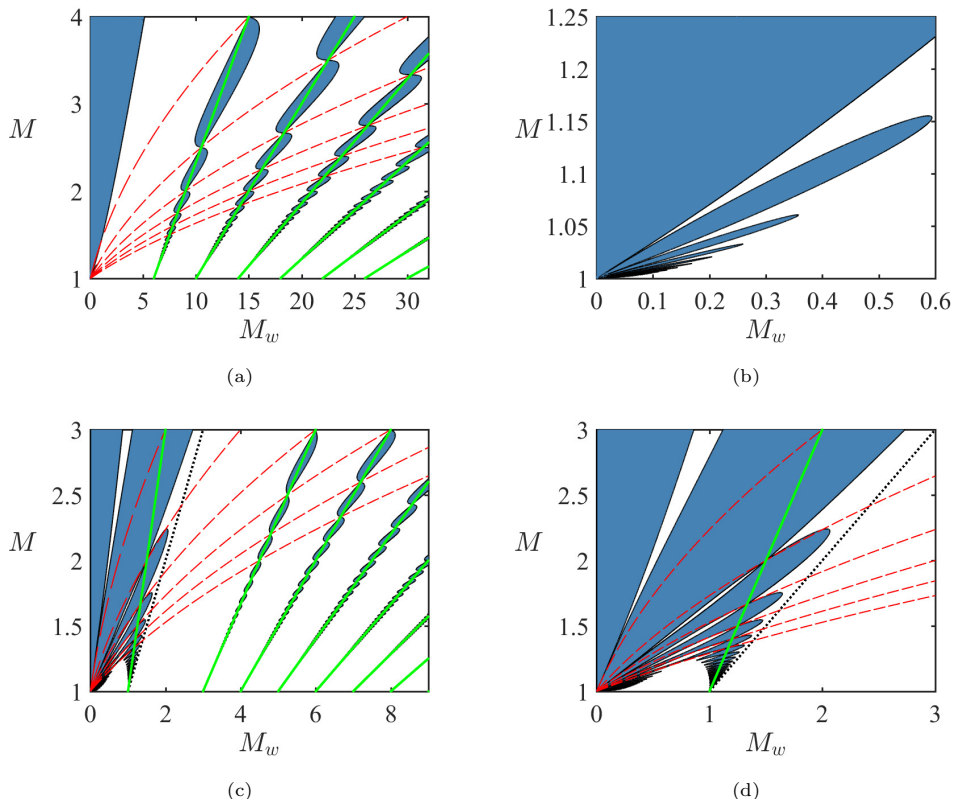


Figure 2: (Filled blue) Instability regions for (a,b) the first ($n = 1$) and (c,d) the fourth ($n = 4$) modes of the finite-chord Nemtsov membrane weakly coupled to the flow in the shallow water limit. The black dotted line is equation $M = M_w$. The green straight lines are given by $M_w = (2j/n + 1)(M + 1)$ for $j \in \mathbb{Z}$ and the red dashed curves by $M_w = k/n(M^2 - 1)$ for $k \in \mathbb{N}$. Notice absence of instability domains in a wide gap centered at $M_w = M + 1$ and corresponding to $j = 0$.

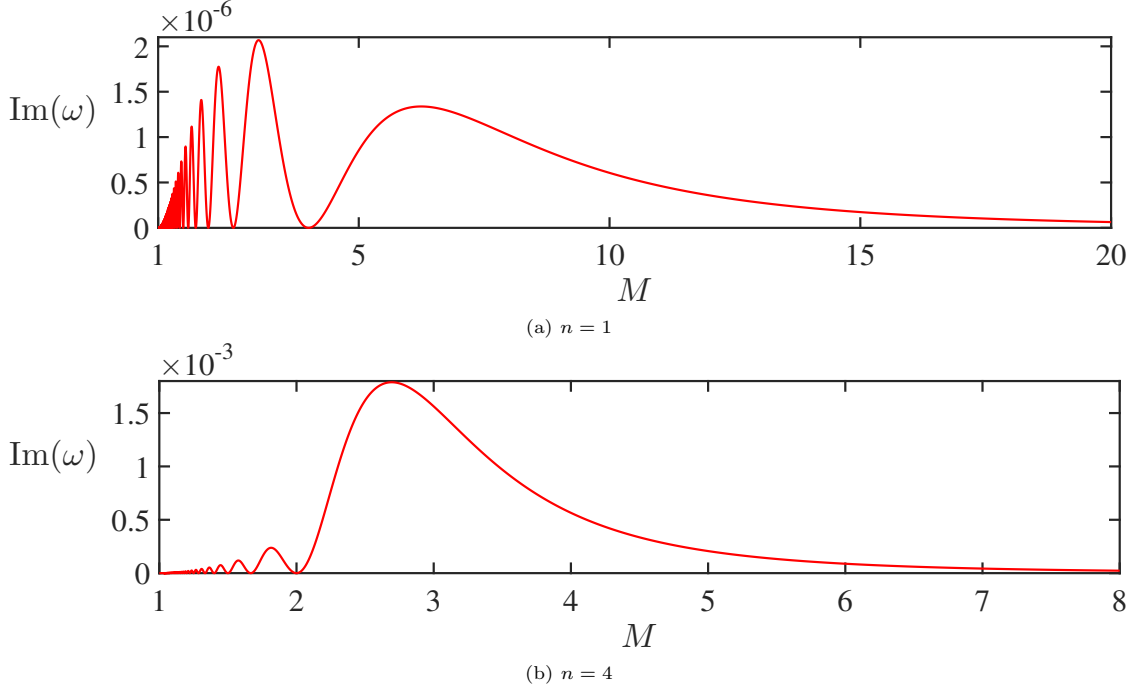


Figure 3: Growth rates of perturbed frequencies of the membrane along the line (42) with $\alpha = 10^{-3}$, $\Gamma = 10$ and (a) $n = 1$ and $j = 1$ with zeros at $M = 1 + 3/k$, $k \geq 1$ and (b) $n = 4$ and $j = -1$ with zeros at $M = 1 + 2/k$, $k > 1$.

infinitely many 'petals' of flutter instability for $M > M_w$ touching each other when $n > 1$, see Fig. 2(c,d). Quite surprisingly, the common points of the petals all belong to straight lines of the following form

$$M_w = \left(\frac{2j}{n} + 1 \right) (M + 1), \quad j \in \mathbb{Z}, \quad (42)$$

where j is a negative integer in the region $M > M_w$. For instance, $n = 4$ and $j = -1$ yield $M = 2M_w - 1$, which is a line passing through the point with $M_w = M = 1$ in Fig. 2(c,d). The growth rate along this line presented in Fig. 3(b) demonstrates vanishing to zero exactly at the common points of the instability regions.

These points are located exactly at the intersections of the straight lines (42) with the curves

$$M_w = \frac{k}{n} (M^2 - 1), \quad k \in \mathbb{N} \quad (43)$$

that are shown as red and dashed in Fig. 2. Solving equations (42) and (43) we obtain the coordinates of the crossing points

$$M = \frac{2j + k + n}{k}, \quad M_w = \frac{(2j + n)(2j + 2k + n)}{kn}. \quad (44)$$

For instance, for $j = -1$, $n = 4$ this yields $M = 1 + 2/k$ and $M_w = 1 + 1/k$ and for $k = 2$ results in $M = 2$ and $M_w = 3/2$, see Fig. 2(c,d) and Fig. 3(b).

Notice absence of instability domains in a wide gap centered at $M_w = M + 1$ and corresponding to $j = 0$ in (42), which is clearly visible in Fig. 2(a,c). In the case of an infinite-chord membrane with vanishing coupling parameter ($\alpha = 0$) the relation $M_w = M + 1$ corresponds to a crossing of dispersion curves of surface gravity waves and elastic waves in the membrane that unfolds into an avoided crossing (stability) for $\alpha > 0$ [26]. We can conclude therefore that this very property of an infinite-chord membrane manifests itself as a stability gap at $M_w = M + 1$ for the finite-chord membrane.

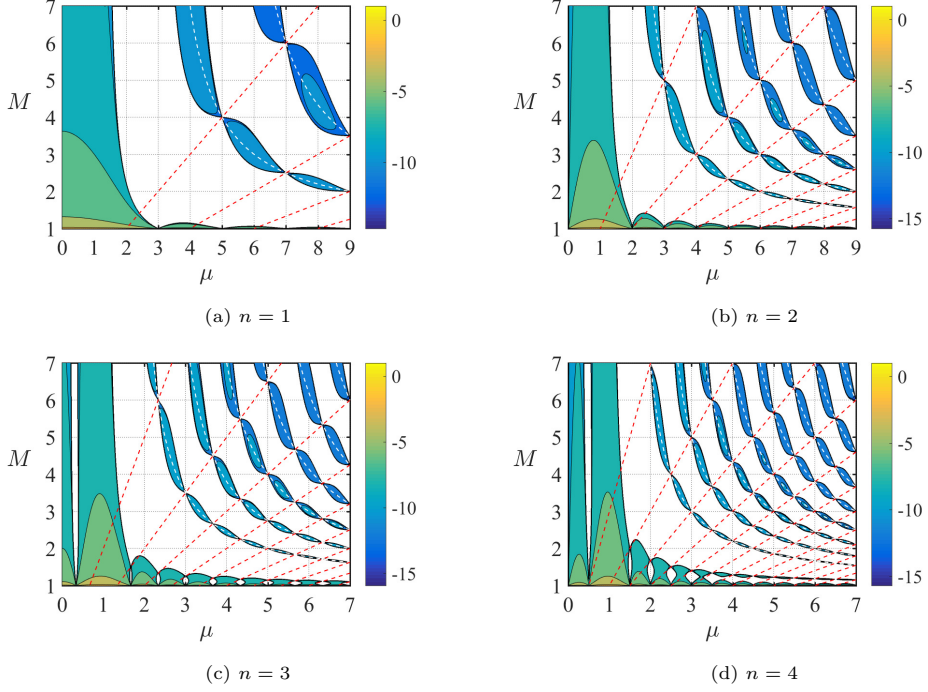


Figure 4: Stability maps with logarithmic scale for the growth rate (41) over $\mu = M_w/(M - 1)$ and M . The dashed white curves and red lines represent the lines (42) and curves (43), respectively, for $\Gamma = 1$, $\alpha = 10^{-4}$ and n according to the caption.

In a strike contrast to the infinite-chord membrane, stability diagrams of Fig. 2 display a regular pattern of intertwined instability tongues, each centered along a line (42) with $j \geq 1$. All the tongues commence at $M = 1$ at the values of M_w that are specified by (42). For instance, if $n = 1$, then the tongues grow from $M_w = 6, 10, 14, \dots, 2(2j + 1), \dots$, see Fig. 2(a). The growth rate along the line (42) corresponding to the tongue with $n = 1$ and $j = 1$ is shown in Fig. 3(a). The growth rate vanishes at $M = 1 + 3/k$, $k \geq 1$, i.e. exactly at the crossing points (44) that subdivide the instability tongue into a collection of infinitely many instability pockets, see Fig. 2. Note that similar intertwined resonance tongues with instability pockets are known for the Hill equation with some specific forms of periodic excitation [53].

In order to highlight the periodic pattern of the instability pockets, finally we plot the stability map in the new coordinates in Fig. 4 by projecting the growth rate onto the (μ, M) -plane, where $\mu = M_w/(M - 1)$. Then, the lines (42) transform into the curves $\mu = (2j/n + 1)(M + 1)/(M - 1)$ and the curves (43) to the lines $\mu = k/n(M + 1)$, see Fig. 4.

3.7. Exploring fluid dynamics analogy to superlight normal and inverse Doppler effects

According to a recent study [46], a source with an internal structure moving in a medium at a velocity that exceeds speed of light in the medium can be excited due to emission of electromagnetic waves (Ginzburg-Frank anomalous Doppler effect [41]) with the Doppler shift of the emitted waves remaining normal at small superluminal velocities and becoming inverted beyond some critical superluminal velocity. As it was emphasized in [46], virtually any wave system in nature, including classical wave systems such as acoustic waves and surface waves can exhibit the analogous phenomena.

Non-dispersive character of surface gravity waves in the shallow water limit implies $M = 1$ as a critical value for the flow velocity to exceed the speed of surface gravity waves and thus as a necessary condition for existence of the anomalous Doppler effect [26, 27]. Indeed, flutter instability tongues in Fig. 2 and Fig. 4 exist at $M > 1$. We need to verify that successive surface gravity waves radiated by the Nemtsov membrane carry wavelengths larger (smaller) than a characteristic value when $M > M_c > 1$ ($1 < M < M_c$).

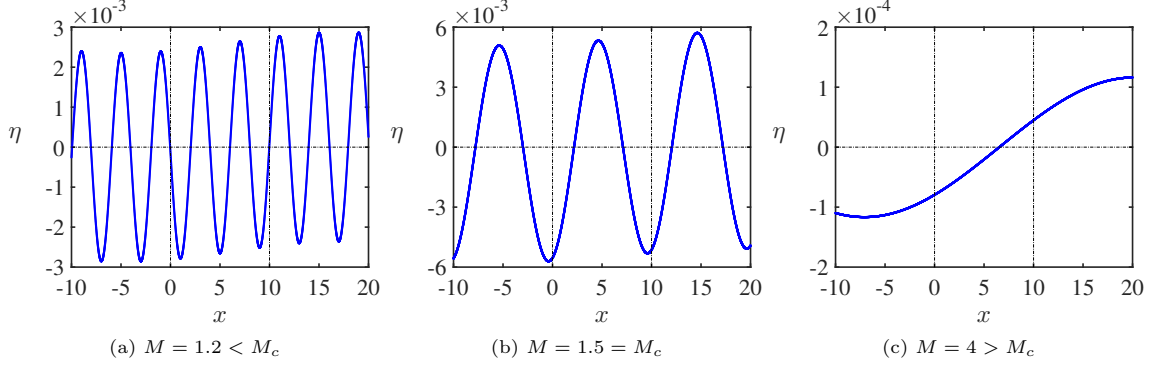


Figure 5: Surface ‘modes’ as given by expression (49) for a fixed ω recovered by first-order in α approximation (39), with parameters $n = 1$, $M_w = 1$, $\Gamma = 10$, $\alpha = 10^{-4}$ and M according to the legend. Dashed vertical lines specify x -coordinates of membrane’s edges.

Using the Bernoulli integral at the free surface ($z = 1$), retaining only linear in ϕ terms [26], and assuming the time dependence $\exp(-i\omega\tau)$, we obtain

$$\eta(x) = -(-i\omega + M\partial_x)\phi(x, z = 1), \quad (45)$$

where the velocity potential $\phi(x, z)$ is obtained as the inverse Fourier transform (6) of the solution of the boundary value problem (7), then evaluated at $z = 1$. Indeed, from the general expression (8), we find

$$\hat{\phi}(\kappa, 1, \omega) = \frac{1}{(\omega - \kappa M)^2 \cosh \kappa - \kappa \sinh \kappa} \int_0^\Gamma \left(i\omega - M \frac{d}{dx'} \right) \xi(x') e^{-i\kappa x'} dx'. \quad (46)$$

Inserting solution (46) into expression (6) and considering the shallow water limit ($\kappa \rightarrow 0$), we arrive at the fluid potential at the free surface ($z = 1$)

$$\phi(x, z = 1) = -\frac{1}{2\pi} \int_0^\Gamma \left(-i\omega + M \frac{d}{dx'} \right) \xi(x') \int_{-\infty}^{+\infty} \frac{e^{i\kappa(x-x')}}{(\omega - \kappa M)^2 - \kappa^2} d\kappa dx', \quad (47)$$

where membrane’s frequency ω and displacement ξ are provided by expressions (39) and (29), respectively.

With the help of (47) equation (45) yields

$$\eta(x) = -\frac{i}{2\pi} \int_0^\Gamma \left(-i\omega + M \frac{d}{dx'} \right) \xi(x') \int_{-\infty}^{+\infty} \frac{(\omega - \kappa M)e^{i\kappa(x-x')}}{(\omega - \kappa M)^2 - \kappa^2} d\kappa dx'. \quad (48)$$

Following a procedure that we used previously to derive expression (13), we apply the Cauchy residue theorem to (48) with exactly the same poles as in (14) and recover the surface wave ‘mode’ (for a given ω) as

$$\eta(x) = -\frac{1}{2(M^2 - 1)} \int_0^\Gamma \left(-i\omega + M \frac{d}{dx'} \right) \xi(x') \left[(M+1)e^{i\kappa^-(x-x')} + (M-1)e^{i\kappa^+(x-x')} \right] dx'. \quad (49)$$

Plotting (49) in Fig. 5, we observe the different regimes $1 < M < M_c$, $M = M_c$ and $M > M_c$ for a certain ‘mode’ of free surface, corresponding to the wavelengths that are shorter, equal and longer than Γ , respectively. To estimate the critical value $M = M_c$ we use the idea of phase synchronisation between modes of the membrane and the surface of the flow [27, 37] that in the infinite-chord membrane case gives a sufficient condition for the presence of an instability domain in the parameter space [26]. For the finite-chord membrane we consider the frequencies ω_n of vibration modes of the free membrane defined by equation (35) and surface waves frequencies ω_f that for simplicity we take from the shallow water dispersion relation of the decoupled system

$$\mathcal{D}_{SW}(\omega, \kappa) = (\omega_f - \kappa M)^2 - \kappa^2 = 0, \quad \omega_f^\pm = \kappa(M \pm 1). \quad (50)$$

The modes $\omega_f^- = \kappa(M - 1)$ correspond to slow surface gravity waves carrying negative energy and thus exciting flutter of the infinite-chord membrane (anomalous Doppler effect) [26, 27]. Choosing $\kappa = 2\pi/\Gamma$ in the equality $\omega_n = \omega_f^-$ allows us to estimate the critical velocity of the flow as

$$M_c = 1 + \frac{nM_w}{2}, \quad (51)$$

which agrees with the threshold observed in Fig. 5 for the surface modes computed from expression (49).

4. Deep water limit of the finite-chord Nemtsov membrane

Let us find the leading term of the factor at $e^{i\kappa(x-x')}$ in the integrand of the improper integral in (10) in the limit $\kappa \rightarrow +\infty$, corresponding to the deep water approximation

$$\frac{1}{\kappa^2} \frac{1 - \kappa(\sigma - M)^2 \tanh \kappa}{[(\sigma - M)^2 - \frac{\tanh \kappa}{\kappa}]} = -\frac{1}{\kappa} + o(\kappa^{-1}). \quad (52)$$

This yields a simplified form of the potential (10)

$$\phi_{DW}(x, \omega) = -\frac{1}{2\pi} \int_0^x (-i\omega + M\partial_{x'}) \xi(x') \int_{-\infty}^{+\infty} \frac{e^{i\kappa(x-x')}}{\kappa} d\kappa dx'. \quad (53)$$

For $x > x'$, the Dirichlet integral in (53) can be calculated around the pole $\kappa = 0$ in the sense of the Cauchy Principal Value (CPV) as follows

$$\text{PV} \int_{-\infty}^{+\infty} \frac{e^{i\kappa(x-x')}}{\kappa} d\kappa = i\pi, \quad (54)$$

where $\text{PV} \int := \lim_{\epsilon \rightarrow 0} \int_{\mathbb{R} \setminus [-\epsilon, \epsilon]}$ and ϵ is the radius of the sphere enclosing the singularity [63]. Inserting (54) into (53) we recover the velocity potential in the deep water approximation

$$\phi_{DW}(x, \omega) = -\frac{1}{2} \int_0^x (\omega + iM\partial_{x'}) \xi(x') dx'. \quad (55)$$

With the potential (55) the equation (11) takes the form

$$\omega^2 \xi + M_w^2 \partial^2 \xi + i\frac{\alpha}{2} \left(\omega + iM \frac{d}{dx} \right) \int_0^x \left(\omega + iM \frac{d}{dx'} \right) \xi(x') dx' = 0. \quad (56)$$

Using the same methodology as before and taking into account the boundary condition $\xi(0) = 0$, we find the Laplace transform of (56)

$$\left(\omega^2 + s^2 M_w^2 + \frac{i\alpha}{2s} (\omega + isM)^2 \right) \bar{\xi}(s) = M_w^2 \xi'(0). \quad (57)$$

Following once again the procedure described in the previous section, we take $s = ip$ in the equation (57) and then inverse the whole expression to finally obtain the displacement as the Bromwich integral

$$\xi(x) = \frac{M_w^2 \xi'(0)}{2\pi i} \lim_{T \rightarrow \infty} \int_{-T-i\nu}^{T-i\nu} \frac{2pe^{ipx}}{2p(\omega^2 - p^2 M_w^2) + \alpha(\omega - pM)^2} dp. \quad (58)$$

Evaluating (58) at $x = \Gamma$ and taking into account the boundary condition $\xi(\Gamma) = 0$, we recover the eigenfrequency equation

$$\xi(\Gamma) = \frac{M_w^2 \xi'(0)}{2\pi i} \oint_{\mathcal{C}_B} \frac{2pe^{ip\Gamma}}{2p(\omega^2 - p^2 M_w^2) + \alpha(\omega - pM)^2} dp = 0, \quad (59)$$

which can be written as follows

$$\xi(\Gamma) = M_w^2 \xi'(0) D(\omega, \alpha) = 0, \quad (60)$$

where

$$D(\omega, \alpha) = \frac{1}{2\pi i} \oint_{\mathcal{C}_B} \frac{e^{ip\Gamma}}{\mathcal{D}(\omega, \alpha, p)} dp \quad (61)$$

and

$$\mathcal{D}(\omega, \alpha, p) = \omega^2 - p^2 M_w^2 + \alpha \frac{(\omega - pM)^2}{2p}. \quad (62)$$

In the case of $\alpha = 0$ the eigenvalue relation (60) reduces to

$$D(\omega, 0) = \frac{1}{2\pi i} \oint_{\mathcal{C}_B} \frac{e^{ip\Gamma}}{\mathcal{D}(\omega, 0, p)} dp = \frac{1}{M_w^2} \frac{1}{2\pi i} \oint_{\mathcal{C}_B} \frac{-e^{ip\Gamma}}{p^2 - p_0^2} dp = 0, \quad (63)$$

where $p_0 = \omega/M_w$. Applying the residue theorem to the last integral in (63), we reproduce the eigenfrequencies ω_n given by equation (35).

Simple roots $\omega(\alpha)$ of the equation $D(\omega, \alpha) = 0$ can be represented as a series in α , $0 < \alpha \ll 1$, as follows [26, 48]

$$\omega = \omega_n - \alpha \frac{\partial_\alpha D}{\partial_\omega D} - \frac{\alpha^2}{2} \left(\frac{\partial_\omega^2 D}{\partial_\omega D} \left(\frac{\partial_\alpha D}{\partial_\omega D} \right)^2 - 2 \frac{\partial_\omega^2 D}{\partial_\omega D} \frac{\partial_\alpha D}{\partial_\omega D} + \frac{\partial_\alpha^2 D}{\partial_\omega D} \right) + o(\alpha^2), \quad \omega(0) = \omega_n. \quad (64)$$

Computing the partial derivatives and evaluating them at $\alpha = 0$ yields

$$\begin{aligned} \partial_\alpha D &= \frac{-1}{2\pi i} \oint_{\mathcal{C}_B} \frac{e^{ip\Gamma} (Mp - \omega_n)^2}{2M_w^4 p(p^2 - p_{0,n}^2)^2} dp, \\ \partial_\omega D &= \frac{-1}{2\pi i} \oint_{\mathcal{C}_B} \frac{2e^{ip\Gamma} \omega_n}{M_w^4 (p^2 - p_{0,n}^2)^2} dp, \end{aligned} \quad (65)$$

where

$$p_{0,n} = \frac{\pi n}{\Gamma}.$$

Applying the residue theorem to the integrals in (65), we find

$$\begin{aligned} \partial_\alpha D &= \frac{iM(-1)^n \Gamma^2}{2M_w^3 \pi n} + \frac{M_w \Gamma^2 [(-1)^n - 1]}{2M_w^3 \pi^2 n^2}, \\ \partial_\omega D &= \frac{-i(-1)^n \Gamma^2}{M_w^3 \pi n}. \end{aligned} \quad (66)$$

With the derivatives (66) the series expansion (64) takes the form

$$\omega(\alpha) = \omega_n + \alpha \frac{M}{2} + i\alpha \frac{M_w}{2\pi n} [(-1)^n - 1] + o(\alpha). \quad (67)$$

Taking into account terms of the second order in α yields the following expression for the growth rate

$$\begin{aligned} \text{Im}(\omega) &= \alpha \frac{M_w}{2\pi n} [(-1)^n - 1] \\ &+ \frac{\alpha^2 \Gamma}{32} \left(\frac{2M_w^2 (4 - \pi^2 n^2)}{\pi^4 n^4} [(-1)^n - 1] - \frac{M^2 (\pi^2 n^2 + 10(-1)^n - 14)}{\pi^2 n^2} - \frac{M^4}{M_w^2} \right) + o(\alpha^2). \end{aligned} \quad (68)$$

For all even $n > 1$ the growth rate (68) is negative up to the terms of higher order than α^2 :

$$\text{Im}(\omega) = -\alpha^2 M^2 \frac{\Gamma}{32} \left(1 - \frac{4}{\pi^2 n^2} + \frac{M^2}{M_w^2} \right) + o(\alpha^2), \quad \text{even } n > 1.$$

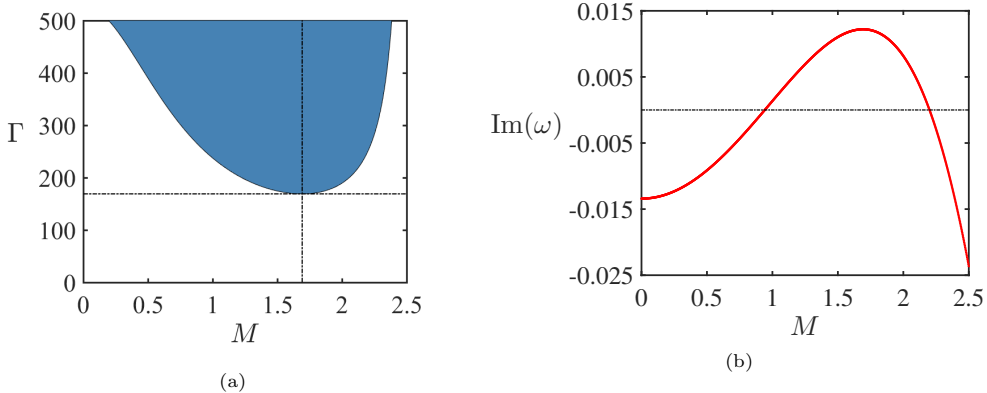


Figure 6: (a): (Blue) Instability domain computed from expression (69) for $n = 1$, $M_w = 2$, and $\alpha = 0.04$, with (dotted lines) the minimum (70) of Γ at the minimizer given by (71). (b): Growth rate for the left figure at a fixed value of $\Gamma = 250$.

In contrast, for odd n the growth rate can take positive values for some combinations of parameters. Equating the growth rate (68) to zero, we find the critical length of the membrane at the onset of flutter for odd n in the explicit form

$$\Gamma = \frac{32M_w^3\pi^3n^3\alpha^{-1}}{4M_w^4(\pi^2n^2 - 4) - M^2M_w^2\pi^2n^2(\pi^2n^2 - 24) - M^4\pi^4n^4}, \quad \text{odd } n \geq 1. \quad (69)$$

For instance, the minimal length of the membrane for $n = 1$ below which there is no flutter, is

$$\Gamma_{\min} = \frac{128\pi^3}{\alpha M_w(\pi^4 - 32\pi^2 + 512)} \quad (70)$$

at

$$M_{\min} = M_w \frac{\sqrt{2}}{2\pi} \sqrt{24 - \pi^2}, \quad (71)$$

as is shown in Fig. 6. Notice that Γ_{\min} quickly increases as α is tending to zero, thus reducing chances for a finite-chord membrane to be unstable in the deep water limit, if the coupling between the membrane and the flow is vanishingly weak.

5. The finite-chord Nemtsov membrane in the finite-depth layer

The case of a fluid layer with finite depth requires further attention in the derivation of eigenfrequency equation than the previously considered limits of shallow and deep water. The main difficulty is the non-polynomial character of the dispersion relation for the finite depth flow [26], which does not allow analytical solution via Cauchy residue theorem of the improper integral in (11) that therefore has to be now exclusively treated numerically. This major difference forces us first to count and localize the poles of the integrand using a combination of complex analysis and iterative solvers to make possible numerical implementation of the residue theorem. This allows us to discretize the integro-differential equation into an algebraic nonlinear eigenvalue problem for ω by means of Galerkin decomposition and solve the resulting equation with an appropriate numerical method. In this section, we present both the derivation of this nonlinear eigenvalue problem and the methods for its solution. We argue that our approach can easily be extended to a wide class of fluid-structure systems composed of a fixed elastic structure that interacts with a moving flow.

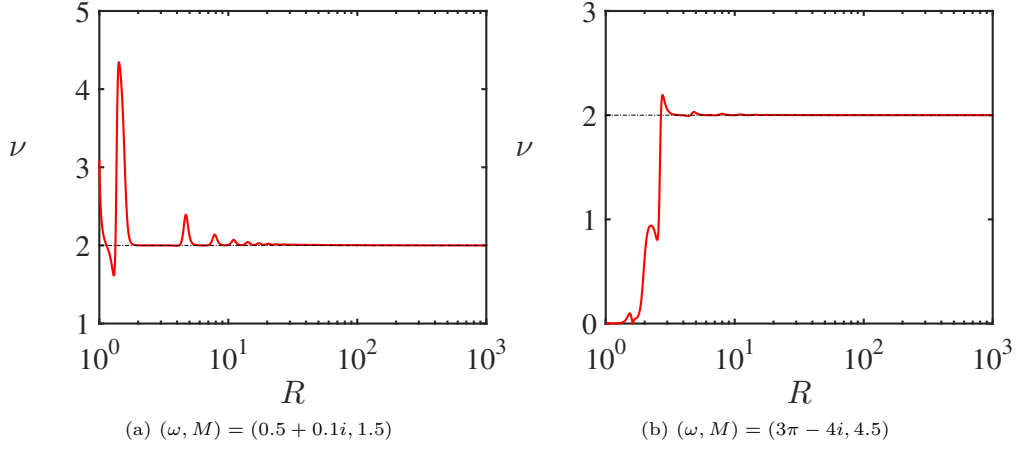


Figure 7: Convergence of expression (76) over the radius R for arbitrary pair of complex eigenfrequencies and Mach numbers. We used $N = 20$ nodes for the trapezoidal quadrature.

5.1. Counting and localizing the poles of a non-polynomial integrand in the integro-differential equation

For the sake of clarity in this section, we reintroduce the wave equation of the finite depth problem (11) in terms of convolution, along with its boundary conditions

$$\mathcal{W}(\xi; x, \omega) = \left(\omega^2 + M_w^2 \frac{\partial^2}{\partial x^2} \right) \xi(x) + \alpha \left(-i\omega + M \frac{\partial}{\partial x} \right) (u * v)(x) = 0, \quad \xi(0) = \xi(\Gamma) = 0, \quad (72)$$

where we have

$$u(x, \omega) = \left(-i\omega + M \frac{\partial}{\partial x} \right) \xi(x), \quad (73)$$

$$v(x, \omega) = \frac{1}{2\pi} \int_{-\infty}^{+\infty} \frac{[\kappa - (\omega - \kappa M)^2 \tanh \kappa] e^{i\kappa x}}{\kappa[(\omega - \kappa M)^2 - \kappa \tanh \kappa]} d\kappa = \frac{1}{2\pi} \int_{-\infty}^{+\infty} F(\kappa) d\kappa. \quad (74)$$

As stated before, the main issue in solving (72) is the presence of the improper integral (74). Indeed, in contrast with the shallow- and deep water cases, the difficulty in direct application of the Cauchy residue theorem to this integral is that it requires knowledge of the poles of the meromorphic function $F(\kappa)$, or equivalently, the zeros of the analytic function

$$f(\kappa) = (\omega - \kappa M)^2 - \kappa \tanh \kappa, \quad (75)$$

since the trivial pole $\kappa = 0$ of $F(\kappa)$ is already known. As one can notice, expression (75) is nothing else but the dispersion relation of the surface gravity waves travelling along a fluid layer with finite depth and infinite extension, moving uniformly along a rigid bottom [26].

Since the characteristic equation (75) is not polynomial in κ we cannot say a priori how many zeroes it has in the complex κ -plane. We determine this number numerically using the standard expression [63, 65]

$$\nu = \frac{1}{2\pi i} \oint_{\mathcal{C}} \frac{f'(\kappa)}{f(\kappa)} d\kappa = \frac{R}{2\pi} \int_0^{2\pi} \frac{f'(Re^{i\theta})}{f(Re^{i\theta})} e^{i\theta} d\theta \quad (76)$$

that relates the integer number ν of zeros of $f(\kappa)$ in the complex κ -plane inside an arbitrary closed contour \mathcal{C} which, for numerical purposes, we choose to be a circle of radius R that is centered at the origin.

Solving (76) numerically using a standard trapezoidal quadrature with $\omega \in \mathbb{C}$ and $M \in \mathbb{R}$ for increasing values of R , demonstrates convergence to $\nu = 2$ with a good accuracy that is evident in Fig. 7. This result is supported by the fact that both in the shallow water limit (when at $\kappa \rightarrow 0$ we have $\tanh(\kappa) \approx \kappa$) and

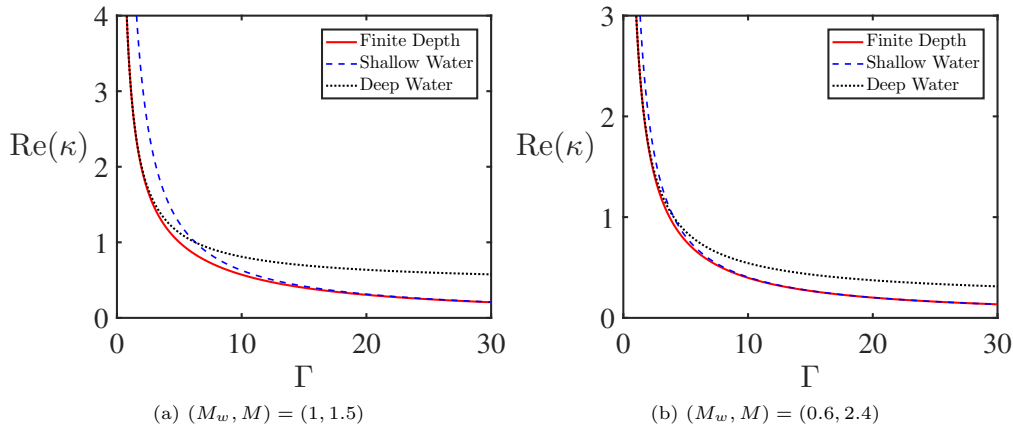


Figure 8: Convergence of zeros of (75) to the roots (77) over Γ , for $\omega = \omega_n + \omega_i$ with fixed values of imaginary parts (a): $\omega_i = 0.001$ and (b): $\omega_i = -0.1$.

in the deep water limit (when $\tanh(\kappa) = 1$ as $\kappa \rightarrow +\infty$), dispersion relation (75) reduces to a quadratic polynomial in κ which therefore has only 2 distinct roots.

Now, when the number of zeros in expression (75) is established, we can use an iterative algorithm such as the standard Newton-Raphson method to locate precisely where these zeros lie in the complex κ -plane. In order for the algorithm to initiate, we need to provide an initial guess that is close enough to the exact value of the desired root. A natural choice is to use the roots of the dispersion relation (75) either in the shallow- or in the deep water limit

$$\kappa_{\pm}^{SW} = \frac{\omega}{M \pm 1}, \quad \kappa_{\pm}^{DW} = \frac{2\omega M + 1 \pm \sqrt{4\omega M + 1}}{2M^2}, \quad (77)$$

which depends on the length Γ of the membrane. Indeed, since $\omega = \omega_n + i\omega_i$, where $\omega_n = n\pi M_w/\Gamma$ is the free membrane frequency (35) and $\omega_i \in \mathbb{R}$ is fixed, we have a clear numerical evidence that the zeros of (75) tend either to κ_{\pm}^{SW} as $\Gamma \rightarrow \infty$ or to κ_{\pm}^{DW} as $\Gamma \rightarrow 0$, see Fig. 8.

Since the location of the poles of the integrand in (74) is now determined, we continue our investigation by applying the residue theorem to this improper integral in the same way as we did in the shallow water limit. This time, due to the presence of a pole at the origin, the contour we consider is decomposed as

$$\mathcal{C} = [-R, -\epsilon] \cup \Delta_\epsilon \cup [\epsilon, R] \cup \Delta_R, \quad \Delta_\epsilon = \{\epsilon e^{it}, -\pi \leq t \leq 0\}, \quad \Delta_R = \{Re^{it}, 0 \leq t \leq \pi\}, \quad (78)$$

where $0 < \epsilon \ll 1$ and $R \gg 1$.

Using the oriented curve (78) in the contour integral (74) yields

$$\oint_{\mathcal{C}} F(\kappa) d\kappa = \int_{-R}^{-\epsilon} F(\kappa) d\kappa + \int_{\Delta_\epsilon} F(\kappa) d\kappa + \int_{\epsilon}^R F(\kappa) d\kappa + \int_{\Delta_R} F(\kappa) d\kappa. \quad (79)$$

Adopting the same argument as in the shallow water case and taking into account that $F(z)$ is a continuous function for $z \in \Delta_R$ and that $\lim_{R \rightarrow +\infty} |g(Re^{i\theta})| = 0$, where $g(\kappa) = F(\kappa)e^{-i\kappa x}$ and $\theta \in [0, \pi]$, we find that the contribution of the arc integral over Δ_R vanishes as we enlarge the radius, according to Jordan's lemma [63].

The contribution of the arc integral over Δ_ϵ in (79) also vanishes as $\epsilon \rightarrow 0$ because

$$\lim_{\epsilon \rightarrow 0} \int_{\Delta_\epsilon} F(\kappa) d\kappa = \lim_{\epsilon \rightarrow 0} i\epsilon \int_{-\pi}^0 e^{i\theta} F(\epsilon e^{i\theta}) d\theta = 0. \quad (80)$$

Finally, taking the two limits of $R \rightarrow +\infty$ and $\epsilon \rightarrow 0$ simultaneously and then applying the residue theorem to (79), we obtain

$$\lim_{\substack{R \rightarrow +\infty \\ \epsilon \rightarrow 0}} \left[\int_{-R}^{-\epsilon} F(\kappa) d\kappa + \int_{\epsilon}^R F(\kappa) d\kappa \right] = \text{PV} \int_{-\infty}^{+\infty} F(\kappa) d\kappa = 2\pi i \sum_{j=1}^2 \text{res}(F(\kappa), \kappa_j), \quad (81)$$

where the improper integral has to be taken in the sense of Cauchy Principal Value and where κ_j are the zeros of (75) lying in the upper-half plane.

A similar argument works as well for an oriented contour \mathcal{C} in the lower half of the complex κ -plane, to enclose the poles with the negative imaginary parts.

Now we are prepared to recover the function $v(x, \omega)$ from the general expression (74) as

$$v(x, \omega) = i \sum_{j=1}^2 \text{res}(F(\kappa), \kappa_j), \quad \kappa_j \in \mathbb{C}, \quad (82)$$

which constitutes the main result of this section.

Note that owing to the fact that the poles are computed numerically and that F in (82) cannot be expanded in the Laurent series, we need to calculate the residues in (82) with an alternative, however equivalent, expression to that used for obtaining (18). Namely, if we consider a meromorphic function $M(z) = a(z)/b(z)$ with a simple pole z_1 that is a root of $b(z)$, then the residue for $M(z)$ at z_1 reads as [63]

$$\text{res}(M(z), z_1) = \lim_{z \rightarrow z_1} \frac{a(z)}{b'(z)}. \quad (83)$$

If the function $M(z)$ has a double pole z_2 , we find similarly that [63]

$$\text{res}(M(z), z_2) = \lim_{z \rightarrow z_2} \frac{6a'(z)b''(z) - 2a(z)b'''(z)}{3[b''(z)]^2}. \quad (84)$$

Expressions (83) and (84) will be utilized in the numerical treatment of equation (72), for instance, in the computation of the corresponding Jacobian.

5.2. Galerkin discretization and reduction to an algebraic nonlinear eigenvalue problem

The last step in solving the integro-differential equation (72) numerically is to introduce a modal form for the displacement $\xi(x)$ that respects the boundary conditions $\xi(0) = \xi(\Gamma) = 0$. For this purpose, we introduce the following Galerkin decomposition, based on a superposition of modes of a free membrane vibrating in vacuum

$$\xi(x) = \sum_{j=1}^N \gamma_j \xi_j^{(0)}, \quad \xi_j^{(0)} = \sin\left(\frac{j\pi x}{\Gamma}\right). \quad (85)$$

Substituting (85) into (72) and using the orthogonality of the modes (85) while integrating over the membrane chord, we find

$$\mathcal{F}_{ij}(\omega) \gamma_j = \sum_{j=1}^N \gamma_j \int_0^\Gamma \mathcal{W}(\xi_j^{(0)}; x, \omega) \xi_i^{(0)} dx = 0. \quad (86)$$

The expression (86) represents the j -th scalar equation of the algebraic nonlinear eigenvalue problem in ω , which matrix pencil can be written as

$$\mathcal{F}(\omega) = -\omega^2 \mathcal{I} + \alpha \mathcal{P}(\omega) + \mathcal{K}, \quad (87)$$

where the matrices in (87) can be explicitly recovered through the following expressions [54]

$$\begin{aligned}\mathcal{I}_{ij} &= \delta_{ij}, \\ \mathcal{K}_{ij} &= \left(\frac{j\pi M_w}{\Gamma}\right)^2 \delta_{ij}, \\ \mathcal{P}_{ij} &= \frac{2}{\Gamma} \int_0^\Gamma P(\xi_j^{(0)}; x, \omega) \xi_i^{(0)} dx,\end{aligned}\quad (88)$$

with δ_{ij} standing for the Kronecker delta. The function P follows from (72) after application of the Leibniz rule (24):

$$P(\xi(x); x, \omega) = i\omega(u * v) - M \left[\left(u * \frac{\partial v}{\partial x} \right) + u(x, \omega)v(0, \omega) \right], \quad (89)$$

where $v(x)$ is given by (82) and

$$\frac{\partial v}{\partial x} = \frac{i}{2\pi} \int_{-\infty}^{+\infty} \frac{[\kappa - (\omega - \kappa M)^2 \tanh \kappa] e^{i\kappa x}}{(\omega - \kappa M)^2 - \kappa \tanh \kappa} d\kappa \quad (90)$$

should be computed separately with the similar approach. Indeed, integral (90) is nothing else but a slightly modified version of expression (74), without the pole located at the origin. Therefore, a similar analysis applied to (90) reduces it to

$$\frac{\partial v}{\partial x} = iv(x) = - \sum_{j=1}^2 \text{res}(F(\kappa), \kappa_j), \quad \kappa_j \in \mathbb{C}. \quad (91)$$

With the expressions (82) and (91) we can recover an explicit form of all the matrices constituting the matrix pencil (87) of the nonlinear eigenvalue problem by direct numerical computation.

5.3. Jacobian of the nonlinear matrix pencil $\mathcal{F}(\omega)$

Nonlinear eigenvalue problems constitute nowadays a challenging and ongoing research topic for a whole community of mathematicians. State-of-the-art reviews [55, 56, 57] identify and classify different classes of methods to solve them, depending on the nonlinearity. Most of the known methods are either based on the Newton-Raphson iterative process or use contour integration [56]. In the present paper we prefer the former.

The Newton-Raphson iterative process needs the derivative of the pencil (87) with respect to ω , or Jacobian of the system. In order to reach an acceptable convergence rate for the method, we compute the analytical form of the Jacobian instead of approximating it numerically.

From (87) we find

$$\frac{d\mathcal{F}}{d\omega} = -2\omega\mathcal{I} + \alpha \frac{d\mathcal{P}}{d\omega}, \quad (92)$$

where the derivative $\frac{d\mathcal{P}}{d\omega}$ involves the derivative of the function $P(x, \omega)$ as defined in (89). Applying the Leibniz rule (24) once again, we obtain

$$\begin{aligned}\frac{\partial P}{\partial \omega} &= i(u * v) + i\omega \left[\left(\frac{\partial u}{\partial \omega} * v \right) + \left(u * \frac{\partial v}{\partial \omega} \right) \right] \\ &\quad - M \left[\left(\frac{\partial u}{\partial \omega} * \frac{\partial v}{\partial x} \right) + \left(u * \frac{\partial^2 v}{\partial x \partial \omega} \right) + \frac{\partial u}{\partial \omega}(x, \omega)v(0, \omega) + u(x, \omega)\frac{\partial v}{\partial \omega}(0, \omega) \right],\end{aligned}\quad (93)$$

where u is given by (73), v by (82), and $\frac{\partial v}{\partial x}$ by (91).

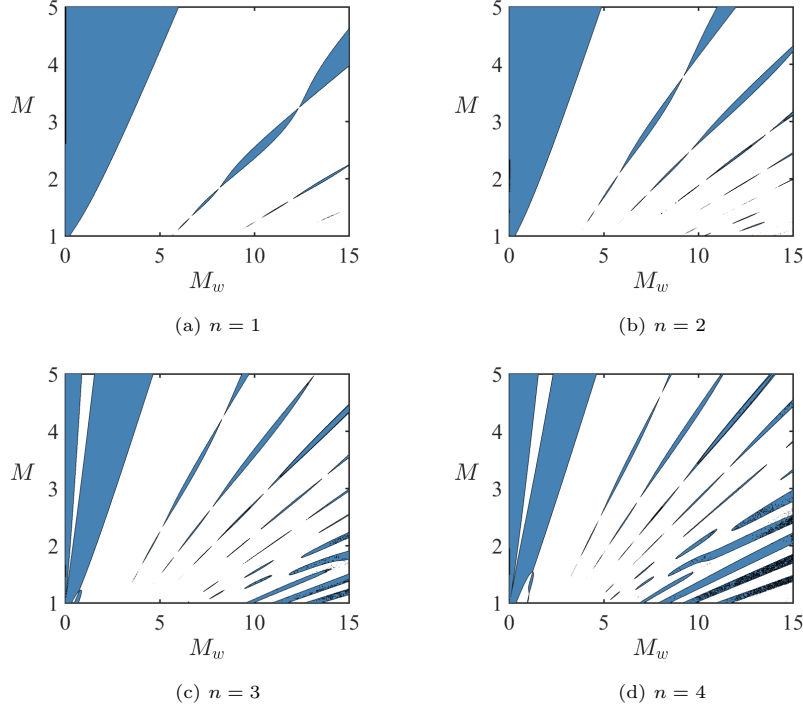


Figure 9: Stability maps in the (M_w, M) -plane from the numerical solution of the matrix pencil (87) for $\Gamma = 10$, $\alpha = 10^{-4}$ and n according to the legend.

As in the previous case, the higher-order derivatives of (74) involve slightly different improper integrals. Their explicit expressions are recovered as

$$\begin{aligned} \frac{\partial v}{\partial \omega} &= \frac{1}{\pi} \int_{-\infty}^{+\infty} \frac{(\omega - \kappa M)(\tanh^2 \kappa - 1)e^{i\kappa x}}{[(\omega - \kappa M)^2 - \kappa \tanh \kappa]^2} d\kappa, \\ \frac{\partial^2 v}{\partial x \partial \omega} &= \frac{i}{2\pi} \int_{-\infty}^{+\infty} \frac{\kappa(\omega - \kappa M)(\tanh^2 \kappa - 1)e^{i\kappa x}}{[(\omega - \kappa M)^2 - \kappa \tanh \kappa]^2} d\kappa. \end{aligned} \quad (94)$$

Despite the numerator in the integrand of (94) is different from (74), the poles remain identical to (90), with the only difference that they are of second order. Therefore, we can apply the same procedure involving the residue theorem as we did in the derivation of (82) (with a particular attention to the pre-factors of the integrals). As the poles are no longer simple, we need to use the expression (84) for the residues when computing derivatives (94).

5.4. Numerical evaluation of the integral in (88)

In our approach, the integrals in the expression (88) and its derivative, as well as in all the convolutions, are integrated using numerical quadrature. Since the domain of integration is one-dimensional and we want to keep high accuracy in our numerical scheme, we prefer to use the Legendre-Gauss-Lobatto quadrature rule to approximate every integral. The nodes and weights of this spectral collocation method are recovered using the Golub-Welsch algorithm [59], which is based on the inversion of a linear system obtained from the three-term recurrence relation for Legendre polynomials. The computed eigenvalues correspond to the quadrature points, while the eigenvectors are used to recover the weights. In this method, the nodes are defined on an interval $[-1, 1]$ before being mapped, using a linear transformation, to the interval of integration $[0, \Gamma]$. This spectral quadrature is able to reach computer accuracy with less than 20 nodes of discretization of the interval $[0, \Gamma]$ and is thus used all over our code.

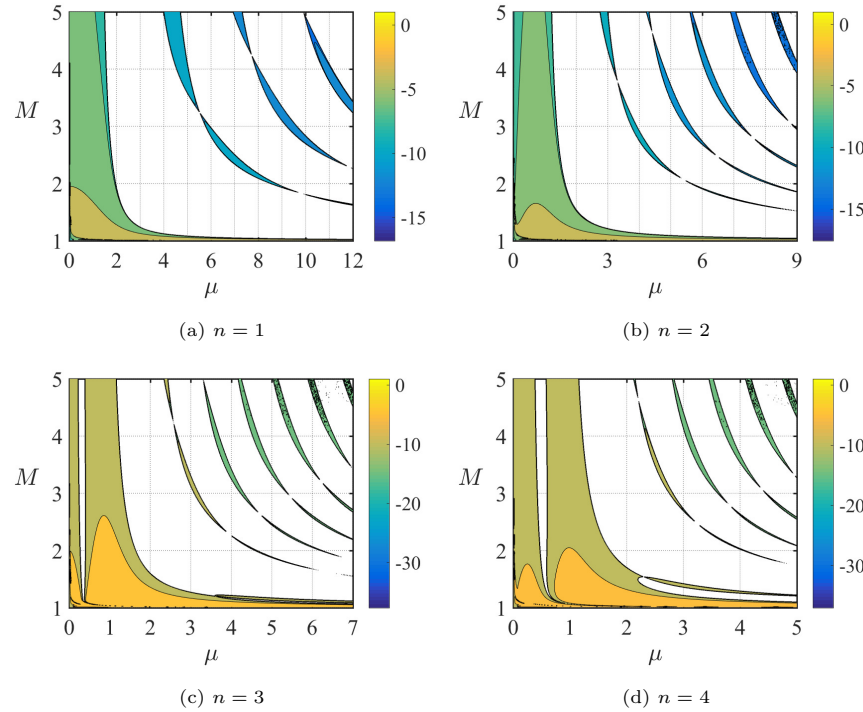


Figure 10: Stability maps in the (μ, M) -plane from the numerical solution of the matrix pencil (87) for $\Gamma = 10$, $\alpha = 10^{-4}$ and n according to the legend. We use a logarithmic scale for the growth rate.

5.5. Newton-like numerical method for solving the nonlinear eigenvalue problem

Now when every element of the matrix pencil (87) and its derivative (92) can be recovered by direct numerical computation, we shall introduce the method that we will be using throughout the stability analysis of the nonlinear eigenvalue problem. This numerical method is introduced in the recent review [55] and is designed to solve the characteristic equation $\det \mathcal{F}(\omega) = 0$ from the inversion of successive linear problems. As always in Newton-like methods, it has to start with an initial guess that is close enough to the exact solution ω . In our case, due to strong nonlinearity in ω in the term (89), we shall restrict ourselves to reasonably low values of α . Indeed, this parameter acts as a linear factor at the nonlinear in ω operator and keeping it sensibly small prevents us from departing too far from the free membrane solution (corresponding to $\alpha = 0$). This allows us to initiate our algorithm by choosing the eigenfrequency of the free membrane (35) as an initial starting point. With this first guess $\omega^{(0)} = \omega_n$, the method of successive linear problems is an iterative routine, where the p -th iteration requires to solve a linear eigenvalue problem

$$\mathcal{F}(\omega^{(p)})\mathbf{u} = \theta \mathcal{F}'(\omega^{(p)})\mathbf{u}. \quad (95)$$

After inversion of expression (95), we re-initiate the method as follows

$$\omega^{(p+1)} = \omega^{(p)} - \theta, \quad (96)$$

where θ is chosen to be the smallest eigenvalue of (95) in the absolute value. As expected from the method, we can easily reach quadratic convergence in ω .

The computational method presented through this section has been fully implemented and parallelized in MATLAB using the Parallel Computing Toolbox available from the software. All stability maps in the parameter spaces that will be presented in the next section are recovered from the direct computation of growth rates $\text{Im}(\omega)$ of the nonlinear matrix pencil (87).

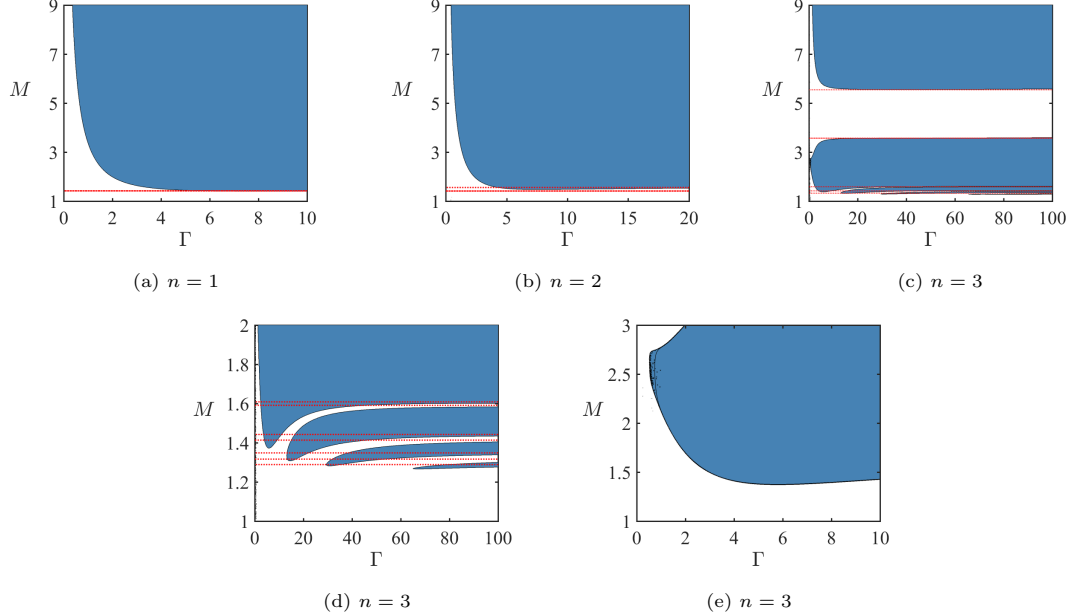


Figure 11: Instability domains (blue) of the finite depth system and finite-chord membrane for the eigenfrequencies ω recovered from the matrix pencil (87). Parameters used are $M_w = 1$, $\alpha = 10^{-4}$ and n according to the legend. Neutral stability line obtained from the first-order expansion of the shallow water growth rate (41) are shown as dotted red.

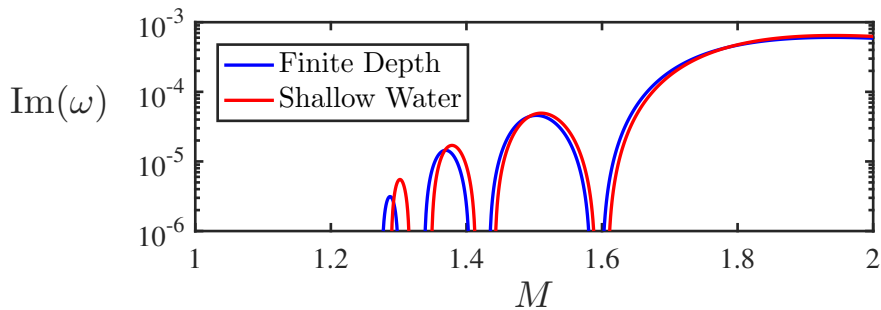


Figure 12: Finite depth growth rates converge to the shallow water ones as $\Gamma \rightarrow \infty$ for $M_w = 1$, $\alpha = 10^{-4}$, $n = 3$, and $\Gamma = 100$.

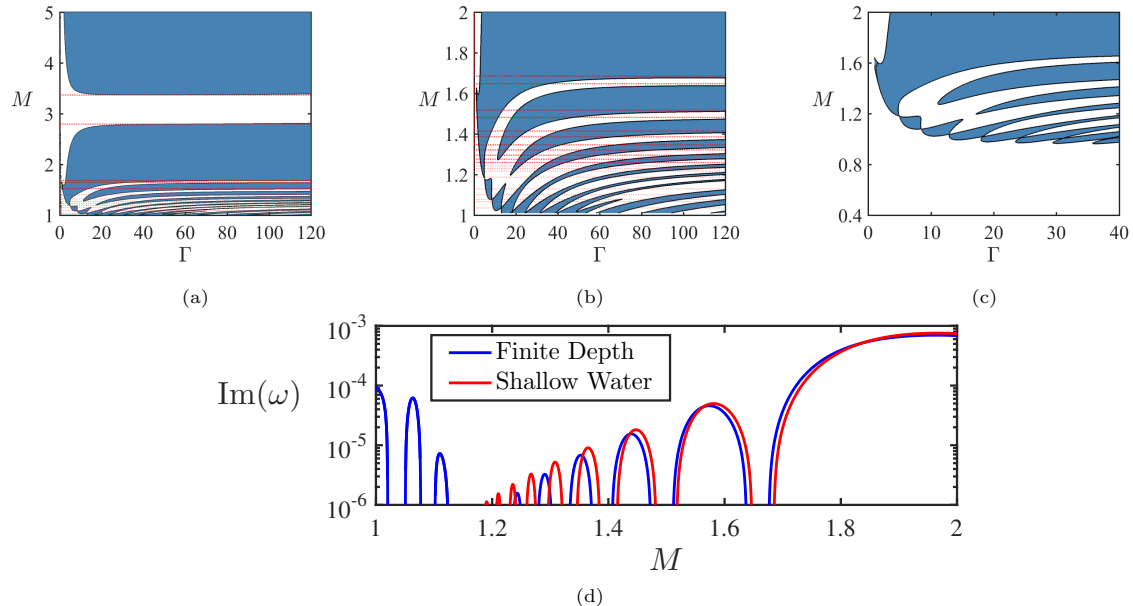


Figure 13: (a) Instability domain and (b,c) its close views (blue) for $M_w = 1$, $\alpha = 10^{-4}$, and $n = 4$. (c) The leftmost tongue never touches the axis $\Gamma = 0$. (d) The lower panel represents growth rates computed at a fixed value of $\Gamma = 120$.

5.6. Stability maps for the finite-chord Nemtsov membrane in the finite-depth flow

Applying the computational method described above to the nonlinear eigenvalue problem defined by the matrix pencil (87), we find frequencies and growth rates of the finite-chord Nemtsov membrane coupled to the free surface flow of finite depth. First, we are benchmarking our method against the analytical solution (41) in the shallow-water limit, corresponding to $\Gamma \rightarrow \infty$, and shown in Fig. 2. In Fig. 9 we show an analogue of Fig. 2 for the membrane with the chord length $\Gamma = 10$ and $\alpha = 10^{-4}$ that demonstrates all the structural characteristics that are present in the shallow water stability map including the tongues of intertwining flutter regions and the wide stability gap. Nevertheless, one can observe that in the case of the finite-chord membrane in the finite-depth flow some of the tongues are either separated to individual instability islands or merged into continuous instability belts. These new effects are caused by the finite values of the chord length of the membrane and the finite depth of the fluid layer.

In a similar way, we produce stability maps in the (μ, M) -plane computed from the numerical solution of the algebraic nonlinear matrix pencil (87) for $\Gamma = 10$ and $\alpha = 10^{-4}$. Comparing the results shown in Fig. 10 with the analytical solutions in the shallow water limit that are visualized in Fig. 4, we notice good qualitative and quantitative agreement of the two approaches.

A drawback of our first-order in α analytical expression (41) for the growth rates in the shallow water approximation was that the size of the membrane Γ in it was only playing the role of a scaling factor and thus did not change the shape of the instability domains as it is the case for the finite depth solution. In contrast, the numerical solution of the nonlinear eigenvalue problem with the pencil (87) allows us to investigate zones of the radiation-induced flutter in a broad range of variation of the chord length Γ .

In Fig. 11(a,b) we present stability maps in the (Γ, M) -plane for the membrane modes with $n = 1, 2$ that show stability close to the critical values $M = 1$ and $\Gamma = 0$ with instability (blue domain) everywhere else. Notice that as $\Gamma \rightarrow \infty$, the lower boundary of the flutter domain for the finite depth layer tends to the horizontal neutral stability curve (shown as a red dotted line) that follows from the first-order in α expansion of the growth rate (41) in the shallow water approximation. On the other hand, in the opposite limit of $\Gamma \rightarrow 0$, corresponding to the deep water approximation, the finite-chord-length Nemtsov membrane is stable, in accordance with the perturbation analysis in section 4. These observations confirm that our numerical results for the finite depth problem are in a very good agreement with the analytical treatment

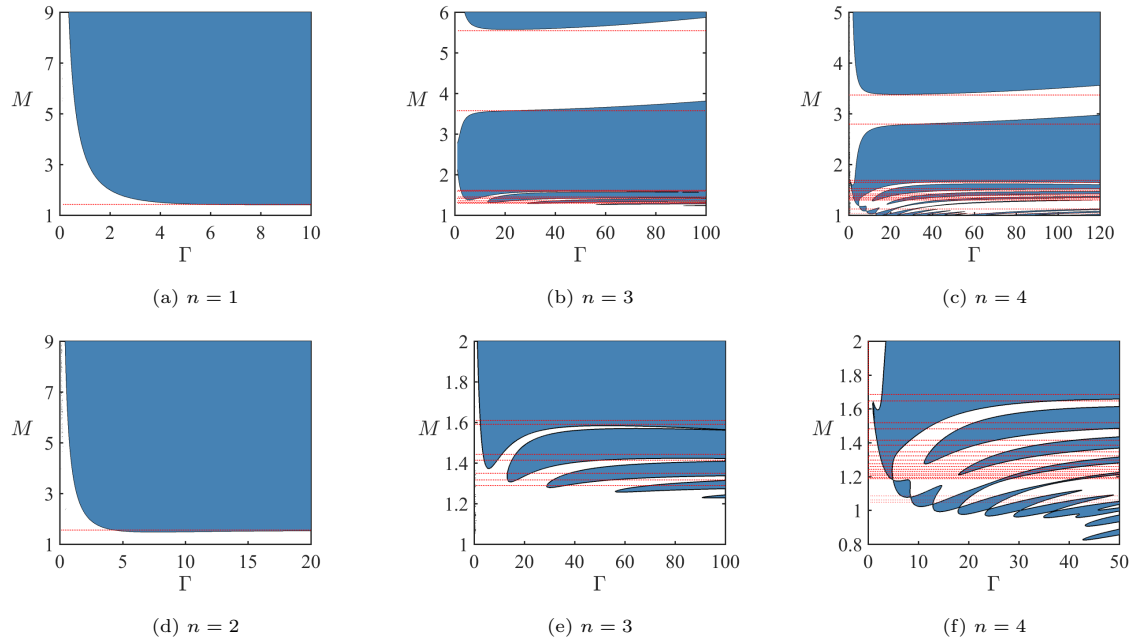


Figure 14: Instability domains (blue) of the finite depth system and finite-chord membrane for the eigenfrequencies ω recovered from the matrix pencil (87). Parameters used are $M_w = 1$, $\alpha = 10^{-3}$ and n according to the legend. The dotted red lines represent the neutral stability curves obtained from the first-order expansion of the shallow water growth rate (41).

presented in the previous sections and that our numerical procedure converges to correct eigenvalues.

Exploring the stability map in the (Γ, M) -plane further for the higher-order membrane modes with $n = 3$ unveils even more intriguing pattern shown in Fig.11(c,d). First, Fig.11(c) highlights a curious structure of two prominent subdomains in the parameter plane with the stability gap corresponding to a sector of stability also visible in the left part of Fig. 11(c). Second, the lower subdomain in Fig.11(c) decomposes to a bunch of instability tongues spreading along the Γ -axis, see Fig. 11(d). Third, for every tongue, even for that commencing very close to the M -axis (Fig. 11(e)), there is a critical value of the chord length Γ such that the shorter membranes are stable, quite in accordance with the analytical results for the deep water reported in section 4, cf. Fig. 6. Fourth, and, probably the most rewarding, is the evidence that in the limit of $\Gamma \rightarrow \infty$ the boundaries of the instability tongues of Fig. 11(d) converge to the shallow water solution shown by red dotted horizontal lines in Fig. 11(d), which is also confirmed by the convergence of the corresponding growth rates shown in Fig. 12. Therefore, the pattern of instability tongues that we discovered first in the shallow water approximation manifests itself also in the general case of the finite-chord membrane in the finite-depth fluid flow. With the increase in n , the instability tongues start to break and intertwine, making the pattern even more intriguing, see Fig. 13 for the stability maps corresponding to $n = 4$.

As is evident in Fig.14 modification of the added mass ratio parameter α by an order of magnitude from $\alpha = 10^{-4}$ to $\alpha = 10^{-3}$ deforms the pattern of instability regions. Although all the qualitative features remain in place, the behaviour of the stability boundaries at large values of Γ does not demonstrate a perfect convergence to the shallow water solution as one can see in the closer views of the stability domains in Fig.14(e,f). Notice, however, that the red dotted lines are obtained from the first order in α perturbation expansion (41) of the full dispersion relation (31). This fact explains the discrepancy and suggests that sensitivity of stability of the Nemtsov membrane to α has been proven to be rather important, quite in accordance with the remark of Barbone and Crighton [7] that the intermediate values of the fluid-loading parameter appear to be the most complicated as it is impossible to label the mode of the fluid-solid system as corresponding solely to a ‘solid mode’ or a ‘fluid mode’. This complication manifests itself in the fact that α is a factor of the nonlinear and non-polynomial in ω operator in (87). By this reason, as soon as α

departs from the origin, the choice of the free membrane mode (35) is less suitable as a first guess to initiate the Newton-like iterative process (96), which therefore works less stably at larger values of α . Parameter continuation proposed, e.g. in [33] in a different setting, only slightly improved performance of our method, reflecting the fact that nonlinear eigenvalue problems of fluid-structure interaction are notoriously hard. Nevertheless, our method allowed to obtain new results in the classical problem in the unprecedentedly broad range of all other important parameters, including, first of all the chord length, dimensionless velocity of the flow, and speed of propagation of elastic waves in the membrane.

6. Concluding Remarks

In this paper we studied conditions for the onset of a radiation-induced instability of the Nemtsov membrane in a uniform flow with free surface. In contrast to previous works [26, 27] that were limited either by the shallow water approximation or by the assumption that the membrane has infinite chord length, we consider the problem in its entirety and take into account both the finite chord of the membrane and the finite depth of the fluid layer.

First, we derive a new integro-differential equation for the deflection of the finite-chord membrane that is coupled to the finite-depth flow.

Then, we develop an analytical procedure allowing to find the eigenvalues of the membrane that is weakly coupled to the flow in the shallow- and deep water approximations. Our original contribution is a systematic procedure that combines Laplace transform, residue calculus, and perturbation of eigenvalues. The analytical solution allowed us to plot detailed stability maps and find a new pattern of intertwining instability tongues that to the best of our knowledge has not been previously reported in the literature. Furthermore, we were able to find analytically the geometrical structure that governs position, orientation and self-intersections of the instability tongues.

Next, we developed an original numerical method to treat the finite-chord membrane in the finite-depth uniform flow with the free surface. With a combination of complex analysis and Galerkin discretization we reduced the boundary eigenvalue problem for an integro-differential equation to an algebraic non-polynomial nonlinear eigenvalue problem and solved it with a Newton-like method. This approach allowed us to explore the onset of instability with respect to the chord length of the membrane, velocity of the flow, and speed of elastic waves propagating along the membrane at small but finite values of the added mass ratio parameter that plays a role of an effective damping due to radiation of surface gravity waves.

We believe we have made a convincing case that the Nemtsov membrane is able to play the same paradigmatic role for understanding radiation-induced instabilities as the famous Lamb oscillator coupled to a string has played for understanding radiation damping. We believe that our procedure is applicable to a broad class of fluid-structure interaction problems that require solving nonlinear eigenvalue problems. An extension of it allowing for a significant continuation with respect to the coupling parameter has proven to be a harder topic that we leave beyond the scope of this paper.

Acknowledgments

We are grateful to Prof. M. L. Overton from the Courant Institute for helpful discussions. We thank the London Mathematical Society for supporting Prof. Overton's visit to Northumbria through the Scheme 4 Research in Pairs grant No 41820. J. L. was supported by a Ph.D. Scholarship from Northumbria University that also provided him with an opportunity to run the code on the High Performance Cluster.

References

- [1] Lamb, H. 1900. On a peculiarity of the wave-system due to the free vibrations of a nucleus in an extended medium. Proc. London Math. Soc. **32**, 208–211.
- [2] Love, A. E. H., 1904. Some illustrations of modes of decay of vibratory motions. Proc. London Math. Soc., **2**, 88–113.
- [3] Beck, G. and Nussenzveig, H. M. 1960. On the physical interpretation of complex poles of the S-Matrix-I. Il Nuovo Cimento, **16**(3), 416–449.

- [4] Ursell, F. 1964. The decay of the free motion of a floating body. *J. Fluid Mech.*, **19**(2), 305–319.
- [5] Nussenzveig, H. M. (ed.) 1972. *Causality and Dispersion Relations*, Mathematics in Science and Engineering 95, Academic Press, New York, NY.
- [6] Crighton, D. G. 1989. The 1988 Rayleigh medal lecture: Fluid loading—the interaction between sound and vibration? *J. Sound Vibr.* **133**(1), 1–27.
- [7] Barbone, P. E. and Crighton, D. G. 1994. Vibrational modes of submerged elastic bodies. *Applied Acoustics* **43**, 295–317.
- [8] Soffer, A. and Weinstein, M. I. 1999. Resonances, radiation damping and instability in Hamiltonian nonlinear wave equations. *Invent. Math.* **136**, 9–74.
- [9] Soffer, A. 2001. Dissipation through dispersion, in: I. M. Sigal and C. Sulem (eds.) *Nonlinear dynamics and renormalization group*, CRM Proceedings and Lecture Notes 27, American Mathematical Society, Providence, RI.
- [10] Fröhlich, J., Gang, Z., 2014. Emission of Cherenkov radiation as a mechanism for Hamiltonian friction. *Adv. Math.* **264**, 183–235.
- [11] Wayne, C. E. and Weinstein, M. I. 2015. *Dynamics of partial differential equations*, Frontiers in Applied Dynamical Systems: Reviews and Tutorials 3, Springer, Cham.
- [12] Olver, P. J. and Sheils, N. E. 2019. Dispersive Lamb systems, *J. Geom. Mech.* **11**(2), 239–254.
- [13] Bertini, M., Noja, D., and Posilicano, A. 2006. Dynamics and Lax-Phillips scattering for generalized Lamb models, *J. Phys. A: Math. Gen.* **39**, 15173–15195.
- [14] Adam, J. A. 2017 *Rays, Waves, and Scattering: Topics in Classical Mathematical Physics*, Princeton Series in Applied Mathematics 56, Princeton University Press, Princeton, NJ.
- [15] Rotter, S. and Gigan, S. 2017 Light fields in complex media: Mesoscopic scattering meets wave control, *Rev. Mod. Phys.* **89**(1), 015005.
- [16] Hagerty, P., Bloch, A. M. and Weinstein, M. I. 2003. Radiation induced instability, *SIAM J. Appl. Math.* **64**(2), 484–524.
- [17] Bloch, A. M., Hagerty, P., Rojo, A. G. and Weinstein, M. I. 2004. Gyroscopically stabilized oscillators and heat baths, *J. Stat. Phys.* **115**, 1073–1100.
- [18] Chandrasekhar, S. 1970. Solutions of two problems in the theory of gravitational radiation. *Phys. Rev. Lett.* **24**(11), 611–615.
- [19] Lindblom, L. and Detweiler, S. L. 1977. On the secular instabilities of the Maclaurin spheroids. *Astrophys. J.*, **211**, 565–567.
- [20] Schutz, B. F. 1980. Perturbations and stability of rotating stars - III. Perturbation theory for eigenvalues. *Mon. Not. R. Astr. Soc.* **190**, 21–31.
- [21] Chandrasekhar, S. 1984. On stars, their evolution and their stability, *Science*, **226**(4674), 497–505.
- [22] Andersson, N. 2003. Gravitational waves from instabilities in relativistic stars, *Class. Quantum Grav.* **20**, R105–R144.
- [23] Belyaev, M. A. 2017. Incompressible modes excited by supersonic shear in boundary layers: Acoustic CFS instability, *Astrophys. J.*, **835**, 238.
- [24] Le Dizès, S. and Billant, P. 2009. Radiative instability in stratified vortices, *Phys. Fluids* **21**, 096602.
- [25] Orozco Estrada, A., Cruz Gómez, R. C., Cros, A., and Le Gal, P. 2020. Coalescence of lenticular anticyclones in a linearly stratified rotating fluid, *Geophys. Astrophys. Fluid Dyn.* **114**(4-5), 504–523.
- [26] Labarbe, J. and Kirillov, O. N. 2020. Membrane flutter induced by radiation of surface gravity waves on a uniform flow. *J. Fluid Mech.*, **901**, A4.
- [27] Nemtsov, B. E. 1985. Flutter effect and emission in the region of anomalous and normal Doppler effects. *Radiophys. Quant. Electronics*, **28**(12), 1076–1079.
- [28] Paidoussis, M. P. 2013 *Fluid-Structure Interactions: Slender Structures and Axial Flow*: 1 2nd edition, Elsevier Academic Press, Cambridge, MA.
- [29] Porter, R. 2015. Linearised water wave problems involving submerged horizontal plates. *Applied Ocean Research*. **50**, 91–109.
- [30] Islam N., Kundu S., and Gayen R. 2019. Scattering and radiation of water waves by a submerged rigid disc in a two-layer fluid. *Proc. R. Soc. A* **475**, 20190331.
- [31] Williams, T. D. and Meylan, M. H. 2012. The Wiener-Hopf and residue calculus solutions for a submerged semi-infinite elastic plate. *J Eng. Math.* **75** 81–106.
- [32] Cho, I. H. and Kim, M. H., 1998 Interactions of a horizontal flexible membrane with oblique incident waves. *J. Fluid Mech.* **367**, 139–161.
- [33] Alben, S. 2008 The flapping-flag instability as a nonlinear eigenvalue problem. *Phys. Fluids* **20**, 104106.
- [34] Shelley, M. J. and Zhang, J. 2011. Flapping and bending bodies interacting with fluid flows. *Annu. Rev. Fluid Mech.* **43** 449–465.
- [35] Mougel, J. and Michelin, S. 2020. Flutter and resonances of a flag near a free surface. *J. Fluids Struct.* **96**, 103046.
- [36] Vedeneev, V. V. 2016. Propagation of waves in a layer of a viscoelastic material underlying a layer of a moving fluid. *J. Appl. Math. Mech.* **80**, 225–243.
- [37] Metrikine, A. V. 1994. Unstable lateral oscillations of an object moving uniformly along an elastic guide as a result of an anomalous Doppler effect. *Acoustical Physics*. **40**, 85–89.
- [38] Gaponov-Grekhov, A. V., Dolina, I. S. and Ostrovskii, L. A. 1983. The anomalous Doppler effect and the radiation instability of oscillator motion in hydrodynamics. *Dokl. Akad. Nauk SSSR* **268**(4), 827–831. In Russian.
- [39] Abramovich, B. S., Mareev, E. A. and Nemtsov, B. E. 1986. Instability in the oscillations of a moving oscillator while it radiates surface and internal waves. *Fluid Dyn.* **21**(1), 147–149.
- [40] Ginzburg, V. L. 1996. Radiation by uniformly moving sources (Vavilov-Cherenkov effect, transition radiation, and other phenomena). *Physics-Uspekhi* **39**(10), 973–982.

- [41] Ginzburg, V. L. and Frank, I. M. 1947. About Doppler effect at superlight velocity. *Dokl. Akad. Nauk SSSR* **56**, 583–586.
- [42] Nezlin, M. V. 1976. Negative-energy waves and the anomalous Doppler effect. *Sov. Phys. Usp.* **19**, 946–954.
- [43] Tamm, I.E. 1960. General characteristics of Vavilov-Cherenkov radiation. *Science* **131**(3395), 206–210.
- [44] Bekenstein, J. D. and Schiffer, M. 1998. The many faces of superradiance. *Phys. Rev. D* **58**, 064014.
- [45] Carusotto, I. and Rousseaux, G. 2013 The Cerenkov effect revisited: from swimming ducks to zero modes in gravitational analogues. In *Analogue Gravity Phenomenology* (ed. D. Faccio, F. Belgiorno, S. Cacciatori, V. Gorini, S. Liberati and U. Moschella), Lecture Notes in Physics, vol. 870. Springer.
- [46] Shi, X., Lin, X., Kaminer, I., Gao, F., Yang, Z., Joannopoulos, J. D., Soljacic, M. and Zhang, B. 2018. Superlight inverse Doppler effect. *Nature Physics* **14**, 1001–1005.
- [47] Minami, H. 1998. Added mass of a membrane vibrating at finite amplitude. *J. Fluids Struct.* **12**, 919–932.
- [48] Kirillov, O. N. 2013. *Nonconservative Stability Problems of Modern Physics*. De Gruyter Studies in Mathematical Physics 14, De Gruyter, Berlin, Boston.
- [49] Kirillov, O. N. and Verhulst, F. 2010 Paradoxes of dissipation-induced destabilization or who opened Whitney's umbrella? *Z. angew. Math. Mech.-ZAMM*, **90**(6), 462–488.
- [50] MacKay, R. S. 1991. Movement of eigenvalues of Hamiltonian equilibria under non-Hamiltonian perturbation, *Phys. Lett. A* **155**, 266–268.
- [51] Haller, G. 1992. Gyroscopic stability and its loss in systems with two essential coordinates. *Int. J. Non-Linear Mech.* **27**, 113–127.
- [52] Bloch, A. M., Krishnaprasad, P. S., Marsden, J. E. and Ratiu, T. S. 1994. Dissipation induced instabilities, *Annales de L'Institut Henri Poincaré – Analyse Non Linéaire* **11**, 37–90.
- [53] Broer, H. and Levi, M. 1995. Geometrical aspects of stability theory for Hill's equations. *Arch. Rational Mech. Anal.* **131**, 225–240.
- [54] Vedeneev, V. V. 2012. Panel flutter at low supersonic speeds. *J. Fluids Struct.*, **29**, 79–96.
- [55] Mehrmann, V. and Voss, H. 2004. Nonlinear eigenvalue problems: A challenge for modern eigenvalue methods. *GAMM-Mitteilungen*, **27**(2), 121–152.
- [56] Bindel, D. and Hood, A. 2015. Localization theorems for nonlinear eigenvalue problems. *SIAM Review*, **57**(4), 585–607.
- [57] Güttel, S. and Tisseur, F. 2017. The nonlinear eigenvalue problem. *Acta Numerica*, 1–94.
- [58] Mensah, G. A., Orchini, A. and Moeck J. P. 2020. Perturbation theory of nonlinear, non-self-adjoint eigenvalue problems: Simple eigenvalues. *J. Sound Vibr.* **473**, 115200.
- [59] Golub, G. H. and Welsch, J. H. 1969. Calculation of Gauss quadrature rules. *Math. Comput.*, **23**(106), 221–230.
- [60] Drela, M. 2014. *Flight Vehicle Aerodynamics*. The MIT Press, Cambridge, MA.
- [61] Schiffer, M. 1960. Analytical theory of subsonic and supersonic flows. In: C. Truesdell (ed.), *Fluid Dynamics / Strömungsmechanik*, Springer, Berlin - Göttingen - Heidelberg.
- [62] Olver, P. J. 2014. *Introduction to Partial Differential Equations*. Springer, Cham.
- [63] Ablowitz, M. S. and Fokas, A. S. 2003. *Complex Variables. Introduction and Applications*. Cambridge Texts in Applied Mathematics, Cambridge University Press, Cambridge, UK.
- [64] Greenbaum, A., Li, R.-C., Overton, M. L. 2020. First-order perturbation theory for eigenvalues and eigenvectors. *SIAM Rev.* **62**, 463–482.
- [65] Delves, L. M. and Lyness, J. N. 1967. A numerical method for locating the zeros of an analytic function. *Math. Comput.*, **21**(100), 543–560.

Conclusion

Throughout this thesis, we have presented and analyzed a series of problems subject all to possible instabilities due to the presence of dissipation or the radiation of wave energy. They all shared the same intrinsic features that are characteristic to this family of systems, i.e. the emission of waves with opposite energy signs and the movement of eigenvalues in the spectrum of the matrix pencil. Although we managed to derive exhaustive dispersion relations for the different configurations, recovering the explicit expressions of growth rates and frequencies from these formulas is most of the time a challenging task to undertake, due to the high polynomial degree or the presence of nonlinear terms. For this purpose, we often made use of the perturbation theory of eigenvalues and the sensitivity analysis of characteristic equations (Kirillov, 2021) to approximate the dispersion curves around critical points. Still, when the settings were too complex to be solved analytically from the latter methods, we developed numerical tools using an *ad-hoc* approach and managed to extract results in agreement with simplified forms of the solutions.

We notably used the perturbation theory of the ideal (undamped) eigenvalues of the Maclaurin spheroids in Chapter 1, to derive a general expression that is valid in the context of simultaneous double damping mechanisms. Once evaluated in the space of the dissipation parameters, the neutral stability surface has a topological singularity known as the Whitney's umbrella, a well-known feature of systems subject to dynamical and dissipation-induced instabilities. As an application for the stability analysis of Maclaurin spheroids, we further consider the critical angular velocity at which a neutron star can rotate, depending on its temperature. This chapter demonstrates the practicality and generality of the results obtained from the different methods that we applied.

The analysis of an isolated stratified geostrophic vortex, as done in chapter 2, is a valuable illustration of the emission of gravitational waves from a single rotating neutron star from the analogy made with the scattering of internal gravity waves. From the consideration of a non-columnar background velocity field, the so-called 'pancake vortex', we perform a linear stability analysis of the equations of motion, by means of the geometrical optics approximation. We therefore recover precedent results on simplified configurations and support the numerical simulations from the literature with original stability domains and instability criteria.

Another interesting double-diffusive system, highlighting a similar behaviour as in the case of the CFS instability, consists of the resistive MHD flows. An extension of already established stability domains is presented in Chapter 3 from a new derivation of the equations of motion, in the form of

a Hain-Lüst differential equation. From a WKB analysis of the latter, we are able to extend the instability maps of this sort of MHD flows in the limit of long-wavelength. This prediction is further confirmed from the numerical simulation of a magnetized Taylor-Couette flow.

Furthermore, we established supplementary connections of our stability results with the physical interpretations present in different domains of application, as in the case of the anomalous Doppler effect and the flutter theory from the Nemtsov membrane (Nemtsov, 1985; Labarbe and Kirillov, 2020; Labarbe and Kirillov, 2021). The latter case, presented in Chapter 4 and Chapter 5, has also been analyzed in terms of the recent discovery of separated domains of inverse Doppler shift, namely the normal (inverse) superlight Doppler effect (Shi et al., 2018). Such connections are, from our point of view, highly important as they enlarge the areas of application of these classical theories and establish thus a more general formulation of these ideas.

From the presentation of these classical problems, we developed a natural treatment for the various dynamical systems involving either dissipation or radiation of wave energy, regardless of their domains of application. We believe that the approaches presented along this thesis are still applicable to a broad range of scientific areas outside of the ones considered here.

FORTHCOMING EXTENSIONS AND FUTURE PROSPECTS

Several continuations are possible due to the general and global aspect of the notion of radiative and diffusive instabilities.

One that could immediately benefit the broadest community would be to consider a boundary value problem associated with the CFS mechanism presented along Chapter 1. Despite demonstrating a highly challenging problem due to the necessity of considering the coupling of Einstein's field equations with the Navier-Stokes system, it would bring new insights on the double-diffusive mechanism and would remove some assumptions on the dynamics of the fluid, e.g., assuming an asymmetric spheroid with arbitrary angular velocity. Moreover, adding thermal diffusion in this seminal problem would be an interesting feature since the hypothesis of isothermal surfaces is not very consistent with the observational data of heated neutron stars.

Chapters 2 and 3 consist in the presentation of original stability results of stratified and magnetized vortices under linear perturbations. Extending the linear stability analysis to the case of nonlinear perturbations is a next step that requires further attention and the use of different analytical and numerical methods.

Regarding Chapters 4 and 5, we could relax physical assumptions of the flow to improve the accuracy of the hydrodynamical model while recovering new physical phenomena and instability windows. Considering the influence of viscosity in the problem of the Nemtsov membrane is indeed left for future works as it destroys the potential aspect of the flow and therefore requires stronger numerical methods to recover the spectrum of the new boundary value problem. Finding a way of considering arbitrary values of the added mass ratio α in the nonlinear problem of the finite membrane is also a challenging but promising objective that shall be considered in the future.

Bibliography

- Abbott, B. P. et al (2016). "Observation of gravitational waves from a binary black hole merger". In: *Phys. Rev. Lett.* 116.6, p. 061102.
- Abramovich, B. S., E. A. Mareev, and B. E. Nemtsov (1986). "Instability in the oscillations of a moving oscillator while it radiates surface and internal waves". In: *Fluid Dynamics* 21.1, pp. 147–149.
- Acheson, D. J. and M. P. Gibbons (1978). "On the instability of toroidal magnetic fields and differential rotation in stars". In: *Philos. Trans. R. Soc. A* 289.1363, pp. 459–500.
- Alben, S. (2008). "The flapping-flag instability as a nonlinear eigenvalue problem". In: *Phys. Fluids* 20, p. 104106.
- Balbus, A. and J.F. Hawley (1992). "A powerful local shear instability in weakly magnetized disks. IV. Nonaxisymmetric perturbations". In: *Astrophys. J.* 400, pp. 610–621.
- Banichuk, N. et al. (2019). *Stability of Axially Moving Materials*. Berlin: Springer.
- Bartello, P. and S.M. Tobias (2013). "Sensitivity of stratified turbulence to the buoyancy Reynolds number". In: *J. Fluid Mech.* 725, p. 1.
- Beckers, M. et al. (2001). "Dynamics of pancake-like vortices in a stratified fluid: experiments, model and numerical simulations". In: *J. Fluid Mech.* 433, pp. 1–27.
- Bekenstein, J. D. and M. Schiffer (1998). "The many faces of superradiance". In: *Phys. Rev. D* 58, p. 064014.
- Benjamin, T. B. (1963). "The threefold classification of unstable disturbances in flexible surfaces bounding inviscid flows". In: *J. Fluid Mech.* 16, pp. 436–450.
- Bigoni, D. et al. (2018). "Flutter and divergence instability in the Pflüger column: Experimental evidence of the Ziegler destabilization paradox". In: *J. Mech. Phys. Solids* 116, pp. 99–116.
- Bilharz, H. (1944). "Bemerkung zu einem Sätze von Hurwitz". In: *Z. Angew. Math. Mech.* 24, pp. 77–82.
- Bindel, D. and A. Hood (2015). "Localization theorems for nonlinear eigenvalue problems". In: *SIAM Review* 57.4, pp. 585–607.
- Bloch, A.M. et al. (1994). "Dissipation induced instabilities". In: *Ann. Henri Poincaré, Anal. Non Linéaire* 11.1, pp. 37–90.
- Bloch, A.M. et al. (2004). "Gyroscopically stabilized oscillators and heat baths". In: *J. Stat. Phys.* 115, pp. 1073–1100.
- Bolotin, V. V. (1963). *Nonconservative Problems of the Theory of Elastic Stability*. United Kingdom: Pergamon Press.
- Braviner, H.J. and G.I. Ogilvie (2014). "Tidal interactions of a Maclaurin spheroid—I. Properties of free oscillation modes". In: *Mon. Not. R. Astr. Soc.* 441.3, pp. 2321–2345.

- Braviner, H.J. and G.I. Ogilvie (2015). "Tidal interactions of a Maclaurin spheroid-II. Resonant excitation of modes by a close, misaligned orbit". In: *Mon. Not. R. Astr. Soc.* 447.2, pp. 1141–1153.
- Broer, H. and M. Levi (1995). "Geometrical aspects of stability theory for Hill's equations". In: *Arch. Rational Mech. Anal.* 131, pp. 225–240.
- Buća, B. and D. Jaksch (2019). "Dissipation induced nonstationarity in a quantum gas". In: *Phys. Rev. Lett.* 123.26, p. 260401.
- Buckingham, C.E., J. Gula, and X. Carton (2021). "The role of curvature in modifying frontal instabilities. Part I: Review of theory and presentation of a nondimensional instability criterion". In: *J. Phys. Oceanogr.* 51.2, pp. 299–315.
- Carusotto, I. and G. Rousseaux (2013). "The Cerenkov Effect Revisited: From Swimming Ducks to Zero Modes in Gravitational Analogues". In: *Analogue Gravity Phenomenology*. Ed. by D. Faccio et al. Cham: Springer, pp. 109–144.
- Chandrasekhar, S. (1961). *Hydrodynamic and hydromagnetic stability*. Oxford: Clarendon Press.
- (1969). *Ellipsoidal Figures of Equilibrium*. Vol. 72. Yale Univ. Press.
- (1970a). "Solutions of two problems in the theory of gravitational radiation." In: *Phys. Rev. Lett.* 24.11, pp. 611–615.
- (1970b). "The effect of gravitational radiation on the secular stability of the Maclaurin spheroid". In: *Astrophys. J.* 161, pp. 561–569.
- Chandrasekhar, S. and F. P. Esposito (1969b). "The $2^{1/2}$ -post-Newtonian equations of hydrodynamics and radiation reaction in general relativity". In: *Astrophys. J.* 158, pp. 153–179.
- Cho, I. H. and M. H. Kim (1998). "Interactions of a horizontal flexible membrane with oblique incident waves". In: *J. Fluid Mech.* 367, pp. 139–161.
- Comins, N. (1979a). "On secular instabilities of rigidly rotating stars in general relativity – I. Theoretical formalism". In: *Mon. Not. R. Astr. Soc.* 189, pp. 233–253.
- (1979b). "On secular instabilities of rigidly rotating stars in general relativity – I. Numerical results". In: *Mon. Not. R. Astr. Soc.* 189, pp. 255–272.
- Das, S., T. Sahoo, and M. H. Meylan (2018). "Dynamics of flexural gravity waves: from sea ice to Hawking radiation and analogue gravity". In: *Proc. R. Soc. A* 474, p. 20170223.
- Davidson, P. (2001). *An Introduction to Magnetohydrodynamics*. Cambridge Texts in Applied Mathematics. Cambridge: Cambridge University Press.
- Deguchi, K. (2017). "Linear instability in Rayleigh-stable Taylor-Couette flow". In: *Phys. Rev. E* 95.2, p. 021102.
- Doaré, O. and E. de Langre (2006). "The role of boundary conditions in the instability of one-dimensional systems". In: *Eur. J. Mech. B/Fluids* 25, pp. 948–959.
- Dritschel, D. G. and Á. Viúdez (2003). "A balanced approach to modelling rotating stably stratified geophysical flows". In: *J. Fluid Mech.* 488, pp. 123–150.

- Eunok, Y., P. Billant, and C. Menesguen (2016). "Stability of an isolated pancake vortex in continuously stratified-rotating fluids". In: *J. Fluid Mech.* 801, pp. 508–553.
- Flowers, E. and N. Itoh (1976). "Transport properties of dense matter." In: *Astrophys. J.* 206, pp. 218–242.
- Gaponov-Grekhov, A. V., I. S. Dolina, and L. A. Ostrovskii (1983). "The anomalous Doppler effect and the radiation instability of oscillator motion in hydrodynamics". In: *Doklady Akad. Nauk SSSR* 268.4, pp. 827–831.
- Ginzburg, V. L. and I. M. Frank (1947). "On the Doppler effect at the superluminal velocity". In: *Dokl. Akad. Nauk SSSR* 56, pp. 583–586.
- Ginzburg, V.L. (1996). "Radiation by uniformly moving sources (Vavilov-Cherenkov effect, transition radiation, and other phenomena)". In: *Physics-Uspekhi* 39.10, pp. 973–982.
- Glampedakis, K. and L. Gualtieri (2018). "Gravitational waves from single neutron stars: an advanced detector era survey". In: *The Physics and Astrophysics of Neutron Stars*. Ed. by Astrophysics and Space Science Library. Vol. 457. Cham: Springer, pp. 673–736.
- Godoy-Diana, R. and J.M. Chomaz (2003). "Effect of the Schmidt number on the diffusion of axisymmetric pancake vortices in a stratified fluid". In: *Phys. Fluids* 15.4, pp. 1058–1064.
- Godoy-Diana, R., J.M. Chomaz, and P. Billant (2004). "Vertical length scale selection for pancake vortices in strongly stratified viscous fluids". In: *J. Fluid Mech.* 504, pp. 229–238.
- Goedbloed, J., R. Keppens, and S. Poedts (2010). *Advanced Magnetohydrodynamics: With Applications to Laboratory and Astrophysical Plasmas*. Cambridge: Cambridge University Press.
- Gula, J., V. Zeitlin, and R. Plougonven (2009). "Instabilities of two-layer shallow-water flows with vertical shear in the rotating annulus". In: *J. Fluid Mech.* 638.27, p. 27.
- Güttel, S. and F. Tisseur (2017). "The nonlinear eigenvalue problem". In: *Acta Numerica*, pp. 1–94.
- Hagerty, P., A.M. Bloch, and M.I. Weinstein (2003). "Radiation induced instability". In: *SIAM J. Appl. Math.* 64.2, pp. 484–524.
- Hain, K. and R. Lüst (1958). "Zur Stabilität zylindersymmetrischer plasmakonfigurationen mit volumenströmen". In: *Z. Naturforsch. A* 13.11, pp. 936–940.
- Hollerbach, R. and G. Rüdiger (2005). "New type of magnetorotational instability in cylindrical Taylor-Couette flow". In: *Phys. Rev. Lett.* 95.12, p. 124501.
- Hollerbach, R., V. Teeluck, and G. Rüdiger (2010). "Nonaxisymmetric magnetorotational instabilities in cylindrical Taylor-Couette flow". In: *Phys. Rev. Lett.* 104.4, p. 044502.
- Holopäinen, E.O. (1961). "On the effect of friction in baroclinic waves". In: *Tellus* 13.3, pp. 363–367.
- Ipser, J.R. and L. Lindblom (1991). "The oscillations of rapidly rotating Newtonian stellar models. II-Dissipative effects". In: *Astrophys. J.* 373, pp. 213–221.

- Kelvin, W. T. B. and P. G. Tait (1867). *Treatise on Natural Philosophy*. Clarendon Press.
- Kirillov, O. and F. Stefani (2013). "Extending the range of the inductionless magnetorotational instability". In: *Phys. Rev. Lett.* 111(6), p. 061103.
- Kirillov, O. N. (2005). "A theory of the destabilization paradox in non-conservative systems". In: *Acta Mechanica* 174.3, pp. 145–166.
- (2007). "Gyroscopic stabilization in the presence of nonconservative forces". In: *Doklady Mathematics* 76.2, pp. 780–785.
- (2017). "Singular diffusionless limits of double-diffusive instabilities in magnetohydrodynamics". In: *Proc. R. Soc. A* 473.2205, p. 20170344.
- (2021). *Nonconservative Stability Problems of Modern Physics*. 2nd rev. and exten. edition. Vol. 14. De Gruyter Studies in Mathematical Physics. Berlin, Boston: De Gruyter.
- Kirillov, O. N. and I. Mutabazi (2017). "Short wavelength local instabilities of a circular Couette flow with radial temperature gradient". In: *J. Fluid Mech.* 818, pp. 319–343.
- Kirillov, O. N., F. Stefani, and Y. Fukumoto (2014). "Local instabilities in magnetized rotational flows: a short-wavelength approach". In: *J. Fluid Mech.* 760, pp. 591–633.
- Kirillov, O. N. and F. Verhulst (2010). "Paradoxes of dissipation-induced destabilization or who opened Whitney's umbrella?" In: *Zeitschrift fur angewandte Mathematik und Mechanik-ZAMM* 90.6, 462 – 488.
- Krechetnikov, R. and J. E. Marsden (2007). "Dissipation-induced instabilities in finite dimensions". In: *Rev. Mod. Phys.* 79.2, pp. 519–553.
- Labarbe, J. and O.N. Kirillov (2020). "Membrane flutter induced by radiation of surface gravity waves on a uniform flow". In: *J. Fluid Mech.* 901, A4.
- (2021). "Radiation-induced instability of a finite-chord Nemtsov membrane". In: *arXiv preprint arXiv:2104.01060*.
- Lamb, H. (1900). "On a peculiarity of the wave-system due to the free vibrations of a nucleus in an extended medium". In: *Proc. London Math. Soc.* 32, pp. 208–211.
- Lazar, A., A. Stegner, and E. Heifetz (2013). "Inertial instability of intense stratified anticyclones. Part 1. Generalized stability criterion". In: *J. Fluid Mech.* 732, pp. 457–484.
- Liénard, A. and M. H. Chipart (1914). "Sur le signe de la partie réelle des racines d'une équation algébrique". In: *J. Math. Pures Appl.* 10.6, pp. 291–346.
- Lindblom, L. (1986). "Estimates of the maximum angular velocity of rotating neutron stars". In: *Astrophys. J.* 303, pp. 146–153.
- (1995). "Critical angular velocities of rotating neutron stars". In: *Astrophys. J.* 438, pp. 265–268.
- Lindblom, L. and S. L. Detweiler (1977). "On the secular instability of the Maclaurin spheroids". In: *Astrophys. J.* 211, pp. 565–567.
- Liouville, J. (1851). "Mémoire sur les figures ellipsoïdales à trois axes inégaux, qui peuvent convenir à l'équilibre d'une masse liquide homogène, douée d'un mouvement de rotation". In: *J. Math. Pures Appl.* 16, pp. 241–254.

- Liu, W. et al. (2006). "Helical magnetorotational instability in magnetized Taylor-Couette flow". In: *Phys. Rev. E* 74.5, p. 056302.
- Lyra, W. and O.M. Umurhan (2019). "The initial conditions for planet formation: Turbulence driven by hydrodynamical instabilities in disks around young stars". In: *Publ. Astron. Soc. Pac* 131.1001, p. 072001.
- Maclaurin, C. (1742). *A Treatise of Fluxions: In Two Books*. 1. Vol. 72. Ruddiman.
- Magri, L. (2019). "Adjoint methods as design tools in thermoacoustics". In: *Appl. Mech. Rev.* 71.2.
- Maïssa, P., G. Rousseaux, and Y. Stepanyants (2016). "Negative energy waves in a shear flow with a linear profile". In: *Eur. J. Mech. B Fluids* 56, pp. 192–199.
- Maïssa, P., G. Rousseaux, and Y. Stepanyants (2016). "Negative energy waves in a shear flow with a linear profile". In: *Eur. J. Mech. B/Fluids* 56, pp. 192–199.
- McIntyre, M. E. (1970). "Diffusive destabilization of the baroclinic circular vortex". In: *Geophys. Fluid Dyn.* 1, pp. 19–57.
- Mehrmann, V. and H. Voss (2004). "Nonlinear eigenvalue problems: A challenge for modern eigenvalue methods". In: *GAMM-Mitteilungen* 27.2, pp. 121–152.
- Mensah, G.A., A. Orchini, and J.P. Moeck (2020). "Perturbation theory of nonlinear, non-self-adjoint eigenvalue problems: Simple eigenvalues". In: *J. Sound Vibr.* 473, p. 115200.
- Metrikine, A.V. (1994). "Unstable lateral oscillations of an object moving uniformly along an elastic guide as a result of an anomalous Doppler effect". In: *Acoustical Physics* 40, pp. 85–89.
- Meyer, C. O. (1842). "De aequilibrii formis ellipsoidicis". In: *J. Reine Angew. Math.* 24, pp. 44–59.
- Mougel, J. and S. Michelin (2020). "Flutter and resonances of a flag near a free surface". In: *J. Fluids Struct.* 96, p. 103046.
- Nemtsov, B. E. (1985). "Flutter effect and emission in the region of anomalous and normal Doppler effects". In: *Radiophys. Quant. Elect.* 28.12, pp. 1076–1079.
- Newman, B. G. and M. P. Paidoussis (1991). "The stability of two-dimensional membranes in streaming flow". In: *J. Fluids Struct.* 5, pp. 443–454.
- Nezlin, M. V. (1976). "Negative-energy waves and the anomalous Doppler effect". In: *Sov. Phys. Uspekhi* 19, pp. 946–954.
- Orozco Estrada, A. et al. (2020). "Coalescence of lenticular anticyclones in a linearly stratified rotating fluid". In: *Geophys. Astrophys. Fluid Dyn.* 114.4–5, pp. 504–523.
- Riemann, B. (1861). "Ein Beitrag zu den Untersuchungen über die Bewegung eines gleichartigen flüssigen ellipsoides". In: *Abh. d. Königl. Gesell. der Wiss. zu Göttingen* 9, pp. 3–36.
- Roberts, P. H. and K. Stewartson (1963). "On the stability of a Maclaurin spheroid of small viscosity". In: *Astrophys. J.* 139, pp. 777–790.
- Rüdiger, G. et al. (2010). "On the stability of an accretion disc containing a toroidal magnetic field". In: *Phys. Rev. E* 82.1, p. 016319.

- Rüdiger, G. et al. (2014). "Astrophysical and experimental implications from the magnetorotational instability of toroidal fields". In: *Mon. Not. R. Astr. Soc.* 438.1, pp. 271–277.
- Russell, J.A. (1844). "Report on waves". In: *Rep. Br. Assoc. Adv. Sci.*, pp. 311–390.
- Schutz, B. F. and J. L. Friedman (1978a). "Langrangian perturbation theory of nonrelativistic fluids". In: *Astrophys. J.* 221, pp. 937–957.
- (1978b). "Secular instability of rotating Newtonian stars". In: *Astrophys. J.* 222, pp. 281–296.
- Seilmayer, M. et al. (2014). "Experimental evidence for nonaxisymmetric magnetorotational instability in a rotating liquid metal exposed to an azimuthal magnetic field". In: *Phys. Rev. Lett.* 113.2, p. 024505.
- Shelley, M. J. and J. Zhang (2011). "Flapping and bending bodies interacting with fluid flows". In: *Annu. Rev. Fluid Mech.* 43, pp. 449–465.
- Shi, X. et al. (2018). "Superlight inverse Doppler effect". In: *Nature Physics* 14, pp. 1001–1005.
- Singh, S. and M. Mathur (2019). "Effects of Schmidt number on the short-wavelength instabilities in stratified vortices". In: *J. Fluid Mech.* 867, pp. 765–803.
- Stefani, F. et al. (2006). "Experimental evidence for magnetorotational instability in a Taylor-Couette flow under the influence of a helical magnetic field". In: *Phys. Rev. Lett.* 97.18, p. 184502.
- Stefani, F. et al. (2009). "Helical magnetorotational instability in a Taylor-Couette flow with strongly reduced Ekman pumping". In: *Phys. Rev. E* 80.6, p. 066303.
- Sygulski, R (2007). "Stability of membrane in low subsonic flow". In: *Int. J. Non-Linear Mech.* 42.1, pp. 196–202.
- Tamm, I.E. (1960). "General characteristics of Vavilov-Cherenkov radiation". In: *Science* 131.3395, pp. 206–210.
- Terquem, C. and J.C. Papaloizou (1996). "On the stability of an accretion disc containing a toroidal magnetic field". In: *Astrophys. J.* 279.3, pp. 767–784.
- Thomson, W. (1887). "On ship waves". In: *Lecture delivered at the "Conversazione" in the Science and Art Museum, Edinburgh*.
- Thorne, K. S. (1969a). "Nonradial pulsation of general-relativistic stellar models. III. Analytic and numerical results for neutron stars". In: *Astrophys. J.* 158, pp. 1–16.
- (1969b). "Nonradial pulsation of general-relativistic stellar models. IV. The weakfield limit". In: *Astrophys. J.* 158, pp. 997–1019.
- Tiomkin, S. and D. E. Raveh (2017). "On the stability of two-dimensional membrane wings". In: *J. Fluids Struct.* 71, pp. 143–163.
- Tuckerman, L.S. (2001). "Thermosolutal and binary fluid convection as a 2×2 matrix problem". In: *Physica D* 156.3–4, pp. 325–363.
- Vedeneev, V. V. (2012). "Pannel flutter at low supersonic speeds". In: *J. Fluids Struct.* 29, pp. 79–96.
- (2016). "On the application of the asymptotic method of global instability in aeroelasticity problems". In: *Proc. Steklov Inst. Math.* 295, pp. 274–301.

- Vidal, J. et al. (2019). "Fossil field decay due to nonlinear tides in massive binaries". In: *A & A* 629, A142.
- Yim, E. and P. Billant (2016). "Analogies and differences between the stability of an isolated pancake vortex and a columnar vortex in stratified fluid". In: *J. Fluid Mech.* 796, pp. 732–766.
- Yim, E., A. Stegner, and P. Billant (2019). "Stability criterion for the centrifugal instability of surface intensified anticyclones". In: *J. Phys. Oceanogr.* 49.3, pp. 827–849.
- Zou, R. and Y. Fukumoto (2014). "Local stability analysis of the azimuthal magnetorotational instability of ideal MHD flows". In: *Prog. Theor. Exp. Phys.* 2014.11, 113J01.
- Zou, R. et al. (2020). "Analysis of azimuthal magnetorotational instability of rotating magnetohydrodynamic flows and Tayler instability via an extended Hain-Lüst equation". In: *Phys. Rev. E* 101.1, p. 013201.